The effects of graphene and other nanomaterials on the electrocatalytic behaviour of phthalocyanines

A thesis submitted in fulfilment of the requirements for the degree

Of

DOCTOR OF PHILOSOPHY

Of

Rhodes University

By

Munyaradzi Shumba

March 2017

DEDICATION

To My Parents (Jethro and Lillian),

Rose T. Shumba my love and Runyararo Lillian Shumba my daughter

My siblings Lonjiva, Rejoice, Nyasha, Josia and Godknows,

indeed only God knew we could make it this far together

Abstract

Carbon based nanomaterials, gold nanorods and metallophthalocyanine nanoconjugates have been developed for electrocatalysis. Carbon based nanomaterials used are multiwalled carbon nanotubes, pristine graphene oxide nanosheets, nitrogen, boron, sulphur, phosphorus doped graphene oxide nanosheets. Cobalt phthalocyanine (CoPc), cobalt tetra aminophenoxy phthalocyanine (CoTAPc), cobalt tetra aminophenoxy phthalocyanine (CoTAPhPc), cobalt mono carboxyphenoxy phthalocyanine (CoMCPhPc) and cobalt tetra carboxyphenoxy phthalocyanine (CoTCPhPc) are the phthalocyanines employed in this work. Metallophthalocyanines were employed either in their bulk form or in their nanosized form. Electrode modification by these nanomaterials was either done sequentially, premixed or linked nanoconjugates. In all sequential modification, phthalocyanines were employed on top of other nanomaterials. Sequentially modified electrodes gave higher detection currents than both premixed and covalently bonded nanoconjugates. The nanomaterials reported here were characterised by transmission electron microscopy, Raman spectroscopy, time of flight secondary ion mass spectrometry, and X-ray diffraction among other techniques. The modified electrodes were further characterised by scanning electron microscopy, scanning electrochemical microscopy, X-ray photoelectron spectroscopy and cyclic voltammetry, while square wave, linear scan and cyclic voltammetry, rotating disc electrode and chronoamperometry have been used to evaluate the electrocatalytic behaviour of the previously mentioned towards either oxidation or reduction of L-cysteine and/or

hydrogen peroxide respectively. Generally, the nanoconjugates resulted in superior catalytic performance compared to the performance of individual nanomaterials.

Zinc octacarboxy phthalocyanine (ZnOCPc) conjugated to either GONS or rGONS were employed to compare electrocatalytic detection of hydrogen peroxide to its luminescence sensing

Acknowledgements

My sincere gratitude goes to my supervisor, **Prof. T. Nyokong** for her invaluable guidance, mentorship and for giving me an opportunity, support and an enabling environment. Thank you Prof for believing in me even when it seemed impossible. I cannot imagine how this journey could have been without you.

I am indebted to Dr Uddin and Francis for all the assistance with XPS, Donovan for the graphics.

S22, guys I cannot single out anyone. You have been such a good family during this journey.

Special thanks to Gail for timely updates on group events and all the administration behind it.

Shirley and Malvern, thank you very much for your patience and assistance with TEM and SEM.

Chemistry Department at large, I thank you.

Rhodes University and National Research Foundation for a PhD funding.

Table of Contents

List of Abbreviations

BE	=	binding energy
CSPE	=	carbon screen printed electrode
CV	=	cyclic voltammetry
DAMN	=	diaminomaleonitrile
DBU	=	1,8-diazabicyclo [5.4.0]undec-7-ene
DCC	=	dicyclohexylcarbodiimide
DMF	=	dimethylformamide
DMSO	=	dimethylsulphoxide
FTIR	=	Fourier transform infra-red
GCE	=	glassy carbon electrodes
GPES	=	general purpose electrochemical system
HOMO	=	highest occupied molecular orbital
LSV	=	linear scan voltammetry
LUMO	=	lowest unoccupied molecular orbital
MPA	=	mercapto propanoic acid
MAPc	=	mono amino phthalocyanine
MPcs	=	metallophthalocyanines

MPS	=	mesoporous silica
MWCNTs	=	multi walled carbon nanotubes
NPs	=	nanoparticles
NRs	=	nanorods
ORR	=	oxygen reduction reaction
PB	=	prussian blue
rBDGONS	=	reduced Boron doped graphene oxide nanosheets
RDE	=	rotating disc electrode
rGONS	=	reduced graphene oxide nanosheets
rNDGONS	=	reduced nitrogen doped graphene oxide nanosheets
rPDGONS	=	reduced phosphorus doped graphene oxide nanosheets
rPNDGONS	=	reduced phosphorus nitrogen co doped graphene oxide nanosheets
rSDGONS	=	reduced sulphur doped graphene oxide nanosheets
SEM	=	scanning electron microscopy
SECM	=	scanning electrochemical microscopy

SNDGONS	=	sulphur nitrogen co doped graphene oxide nanosheets
SPAuE	=	screen printed gold electrode
SWV	=	square wave voltammetry
TAPc	=	tetra amino phthalocyanine
TBAB	=	tetra butyl ammonium bromide
TEM	=	transmission electron microscopy
TIP	=	tetra-iso-pentyloxyphthalocyanine
TTMP	=	Tetra-α-(2,2,4- trimethyl-3-pentyloxy)
TSPc	=	tetra sulfo phthalocyanine
ORR	=	oxygen reduction reaction
HRP	=	horse radish peroxidise
UME	=	ultra-micro electrode
UV/vis	=	ultraviolet/visible
XPS	=	X-ray photoelectron spectroscopy
XRD	=	X-ray diffraction

List of Symbols

β	=	adsorption equilibrium constant
C_o	=	bulk concentration
k_{cat}	=	catalytic rate constant
I_{cat}	=	currents in the presence of analyte
I_{buf}	=	currents in the absence analyte
D	=	diffusion coefficient
A	=	effective electrode area
F	=	Faraday's constant
F_0	=	fluorescence intensities in the absence of H_2O_2
F	=	fluorescence intensities in the presence of H_2O_2
ΔG	=	Gibbs energy change due to adsorption
V	=	kinematic viscosity
I_l	=	limiting current
I_{max}	=	maximum current
n_a	=	number of electrons involved in the rate determining step
E_p	=	peak potential
ΔE	=	peak potential separation
I_p	=	peak current
ω	=	rotational
υ	=	scan rate
K	=	Stern–Volmer quenching rate constant

Γ	=	surface coverage
σ	=	standard deviation
T	=	temperature (298 K)
α	=	transfer coefficient
R	=	universal gas constant

Chapter One

1. Introduction

The main aim of this work is to develop novel hybrids of metallophthalocyanine (MPcs), with carbon-based nanomaterials {multiwalled carbon nanotubes (MWCNTs), reduced graphene oxide nanosheets (GONS)} and gold nanorods (AuNRs) for electrocatalysis. A small section deals with optical detection for comparison purpose.

1.1 Metallophthalocyanines

1.1.1 Synthesis and general applications.

Metallophthalocyanine (MPc) complexes have traditionally been used as dyes and pigments due to their chemical, thermal, and photo stability [1]. These attractive properties have of late seen phthalocyanines being used in a myriad of fields such as in photodynamic therapy [2–4], as pigments in the paint industry [5], as electrocatalysts [6–8] and in optical sensing [9,10] among other fields. Properties of MPcs are influenced by factors such as the central metal, its oxidation state and the nature of substituent at alpha (α) or beta (β) positions. General synthesis of phthalocyanines mainly utilises a host of substituted phthalic acid derivatives, which includes anhydrides, imides, amides and nitriles. Phthalic acids can be converted into all the precursors as demonstrated in **Scheme 1.1**. The phthalonitriles become the most important precursor in the laboratories while phthalic acid is the industrial precursor for phthalocyanine synthesis. In order to identify substitution positions, two numbering systems for the carbon atoms of the phthalocyanine core are adopted and given in **Fig. 1.1.** Positions 1, 4, 8, 11, 15, 18, 22, 25

are referred to as α positions while positions 2, 3, 9, 10, 16, 17, 23 and 24 are referred to as β.

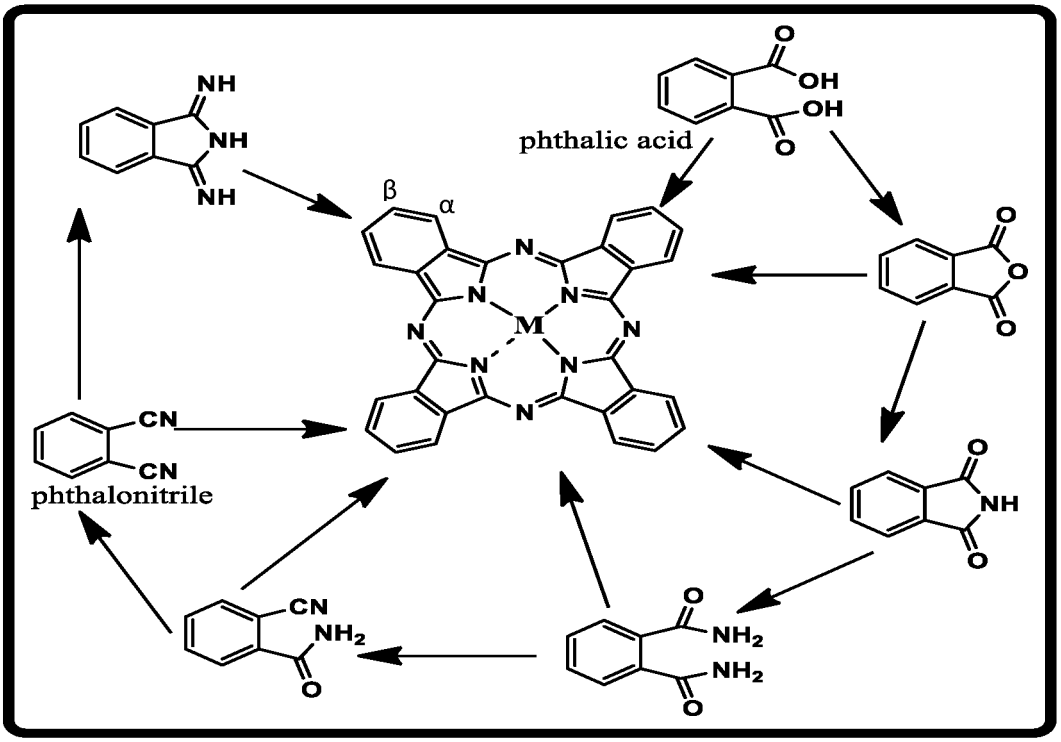

Scheme 1.1 Metallophthalocyanine synthesis [1].

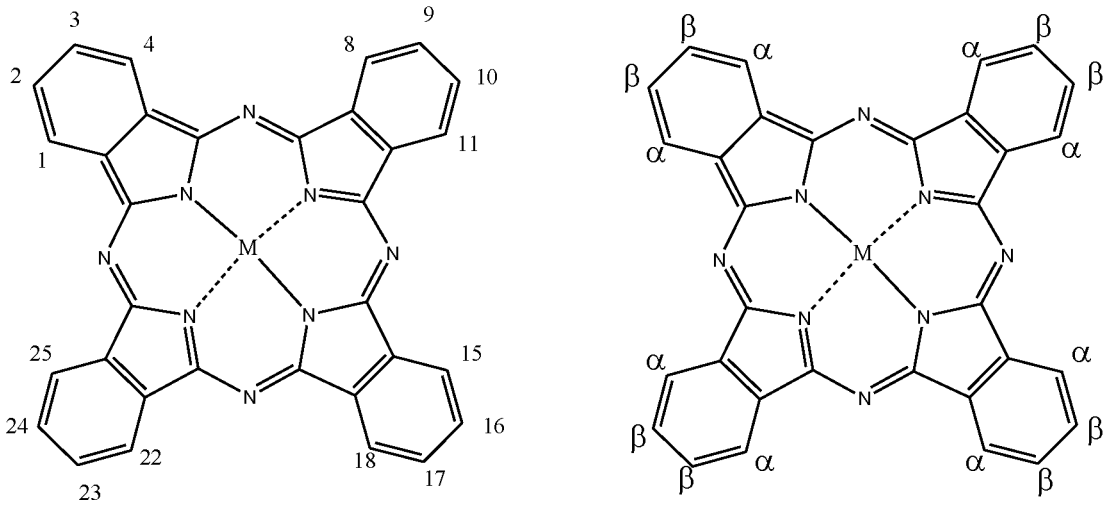

Fig. 1.1 Numbering Scheme for phthalocyanine core

1.1.1.1. Tetra substituted Metallophthalocyanines

Symmetric tetra substituted MPcs are obtained through cyclotetramerization of phthalic acid derivatives. The commonly used substituted phthalic acid derivatives in the laboratory are either 3 or 4 phthalonitrile. The cyclotetramerization reaction takes place at high temperatures in the presence of a solvent, catalyst, the desired substituted phthalic acid derivative and a metal salt of choice. Synthesis of tetra-substituted phthalocyanines however results in a number of isomers. **Fig 1.2** shows the different positional isomers that result from the synthesis of tetra α-substituted phthalocyanines. The yields of each are usually influenced by the nature of the substituent [1]. In most cases the separation of these isomers is a challenge since they have comparable solubility in many solvents and similar retention factors in a number of chromatographic systems leading to application in their mixed isomer forms [11]. The different isomers were not separated when used in this work.

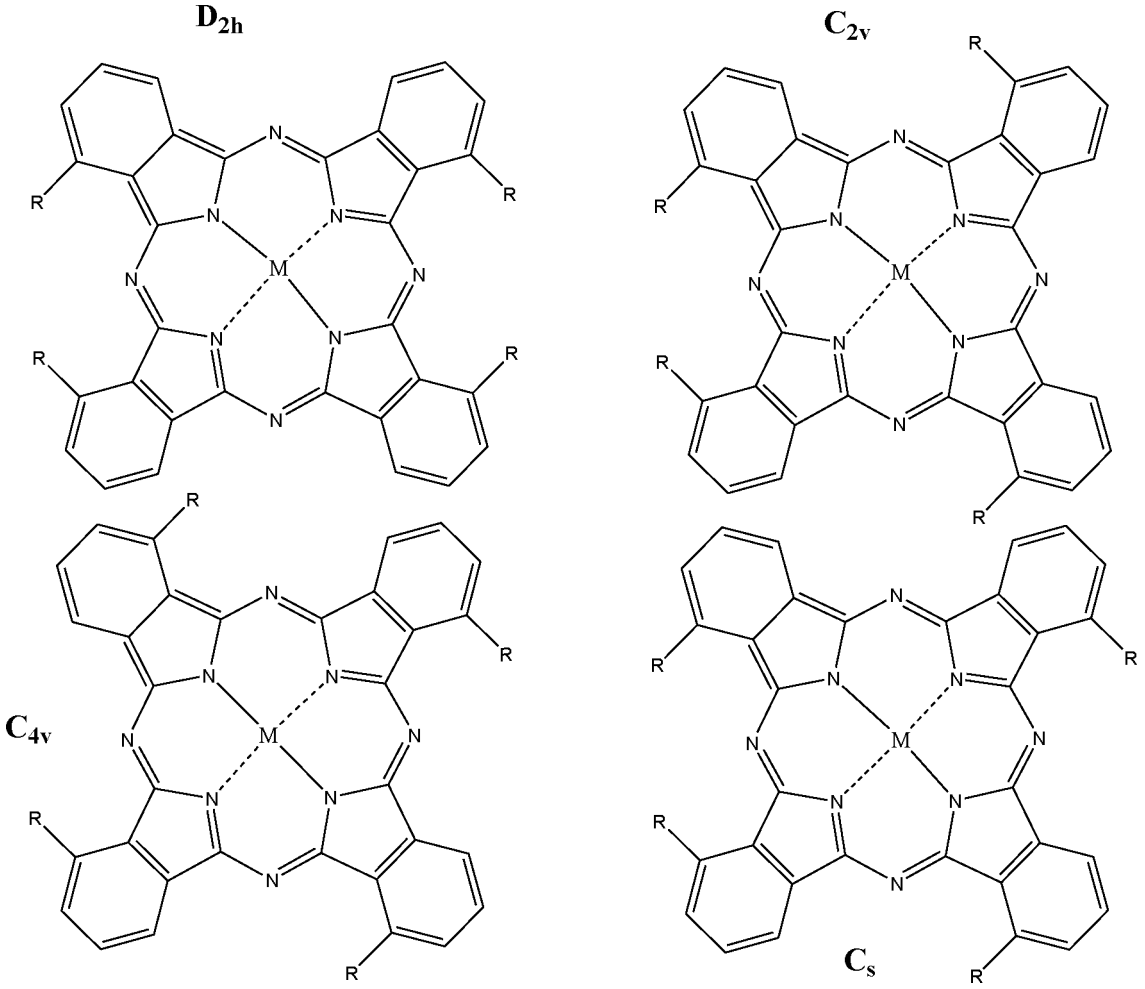

Fig. 1.2 Position isomers resulting from α-tetra substituted phthalocyanines

1.1.1.2 Mono substituted MPcs

The use of phthalonitrilederivatives with different substituents for the synthesis of phthalocyanines results in asymmetric products as illustrated in **Scheme 1.2.** A number of approaches have been used to attaining the desired product among them; cross condensation between two phthalonitrile components, the subphthalocyanine ring-expansion method, post modification approaches on pre-formed symmetric or asymmetric phthalocyanine systems [12] and polymer support synthesis [13]. The most common approach however is the cross condensation between two

phthalonitrile components or diiminoisondolines in a ratio that favours the desired product. Use of 3:1 ratio favours A_3B formation even though the other products may not be completely avoided. Separation from other products by chromatography is a challenge and normally results in very small yields [14].

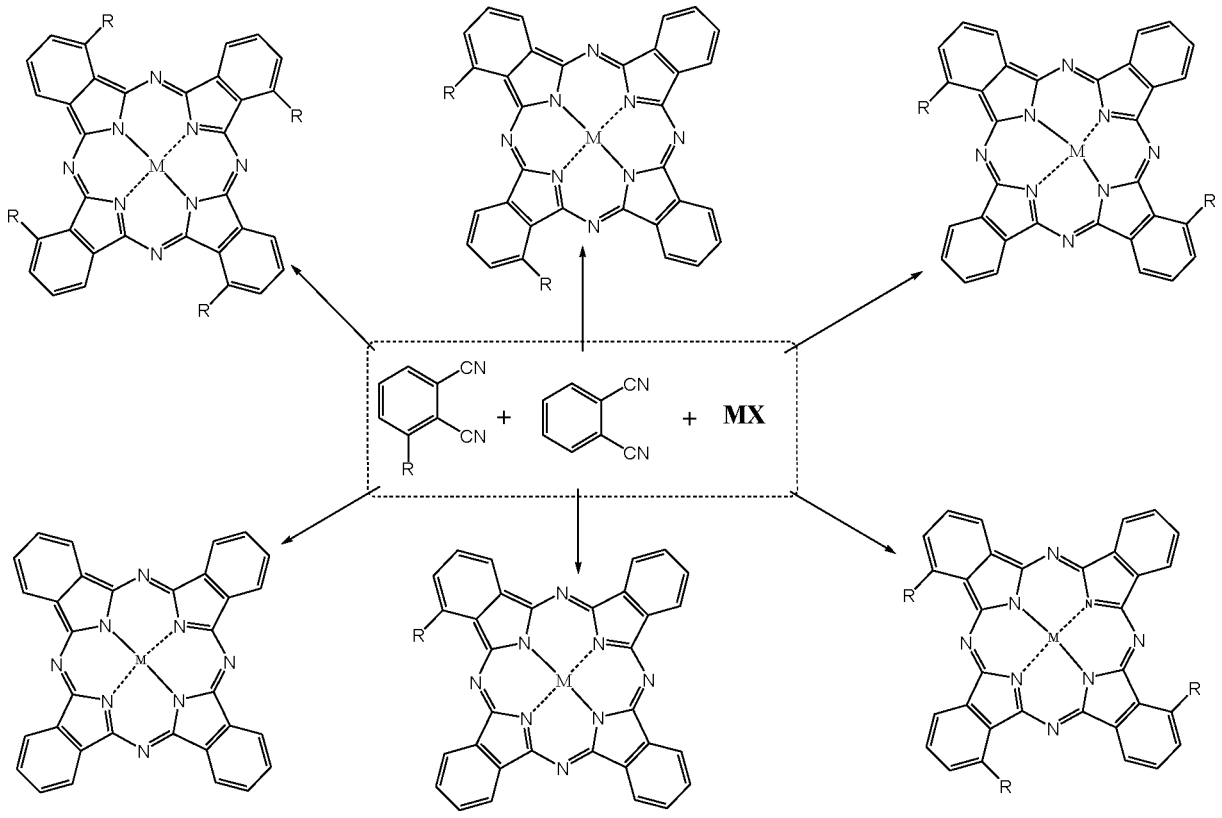

Scheme 1.2 Asymmetric MPcs synthesis.

1.1.2 Metallophthalocyanines used in this Thesis

Cobalt based phthalocyanines [Co tetra aminophenoxy phthalocyanine {CoTAPhPc (**1**)}, Co tetracarboxy phenoxy phthalocyanine {CoTCPhPc (**2**)}, Co phthalocyanine {CoPc(**3**)}, Co mono carboxy phenoxy phthalocyanine {CoMCPhPc(**4**)} and Co tetra amino phthalocyanine {CoTAPc (**5**)}, **Fig.1.3**, were used for electrocatalytic detection of either L-cysteine or hydrogen peroxide or both. The choice of cobalt based MPcs was influenced by the fact that these

are well known for their catalytic activity [6,7,15,16]. The choice for **4** (reported in this work for the first time) was influenced by the possibility of specific binding site to the graphene oxide nanomaterials since it contains only one substituent. The use of **1** and **2** was influenced by bulky substituent groups which have a significant influence on discouraging aggregation [17] as compared to **3** and **5**. Complex **2** [18] and **5** [19,20] have been reported before while complex **3** and **5** are commercially available. Different forms of linkage, (π-π, amide, gold-nitrogen and gold-sulphur) of the MPcs to graphene oxide, multiwalled carbon nanotubes and AuNRs were established before testing the hybrids towards the electrocatalysis of hydrogen peroxide or L-cysteine.

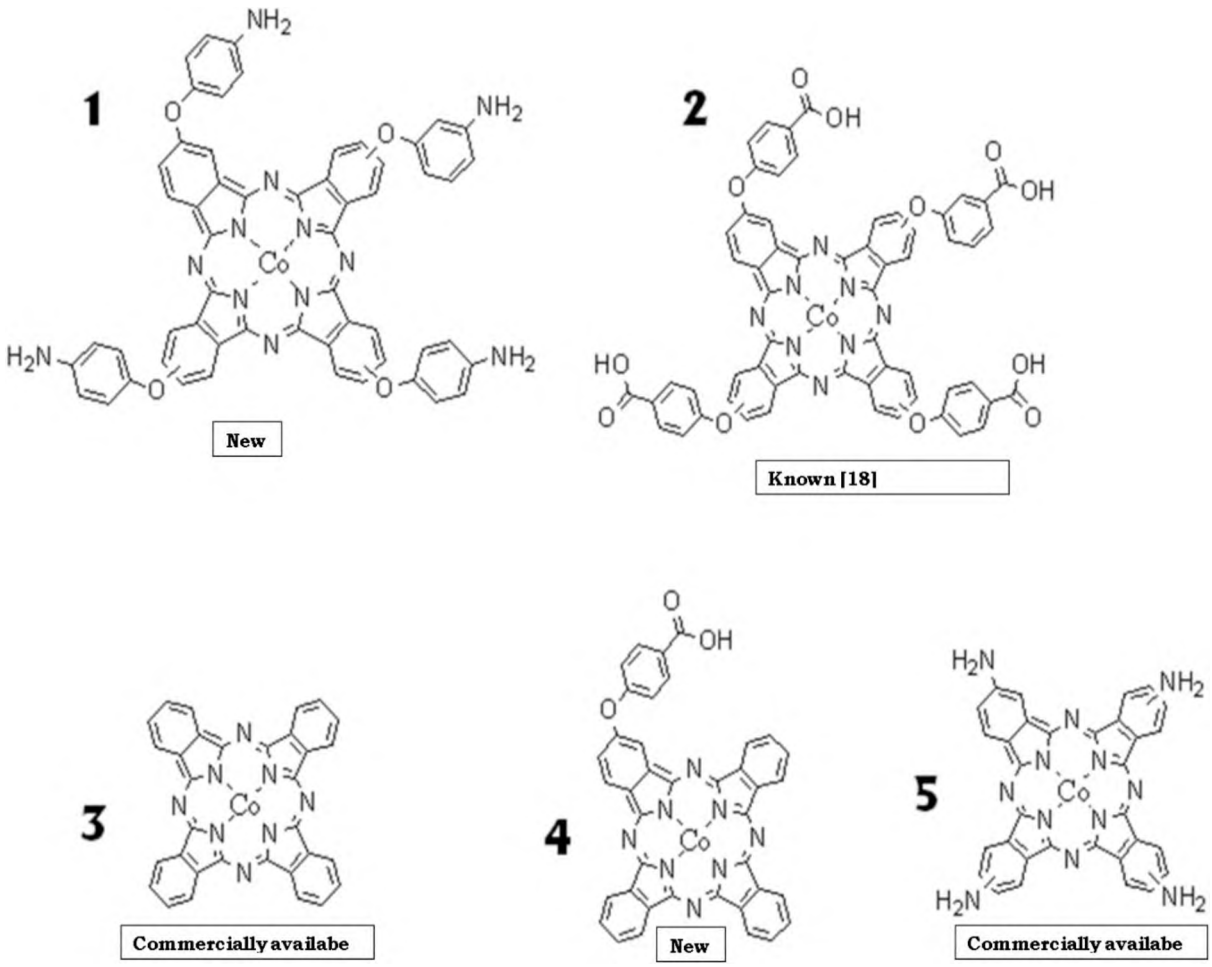

Fig. 1.3 Structures of monomeric MPcs used in this thesis.

1.1.3 Nanosized Phthalocyanines

One of the problems limiting the application of phthalocyanines in a number of fields has been their tendency to aggregate. Aggregation has proved to limit the electrocatalytic properties of phthalocyanines. Complexes **1**, **3** and **5** were nanosized in this thesis in order to improve their catalytic properties [6,8].

Three methods of nanoparticles fabrication have been reported namely vapour deposition, liquid and solid phases. Efforts to reduce the size of phthalocyanine aggregates dates back to 1990 when Oxo titanium Pc nanoparticles around 100 nm were obtained by milling bulk Pcs [21]. Oxo

titanium phthalocyanines have also been downsized to around 50 nm by dispersing them in polycarbonate resin by the method of mechanical sand grinder in search of better spectroscopic and catalytic properties [22]. The above two approaches constitute the solid phase methods.

Vapour deposition methods have been exploredfor the formation of phthalocyanine nanoribbons or nanowires. This was achieved by thermal evaporation of precursors into a tube furnace under argon [23].

One of the ways in which the aggregation problems can be solved is to introduce surfactants in liquid phase (**Scheme 1.3**). This thesis reports on the nanosizing of phthalocyanines into significantly smaller sizes which is accompanied by improved electrocatalysis [6,8]. The improved electrocatalysis can be explained by the fact that by nanosizing phthalocyanines, more metal centres are open for the interaction with the analyte. The nanosized phthalocyanines are for the first time conjugated to carbon based nanomaterials and gold nanoparticles and applied towards the detection of hydrogen peroxide in this thesis.

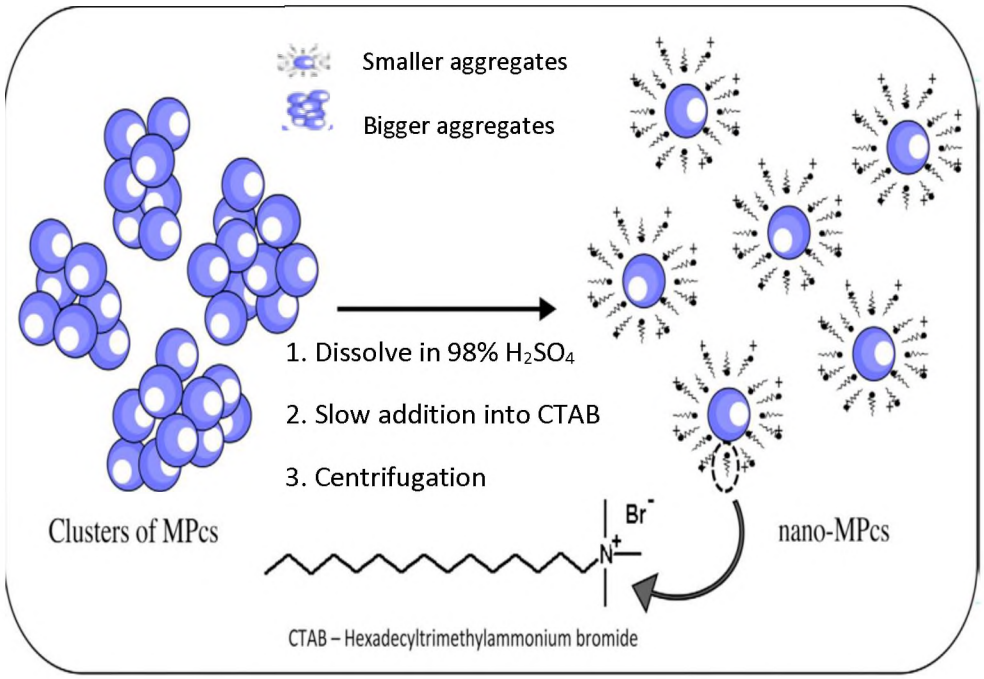

Scheme 1.3 A cartoon representation depicting the synthetic process of nanostructured metallophthalocyanines [8].

1.2 Nanomaterials

1.2.1 Carbon Nanomaterials {Graphene oxide nanomaterials (GONS) and multiwalled carbon nanotubes (MWCNTs)}

Carbon based nanomaterials have of late gained a lot of attention in research and subsequently application in a myriad of fields. This has been particularly possible mainly because they have large surface area, acceptable biocompatibility, chemical and electrochemical stability, good electrical conductivity, are inexpensive, are readily available from organic sources and their ability to be structurally and chemically tenable [24–26]. Their ease of structural tenability is evidenced by the variety of forms of these nanomaterials which include single walled carbon nanotubes [27–29], multi-walled carbon nanotubes [30,31], graphene oxide nanosheets [32–34],

fullerenes (carbon balls) [35,36] and graphene quantum dots [37–40]. The main source of nanosized carbon materials is graphite. Graphite can be oxidised and exfoliated to form graphene oxide nanosheets, which in turn can be folded into different shapes resulting in carbon nanotubes and fullerene. The graphene sheets can be further cut into smaller sizes to form graphene oxide quantum dots [41,42]. Because these carbon based materials have their dimensions in nanometre scale, their properties become easily manipulated as in this range properties become largely dependent on shape and size. This thesis reports on the effect of graphene oxide nanosheets (GONS) and multiwalled carbon nanotubes (MWCNT) on the electrochemical sensing ability of phthalocyanines. The GONS are tuned by introducing heteroatoms either chemically or physically to probe the effects of these in the field of electrocatalysis. The influence of GONS on MPcs towards the optical sensing of hydrogen peroxide is also presented.

1.2.1.1 Graphene oxide nanosheets (GONS)

These are one atom thick, two dimensional sp^2 carbon honeycomb that are normally characterised by basal oxygen species that tend to distort the nanomaterials' aromaticity by introducing sp^3 carbons [33,34]. The presence of the carbon sp^3 species though compromising the electrical conductivity of the material enables the exfoliation of the individual sheets and ease of heteroatom introduction, which comes with a host of advantages for the purposes of the present work.

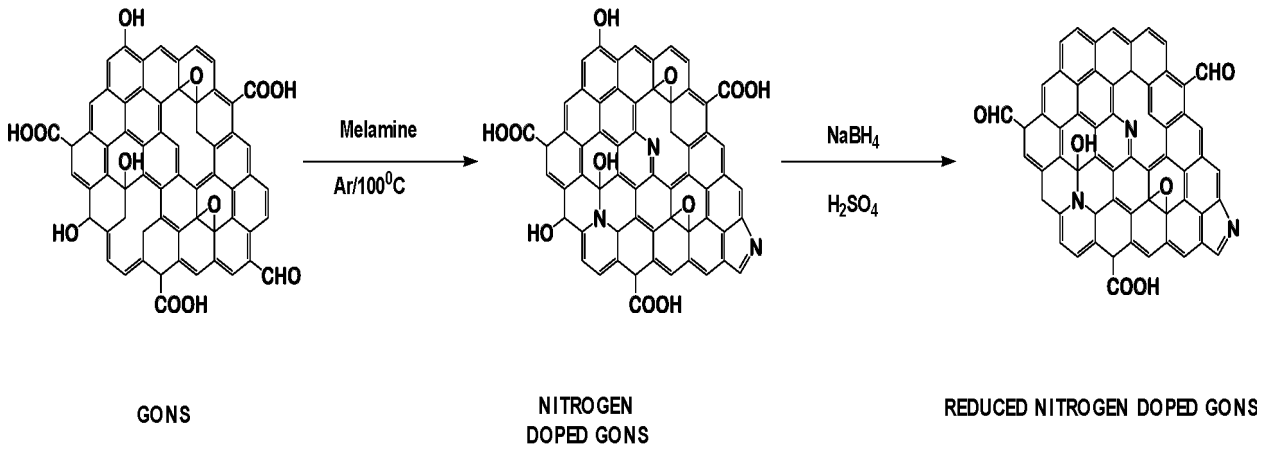

Scheme 1.4 Schematic representation of graphene oxide nanosheets doping.

Non-metallic heteroatoms such as boron, sulphur, phosphorus and nitrogen have been successfully doped into graphene oxide nanosheets and applied successfully as glassy carbon electrode modifiers for electrocatalysis. Doping of GONS is followed by reduction thereby restoring the sp^2 configuration (**Scheme 1.4** using N doping as an example) to give reduced nitrogen doped graphene oxide nanosheets (rNDGONS). Heteroatoms also break the electro neutrality of the carbon skeleton hence provoking the much-needed electron driving force for possible electrocatalytic applications. Electron rich guest atoms such as sulphur, nitrogen and phosphorus enhance the delocalised π electron system that increases the communication between adjacent sheets. This work demonstrates through X-ray diffraction (XRD) data that doping results in shorter intersheet distances. In this thesis, the effect of pristine GONS, P, S, N and B doped GONS, (PDGONS, SDGONS, NDGONS and BDGONS) on the electrocatalytic activity of CoPc derivatives is reported. Since both GONS and CoPc are catalytic, it is expected that the synergy between the two will enhance electrocatalytic activity. Co-doped S/N and P/N doped

GONS (SNDGONS and PNDGONS) are also employed. **Table 1.1** lists MPcs which have been studied in the presence of GONS or MWCNT[43–54]. No asymmetric MPcs have been employed as hybrids for electrocatalysis hence are reported for the first time in this thesis. In addition, no PDGONS or BDGONS have been used in the presence of MPcs for electrocatalysis. Covalent bonding of MPcs and either pristine or doped GONS has not been extensively studied before hence reported in this thesis. As **Table 1.1** shows, there have been no studies on nanocomposites of GONS or MWCNTs with nanosized MPcs for electrocatalysis. This thesis reports for the first time on these nanocomposites. In addition, even though MPcs have been studied for electrocatalysis in the presence of GONS, this is the first time that heteroatom co-doped GONS are employed.

Reports have been made on π-π conjugates of metallophthalocyanines and doped or pristine graphene oxide nanosheets (not reduced) for electrocatalysis but no covalent linked have been reported for this purpose hence the need to explore this. Metallophthalocyanine and reduced doped graphene oxide nanosheets hybrids have not been utilised for electrocatalysis before, making this work the first to do so.

Both *insitu* and post synthesis doping of graphene oxide nanosheets has been reported in literature. This thesis reports on the post synthesis doping and demonstrates the use of ordinary small compounds as sources of the heteroatoms. Some of the post synthesis approaches reported in literature include microwave assisted [55], thermal annealing [56,57] and hydrothermal doping [58]. It has been demonstrated that doping of graphene oxide proceeds

with simultaneous reduction [58] to form rGONS which is desirable in improving the conductivity of the material with the prospect of also enhancing the catalytic currents during electrocatalysis. The present work however demonstrates that further chemical reduction of the doped material is of great significance. Complex **4** was studied in the presence of different forms of GONS after covalent linkage to evaluate the effects of doping towards electrocatalysis. Complexes **1**, **3** and **5** were used to sequentially modify electrodes in the presence of differently doped GONS. There has been literature reports on the use of pristine graphene oxide nanosheets decorated with gold nanoparticles for electrocatalysis [59–62], **Table 1.1**. This work demonstrates the enhanced electrocatalysis of MPcs in the presence of GONS and rod shaped gold nanoparticles. This thesis reports the combination of the three (MPcs, AuNRs, GONS or MWCNT) for electrocatalysis.

1.2.1.2 Multiwalled carbon nanotubes (MWCNTs)

Multiwalled carbon nanotubes are rolled up concentric graphene sheets. They have been used in a number of electrochemical sensor platforms and have proved to improve the detection currents [48]. The synthesis of CNT was first reported in the early 1990s [63]. The method of electrode modification and the order in which the electrode modifiers are added to the electrode plays an important role in the performance of the modified surface. In this work either the modifiers were sequentially added, linked or were mixed before modification of the electrode. Previous studies show that in sequential modification, it is best to place MPcs on top of the nanomaterials [64],

therefore in case of sequential modification, the MPcs were always placed on top of the MWCNTs.

1.2.2 Gold Nanoparticles (AuNPs)

Gold nanoparticles (AuNPs) have been used as electrode modifiers of a range of electrodes with impressive electrocatalytic results over the past years. They exhibit size and shape dependent optical and electrical properties. Through the manipulation of reaction conditions, reagent amounts and reaction times, it has been possible to synthesize gold nanoparticles of the following shapes; nanorods [65], spheres [66], nanocages [67,68], nanostars [61,69], among others. Manipulations of shape usually require surfactants that allow growth in certain planes whereas restricting it in other planes. Research has shown that different amounts of reducing agents affect the growth rates and hence the resultant particle size. AuNPs have been grown on multiwalled carbon nanotubes and graphene oxide nanosheets and utilised for electrocatalysis in fuel cells [59], hydrazine [70,71], hydrogen peroxide [66] and glucose [59] detection among others. The combination of metal nanoparticles (MNP) and GONS/CNT has been reported to create channels for electrolyte flow enhancing the electrocatalytic performance of the conjugates. Gold has a high affinity for sulphur and nitrogen hence this work reports for the first time on the nanoconjugates of reduced sulphur/nitrogen co-doped graphene oxide nanosheets (for linking to AuNRs) and nanosized cobalt phthalocyanines for the electrocatalysis of hydrogen peroxide. Gold nanorods (AuNRs) were selected instead of spherical nanoparticles, since the former are known to show better electrocatalysis [72]. The use of AuNRsis presumed to prevent

restacking of the graphene nanosheets and improve the electrocatalytic behaviour of the conjugates in a synergistic manner. The AuNPs/MWCNT hybrid modified glassy carbon electrode has been reported [73] to have good electrocatalytic properties for oxygen reduction in acid media hence the hybrid is used in this work with the prospect of it improving the electrocatalytic behaviour of MPcs for reduction of hydrogen peroxide. **Table 1.1** shows known MPcs-AuNPs conjugates applied for electrocatalysis [64,74–78]. No gold nanorods have been used in the presence of MPcs for electrocatalysis, making this thesis the first to address this. While MWCNT, GONS, AuNPs and MPcs have been used to modify electrodes for electrocatalysis, the combination of MWCNT/AuNRs or GONS/AuNRs and MPcs have not been investigated until now.

Table 1.1 Sensing applications of nanomaterials and MPcs hybrids.

Nanomaterial/Nanoconjugate	**Mode of detection**	**Analyte**	**Refs**
Carbon Nanomaterials			
CoPc@MWCNT	electrocatalysis	kanamycin	[48]
CoPc@GONS film	electrocatalysis	nitrite	[44]
FePPc@CNT	electrocatalysis	ORR	[50]
CoPc@MWCNT	electrocatalysis	ORR	[46]
FePc@MWCNT	electrocatalysis	ORR	[46]
polyNiTSPc@MWCNT	electrochemiluminenscence	hydrogen peroxide/glucose	[47]
CuTIPPc@SWCNT	electrocatalysis	ammonia	[49]
CuTTMPPc@SWCNT	electrocatalysis	ammonia	[49]
FePc@CNT	electrocatalysis	hydrogen peroxide	[43]
CoPc@GONS	electrocatalysis	L-cysteine	[45]
CoPc@NDGONS	electrocatalysis	L-cysteine, reduced L-glutathione 2-mercaptoethane sulfonic acid	[51]
CoTAPc@SWCNT	electrocatalysis	2-mercaptoethanol	[52]
CoTAPc@MWCNT	electrocatalysis	rhodamine 6G	[53]
FePc@rGONS	electrocatalysis	ORR	[54]
Gold Nanoparticles			
NiTSPc@AuNPs	electrocatalysis	nitrite	[75]
FeMAPc-(MPA)-AuNPs	electrocatalysis	nitrite	[78]
Nanomaterial/Nanoconjugate	**Mode of detection**	**Analyte**	**Refs**
CoPc-(MPS)-AuNPs	electrocatalysis	ORR	[77]

poly-CoTAPc@AuNPs-GCE	electrocatalysis	nitrite	[64]
NiTAPc@AuNPs	electrocatalysis	Hydrazine	[74]
ZnPc-(MPS)-AuNPs	electrocatalysis	ORR and CO_2 reduction	[76]

TIP; tetra--iso-pentyloxyphthalocyanine, TTMP; Tetra-α-(2,2,4- trimethyl-3-pentyloxy)MPA; mercapto propanoic acid, MPS; mesoporous silica, TAPc; tetra amino phthalocyanine, MAPc; mono amino phthalocyanineTSPc; tetra sufo phthalocyanine, ORR; oxygen reduction reaction"()" capping agent in brackets

1.2.3 MPcs Nanomaterial hybrids used in this work.

All the MPc-nanomaterial hybrids used in this work are listed in **Table 1.2**. The nanocomposites may be divided into groups depending on the intended study.

Group A; Effect of nanomaterials on bulk MPcs.

Nano materials such as CNTs [43], GONS [54], metal nanoparticles [74,76] and semiconductor quantum dots [79] have been reported to improve detection currents, electrode stability and lower detection potentials of MPcs towards a number of analytes which include hydrogen peroxide, nitrite, L-cysteine, ammonia among others. It has been reported that MPc functionalised GONS or MWCNTs show highly attractive electron transfer ability and enhanced detection currents as well as lower oxidation potentials of uric acid and isoniazid [80]. The electrocatalysis of bulk complex **1** (CoTAPhPc) was studied in the presence of MWCNT, AuNRs, rGONS, MWCNT/rGONS(mix), MWCNT-rGONS(seq), MWCNT-AuNRs(seq) andMWCNT/AuNRs(mix) for L-cysteine detection (bulk is denoted without **NP** in **Table 1.2**. It has been reported before that premixing MWCNTs and GONS

discourages stacking of GONS and results in improved electrocatalytic ability of MPcs towards the oxidation of paraquat [81]. The hybrids were either developed by sequential dropcasting of the individual nanomaterials on the electrode before addition of complex **1** {denoted with (seq)}, or drop casting the mixture {denoted with (mix)} of the nanomaterials on the electrode followed by addition of complex **1.** Bulk **2** was studied in the presence of MWCNT only, to compare linking with mixing. While bulk **4** was studied in the presence of differently doped GONS, to compare the effects of different dopants. Both covalent linkage and π-π between the MPcs and the nanomaterials were explored.

Group B; Comparison of Nano MPcs with Bulk MPcs

Complex **1** (CoTAPhPc**NP**) and its bulk form CoTAPhPc (**1**) were studied alone and in the presence of rGONS, AuNRs and MWCNTs and mixture of the AuNRs and carbon nanomaterials for hydrogen peroxide detection to illustrate the effect of nanosizing the MPcs on electrocatalysis (**Table 1.2**). Transforming MPcs into nanoparticles has recently opened a new interest in the electrocatalytic detection of a number of physiologically important molecules [6,82–84]. Phthalocyanine nanoparticles have been reported [83,84] to show improved electrocatalytic behaviour compared to their bulk counterparts due to increased surface area hence their employment in this thesis.

Group C; Effect of ring substituent on catalytic behaviour of MPcs

The catalytic behaviour of MPcs are affected by the ring substituent among other factors. This thesis also seeks to understand the extent to which carboxylic and amine appended MPcs are involved in electrocatalysis. Bulk complexes **1** and **2** tetra substituted with aminophenoxy (**1**) or carboxy phenoxy (**2**) were studied alone or in the presence of MWCNT towards the detection of hydrogen peroxide. Literature reports that MPcs with carboxylic substituents can have their activity enhanced by amine appended SWCNTs [85]. Bulk complexes **2** and **4** (without nanomaterials) were studied to establish the effect of the number of substituents and symmetry on the catalytic ability of MPcs.

Group D; Effect of spacer between amine group and MPc ring

The continuity of the π electron delocalisation throughout the macrocycle could have some influence on the electrocatalytic behaviour of MPcs. This work therefore attempts to understand the effect of a spacer (phenyl) group towards the detection of hydrogen peroxide. Nanosized complexes **1** (spacer) and **5** (no spacer) were compared for the detection of hydrogen peroxide alone or in the presence of rGONs and rSDGONS.

Group E; Effects of linking MPcs to MWCNT versus mixing

Hybrids of carbon based nanomaterials have been fabricated for electrocatalysis either by covalent linkage or mixing [17]. Complex **2** was studied with MWCNT when linked or mixed towards the detection of hydrogen peroxide. The mixed form of complex **2** and MWCNT results in π-π interaction

since both species are delocalised π-electron rich. Covalent bonding was necessitated by carboxylation of the MWCNT into MWCNT-COOH, which was then linked via a diaminomaleonitrile (DAMN) linker to establish amide bonds. Covalent linkage is thought to facilitate a more defined electron transport system, which should see a more stable electrode modifier as compared to π-π stacking. It should however be noted that the two hybrids may result in different loadings of the MPcs depending on the available points of linkages as determined by the extent of carboxylation on the MWCNTs.

Table 1.2. Summary of all carbon nanomaterials, Pc or Pc carbon nanomaterials used in this work[a]

Modified Electrode	**Application**
(A) Complex 1	
CoTAPhPc(**1**)-GCE	L-cysteine electrooxidation/Hydrogen peroxide electrooxidation/reduction
CoTAPhPc**NP**(**1**)-GCE	Hydrogen peroxide electrooxidation
Complex 1 adsorbed onto GCE modified with one type of nanomaterials and Complex 1 linked to AuNRs	
CoTAPhPc(**1**)@ MWCNT-GCE	L-cysteine electrooxidation
CoTAPhPc(**1**)@AuNRs-GCE	hydrogen peroxide electrooxidation/reduction
CoTAPhPc(**1**)@rGONS-GCE	L-cysteine electrooxidation/Hydrogen peroxide electrooxidation/reduction
CoTAPhPc**NP**(**1**)@MWCNT-GCE	Hydrogen peroxide electrooxidation / reduction
CoTAPhPcNP-AuNRs(linked)-GCE	Hydrogen peroxide electrooxidation / reduction
CoTAPhPc**NP**(**1**)@AuNRs-GCE	Hydrogen peroxide electrooxidation / reduction
CoTAPhPc**NP**(**1**)@rGONS-GCE	Hydrogen peroxide electrooxidation / reduction
CoTAPhPc**NP**(**1**)@rNDGONS-GCE	Hydrogen peroxide electrooxidation / reduction
CoTAPhPc**NP**(**1**)@rSDGONS-GCE	Hydrogen peroxide electrooxidation / reduction
CoTAPhPc**NP**(**1**)@rBDGONS-GCE	Hydrogen peroxide electrooxidation / reduction
CoTAPhPc**NP**(**1**)@rPDGONS-GCE	Hydrogen peroxide electrooxidation / reduction
CoTAPhPc**NP**(**1**)@rPNDGONS-GCE	Hydrogen peroxide electrooxidation / reduction
CoTAPhPc**NP**(**1**)@rSNDGONS-GCE	Hydrogen peroxide electrooxidation / reduction
Complex 1 adsorbed onto GCE modified with two types of nanomaterials	
CoTAPhPc(**1**)@MWCNT/rGONS(mix) -GCE	L-cysteine electrooxidation
CoTAPhPc(**1**)@MWCNT-rGONS (seq) -GCE	L-cysteine electrooxidation

Modified Electrode	**Application**
CoTAPhPc (**1**)@rGONS-MWCNT(seq)-GCE	L-cysteine electrooxidation
CoTAPhPc(**1**)@MWCNT/AuNRs(mix)-GCE	Hydrogen peroxide electrooxidation/reduction
CoTAPhPc**NP**(**1**)@MWCNT/AuNRs(mix) -GCE	Hydrogen peroxide electrooxidation / reduction
CoTAPhPc**NP**(**1**)@ rGONS/AuNRs(mix) -GCE	Hydrogen peroxide electrooxidation / reduction
CoTAPhPc**NP**(**1**)@rNDGONS-AuNRs (linked)-GCE	Hydrogen peroxide electrooxidation / reduction
CoTAPhPc**NP**(**1**)@rSDGONS-AuNRs (linked)-GCE	Hydrogen peroxide electrooxidation / reduction
CoTAPhPc**NP**(**1**)@rSNDGONS-AuNRs (linked) -GCE	Hydrogen peroxide electrooxidation / reduction
CoTAPhPc**NP**(**1**)@AuNRs-rSNGONS(seq)-GCE	Hydrogen peroxide electrooxidation / reduction
CoTAPhPc**NP**(**1**)@rSNGONS-AuNRs(seq)-GCE	Hydrogen peroxide electrooxidation / reduction
(B) Complex 2 mixed with or linked to MWCNT before adsorption onto GCE	
CoTCPhPc(**2**) -GCE	Hydrogen peroxide electrooxidation / reduction
CoTCPhPc(**2**)@DAMN-MWCNT(mix) -GCE	Hydrogen peroxide electrooxidation / reduction
CoTCPhPc(**2**)-DAMN-MWCNT(linked) -GCE	Hydrogen peroxide electrooxidation / reduction
(C) Complex 3 adsorbed onto GCE modified with pristine or doped GONS	
CoPc(**3**) -GCE	Hydrogen peroxide electrooxidation / reduction
CoPc**NP**(**3**) -GCE	Hydrogen peroxide electrooxidation / reduction
CoPc**NP**(**3**)@rSDGONS-GCE	Hydrogen peroxide electrooxidation / reduction
CoPc**NP**(**3**)@rGONS-GCE	Hydrogen peroxide electrooxidation / reduction
CoPc**NP**(**3**)@rNDGONS-GCE	Hydrogen peroxide electrooxidation / reduction

Modified Electrode	**Application**
CoPc**NP**(**3**)@rPDGONS-GCE	Hydrogen peroxide electrooxidation / reduction
CoPc**NP**(**3**)@rPNDGONS-GCE	Hydrogen peroxide electrooxidation / reduction
(D) **Complex 4 adsorbed onto GCE modified with doped GONS or linked to GONS before adsorption**	
CoMCPhPc(**4**) -GCE	Hydrogen peroxide electrooxidation / reduction
CoMCPhPc(**4**)@(DAMN)-GONS-GCE	Hydrogen peroxide electrooxidation / reduction
CoMCPhPc(**4**) @(DAMN)-SDGONS-GCE	Hydrogen peroxide electrooxidation / reduction
CoMCPhPc(**4**)@(DAMN)-NDGONS-GCE	Hydrogen peroxide electrooxidation / reduction
CoMCPhPc(**4**)@(DAMN)-SNDGONS-GCE	Hydrogen peroxide electrooxidation / reduction
CoMCPhPc(**4**)-(DAMN)-GONS(linked)-GCE	Hydrogen peroxide electrooxidation / reduction
CoMCPhPc(**4**)-(DAMN)-NDGONS(linked)-GCE	Hydrogen peroxide electrooxidation / reduction
CoMCPhPc(**4**)-(DAMN)-SDGONS(linked)-GCE	Hydrogen peroxide electrooxidation / reduction
CoMCPhPc(**4**)-(DAMN)-SNDGONS(linked)-GCE	Hydrogen peroxide electrooxidation / reduction
(E) Complex 5 adsorbed onto GCE modified with pristine and SDGONS	
CoTAPc(**5**)-GCE	Hydrogen peroxide electrooxidation / reduction
CoTAPc**NP**(**5**)-GCE	Hydrogen peroxide electrooxidation / reduction
CoTAPc**NP**(**5**)@rGONS-GCE	Hydrogen peroxide electrooxidation / reduction
CoTAPc**NP**(**5**)@rSDGONS-GCE	Hydrogen peroxide electrooxidation / reduction

[a] "@" = Pc adsorbed onto the nanomaterials; "/" =a mixture of different nanomaterials; "-" covalent bond between different modifiers when used in combination with "linked"; "-" =sequential modification when used with "seq" DAMN = diaminomaleonitrile; mix = mixed before electrode modification; seq = sequentially added to the electrode; "r" in front of GONS = reduced; if no "r", the GONS were not reduced.

1.3 Electrode modification and catalysis

1.3.1 Basics of electrocatalysis

Electrocatalysis may be defined as the variation of rate of an electrochemical reaction with change in electrode material [86]. **Fig. 1.4** shows the MPc facilitated electron transfer steps during the oxidation of an analyte at the MPc modified electrode surface utilising M^{II}/M^{III} redox couple. Electrocatalysts or electrode modifiers should be capable to offer an alternative reaction route [87] that either utilises less energy (low overpotential) or is capable of occurring at high current densities (faster) or both [88] **(Fig 1.4)** [89].

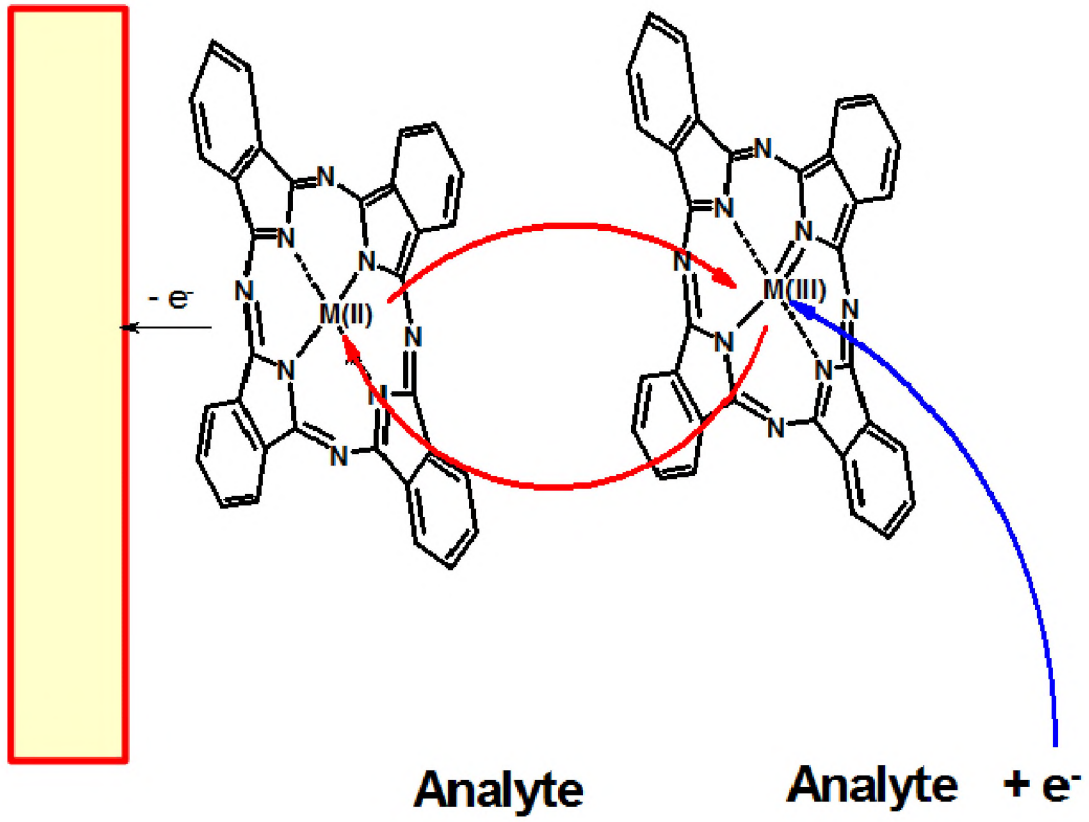

Fig. 1.4 Typical electrocatalytic process of metallophthalocyanines immobilized on electrodes [89].

For CoPcs, Co^{III}/Co^{II} and Co^{II}/Co^{I} couples are involved in oxidation andreduction respectively, (**Eqn 1.1 – 1.4**).

Oxidation

$$Co^{II}Pc \longrightarrow [Co^{III}Pc]^{+} + e^{-} \qquad 1.1$$

$$[Co^{III}Pc] + R \longrightarrow Co^{II}Pc + P \qquad 1.2$$

Or Reduction

$$Co^{II} + e^{-} \longrightarrow Co^{I}Pc \qquad 1.3$$

$$Co^{I}Pc + R \longrightarrow Co^{II}Pc + P \qquad 1.4$$

where R and P are the reactant and product respectively

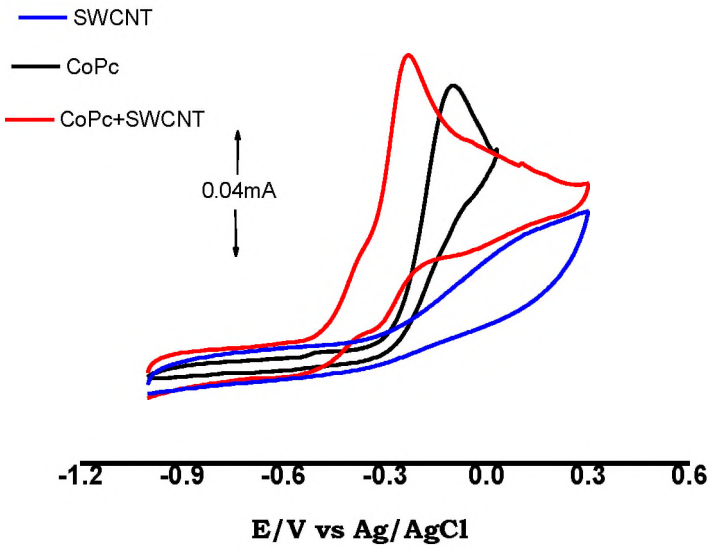

Fig. 1.5 Cyclic voltammograms of N_2H_4 (2.6 mM) in 0.2 M NaOH aqueous solution at different GC electrodes. Scan rate: 50 mV/s [90].

Such enhanced reactivity was preveously illustrated when glassy carbon electrode was modified with either CoPc or SWCNTs or both (**Fig. 1.5**) [90]. Both CoPc and SWCNTs (when adsorbed on the glassy carbon electrode) improve the detection currents and lower the detection potential of hydrazine as compared to the bare electrode (voltammogram not shown). The two modifiers further show synergistic effect when co-used to modify the electrode as is illustrated by further lowering the detection potential and enhancement of the detection currents (**Fig. 1.5)**. Electrocatalysts do not take part in the overall reaction but may undergo transformation during the reaction before being regenerated again as illustrated in **Eqns. 1.1 - 1.4**.

1.3.2 Methods of electrode modification

Conventional non-precious metal electrodes are characterised by low detection currents and high overpotentials though they are significantly inexpensive. They of late however been successfully modified by a range of non-expensive materials to improve the detection currents and lower the detection overpotentials. A number of modification approaches have been adopted for electrode modification, which include electro polymerization, self-assembled monolayers, adsorption (dip/dry and drop/dry), click chemistry and electro grafting. This work reports on adsorption (drop/dry) hence it is briefly described below. MPcswere generally placed on top of the respective nanomaterials as illustrated in **Fig.1.6** for MPc@GONS-GCE.

Drop/dry utilises deposition of a known amount of the catalyst on the electrode surface. This offers a simple and fast method of electrode

modification. The choice of this method was informed by the possibility of MPcs, graphene nanosheets and multiwalled carbon nanotube's readily available π electron system, which can meaningfully interact with the π electron system of the glassy carbon electrode thereby forming a relatively stable π stacked catalyst film on the electrode. Drop dry is more favourable than dip dry since in the former there is room to control amounts adsorbed thereby increasing reproducibility of experimental conditions and of as such results.

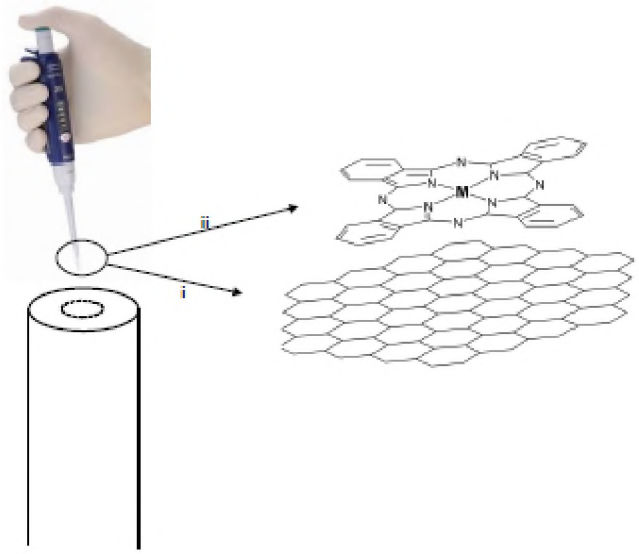

Fig. 1.6 A schematic illustration of sequential electrode modification using GONS and MPc. (i) GONS added first on the GCE (ii) MPc added on top of GONS

1.3.3 Characterisation of modified electrodes

The electrocatalytic behaviour of modified electrodes is largely dependent on both their electrochemical behaviour and surface morphology. For this reason, the modified electrodes were characterised by different techniques before examining their electrocatalytic nature. Scanning electron microscopy

(SEM), Time of flight secondary ionisation mass spectrometry (TOF-SIMS), scanning electrochemical microscopy (SECM), rotating disc electrode (RDE) and cyclic voltammetry (CV) were employed for this purpose in the current work. TOF-SIMS and SECM are briefly described in the following sections since they are not as common as the others.

1.3.3.1 TOF-SIMS

This is a surface chemistry technique that provides the ionic composition of a solid surface after ionisation and hence is used to give information on the distribution of the modifier on the surface of the electrode [91]. A beam of molecular ions is directed towards the surface of the substrate (modified glassy carbon plate in this work) which sputters fragments of the modifier of different masses. These are then accelerated in a high magnetic vacuum tube, which then allows their separation according to mass to charge ratio eventually reaching the detector at different times. Surface mapping and depth profiling are possible with appreciable sensitivities. The former is however of significance to the present work. **Fig. 1.7** shows an image of the instrument (**A**) and the obtainable mass spectra (**B**).

This technique therefore can inform us on the heterogeneity or uniformity thereof of the electrode surface as well as the dominating chemical species. For this reason it is an investigative technique which provides information on whether modification has taken place or not, if there is modification, then to what extent [92,93].

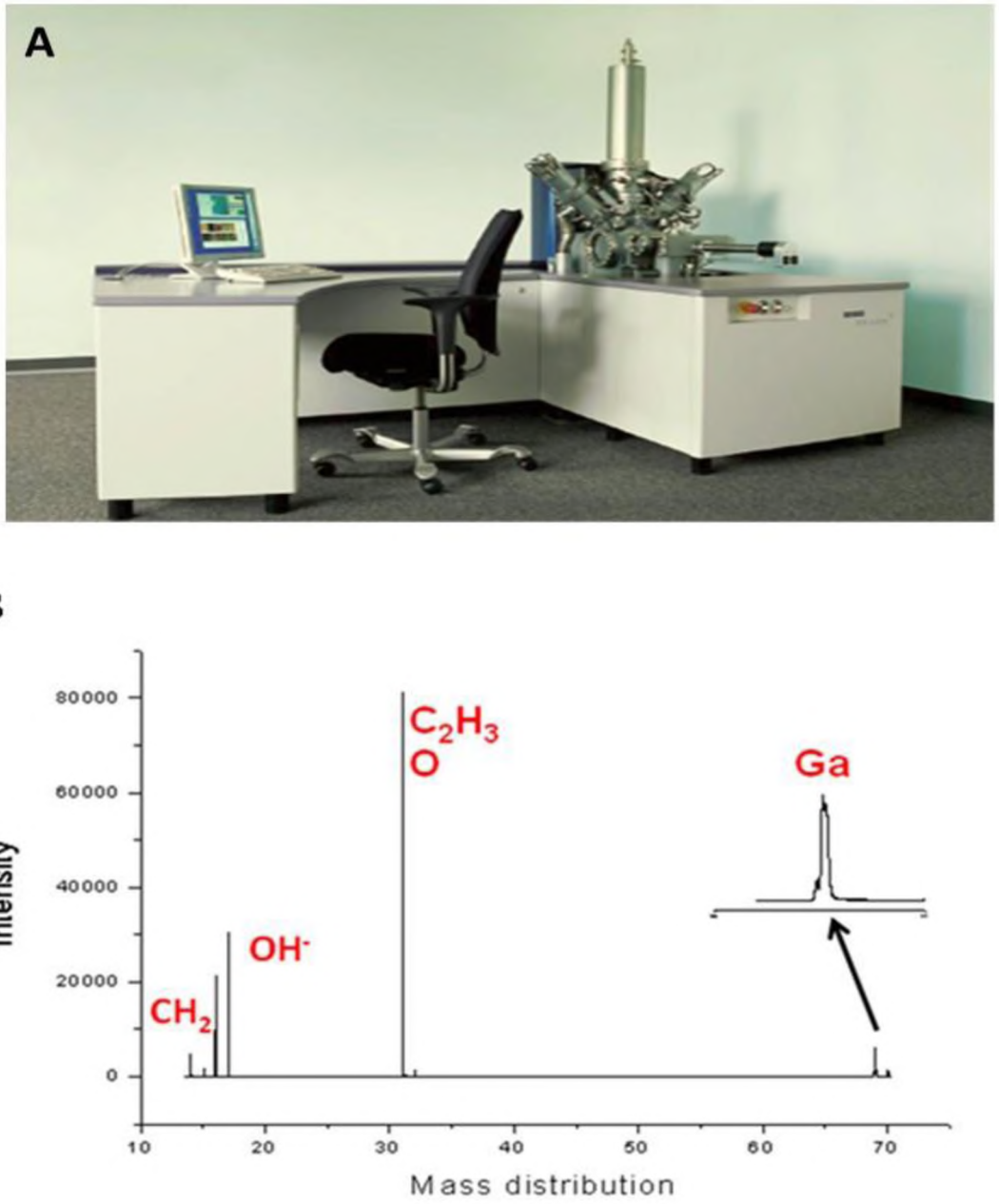

Fig. 1.7 Image of TOF-SIMS and Secondary ion mass spectrum for gallium chloride porphyrin/Pluronic F127. **Unpublished work**

1.3.3.2 Scanning Electrochemical Microscopy (SECM)

SECM is a relatively new technique used to analyse the electrochemical morphology and topography of electrode surfaces. The set up is shown in **Fig 1.8A**. SECM has a wide range of applications in electrochemical imaging, chemical kinetics, biological redox processes, and electrocatalytic reactions,

among others [94–96]. SECM monitors the electric current that flows through the tip of an ultra-microelectrode (UME) to which a potential has been applied when moved laterally or towards a substrate.

In this work, the feedback modeis employed. The tip is kept at a potential high enough for oxidation of the analyte (usually Fe^{II}/Fe^{III} system). The modified electrode is used as the substrate whose ability to reduce the generated oxidised species (catalysis) is then monitored by the current flux changes on the UME tip. The better the modified electrode can reduce the generated oxidised species, the higher the currents recorded. The opposite is observed for an insulating surface. The UME tip was either kept at a constant height from the modified electrode to obtain an area scan or moved towards the modified electrode surface (along the z-axis) to obtain an approach curve.

In the case of a conducting surface (**Fig. 1.8C)** [97,98], the currents at the UME tip continue to increase [**Fig. 1.8D (1)**] with diminishing distance between the UME and the substrate due to the improved regeneration of the reduced species (positive feedback). On the other hand as the UME tip approaches an insulating surface (**Fig. 1.8B**), currents drop as illustrated in **Fig. 1.8D (2)** due to restricted diffusion of the reduced species since no electrons are generated from the substrate (negative feedback).

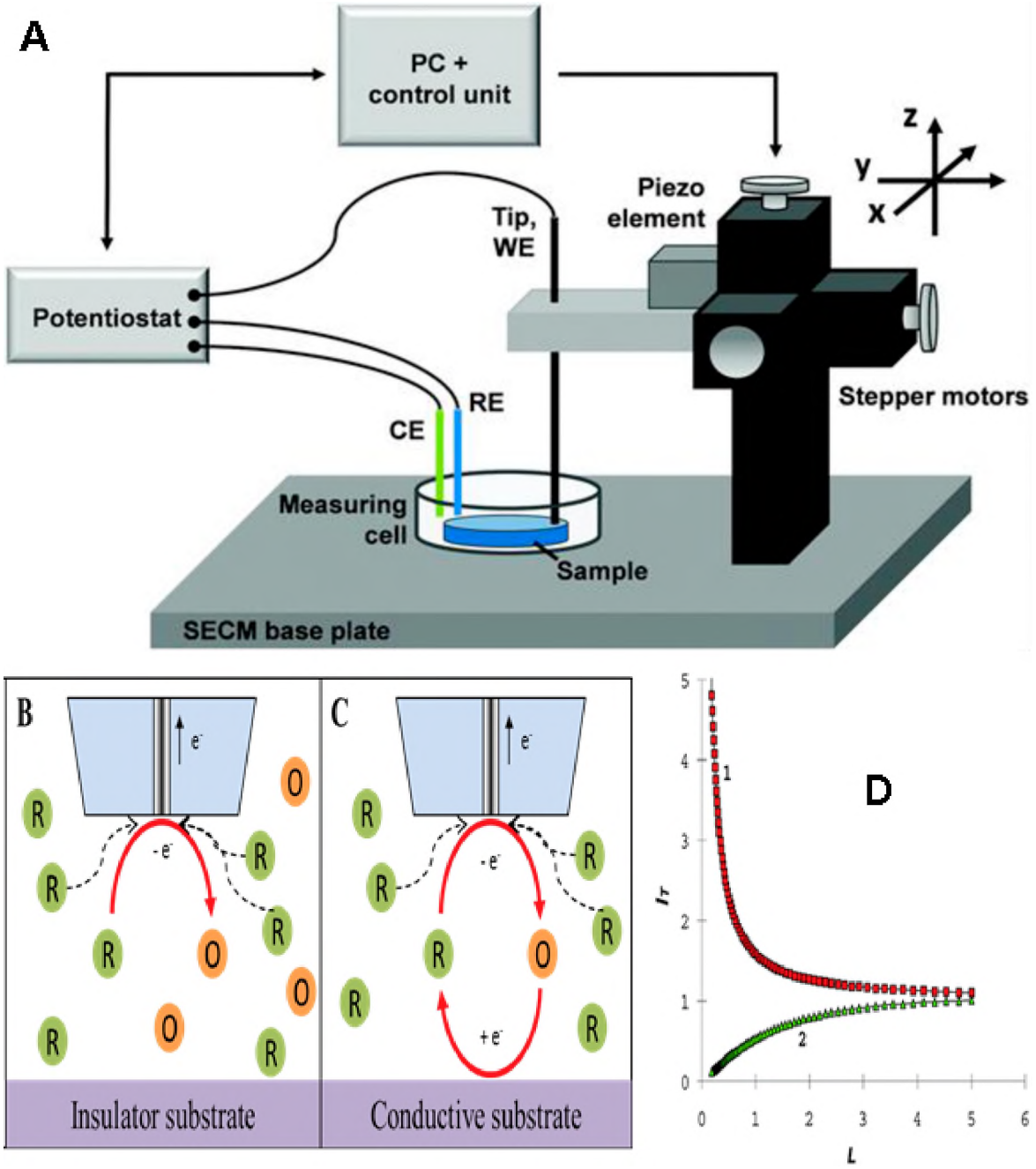

Fig. 1.8(A) SECM Set up [94], **(B)** negative feedback **(C)** positive feedback [98] and **(D)** approach curves [97]. 1-conducting surface, 2-insulating surface

1.4 Test analytes in this work

The potential of the electrocatalysts developed in this work was examined by the use of hydrogen peroxide and L-cysteine as examples.

1.4.1 L-cysteine

L-cysteine is a semi essential protein whose thiol end mostly act as a nucleophile in enzymatic reactions [99]. Pathogens, neoplasia, hemo dialysis, aphaeresis, genetic condition, exposure to toxic agent, old age, excessive exercise, and so on, have been reported to result in L-cysteine deficiency in the cells of the host [99,100]. The normal body concentration of L-cysteine is between 1x 10^{-5} M and 2 x 10^{-5} M, which falls when someone is stressed [100]. It is in this light that the development of probes with low detection limits for L-cysteine becomes so important. Literature reports on analysis of L-cysteine on glassy carbon electrodes modified with MPcs and MWCNT [101–103], but none have reported on the use of MPcs and GONS or MPcs, MWCNT and rGONS making this work the first to report this.

1.4.2 Hydrogen peroxide

Hydrogen peroxide is generated in vivo by a number of processes that include dismutation of superoxide radical (O_2^{*-}). The other source of hydrogen peroxide in human physiology is by ingestion. Beverages such as instant coffee contain substantial amounts of hydrogen peroxide [104]. Phagocytic cells at inflammation points during a pathological condition can also trigger the production of hydrogen peroxide [104,105]. The ease of diffusion across cells makes hydrogen peroxide a good signalling molecule [105,106] hence making its accurate detection and quantification important. This is the first time co-doped P/N GONS, N/S GONSare employed with MPcs for electrocatalysis. Co-doped P/N GONS (in the absence of MPcs) have been reported to show improved electrocatalysis than individual components [107],

hence are employed in this work together with phthalocyanines. This thesis reports for the first time rSDGONS, rNDGONS, rBDGONS, rPDGONS, rPNDGONS and rSNDGONS in combination with nanosized MPcs for electrocatalysis of hydrogen peroxide. This is the first time that a nanocomposite consisting of MWCNTs, S/N rGONS, rSDGONS, rNDGONS, MPc nanoparticles, and rod shaped gold nanoparticles have been prepared for electrocatalysis. Most of the electrochemical probes used to detect hydrogen peroxide utilise electro reduction [108–110]. This work utilises both electro reduction and electro oxidation with remarkably low detection limits and significantly low overpotentials. Reduction suffers interference from oxygen reduction hence oxidation is preferred.

1.5 Optical sensing.

Zinc phthalocyanines have been utilised for fluorescent sensing of a variety of analytes among them metal ions [111] in a "turn off" mechanism. GONS (a zero band gap conductor) act as an efficient fluorescence quencher of MPcs, with the possibility of certain analytes having the ability of restoring the fluorescence in a turn on mechanism. GONS quench fluorescence of molecules such as MPcs as a result of photo-induced electron transfer (PET) where the graphene moiety acts as an electron acceptor and the Pc as an electron donor in the excited state and the reverse in the ground state [112]. However, fluorescence sensing of analytes in solution of conjugates of MPcs with graphene oxide has not been extensively reported. **Table 1.3** shows MPc conjugates with carbon nanomaterials used for fluorescence sensing [111,113,114]. This restoration of fluorescence can be exploited for the

measurement of different metal ions in environmental samples. Analytes can interact with GONS functional groups, obstructing the electron transfer between GONS and the MPc, hence restoring the fluorescence of the MPc. The obstruction is as a result of the analyte acting as a spacer between the fluorescent species (MPc) and the quencher (GONS) [112]. This work reports the interaction of Zn octacarboxy phthalocyanine (ZnOCPc, **6 Fig 1.9**) with either rGONS or GONS through π-π stacking. ZnOCPc (**6**) was chosen due to its lack of aggregation and high water solubility [115]. Complexes **1**, **3, 4** and **5** are not water-soluble while complex **2** is water-soluble but aggregated. The conjugates of complex **6** and rGONS or GONS are employed for optical sensing of hydrogen peroxide. An ideal fluorescent probe must show selectivity. Hence, the selectivity of the proposed ZnOCPc-GONS/rGONS fluorescence sensor towards H_2O_2 in the presence of excess of co-existing biologically active species such as cysteamine (cys), glutathione (GSH), urea, NO_2^-, NO_3^-, L-cysteine (L-cys) and tert-butylhydro peroxide (TBHP) is investigated in this thesis.

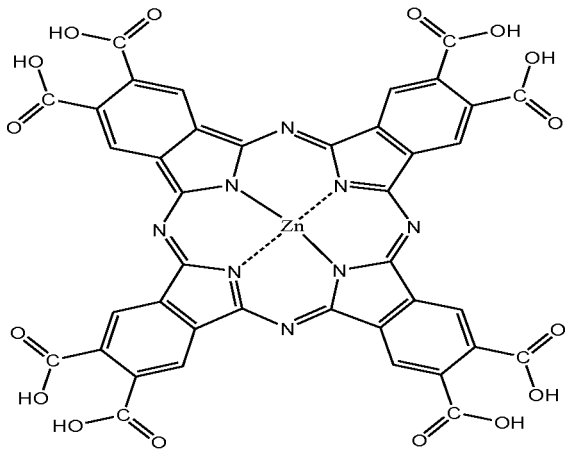

Fig. 1.9. Structure of Zinc octacarboxy phthalocyanine

Table 1.3 Metallophthalocyanines and carbon nanomaterials for Optical sensing

Nanomaterial	**Mode of Detection**	**Analyte**	**Ref**
4T-ZnPc	Fluorescence quenching	Hg^{2+}	[111]
QDs-AlTAPc	Fluorescence enhancement	hydrogen peroxide	[113]
QDs-NiTAPc	Fluorescence enhancement	hydrogen peroxide	[113]
QDs-ZnTAPc	Fluorescence enhancement	hydrogen peroxide	[113]
SNGQDs–TEMPO-ZnPc	Fluorescence enhancement	Ascorbic acid	[114]

4T-ZnPc=tetra-(thymin- 1-yl-acetamido)-phthalocyanine Zn(II); SNGQDs = S and N co-doped Graphene Quantum Dots; TEMPO = (2,2,6,6-tetramethylpiperidin-1-yl)oxyl; TAPc = tetra amino phthalocyanine

1.6. Summary of the aims of thesis

This work was aimed at enhancing the optical and electrocatalytic detection capabilities of MPc by either conjugating them to carbon based nanomaterials or metallic nanoparticles. This was done through

1. Synthesis of new CoTAPhPc(**1**) and CoMCPhPc(**4**).
2. Nanosizing the MPcs to improve electrocatalytic behaviour

3. Development of optical and electrochemical sensing platforms capable of hydrogen peroxide and/or L-cysteine detection.

4. Doping graphene nanosheets with non-metallic heteroatoms (S, N, P and B) to disturb the electro neutrality hence improve conductivity

5. Development for the first time of nanoprobes based on conjugates MPcs, AuNRs, and doped GONS or MWCNT

6. Covalently linking the MPcs to carbon based nanomaterials to improve current fluxes during detection

7. Sequentially modifying electrodes with layers of carbon based nanomaterials and MPcs

8. Comparison of covalently linked, premixed and sequentially modified electrodes towards electrocatalysis.

9. In-depth study of the electrode kinetics during the electrocatalysis of hydrogen peroxide and L-cysteine through cyclic voltammetry, linear sweep voltammetry, rotating disk electrode and chronoamperometry.

10. Characterise the nanocomposites by several techniques such as TEM, SECM, SEM, XPS and TOF-SIMS.

Chapter Two

2. Materials and Experimental

2.1 Materials

Dimethyl sulfoxide (DMSO) was obtainedfrom Associated Chemical Enterprises. Dicyanobenzene, phenyl phosphine, cobalt phthalocyanine, graphene oxide nanosheets (GONS), urea, reduced L-glutathione (GSH), sodium borohydride, alumina (<10 mm), hexadecyltrimethyl ammonium bromide, N-(3-Dimethylaminopropyl)-N′-ethylcarbodiimide hydrochloride (EDC) 98%, *N*-Hydroxysuccinimide 98%, thionyl chloride ($SOCl_2$), ammonium sulphate [$(NH_4)_2SO_4$], diaminomaleonitrile (DAMN), cobalt chloride, $K_4Fe(CN)_6$, $K_3Fe(CN)_6$, $HAuCl_4{\cdot}6H_2O$ and multiwalled carbon nanotubes (MWCNT, diameter= 110–170 nm, length = 5–9 μm>90% carbon), boric acid, melamine, L-cysteine were from Sigma Aldrich. $(NH_4)_2HPO_4$, and potassium permanganate were from Saarchem. Hydrogen peroxide and 1,8-diazabicyclo [5.4.0] undec-7-ene (DBU) were purchased from Fluka. Sodium nitrate and sodium nitrite were purchased from BDH laboratory reagents. Buffer tablets pH 7, pH 4 tert-Butylhydroperoxide (TBHP), and quinoline were purchased from Merck-Schuchardt. Tetrahydrofuran (THF), dimethyformamide (DMF) was from B & M Scientific. Aqueous solutions of hydrogen peroxide in pH 7 and L-cysteine in pH 4 buffer were prepared using millipore water from Milli-Q Water Systems (Millipore Corp. Bedford, MA, USA). The synthesis of Au nanorods (AuNRs) [65,116], 4-carboxyphenoxy phthalonitrile [18] and 4-aminophenoxy phthalonitrile [117] has been reported. Zinc octacarboxy phthalocyanine (ZnOCPc, **6**)[118] and cobalt tetraamino phthalocyanine

(CoTAPc, **5**)[19,20], cobalt tetra carboxy phenoxy phthalocyanine, (CoTCPhPc,**2**), [18] were synthesized according to literature methods.

2.2 Equipment

- Shimadzu UV–vis 2550 spectrophotometer was used for Uv-Vis electronic absorption spectral measurements.

- Fluorescence excitation and emission spectral measurements were recorded on Varian Eclipse fluorescence spectroflourimeter.

- Fluorescence lifetimes were recorded with time correlated single photon Counting setup (TCSPC) (FluoTime 200, Picoquant, GmbH) with a diode laser (LDH-P-670) with PDL800-B. Fluorescence was detected under the magic angle with a peltier cooled photomultiplier tube (PMT) (PMA-C 192-N-M, Picoquant) and integrated electronics (Pico Harp 300E, Picoquant GmbH). A monochromator with a spectral width of about 4 nm was used to select the required emission wavelength band. A scattering Ludox solution (DuPont) was used to measure the response function of the system and had a full width at half maximum (FWHM) of about 280 ps. To obtain good statistics, the ratio of stop to start pulses was kept low (below 0.05). Measurement of the entire luminescence decay curve (range 0–200 ns) was at the maximum of the emission peak. Data analysis was done using the program Fluofit (Picoquant GmbH). Estimation of the decay error times was carried out using the support plane approach.

- Thermo-gravimetric analyses (TGA) were performed using a Shimadzu simultaneous DTA-TG apparatus (DTG-60A). The analyses were carried out under nitrogen at a flow rate of 120cm^{-3} min^{-1}. The weighed samples were heated from 30 to 800 °C at a heating rate of 10 °C min^{-1} using Al pans.

- Scanning electrochemical microscopy (SECM) experiments were carried out using Uniscan Model 370 equipment. SECM approach curves were done using a 25 μm Pt microelectrode with a Pt counter electrode and Ag|AgCl wire as the pseudo-reference electrode. Images were obtained by maintaining the tip at a constant Z position and scanning in the X–Y plane over the desired area (constant-height mode of SECM) and monitoring changes in the steady-state current of $K_3[Fe(CN)_6]/K_4[Fe(CN)_6]$ following oxidation at 0.1 V vs. Ag|AgCl. Glassy carbon plates (Goodfellow, UK) of 1×1 cm and 2 mm thick were used as substrates for SECM.

- Transmission Electron Microscopy (TEM) images were obtained from a Zeiss Libra TEM 120 model operated at 90kV.

- Time-of-Flight-Secondary Ion Mass Spectrometer (TOF-SIMS) data were recorded with ION TOF GmbH TOF SIMS 5 – 100 run in micro-raster mode. The raster area was 3000 μm x 3000μm, and the sample was run in both positive and negative ion modes. The analyzer was set to a standard operating mode with a cycle time of 100 μs, whilst the primary beam was a Bi_3 ion cluster gun with a current of 0.4 pA

and an energy of 3000 eV (termed as spectrometry mode). The Bi_3 cluster and electron flood gun was used to get a better ion signal from the sample. Charge compensation was used to account for the electron flood gun. The raw data was processed using the Surface Lab 6.5 software provided by ION TOF. Glassy carbon plates (Good fellow, UK) of 1×1 cm and 2 mm thick were used as substrates for TOF-SIMS.

- Infrared spectra were recorded on a Perkin Elmer 100 ART FT-IR spectrometer.

- BAS 100B electrochemical analyzer was used for the rotating disk electrode (RDE) studies

- Other electrochemical experiments (cyclic, linear scan voltammetry and chronoamperometric) were performed using Autolab Potentiostat PGSTAT 302 (Eco Chemie, Utrecht, The Netherlands) driven by the general purpose Electrochemical System data processing software (GPES, software version 4.9).

- Electrochemical impedance spectroscopy (EIS) studies were performed using an Autolab Potentiostat PGSTAT30 equipped with GPES software version 4.9. The studies were performed between 0.1 Hz and 10 Hz, using a 5 mV rms sinusoidal modulation. A non-linear least squares (NLLS) method based on the EQUIVCRT programme was used for automatic fitting of the obtained EIS data.

- Raman spectra were obtained using a Bruker Vertex 70-Ram II Raman spectrometer (equipped with a 1064 nm Nd: YAG laser and liquid nitrogen cooled germanium detector).

- Elemental analyses were carried out on a Vario EL III Micro Cube CHNS Analyser.

- Mass spectral data were collected with a Bruker Auto FLEX III Smartbeam TOF Mass spectrometer. The spectra were acquired using α-cyano-4-hydroxycinnamic acid as the MALDI matrix.

- Scanning electron microscopy (SEM) images of modified glassy carbon plates (Goodfellow, UK) were obtained using a TESCAN Vega TS 5136LM Electron microscope.

- X-ray photoelectron spectroscopy (XPS) was done using a Kratos Axis Ultra DLD, using an Al (monochromatic) anode, equipped with charge neutralizer and the operating pressure kept below 5 x 10^{-9} torr. For wide/survey XPS scans, the following parameters were used: emission current was kept at 5 mA and the anode voltage at 15 kV. The resolution used to acquire wide/survey scans was at 160 eV pass energy using a hybrid lens in the slot mode. For high-resolution scans, the resolution was changed to 40 eV pass energy in the slot mode. Curve fitting was performed using Gaussian-Lorentzian peak shape after performing a linear background correction. Glassy carbon plates (Goodfellow, UK) of 1×1 cm and 2 mm thick were also

used as substrates for XPS, following modification as was done for GCE below.

- X-ray diffraction (XRD) spectra were performed on a Bruker D8 Discover diffractometer, equipped with a LynxEye detector, under Cu-Kα radiation (λ= 1.5405 Å). Data were collected in the range from 2θ = 10° to 100°, scanning at 0.010° min^{-1} and 192 s per step.

2.3 Synthesis of MPcs

2.3.1 Synthesis of cobalt tetra aminophenoxy phthalocyanine {CoTAPhPc (1)} (Scheme 3.1.)

CoTAPhPc (**1**) was synthesized as follows: a mixture of 4-amino-phenoxy phthalonitrile [117], (300 mg, 1.29 mmol), anhydrous cobalt chloride (42 mg, 0.32 mmol), quinoline (3 mL) and three drops of DBU was refluxed for 24 h. The product was cooled to room temperature before being washed several times with methanol, ethanol, n-hexane, warm water and diethyl ether successively. The dried residue was subjected to Soxhlet extraction in ethanol/water 1:1 solvent mixture for seven days before oven drying at 80 °C for 48 h. Yield of 80% was obtained. UV/VIS (DMSO) λ_{max} nm, (log ε): 349 (2.56), 678 (4.27), 618 (1.39). Elemental analysis Calc. for $C_{56}H_{36}CoN_{12}O_4.5H_2O$: C 61.71, H 4.25, N 15.42, Found; C 61.33, H 3.87, N 14.18. FT-IR [ATR] (υ_{max}/cm^{-1}) 3311, 3307 (N-H stretch), 3051 (C-H aromatic), 1714, 1665 (C=N imine), 1605, 1539 (N-H bend), 1473 (C=C aromatic), 1468, 1404 (C-N aryl), 1222 (C-O-C), 1092, 949, 830, 744, 500 (Phthalocyanine skeleton). MALDI TOF MS m/z cal. For $C_{56}H_{36}CoN_{12}O_4$ 999, found 999 [M+].

2.3.2 Synthesis of cobalt mono carboxy phenoxy phthalocyanine (4) (Scheme 3.2)

CoMCPhPc (**4**) was synthesized as follows: a mixture of 4-carboxy-phenoxy phthalonitrile [18] (450 mg, 1.70 mmol), dicyanobenzene (750 mg, 5.86 mmol), anhydrous cobalt chloride (42 mg, 0.32 mmol), pentanol (3 mL) and three drops of DBU were refluxed for 24 h under argon. The product was cooled to room temperature and precipitated out in methanol before being washed several times with methanol, ethanol, (1 M) HCl, warm water and diethyl ether successively and oven dried at 80 °C for 48 h. The obtained impure CoMCPhPc (**4**) was dissolved and chromatographed on Si_{60} column with methanol/tetrahydrofuran (5% methanol). Yield of 4.7 % was obtained. UV/VIS (DMSO) λ_{max} nm, (log ε): 325 (1.45), 595 (0.70), 665 (3.11). Elemental analysis Calc. for $C_{39}H_{20}CoN_8O_3.4H_2O$: C 60.08, H 3.62, N 14.37 Found: C 59.15, H 4.08, N 15.55. FT-IR [ATR] (v_{max}/cm^{-1}) 3403 (O-H stretch), 2923 (C-H aromatic), 1684 (C=N imine, C-N aryl), 1446 (C=C aromatic), 1210 (C-O-C), 1064, 956, 807, 708 (Phthalocyanine skeleton). MALDI TOF MS m/z cal. For $C_{39}H_{20}CoN_8O_3$ 707.56, found 709.91 [M^{+}+2H].

2.3.3 Nanosized cobalt tetra amino phthalocyanine {CoTAPcNP (5)}, cobalt tetra aminophenoxy phthalocyanine {CoTAPhPcNP (1)} and cobalt phthalocyanine {CoPcNP (3)}

Nanosized phthalocyanine were prepared as described elsewhere [6] with some modification. Briefly, 0.15 g (0.26, 0.15 or 0.24 mmol) of CoPc (**3**), CoTAPhPc (**1**) or CoTAPc (**5**) respectively, was dissolved in 98% sulphuric acid

(5 ml). Then, the solution was added drop-wise to a vigorously stirring 300 ml aqueous solution of hexadecyltrimethyl ammonium bromide (0.45 g, 123 mmol). The resulting solution was washed successively with Millipore water until wash water was at pH 7. The solid residue was dried at 80 °C in an oven for 24 h. The resulting nanoparticles were dispersed in dry DMF by sonication for 1 h.

2.4 Preparation of nanomaterials

2.4.1 Reduced graphene oxide nanosheets (rGONS)

Reduced graphene oxide nanosheets (rGONS) were prepared according to literature methods [119]. Briefly, 0.1 g graphene oxide nanosheets (GONS) were dispersed in 100 mL millipore water through ultra-sonication. Sodium borohydride (0.57 g, 15 mmol) was added followed by heating at 70 °C for 3h. The black solid product obtained by filtration over a fritted glass funnel was washed five times with 50 mL portions of millipore water and dried in an oven at 80 °C for 48 h.

2.4.2 Reduced boron doped graphene oxide nanosheets (rBDGONS)

Boron doped graphene oxide nanosheets (BDGONS) were prepared according to literature methods [120] with slight modifications as follows. GONS (300 mg) was mixed with 1.5 g boric acid and ground together. The mixture was loaded in corundum and placed at the centre of a tube furnace, followed by purging with argon for 20 min before starting to heat the furnace. The temperature was increased at a steady rate of 10 °C per min until a temperature of 500 °C and kept there for 20 min. The temperature was then

increased at the same rate up to 1000 °C where it was maintained for a further 60 min before switching off and allowing it to fall to room temperature. The product was washed with copious amounts of warm water to get rid the unreacted boric acid. Reduced boron doped graphene oxide nanosheets (rBDGONS) were obtained as described for rGONS above.

2.4.3 Reduced nitrogen doped graphene oxide nanosheets (rNDGONS)

Reduced nitrogen doped graphene oxide nanosheets were synthesised according to literature methods with minor modifications [121]. Briefly GONS and melamine were mixed together with a mass ratio of 1:5 by grinding, forming a uniform grey mixture. This mixture in a crucible was then placed into a corundum tube with a flow of argon atmosphere for 20 min. The mixture was then heated to 500 °C at a rate of 10 °C/min where the temperature was maintained for 20 min. Heating was then continued to 1000 °C and temperature maintained for another 1 h before the furnace was allowed to cool to room temperature. Reduction of NDGONS to rNDGONS was then done as described for rGONS discussed above.

2.4.4 Reduced sulphur doped graphene oxide nanosheets (rSDGONS)

GONS (500 mg) were premixed with 1.5 ml concentrated sulphuric acid and heated to 500 °C and the temperature maintained for 20 min in a tube furnace. The temperature was then raised to 1 000 °C and maintained for 1 h before allowing the furnace to cool to room temperature. This is the first time sulphuric acid is usedas a precursor for sulphur doping. The resultant product (SDGONS) was washed with methanol, ethanol and copious amounts

of millipore water up to pH 7 before being dried in an oven at 80 °C for 48 h. SDGONS were then reduced as described for rGONS to obtain rSDGONS.

2.4.5 Synthesis of reduced phosphorus doped graphene oxide nanosheets. (rPDGONS)

Phenyl phosphine (as source of phosphorus) (300 mg, 2.73 mmol) and 500 mg GONS were dispersed in a water ethanol mixture 1:1 ratio by ultra-sonication for 3 h [122]. The mixture was then freeze-dried to obtain a black solid. The product was loaded in corundum and placed at the centre of a tube furnace, followed by purging with argon for 20 min and heated as described above for BDGONS to give PDGONS, which were then reduced as described for rGONS to give rPDGONS.

2.4.6 Reduced phosphorus-nitrogen co-doped graphene oxide nanosheets (rPNDGONS)

Phosphorus-nitrogen co-doped graphene oxide was prepared according to literature methods [107]. Briefly 500 mg of GONS was mixed with 150 mg, 1.14 mmol of $(NH_4)_2HPO_4$ (as source of both nitrogen and phosphorus) in 200 ml of millipore water at room temperature under stirring in an open beaker. The sample was freeze dried and left for 20 min in a tube furnace under the flow of argon atmosphere, before heating as described above for PDGONS to give PNDGONS. The product was then reduced as described for rGONS to give rPNDGONS.

2.4.7. Synthesis of reduced sulphur-nitrogen co-doped graphene oxide nanosheets (rSNDGONS)

This work reports the dual doping of GONS with sulphur and nitrogen using $(NH_4)_2SO_4$ as both nitrogen and sulphur source. Briefly 500 mg of GONS was mixed with 150 mg, 1.14 mmol of $(NH_4)_2SO_4$ (as a source of both nitrogen and sulphur) in 200 mL of millipore water at room temperature under stirring in an open beaker. The sample was freeze dried before being transferred into a quartz boat in the centre of a tube furnace under the flow of argon atmosphere for 20 min and heated as described above for BDGONS to give SNDGONS, which were then reduced as described for rGONS to give rSNDGONS.

2.4.8 Non covalent bonding of MWCNT and rGONS

MWCNT and rGONS (1 mg/ml each) were separately suspended in DMF and sonicated for 1 h. The two suspensions were then mixed and left stirring for 24 h to allow for π-π stacking. The product is referred to as MWCNT/rGONS(mix) in this work.

2.4.9. Diaminomaleonitrile functionalised MWCNT [(DAMN)-MWCNT] {Scheme 3.5A}

Multiwalled carbon nanotubes were carboxylated following literature methods [123] with slight modification. Briefly 1 g of MWCNT was refluxed in 55% nitric acid for 3 h to give carboxylated MWCNTs (MWCNT-COOH). This method is mild and does not result in cutting short the MWCNTs. The resultant brown suspension was successively washed with copious amounts of millipore water

until the wash water reached pH 7. The product was then dried overnight in an oven at 70 °C. MWCNT-COOH was then linked to diaminomaleonitrile (DAMN) as reported before with minor modifications [124,125]. Briefly MWCNT-COOH (50 mg) were transferred into a clean vial containing DMF (10 mL) and $SOCl_2$ (5 ml) and stirred for 48 h in an airtight vial at room temperature to activate the carboxyl groups. This was followed by addition of diaminomaleonitrile (70 mg; 0.65 mmol) to obtain diaminomaleonitrile functionalized MWCNT {(DAMN)-MWCNT} whose purification was achieved by centrifugation at 3000 rpm in methanol and then ethyl acetate and drying at 110 °C in the oven.

2.4.10 Conjugation of CoTCPhPc (2) to (DAMN)-MWCNT

2.4.10.1 Covalent to form CoTCPhPc(2)-(DAMN)-MWCNT(linked) (Scheme 3.5B)

CoTCPhPc (**2**) (0.5 g, 70.43 mmol) was activated in the presence of 1;1 EDC, (1.1 g, 7 mmol) and NHS (0.8 g, 7 mmol) before 1 mg (DAMN)-MWCNT was added and the mixture was left stirring for another 48 h. The resultant mixture was washed several times with warm water and THF respectively to remove the unbound CoTCPhPc(**2**), EDC and NHS. The product was dried overnight at 70 °C in an oven. The product is represented as CoTCPhPc(**2**)-(DAMN)-MWCNT(linked).

2.4.10.2 Non-covalent to form CoTCPhPc/(DAMN)-MWCNT(mix)

The MPc and DAMN-MWCNT were separately dispersed in DMF to form a concentration of 1 mg/ml of each before sonicating in the dark for 1 h. The

resultant suspension was stirred for 24 h to form CoTCPhPc(**2**)/(DAMN)-MWCNT(mix), since it is assumed that there will be π-π stacking between CoTCPhPc(**2**) and MWCNTs.

2.4.11 Nanocomposites of AuNRs with CoTAPhPcNP (1), rSDGONS, rNDGONS, or rSNDGONS (Scheme 3.3)

Pristine (rGONS), nitrogen (rNDGONS), sulphur (rSDGONS) or sulphur/nitrogen (rSNDGONS) doped graphene oxide nanosheets were separately suspended in an aqueous AuNRs (1 mg/mL) solution to form a concentration of 1 mg/ml of each with intermittent sonicating to avoid the settling of the nanosheets. The suspensions were left for 24 h under stirring to allow for Au-S or Au-N or both bond formation [126] for doped GONS. The nanocomposites are represented as rNDGONS-AuNRs(linked), rSDGONS-AuNRs(linked) and rSNDGONS-AuNRs(linked), respectively. CoTAPhPc**NP** (1 mg/ml, 1 μM), and AuNRs (1 mg/mL) solution in DMF was allowed to form Au-N bonds by leaving the mixture to stand for 24 h under stirring. The nanocomposite is represented as CoTAPhPc**NP(1)**-AuNRs(linked). Complex **1** and AuNRs were also added separately to the electrode and represented as CoTAPhPc**NP(1)**@AuNRs.

2.4.12. Conjugation of CoMCPhPc (4) to NDGONS, SDGONS and SNDGONS (Scheme 3.4)

The COOH groups on CoMCPhPc**(4)**, NDGONS or SDGONS or SNDGONS or pristine GONS were first converted to acid chloride according to literature [127] as follows {note that GONS were not reduced since –COOH is needed for

the formation of an amide linkage}: CoMCPhPc (**1**) (0.5 g, 0.71 mmol), or 0.2 g of pristine (or doped GONS) were separately added to 5 ml of $SOCl_2$ in 10 ml of anhydrous DMF, followed by stirring for 48 h, resulting in acid chloride derivatives, step 1, **Scheme 3.4**. Acid chloride derivatized NDGONS, SDGONS, SNDGONS or pristine GONS were then linked to diaminomaleonitrile (DAMN) as follows: 1 g (9.25 mmol) of diaminomaleonitrile was added to each mixture, followed by stirring for 48 h, step 2, **Scheme 3.4**. The diaminomaleonitrile functionalized pristine or doped GONS were washed several times with ethanol and THF to remove unbound DAMN. The resultant solid was dried at 70 °C overnight before adding it to the solution of acid chloride functionalized CoMCPhPc (**4**) and leaving it to react for another 48 h (step 3, **Scheme 3.4**), to give CoMCPhPc(**4**)-(DAMN)-NDGONS(linked) or CoMCPhPc(**4**)-(DAMN)-SDGONS(linked), CoMCPhPc(**4**)-(DAMN)-SNDGONS(linked) or CoMCPhPc(**4**)-(DAMN)-GONS(linked).

2.5 Electrode modification

Glassy carbon electrode (GCE) was used as the working electrode, the silver | silver chloride (saturated potassium chloride) as the reference electrode and platinum wire as the counter electrode. The GCE was polished on a Buehler-felt pad using alumina (<10 μm). Between each polishing step, Millipore water was used to remove any impurity by sonicating for 10 min. The electrode was then rinsed with millipore water and dried before use. The GCE were modified via the drop dry method. All the solutions were purged

with argon gas for 20 min to drive off oxygen before analysis. The argon atmosphere was maintained above the solution during different determinations.

2.6 Optical Sensing

2.6.1 Formation of reduced graphene oxide/graphene oxide–ZnOCPc(6) conjugate.

ZnOCPc(**6**) (0.2 mg) was dissolved in 100 mL DMSO to give an initial concentration of 2.0 x 10^{-6} M. Then, 7 mg of rGONS or GONS were added to give a concentration of 70 mg mL^{-1} and the mixture sonicated in the dark for 1h followed by stirring in the dark for 24h [128]. The conjugates were re-precipitated in ethanol, centrifuged and washed with several portions of ethanol to remove unbound ZnOCPc(**6**).

2.6.2. Procedures for the optical recognition of hydrogen peroxide

Different concentrations of H_2O_2 were prepared in DMSO from a 30% H_2O_2 stock solution. The fluorescence spectra of ZnOCPc(**6**) alone, ZnOCPc(**6**)-rGONS or ZnOCPc(**6**)-GONS (both at the same absorbance as for ZnOCPc (**6**) alone) were recorded. The fluorescence was quenched for both ZnOCPc(**6**)-rGONS and ZnOCPc(**6**)-GONS as compared to ZnOCPc alone. Then different concentrations of H_2O_2 were added to make a total volume of 5 mL from a volume of 4.5 mL of the nanoconjugates or ZnOCPc(**6**) alone. The fluorescence was restored by the addition of H_2O_2. Fluorescence measurement was done within five min of analyte introduction for all samples.

Publications

This work comprises of published or submitted material in the following peer reviewed journals. These publications have not been referenced in text.

1. Munyaradzi Shumba and Tebello Nyokong**,** Development of nanocomposites of Phosphorus-Nitrogen Co-doped graphene oxide nanosheets and Nanosized Cobalt Phthalocyanines for electrocatalysis. *Electrochimica Acta 213 (**2016**) 529–539*

2. Munyaradzi Shumba and Tebello Nyokong, Electrocatalytic activity of nanocomposites of sulphur doped graphene oxide and nanosized cobalt Phthalocyanines *Electroanalysis* **2016**, 28, 3009-3018

3. Munyaradzi Shumba and Tebello Nyokong, Electrode modification using nanocomposites of boron or nitrogen doped graphene oxide and cobalt (II) tetra aminophenoxy phthalocyanine nanoparticles" *Electrochimica Acta 196* **(2016)** *457 - 469*

4. Munyaradzi Shumba and Tebello Nyokong, Characterization and Electrocatalytic activity of nanocomposites consisting of nanosized cobalt tetraaminophenoxy phthalocyanine, multi-walled carbon nanotubes and gold nanoparticles, *Electroanalysis* **2016**, 28, 1478 – 1488

5. Munyaradzi Shumba, Philani Mashazi,Tebello Nyokong, "Turn-on" fluorescence enhancement of Zn octacarboxy phthalocyanine graphene oxide conjugates by hydrogen peroxide, *Journal of Luminescence* 170 **(2016)** 317-324.

6. M. Shumba, S. Nyoni, J. Britton, T. Nyokong, Characterization of electrodes modified with nanocomposites of cobalt tetra aminophenoxy

phthalocyanine, reduced graphene and multi-walled carbon nanotubes, *Int. J. Nanoscience* **(2016), Accepted with revision.**

7. Munyaradzi Shumba, Sitholile Centane, Francis Chindeka, Tebello Nyokong, Nanocomposites of Sulphur-Nitrogen Co-doped graphene oxide nanosheets and Cobalt Mono Carboxyphenoxy Phthalocyanines for Facile electrocatalysis. *Journal of Electroanalytical Chemistry* 791 **(2017)** 36–48.

8. Munyaradzi Shumba and Tebello Nyokong, Effects of covalent versus non-covalent interactions on the electrocatalytic behaviour of tetra carboxy phenoxy phthalocyanine in the presence of multiwalled carbon nanotubes. *J. Coordination Chemistry*. **(2017) In press.**

9. Munyaradzi Shumba and Tebello Nyokong, Electrocatalytic application for gold nanoparticles decorated sulphur-nitrogen co-doped graphene oxide and nanosized cobalt tetra aminophenoxy phthalocyanine conjugates. *Electrochimica Acta.* 236 **(2017)** 212–220.

Chapter Three

3. Characterization

This Chapter deals with characterization of Pcs, the nanomaterials and their conjugates

3.1. Characterisation of GONS and their conjugates with other nanomaterials.

This section focuses on elucidation of the chemical nature and thermal stability of the GONS intended to be applied as electrocatalysts and optical nanoprobes. MWCNT and (DAMN)-MWCNT are not new hence only discussed in the presence of phthalocyanines.

3.1.1 TEM images of GONS

Transmission electron microscopy (TEM) images were obtained to confirm the sheet like nature of graphene oxide nanomaterials and determine any associated changes in the morphology with either reduction or heteroatom doping of pristine graphene oxide nanosheets (GONS). **Fig. 3.1** shows that doping is accompanied by development of increased folds as evidenced by rNDGONS and rSNDGONS. The increased folds in rNDGONS and rSNDGONS could suggest the complex bonding network that result from doping and could point out to increased surface area for electrochemical catalysis as the nanomaterials change from 2D closely stacked layer to a 3D porous structure [129]. There is alsoimproved transparency in doped materials as compared to pristine GONS, being more pronounced in sulphur doped graphene oxide nanosheets (rSDGONS and rSNDGONS). This is evidence of effective

exfoliation because of doping probably due to the atomic size difference of the heteroatoms (rSDGONS and rSNDGONS) to that of the carbon skeleton. Phosphorus doping (rPDGONS and rPNDGONS) show pronounced deviation in morphology when compared to pristine GONS for the same reasons given above.

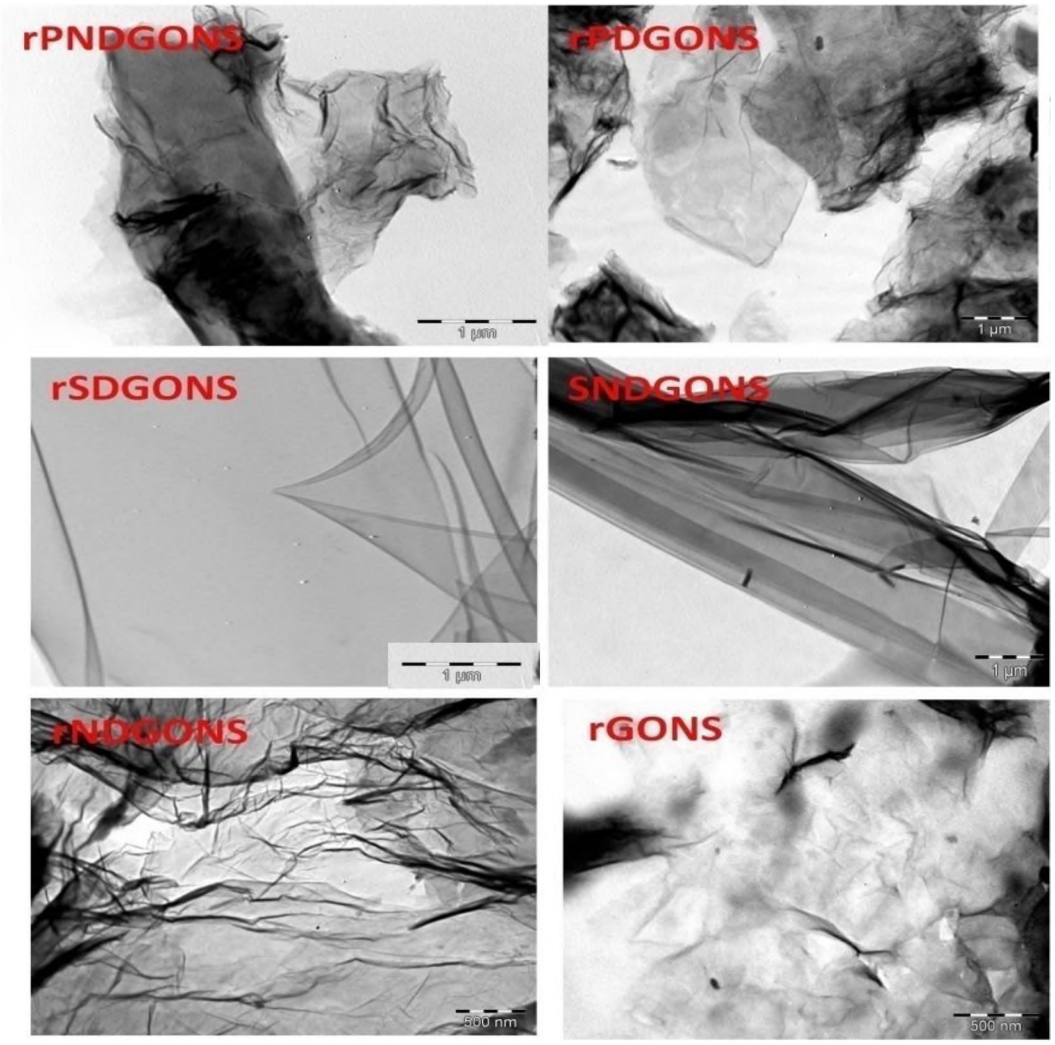

Figure 3.1 TEM images for graphene oxide nanosheets.

In the presence of AuNRs, there is evidence of the sheets being evenly decorated by the gold nanorods. **Fig. 3.2** clearly shows the dominance of rod shaped particles with an aspect ratio 3.5. For S and or N doped GONS, the

nanorods interact via Au-N/S bonds while for pristine GONS weak Van Der Waals forces may be at play.

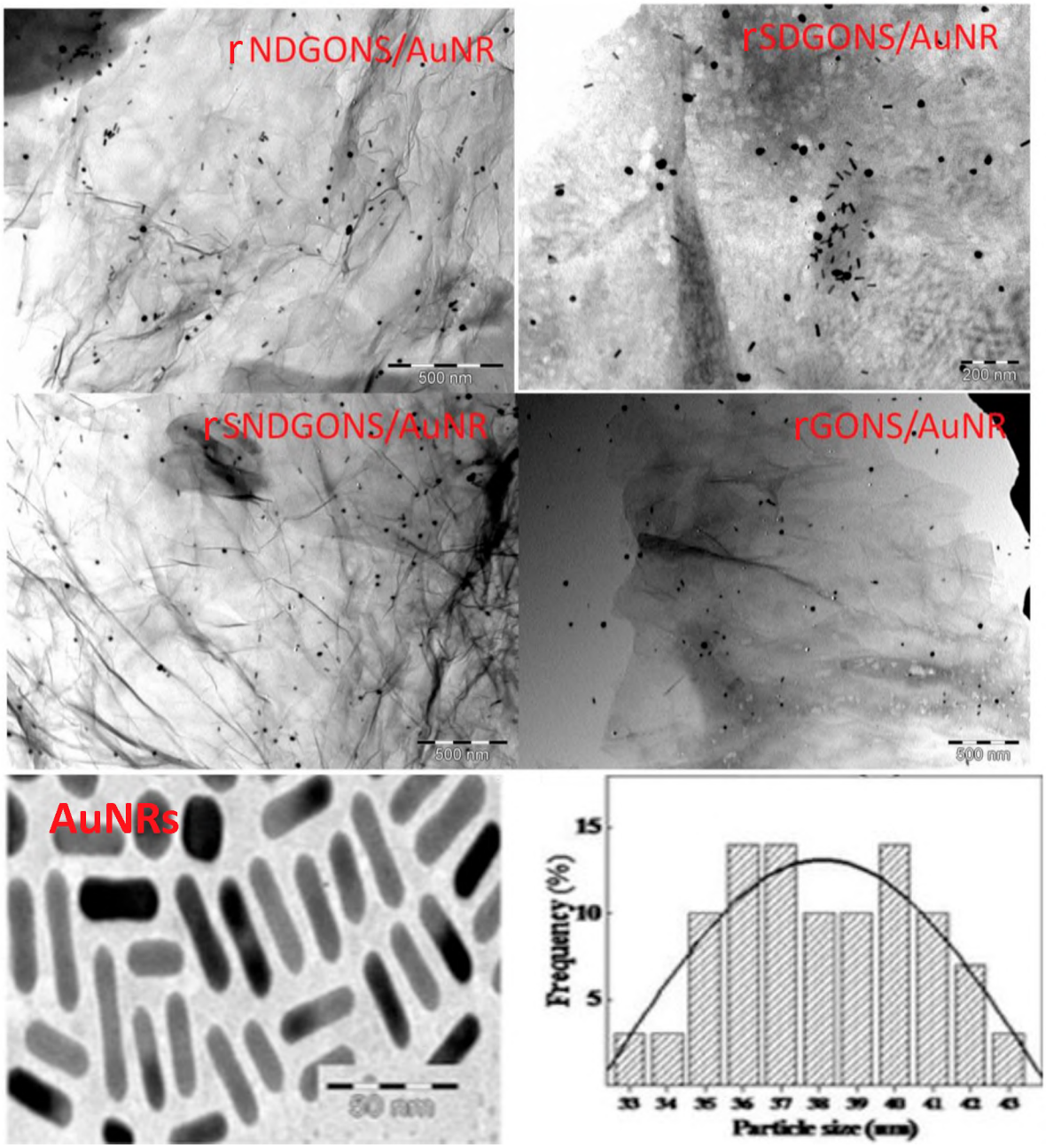

Fig. 3.2 TEM images for GONS and AuNRs conjugates.

3.1.2 XRD patterns

X-ray diffraction was usedto determine the interlayer distance of different forms of graphene oxide nanosheets. Generally, pristine graphene oxide is

characterised by a 001 plane peak around 2Θ = 18° which shifts to 2Θ~ 25° on reduction. The interlayer distance was determined using Bragg's law, **equation 3.1** [130]

$$\lambda = 2d\sin\theta \qquad 3.1$$

where λ is the wavelength of the X-ray beam (0.154nm), d is the distance between the adjacent GONSor layers, θ is the diffraction angle. Generally, reduction of GONS results in the elimination of oxygen functionalities and restoration of π conjugation. Improved π conjugation and elimination of out of plane oxygen functionalities is evidenced by a shift to higher 2 theta values of the 001 planes which correspond to deceased interlayer separations. A further shift to higher 2 theta values is observed upon doping graphene oxide nanosheets by heteroatoms. The decrease in the interlayer distances observed upon doping can be attributed to effective π-π interactions as defects become less [131] (**Table 3.1 and Fig 3.3A**). Nanoconjugates of AuNRs and GONS were also studied by XRD {using AuNRs-rSNDGONS(linked) as an example} to establish the Braggs reflections. Spectra for rSNDGONS-AuNRs(linked), **Fig. 3.3B(a)** show an overlap of the graphene 002 plane with AuNRs 111 and 200 planes giving an impression of an amorphous nanohybrid. The AuNRs show distinct Braggs reflections corresponding to planes {111}, {200}, {220}, {311} and {222}, **Fig. 3.3B(b)**. The diffraction patterns were indexed to the face centred cubic crystal structure of the gold nanoparticles, which conclusively proves the formation of gold nanocrystals with reference to the crystal structures from the PCPDFWIN: Au (#04-0784) [132].

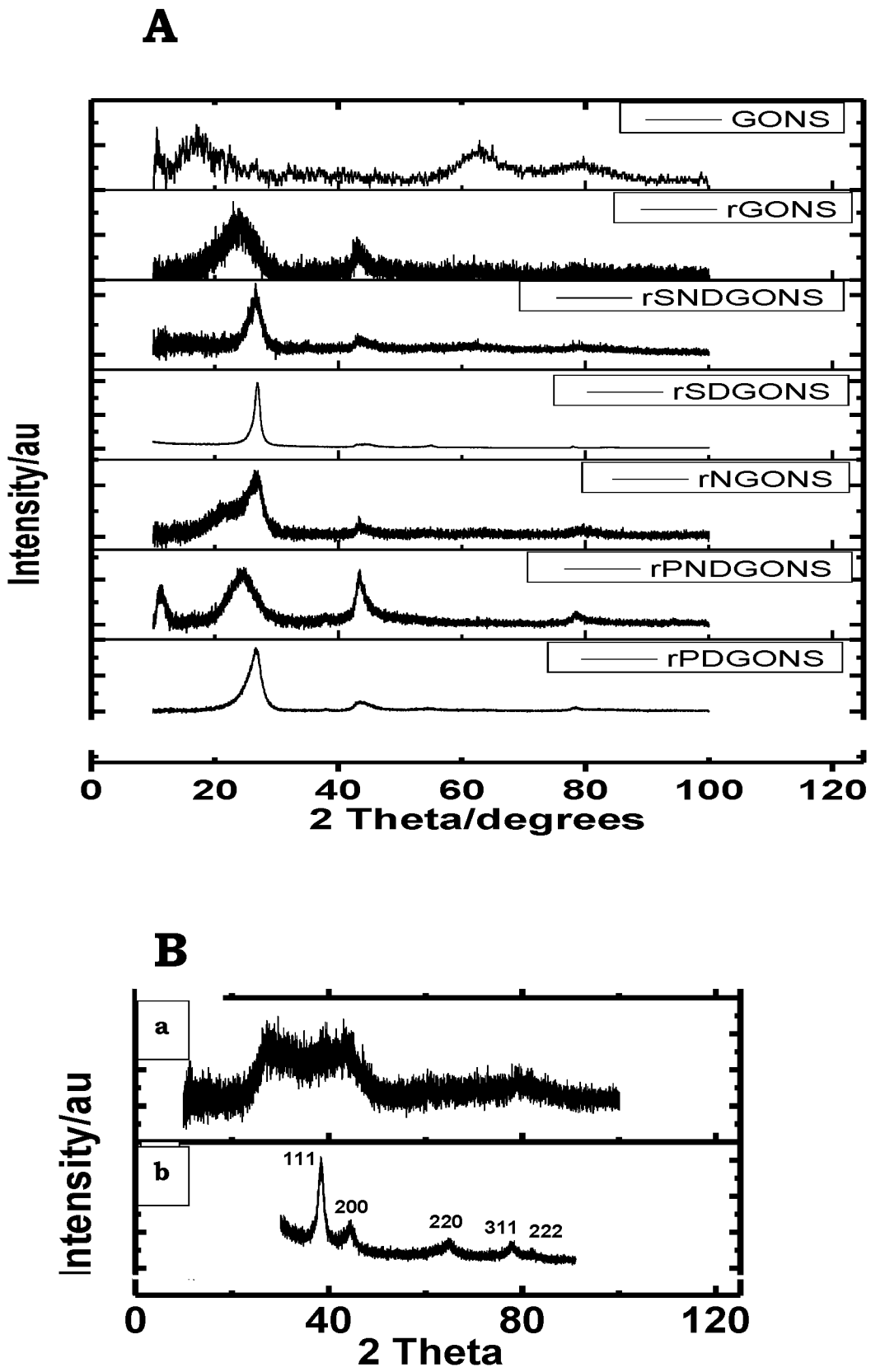

Figure 3.3 XRD spectra for (A) graphene oxide nanosheets, B (a) rSNDGONS-AuNRs(linked) and (b) AuNRs

Table 3.1. Interlayer spacing of graphene oxide nanomaterials

Nanomaterial	2Θ/degrees	interlayer spacing/nm
rGONS	25.63	0.35
rBDGONS	26.30	0.34
rNDGONS	26.78	0.33
rSDGONS	27.07	0.33
rPDGONS	26.67	0.33
rSNDGONS	26.79	0.33
rPNDGONS	26.44	0.33

3.1.3. Raman spectra

Raman spectra for rGONS and rNDGONS (used as examples)with characteristic tangential mode peak (G band) at 1592 and 1598 cm^{-1} respectively while the D band for both species was observed at 1288 cm^{-1}(**Fig. 3.4**). The D/G ratios for the rGONS and rNDGONS were found to be 1.59 and 0.93 respectively. This suggests that there are less defects for rNDGONS due to doping compared to rGONS. This is plausible given that the nitrogen replaces the out of plane oxygen functionalities while it gets incorporated into the carbon honeycomb as confirmed later in this section by XPS data.

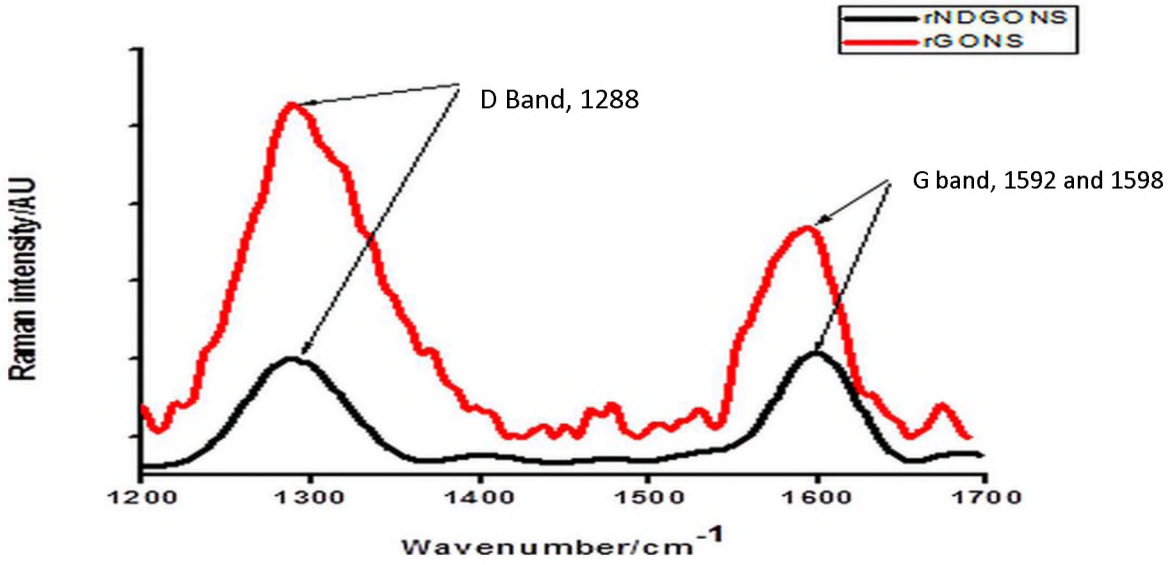

Figure 3.4 Raman spectra of selected graphene oxide nanosheets.

3.1.4. TGA

Thermal stability of the graphene moieties was investigated using thermal gravimetric analysis. It is interesting to note that reduction improves thermal stability of graphene oxide nanosheets (**Fig. 3.5**). This is so because therGONS has less labile oxygenated carbons. Thermal stability is even more significantly improved upon introducing heteroatoms into the carbon skeleton of graphene oxide nanosheets. This is evidence of effective doping as the heteroatoms become part of the carbon network and not easily decomposed upon the increase of temperature under inert condition. This information seems to agree very well with the XRD data, which show that doping results in low interlayer separations because of the heteroatom occupying the planar positions just as the carbon atoms. As such doped graphene oxide nanosheets only begin to significantly decompose at temperatures above 600°C while their pristine counterparts decompose at temperatures as low as 200°C. Thermal stability can be ranked by quoting the percentage residual masses at 800°C

and improves in the order GONS (30%) < rGONS (63%) < rPNDGONS (72%) <rNDGONS (74%) < PDGONS (85%) < rBDGONS (87%).

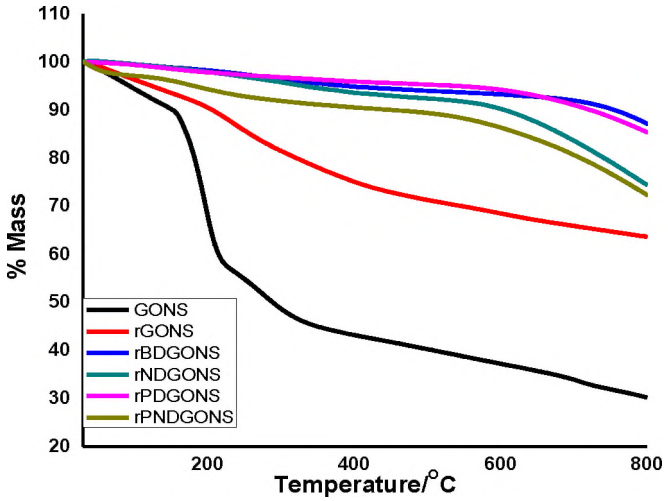

Figure 3.5 Thermograms Graphene oxide nanosheets.

3.1.5. XPS

The nature of different atoms in the different forms of graphene moieties was investigated using X-ray photoelectron spectroscopy (XPS). All the doped graphene oxide nanosheets showed the presence of the heteroatoms confirming successful doping of the pristine graphene oxide nanosheets. Nitrogen was observed in rNDGONS, rPNDGONS and rSNDGONS at around 400 eV, boron in rBDGONS at around 92 eV and sulphur in both rSDGONS and rSNDGONS at around 162 eV [survey scans shown for rNDGONS and rSNDGONS as examples, (**Fig. 3.6A**)]. The individual peaks were further deconvoluted to establish the nature of bonding between the different atoms that form the graphene skeleton.

The high-resolution N 1s spectrum (**Fig. 3.6B**) show that graphitic nitrogens dominate in rSNDGONS while pyridinic nitrogens dominate in rPNDGONS and rNDGONS. S being a group six element unlike group five N and P seem to have a different influence on the nature of nitrogen incorporation into the carbon skeleton. The presence of pyridinic and graphitic nitrogen suggests effective doping of nitrogen into the sp_2 configurations [129]. N1s for rSNDGONS is characterised by four peaks at 397.7 eV, 398.7 eV, 400.0 eV and 401.3 eV. The first three peaks were assigned according to literature to pyridinic, pyrrolic and graphitic nitrogens [133–135], while the fourth peak at 401.3 eV was attributed to N-S or N-O bonding [129] **(Fig. 3.6B)**. Spectra for rPNDGONS, **Fig. 3.6B**, also showed four types of nitrogens, which are shifted up field, compared to those of rSNDGONS: pyridinic (399.1 eV), pyrrollic (401.6 eV), graphitic (404 eV) and quaternary oxides of nitrogen (406 eV). The peaks at binding energies at 399.1 and 401.6 may also be due to P=N, P-N bonds forming [136]**.** It is noteworthy that co-doping as represented by rPNDGONS and rSNGONS results in an extra nitrogen oxide peak absent in rNDGONS **Fig. 3.6B**.

High-resolution B1s spectra for rBDGONS show two types of borons as shown in **Fig. 3.6C** confirming chemical incorporation of boron into the carbon network of graphene oxide.

Fig. 3.6D shows effective doping of sulphur into the graphene carbon network for both rSDGONS and rSNDGONS. Thiophene moieties centred at 163,97 eV and 165.18 eV in agreement with the reported $2p_{3/2}$ and $2p_{1/2}$ assignment, as a result of spin orbit coupling [134,137,138] for rSDGONS. There is also

evidence for oxidised sulphur at 166.38 and 167.56, which may be attributed to sulphite and sulphates respectively. The peak at 162.49 corresponds to thiols. The S2p for rSNDGONS peak was characterised by four species at binding energies, 161.6 eV, 163.8 eV, 165.2 eV and 166.9 eV corresponding to thiol, thiophene (two peaks), and some oxides of sulphur, **Fig. 3.6D**. The presence of high amounts of the two thiophene forms $S2p_{3/2}$ and $S2p_{1/2}$ in both rSDGONS and rSNDGONS is evidence of effective incorporation of sulphur into the carbon honeycomb of graphene. Thiol and sulphur oxides represent terminally positioned sulphur forms at 161.6 eV and 166.9 eV, respectively [139]. These forms of sulphur are thought to compromise the conductivity of the graphene skeleton since they disrupt the aromaticity of the substance unlike thiophene moieties, however, their percentage contribution is appreciatively low (**Fig. 3.6D**).

Three phosphorus 2p peaks are observed for rPDGONS, centred at 130.5 eV, 131.8 eV and 133.4 eV (**Fig. 3.6E**) while rPNDGONS show four peaks centred at 130.1 eV, 131.9 eV, 133.3 eV and 134.4 eV, **Fig. 3.6E**. The peak at 134.4 eV for rPNDGONS absent in rPDGONS, can be attributed to metaphosphates which form due to the condensation of pyrophosphates. The peak around 130.1 eV can be attributed to P-C, the one around 133.3 eV is reported to be C-O-PO_3 [122,136]. It is notable that phosphorus was only incorporated to a very small extent [140] compared to N, this is judged by the low % P in rPNDGONS when compared to % N in **Table 3.2**. This could be because of the differences in atomic size of phosphorus as compared to that of carbon hence not favourably incorporated as is the case with nitrogen. It is also interesting

to note that the amount of phosphorus is higher in rPNDGONS compared to rPDGONS, which may suggest synergistic interaction of phosphorus with nitrogen [122].

It is also noteworthy that co-doping results in higher oxygen percentage **(Table 3.2)** even after subsequent reduction coupled with a lower total heteroatom incorporation as compared to single element doping; compare SDGONS (1.79% O, 2.66% S) with SNDGONS (8.62% O, 1.95% S + N), also compare NDGONS (1.29% O, 3.44% N) with SNDGONS (8.62 % O, 1.95% S + N) or PNDGONS (3.23% O, 1.61% P + N); PDGONS (2.66% O, 0.10% P) with PNDGONS (3.23% O, 1.61% P + N); as shown in **Table 3.2**.

To prove the interaction of gold nanoparticles with sulphur and nitrogen, high-resolution Au4f spectra for rSNGONS-AuNRs(linked)-GCE were recorded, **Fig. 3.6F**. Both Au-N and Au-S bonds are possible. Au4f spectrum in AuNPs is usually characterised by two peaks at around 84 eV and 88 eV corresponding to the spin orbit splitting $Au4f_{7/2}$ and $Au4f_{5/2}$ respectively [141] which are seen for rSNGONS-AuNRs(linked) at 84.4 eV and 88.1 eV respectively, **Fig. 3.6F**. There is however emergence of smaller peaks centred at 85.6 eV, 86.4 eV and 89.8 eV corresponding to $Au4f_{7/2}$ Au-S, $Au4f_{7/2}$ Au-N, and $Au4f_{5/2}$ Au-S [141] (**Fig. 3.6F**). The presence of Au-S and Au-N bonds confirms that both the N and S of SNGONS interact with AuNRs.

A

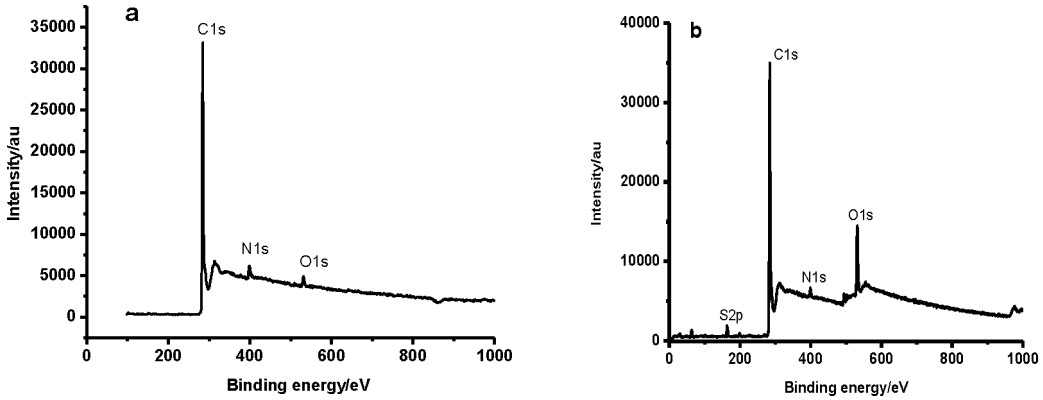
a
C1s
N1s
O1s
Intensity/au
Binding energy/eV
b
C1s
O1s
N1s
S2p
Intensity/au
Binding energy/eV

B

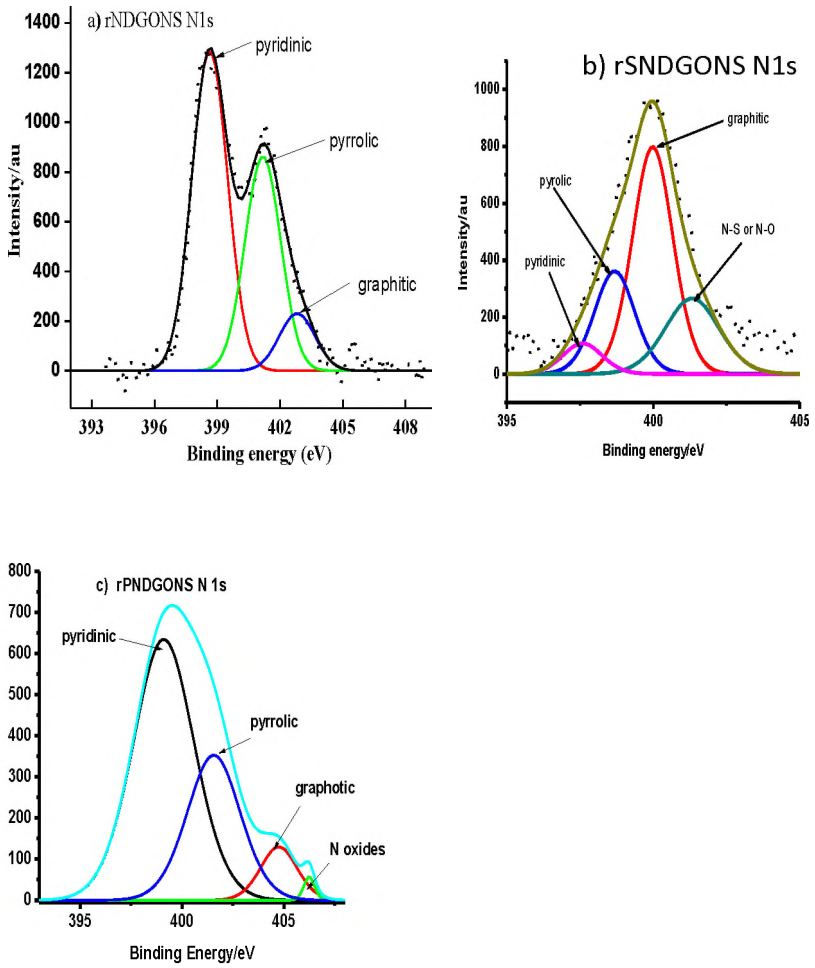
a) rNDGONS N1s
pyridinic
pyrrolic
graphitic
Intensity/au
Binding energy (eV)
b) rSNDGONS N1s
graphitic
pyrolic
N-S or N-O
pyridinic
Intensity/au
Binding energy/eV
c) rPNDGONS N 1s
pyridinic
pyrrolic
graphotic
N oxides
Intensity/au
Binding Energy/eV

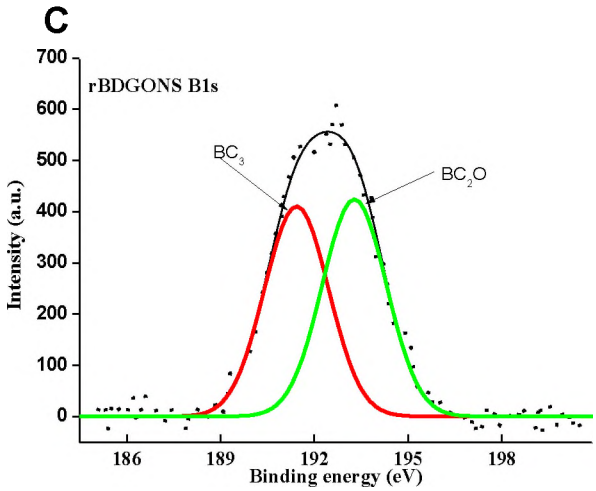
C
rBDGONS B1s
BC3
BC2O
Intensity (a.u.)
Binding energy (eV)

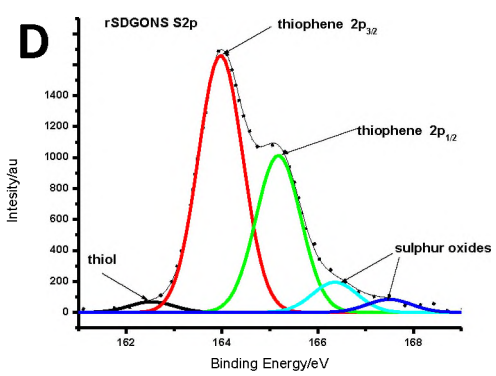
D
rSDGONS S2p
thiophene 2p3/2
thiophene 2p1/2
sulphur oxides
thiol
Intesity/au
Binding Energy/eV

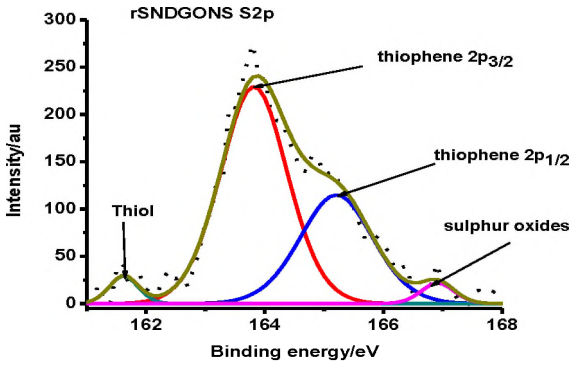
rSNDGONS S2p
thiophene 2p3/2
thiophene 2p1/2
sulphur oxides
Thiol
Intensity/au
Binding energy/eV

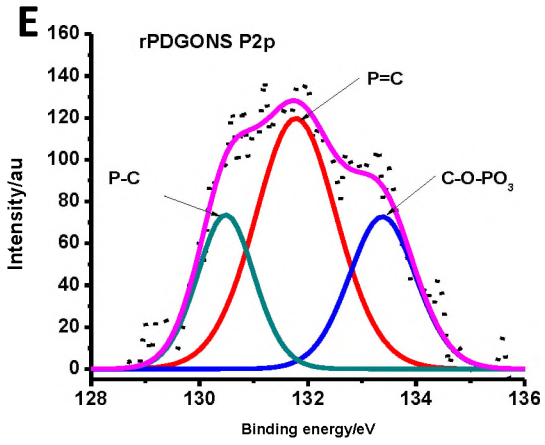
E
rPDGONS P2p
P=C
P-C
C-O-PO3
Intensity/au
Binding energy/eV

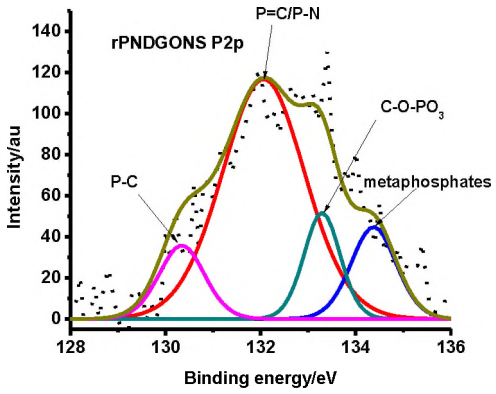
rPNDGONS P2p
P=C/P-N
C-O-PO3
metaphosphates
P-C
Intensity/au
Binding energy/eV

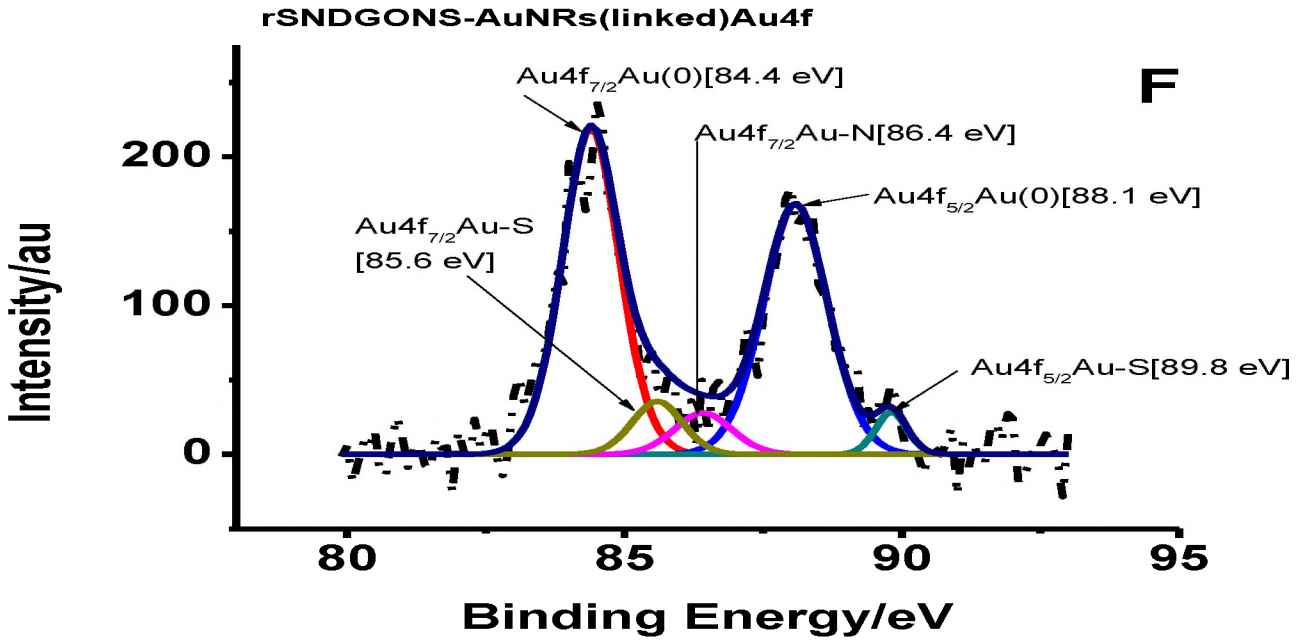

Figure 3.6. (A) wide scan XPS spectra for (a) rNDGONS and (b) rSDGONS, (B-F) high resolution XPS spectra for doped Graphene oxide moieties and of dopant heteroatom.

Table 3.2. A summary of % atomic concentration XPS data of GONS

Electrode	Carbon	Boron	nitrogen	phosphorus	sulphur	oxygen
rNDGONS	95.27	-	3.44	-	-	1.29
rSDGONS	90.62	-	-	-	2.66	1.79
rSNDGONS	89.44	-	1.69	-	0.26	8.62
rPNDGONS	95.17	-	1.44	0.17	-	3.23
rPDGONS	97.24	-	-	0.10	-	2.66
rBDGONS	79.37	3.17	-	-	-	15.98

3.2Synthesis and characterisation of metallophthalocyanines

3.2.1 Synthesis

3.2.1.1 Synthesis of complexes 1 and 4 (Schemes 3.1 and 3.2)

Complexes **2**, **3** and **5** are known while complexes **1** and **4** are new hence discussed here. Mono carboxyphenoxy and tetra aminophenoxy phthalocyanines are known for central metals such as Zn [142], the Co derivative is reported in this work for the first time. Complexes **1** and **4**were synthesized according to **Schemes 3.1** and **3.2** and are soluble in DMSO and DMF. FTIR, Mass spectrometry and elemental data were obtained for the products and the results were as expected for both Complexes **1** and **4**. NMR spectra were not recorded due to the paramagnetic nature of the central metal (Co).

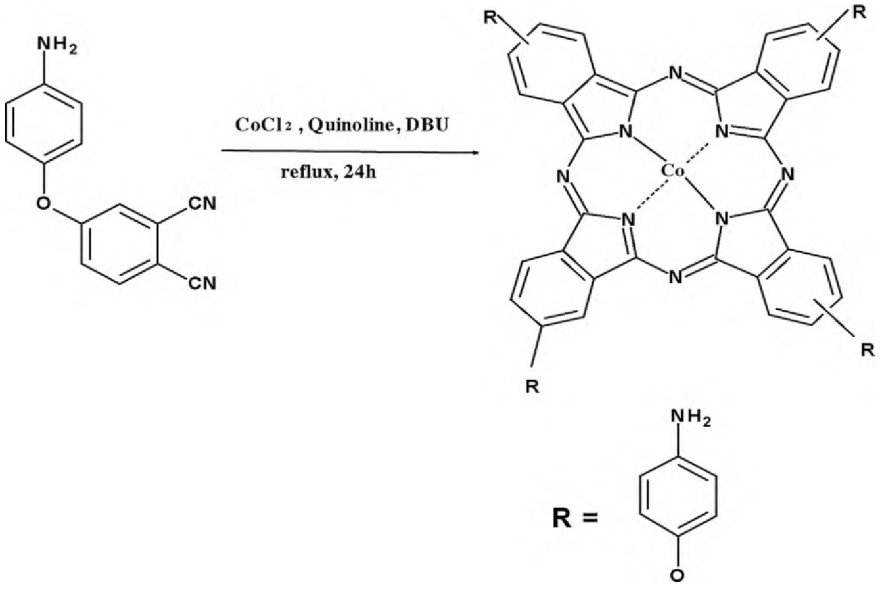

Scheme 3.1 Synthesis of cobalt tetra aminophenoxy phalocyanine (**1**)

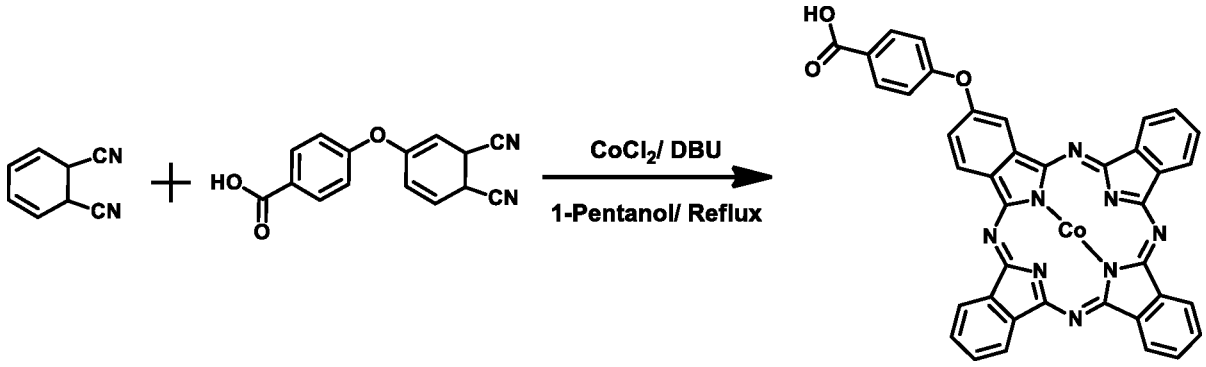

Scheme 3.2 Synthesis of cobalt mono carboxyphenoxy phthalocyanine (**4**)

3.2.1.2 Synthesis of MPc nanoparticles (Scheme 1.3)

Nanosized phthalocyanines were prepared as described in experimental section by dissolving the MPcs in 98% sulphuric acid followed drop-wise addition to a vigorously stirring aqueous solution of hexadecyltrimethylammonium. The resulting solution was washed successively with millipore water until wash water was at pH 7. The solid residue was dried at 80 °C in an oven for 24 h. The resulting nanoparticles were dispersed in dry DMF by sonication for 1h.

3.2.2 UV-Vis spectra

The UV-Vis spectrum of CoTAPhPc(**1**) is shown in **Fig. 3.7.** The Q band for **CoTAPhPc(1)** is observed at 678 nm and vibronic band at 618 nm, **Table 3.3**. The Soret band was observed at 349 nm. The broadness of the Q band is typical of amino substituted phthalocyanines [143]. Following the formation of nanoparticles for CoTAPhPc**NP**(**1**), there was no significant change in the Q band, except for the narrowing of the peak (**Fig. 3.7**), showing stability of the complex to the acid environment **Table 3.3**.

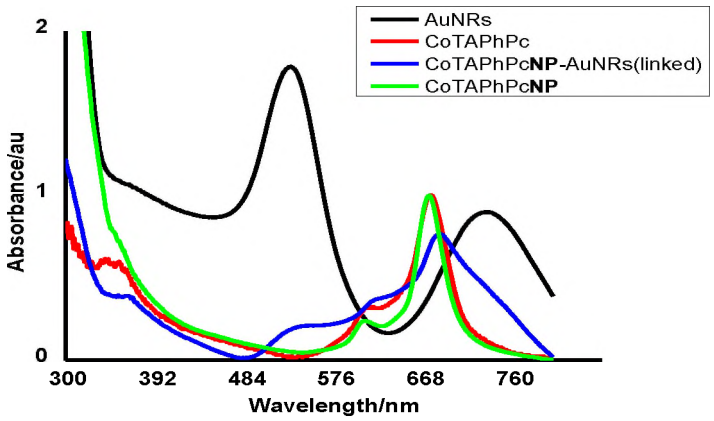

Figure 3.7 UV-Vis spectra of CoTAPhPc(**1**) (concentration ~1 x 10^{-6} M), CoTAPhPc**NP**(**1**), CoTAPhPc**NP**-AuNRs(linked) in DMF and AuNRs in water.

The ground state electronic absorption spectra for CoMCPhPc(**4**) and its conjugates are shown in **Fig. 3.8**. The Q band for CoMCPhPc(**4**) is observed at 665 nm and vibronic band at 618 nm, **Table 3.3**. The Soret band was observed at 349 nm.

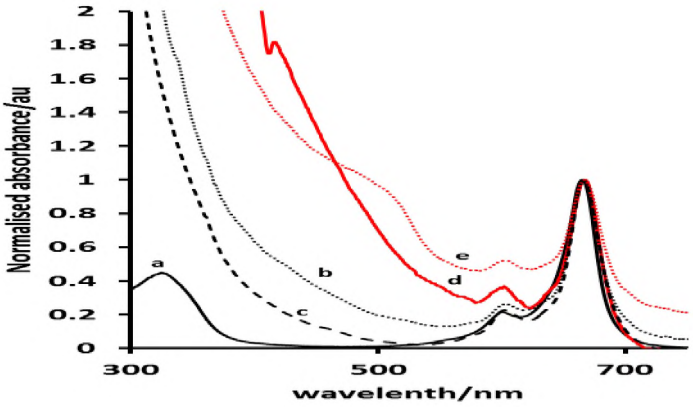

Fig. 3.8 Absorption spectra of (a) CoMCPhPc (**4**), (b) CoMCPhPc(**4**)-(DAMN)-GONS(linked), (c) CoMCPhPc(**4**)-(DAMN)-SDGONS(linked), (d) CoMCPhPc(**4**)-(DAMN)-NDGONS(linked) and (e) CoMCPhPc(**4**)-(DAMN)-SNDGONS(linked) in DMF [CoMCPhPc(**4**)] = 8 x 10^{-6} M.

Table 3.3 Nanomaterials linked to Pcs

Nanoconjugates	**Bonding**	**Q or SPR Uv/Vis band/nm in DMF**
rNDGONS-AuNRs(linked)	Au-N	530, 732 (SPR)
rSDGONS-AuNRs(linked)	Au-S	530, 732 (SPR)
rSNDGONS-AuNRs(linked)	Au-N, Au-S	530,732 (SPR)
CoTAPhPc (**1**)	-	678 (Q)
CoTCPhPc (**2**)	-	663(Q)
CoPc (**3**)	-	663 (Q)
CoMCPhPc (**4**)	-	665 (Q)
CoTAPc (**5**)	-	668 (Q)
ZnOCPc (**6**)	-	696 (Q)
1-AuNRs(linked)	Au-N	685 (Q), 530, 732 (SPR)
2/(DAMN)-MWCNT(mix)	ππ	663 (Q)
2-(DAMN)-MWCNT(linked)	amide	672 (Q)
4-(DAMN)-GONS(linked)	amide	666 (Q)
4-(DAMN)-NDGONS(linked)	amide	666 (Q)

Nanoconjugates	**Bonding**	**Q or SPR Uv/Vis band/nm in DMF**
4-(DAMN)-SDGONS(linked)	amide	666 (Q)
4-(DAMN)-SNDGONS(linked)	amide	667 (Q)
6/rGONS	ππ	696 (Q)
6/GONS	ππ	698 (Q)

[a]"/" =a mixture of different nanomaterials; "-, accompanied by linked" covalent bond. DAMN = diaminomaleonitrile; mix = mixed before electrode modification; "r" in front of GONS = reduced; if no "r", the GONS were not reduced.

3.2.3 TEM

The TEM images for the nanosized phthalocyanines (**Fig. 3.9)** show a mono dispersed array of nanoparticles, which is evidence for an effective downsizing of the phthalocyanines. The average sizes for CoTAPhPc**NP(1)**, CoTAPc**NP(5)** and CoPc**NP(3)** are 14 nm, 9.98 nm and 6.50 nm respectively. This shows that the sizes of the nanoparticles are depended on the molecular size of the bulk form of the metallophthalocyanine hence CoPc**NP** (**3**) gives the smallest nanoparticles and CoTAPhPc**NP** (**1**) the largest nanoparticles. The dark grey region, more pronounced in the CoTAPhPc**NP** (**1**) is due to the solvent.

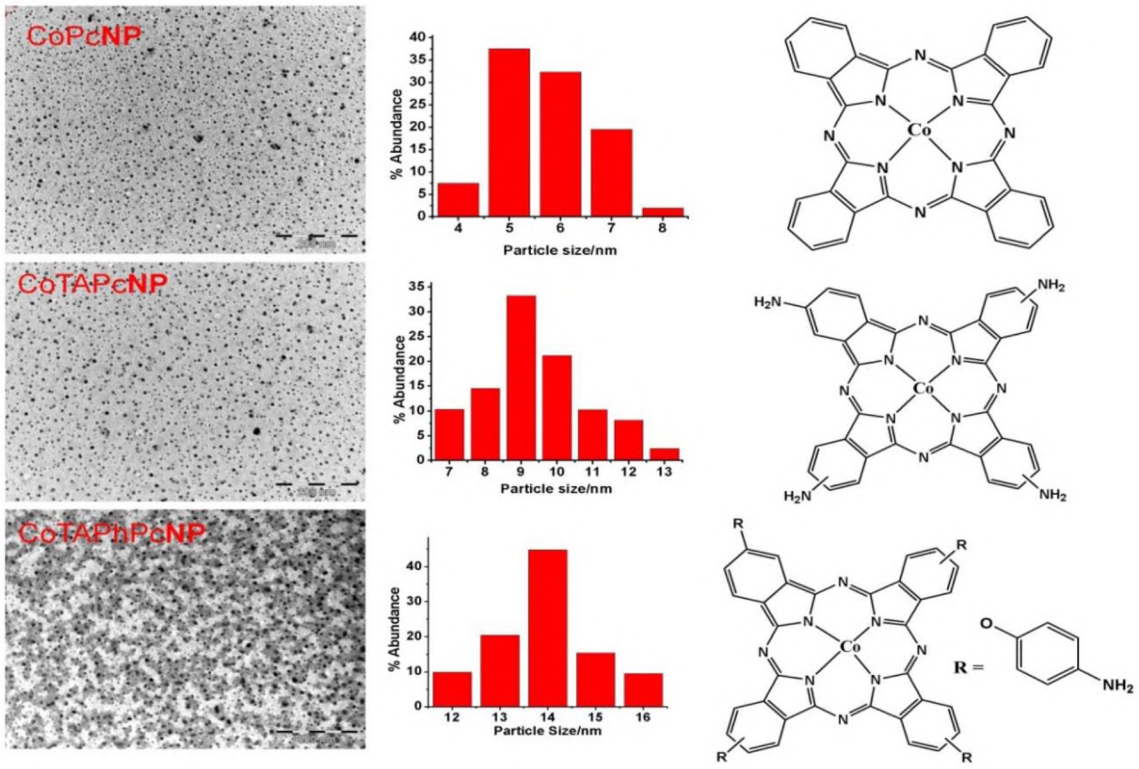

Fig.3.9 TEM images for metallophthalocyanine nanoparticles, their corresponding histograms and molecular structures.

3.3 Synthesis and characterisation of Complex 1 with AuNRs (Scheme 3.3)

Complex **1** was linked chemically to AuNRs as explained in the experimental section, **Scheme 3.3**. It is expected that Au-N bonds will form [126].The nanocomposite is represented as **1**-AuNRs (linked), **Table 3.3**.

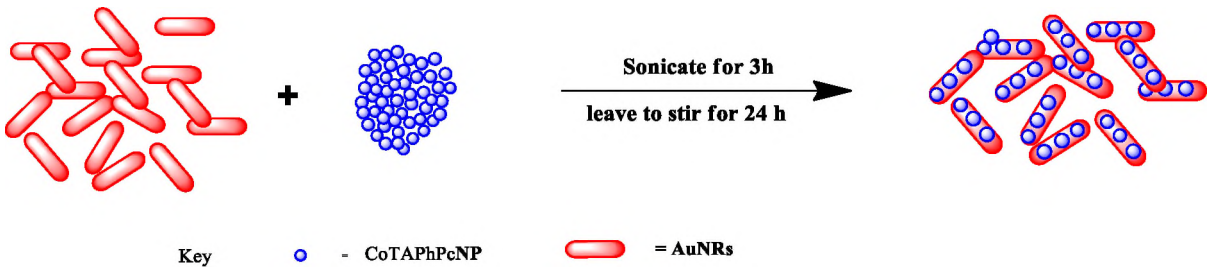

Scheme 3.3 Formation ofCoTAPhPc**NP**(**1**)-AuNRs(linked)

3.3.1 UV/Vis

The UV-Vis spectra of AuNRs show the characteristic surface resonance plasmon (SPR) band at 732 nm (longitudinal) and 530 nm (transverse) (**Fig. 3.7**). The existence of multiple bands is typical [116] of nonspherical Au nanoparticles. The CoTAPhPc**NP**(**1**)-AuNRs(linked) conjugate shows a broadened Q band that is more red-shifted because of its overlap with the SPR longitudinal band **Fig. 3.7 and Table 3.3.** The spectra is also characterised by some ground state absorption in the region of the transverse band further confirming the conjugation.

3.3.2 XPS

XPS was run to probe the elemental composition and the chemical nature of CoTAPhPc**NP**(**1**)-AuNRs(linked). To prove the interaction of gold nanoparticles with sulphur and nitrogen, high resolution Au4f spectrum for CoTAPhPc**NP**(**1**)-AuNRs(linked) was recorded, **Fig. 3.10**. For CoTAPhPc**NP**(**1**)-AuNRs(linked) only Au-N bonds are expected. As described above, Au4f spectrum in AuNPs is usually characterised by two peaks at around 84 eV and 88 eV corresponding to the spin orbit splitting $Au4f_{7/2}$ and $Au4f_{5/2}$ respectively [141] which are seen for SNDGONS-AuNRs(linked)-GCE at 84.4 eV and 88.1 eV respectively, **Fig. 3.6F**. For CoTAPhPc**NP**(**1**)-AuNRs(linked), the $Au4f_{5/2}$, peak shifted to 87.8 eV from 88.1 eV in rSNDGONS-AuNRs(linked), (**Fig. 3.6F**). The $Au4f_{7/2}$ remained at 84.4 eV for CoTAPhPc**NP**(**1**)-AuNRs(linked). The $Au4f_{5/2}$ Au-S peak observed at 89.8 eV and the $Au4f_{7/2}$ Au-S at 85.6 eV for SNDGONS-AuNRs(linked) (**Fig. 3.6F**) are not present in CoTAPhPc**NP**(**1**)-AuNRs(linked) proving there are no Au-S

bonds as expected, (**Fig. 3.10**). Au4f$_{7/2}$ Au-N peak is shifted by 0.2 eV for CoTAPhPc**NP**(**1**)-AuNRs(linked) at 86.2 eV compared to 86.4 for rSNDGONS-AuNRs(linked). This confirms that Au interacts both with nitrogen and sulphur in rSNDGONS and with nitrogen only in CoTAPhPc**NP**.

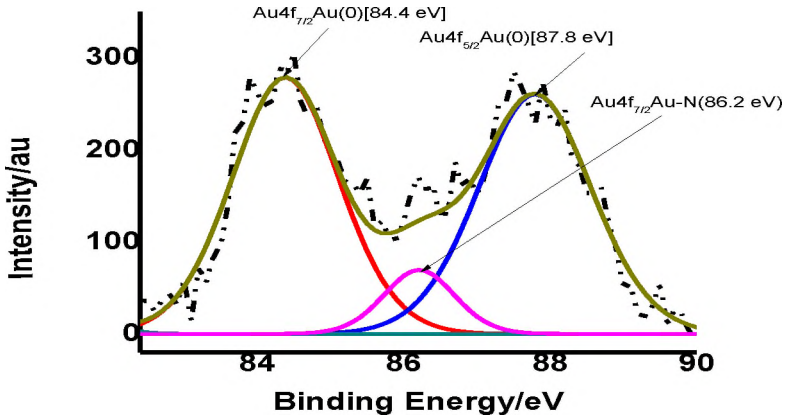

Fig. 3.10 XPS high-resolution spectra for complex **1**-AuNRs(linked) Au4f.

3.4 CoMCPhPc(4) and its conjugates

3.4.1 Synthesis of conjugates (Scheme 3.4)

Thionyl chloride was used to chlorinate the carboxylate groups on either GONS or CoMCPhPc(**4**) to give acid chloride GONS or Pc, respectively. (**Scheme 3.4, step 1)**. Diaminomaleonitrile (DAMN) was then linked to the GONS acid chloride via an amide bond to form (DAMN)-GONS (as an example). The Pc was then linked to the other side of DAMN via another amide bond. The product CoMCPhPc(**4**)-(DAMN)-GONS(linked), (as an example) was then left to dry in an oven at 70 °C for 48 h.

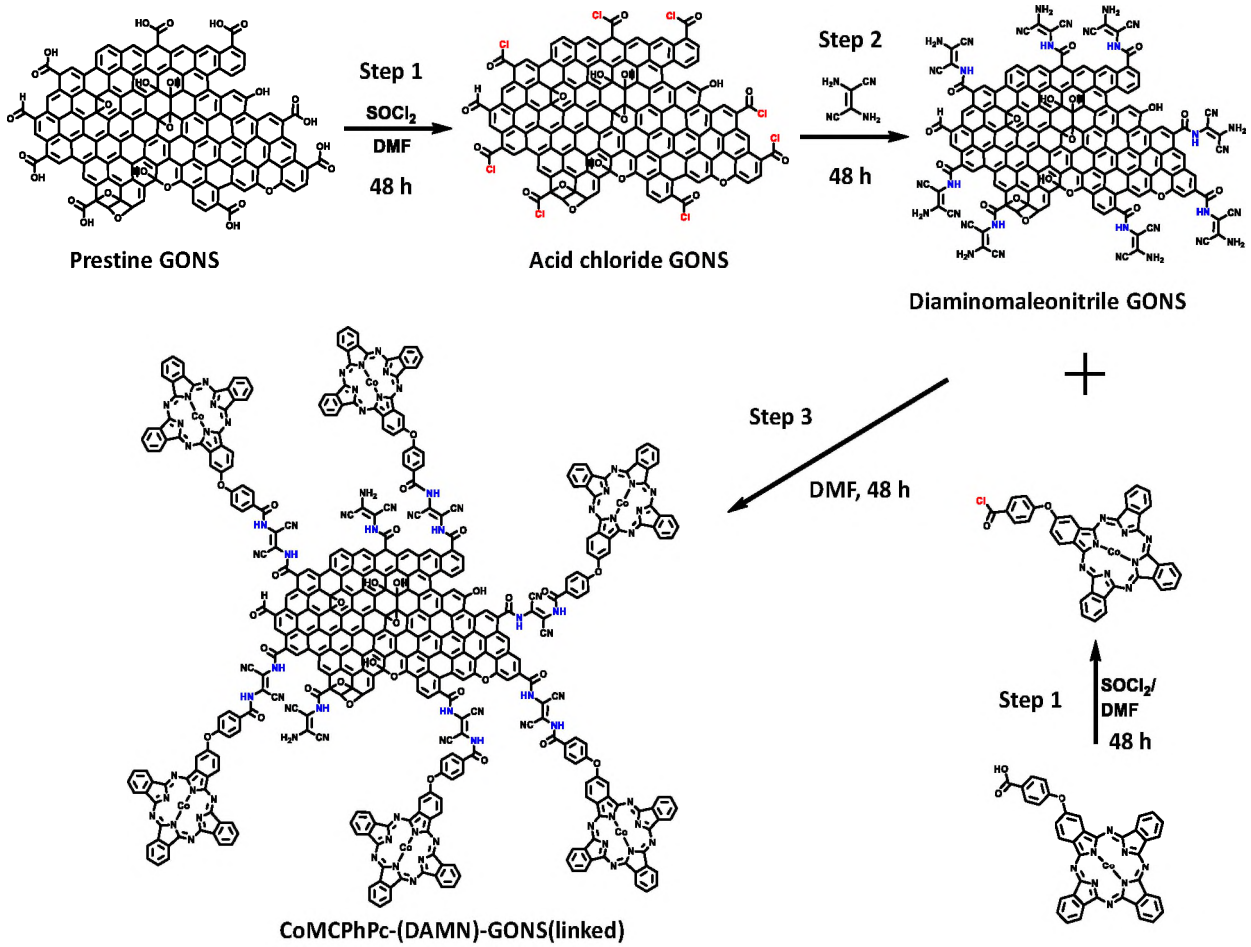

Scheme 3.4 Conjugation of cobalt mono carboxyphenoxy phthalocyanine (**4**) to graphene oxide nanosheets (GONS)

3.4.2 UV-VIS

There was no significant shift in the Q band of CoMCPhPc(**4**) following conjugation to pristine and doped GONS. The Q band maxima were as follows: CoMCPhPc (**4**) (665 nm), CoMCPhPc(**4**)-(DAMN)-GONS(linked) (666 nm), CoMCPhPc(**4**)-(DAMN)-NDGONS(linked) (666 nm), CoMCPhPc(**4**)-(DAMN)-SDGONS(linked) (666 nm) and CoMCPhPc(**4**)-(DAMN)-SNDGONS(linked) (667

nm), **Fig. 3.8**, **Table 3.3**. The increase in the background below 600 nm is due to the presence on GONS.

3.4.3 FTIR

The formation of an amide bond in the linked conjugates was confirmed by FTIR. The C=O stretch at 1659 cm^{-1} became more pronounced upon conjugating CoMCPhPc (**4**) to different forms of GONS. The amide N-H stretch appeared at 1605 cm^{-1} confirming successful amidation as reported elsewhere [124]. The nitrile stretch for the conjugates observed at 2319 cm^{-1} is as a result of the diaminomaleonitrile linker.

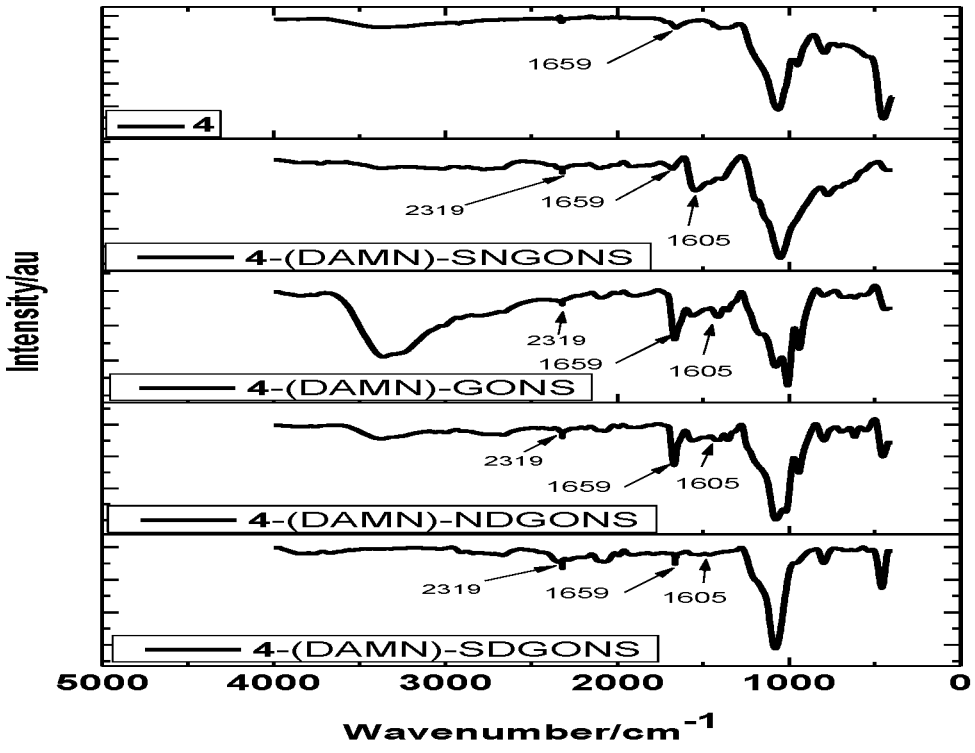

Fig. 3.11 FTIR spectra for Conjugates of Complex **4**.

3.4.4 XPS

XPS was recorded in order to probe the elemental composition and the chemical nature of the elements in both SNDGONS (as an example) and its phthalocyanine conjugates. The survey spectrum for SNDGONS, **Fig. 3.12A** show the peaks for N, S, C and O as expected same as rSNDGONS in **Fig. 3.6(c)**. The survey spectrum for CoMCPhPc(**4**)-(DAMN)-SNDGONS (linked), shows the presence of Co from CoMCPhPc (**4**) in addition to rSNDGONS peaks.

The high-resolution N1s peak for SNDGONS was described in earlier sections of this work but for rSNDGONS. The emergence of an up field peak at 402.2 eV in the deconvoluted N1s spectra of CoMCPhPc(**4**)-(DAMN)-SNDGONS(linked) which is absent in both CoMCPhPc(**4**) and SNDGONS confirms an amide bond that forms upon conjugation [144]. Different forms of nitrogens present in SNDGONS experienced a downfield shift, which is reminiscent of an increased electron density upon conjugation to CoMCPhPc(**4**). The graphitic N1s shifted from 400.0 eV in SNDGONS to 400.8 eV in the CoMCPhPc(**4**)-(DAMN)-SNDGONS(linked) conjugate masking the Co-N contribution from the CoMCPhPc(**4**) alone originally centred on 400.2 eV, **Fig. 3.12**. The pyrrolic nitrogen also experienced shift from 398.7 eV in SNDGONS to 399.6 eV in the conjugate also masking the C=N contribution from CoMCPhPc(**4**) at 398.6 eV [53]. The downfield shift upon conjugation is indicative of the incoming of an electron rich group. Such electron enriching can be attributed to the presence of the delocalised π electron system in both the SNDGONS and CoMCPhPc(**4**).

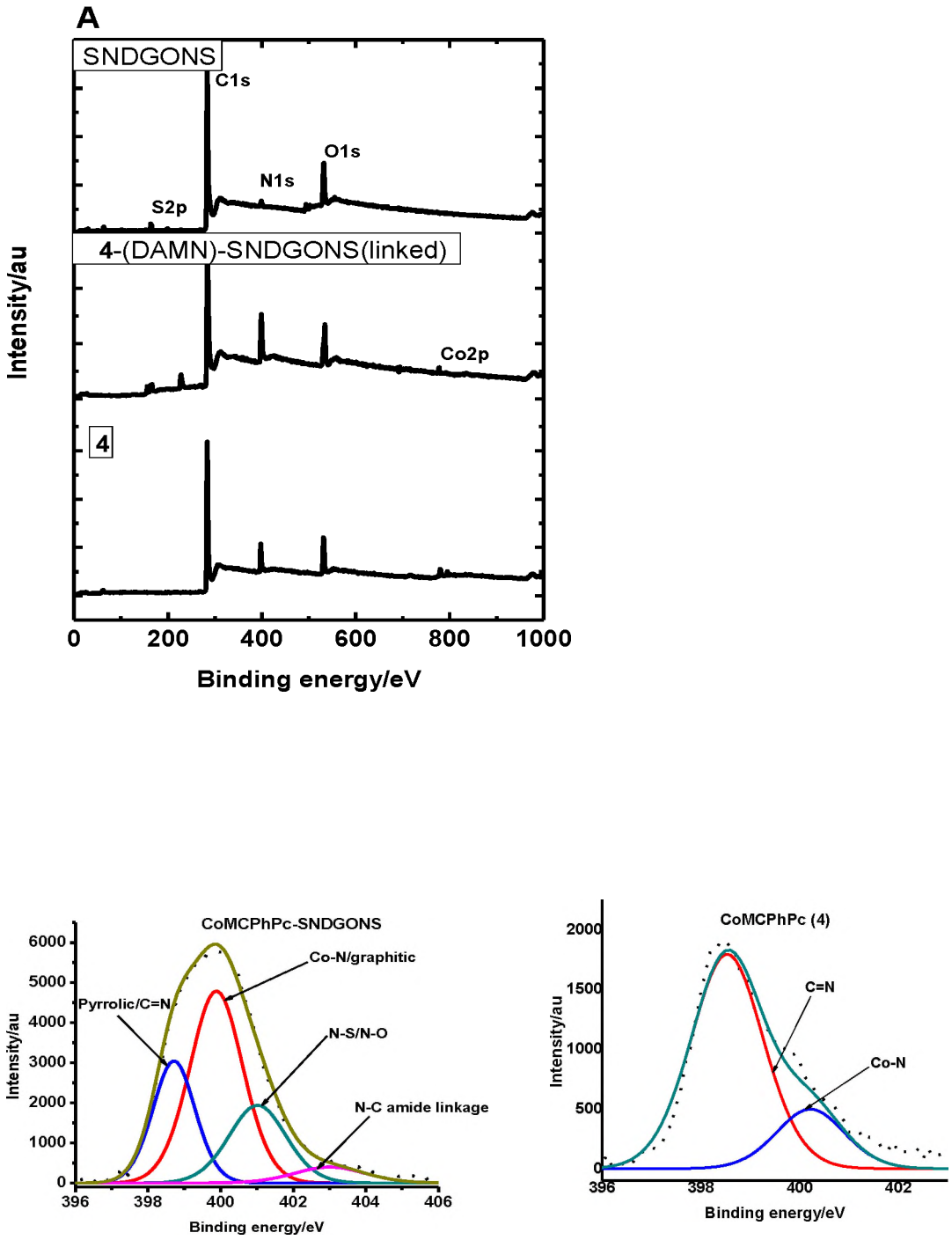

Fig.3.12 XPS for CoMCPhPc (**4**) based electrodes.

3.5 CoTCPhPc (2) and MWCNT conjugates

3.5.1 Synthesis (Scheme 3.5)

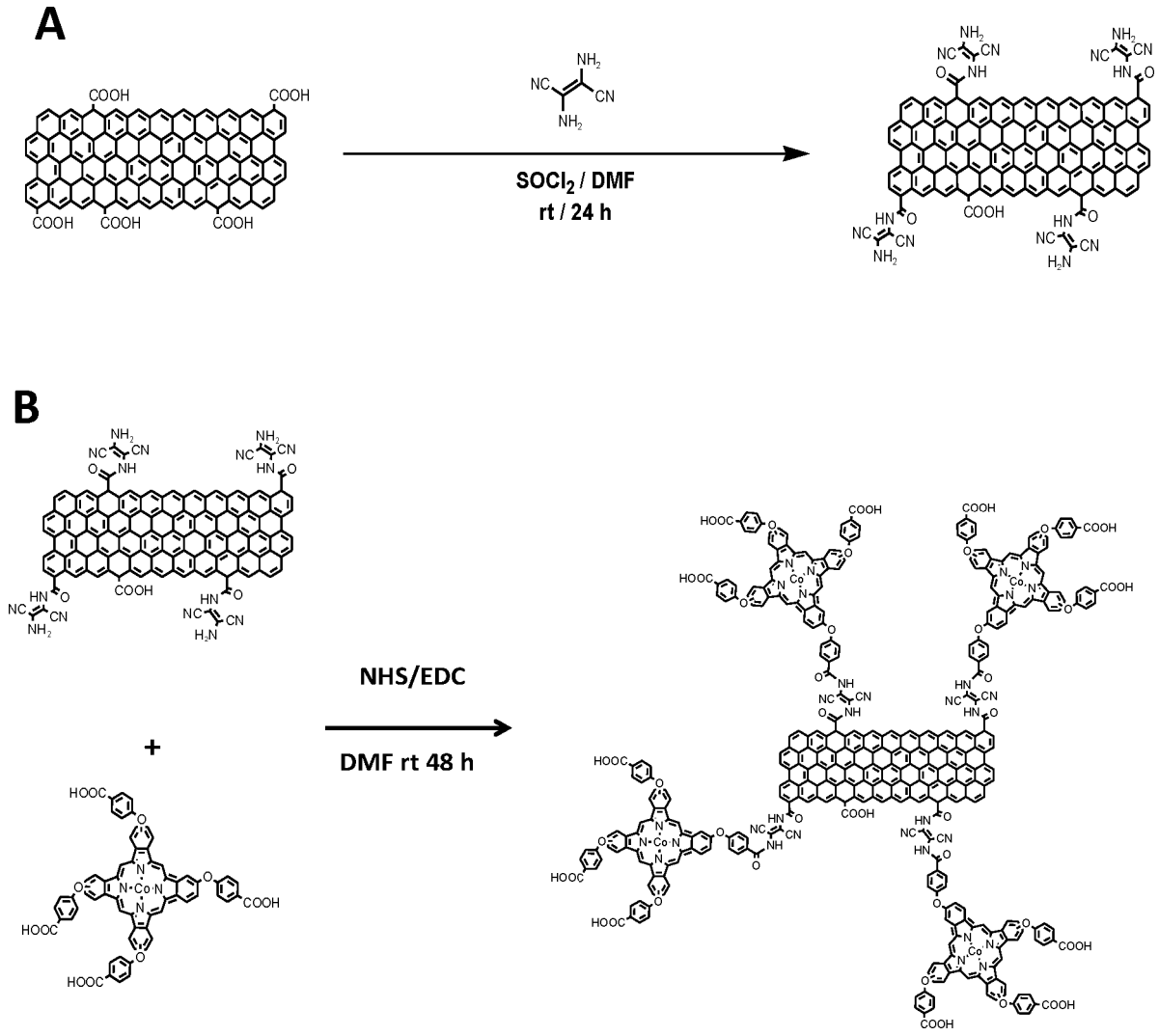

Scheme 3.5 Conjugation of CoTCPhPc (**2**) to MWCNTs

Carboxylation of MWCNT was done as reported by Sanusi et, al., [123]. Functionalization of MWCNT with diaminomaleonitrile {(DAMN)-MWCNT) has been reported before[125]. In this work thionyl chloride was used to activate the carboxylic groups of MWCNT-COOH, as reported by Moyo et, al.,[124] **Scheme 3.5A.** Separately, CoTCPhPc (**2**) was activated by EDC/NHS. The

mixture of activated CoTCPhPc (**2**) and (DAMN)-MWCNT was allowed to react to form an amide bond, **Scheme 3.5**. The product is represented as CoTCPhPc(**2**)-(DAMN)-MWCNT(linked), **Scheme 3.5B**.

3.5.2 UV-Vis spectra.

Fig. 3.13 shows the ground state absorption spectra of the CoTCPhPc(**2**) and its conjugates in DMF. There is significant red shifting from 663 nm to 672 nm upon covalent bonding with (DAMN)-MWCNT, **Table 3.3**. This could be as a result of the electron donation from the π electron rich DAMN-MWCNT to the MPc which result in lowering of the energy gap between the highest occupied molecular orbital (HOMO) to lowest unoccupied molecular orbital (LUMO) [145]**.** No shift of the Q band was observed when the MPc was mixed with (DAMN)-MWCNT. The covalent functionalization of MPc complexes and carbon nanomaterials (such as graphene), often results in red-shifting of the Q band because of the increase in the π-electron density [146,147]. The more the red shifting, the stronger π–π interaction and charge transfer between MPc complex and the carbon nanomaterial. The absence of red-shifts suggests weak electronic communication between the carbon nanomaterial and the MPc [147]. Thus, the observation of a red shift for CoTCPhPc(**2**)-(DAMN)-MWCNT(linked) and no shift for CoTCPhPc(**2**)/(DAMN)-MWCNT(mix), suggests stronger interaction (and enhanced charge transfer) of CoTCPhPc**(2)** with (DAMN)-MWCNT when the two are linked in the former, and minimal interaction when they are mixed in the latter. The lack of red-shifting in the Q band of Pcs in the presence of carbon nanomaterials has been observed [147].

The possibility of the red shift being due to aggregation was investigated. In phthalocyanines, blue shifting of the Q-band evidences "H" aggregation. The rare "J" aggregates are characterized by red shifting of the Q band. The absence of aggregation was confirmed by the lack of decrease in the red-shifted Q band on diluting the solution, this would have been accompanied by an increase in the monomer peak.

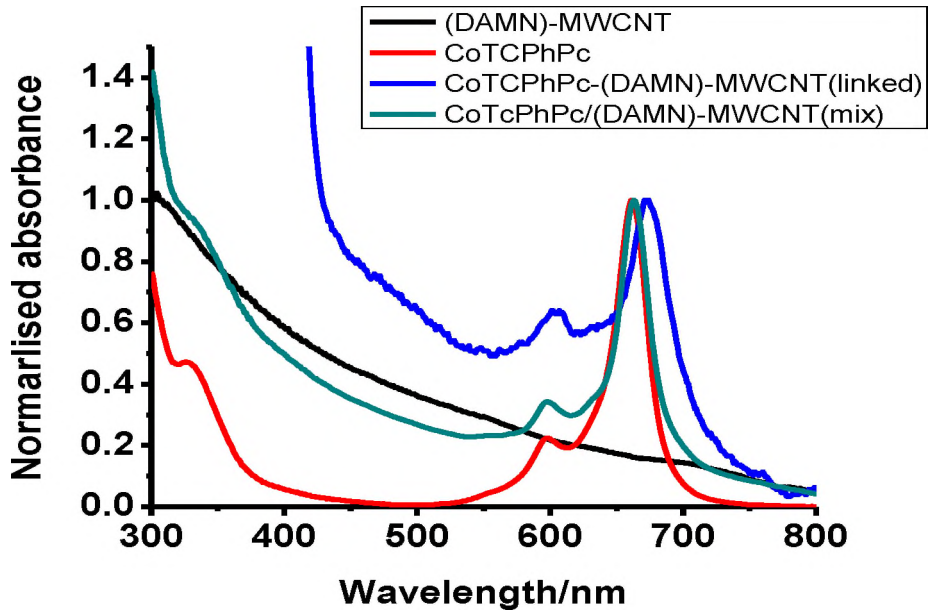

Fig. 3.13 Ground state absorption spectra in DMF, (CoTCPhPc (**2**) ~ 2 x 10^{-6} M)

3.5.3 FTIR

FTIR was used to confirm amide bond formation between CoTCPhPc(**2**) and (DAMN)-MWCNT to form CoTCPhPc(**2**)-(DAMN)-MWCNT(linked). However, (DAMN)-MWCNT on its own has an amide bond. The appearance of a band around 3431 cm^{-1} in both (DAMN)-MWCNT and CoTCPhPc(**2**)-(DAMN)-MWCNT(linked) signifies the N-H stretch of the amide (**Figure 3.14**). For

(DAMN)-MWCNT an amide C=O stretch is observed at 1669 cm^{-1} accompanied by an amide N-H stretch at 1612 cm^{-1}. The peak at 1669 cm^{-1} that becomes more pronounced in CoTCPhPc(**2**)-(DAMN)-MWCNT(linked) when compared to DAMN-MWCNT is evidence of an increased amidation process as the second amide bond is formed on DAMN upon conjugation to the CoTCPhPc(**2**). The amide bond is further confirmed by the emergence of the amide N-H stretch around 1311 cm^{-1} as reported elsewhere [124]. The characteristic O-H stretch of the carboxylic group in CoTCPhPc(**2**) is observed at 3381 cm^{-1}. The CN-stretch at 2243 cm^{-1} is observed in the IR spectrum of (DAMN)-MWCNT and CoTCPhPc(**2**)-(DAMN)-MWCNT(linked) which is absent in CoTCPhPc(**2**)**.** It is known that shifts in IR bands confirm structural changes [148]. Even though both (DAMN)-MWCNT and CoTCPhPc(**2**)-(DAMN)-MWCNT(linked) have amide bonds, the changes in intensity and shifts in the FTIR bands confirm formation of different structure.

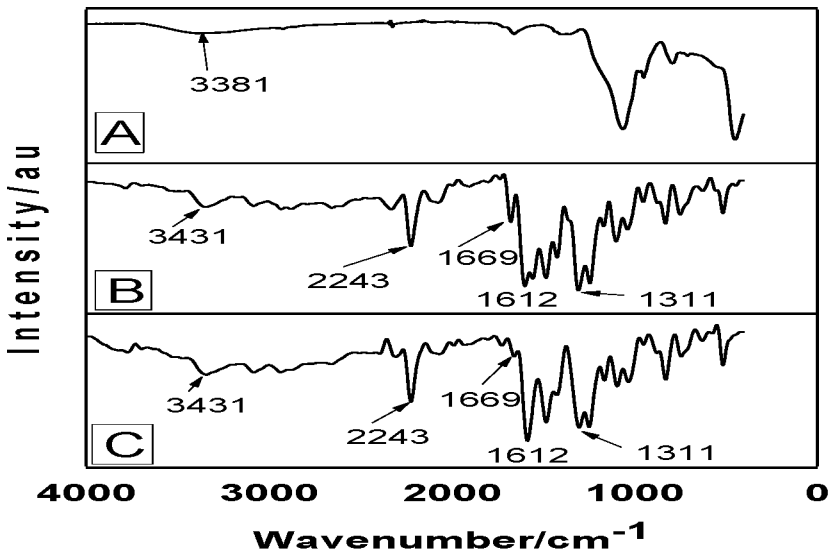

Figure. 3.14 FTIR spectra (A) CoTCPhPc (**2**), (B) CoTCPhPc(**2**)-(DAMN)-MWCNT(linked) and (C) (DAMN)-MWCNT.

3.5.4 XPS

To confirm the formation of the amide linkage between the CoTCPhPc (**2**) and the (DAMN)-MWCNT, high-resolutionXPS N1s spectra were recorded. The high resolution N1s spectrum for CoTCPhPc(**2**)-(DAMN)-MWCNT(linked), **(Fig. 3.15)** shows the presence of the amide peak at 402.9 eV in the covalently CoTCPhPc(**2**)-(DAMN)-MWCNT(linked) conjugate which is also present in CoTCPhPc(**2**)/(DAMN)-MWCNT(mix) but shifted to 401.8 eV. The slight shift in the amide bond may suggest different environments. The spectra also show the nitrogen bonding in the phthalocyanine as comprising of the pyrrole nitrogen linked to the Co central metal and the aza nitrogen existing in distinct chemical environments. The nitrile peak observed in both the mixed

and the linked is from the diaminomaleonitrile as observed in the FTIR spectra (**Fig. 3.14**).

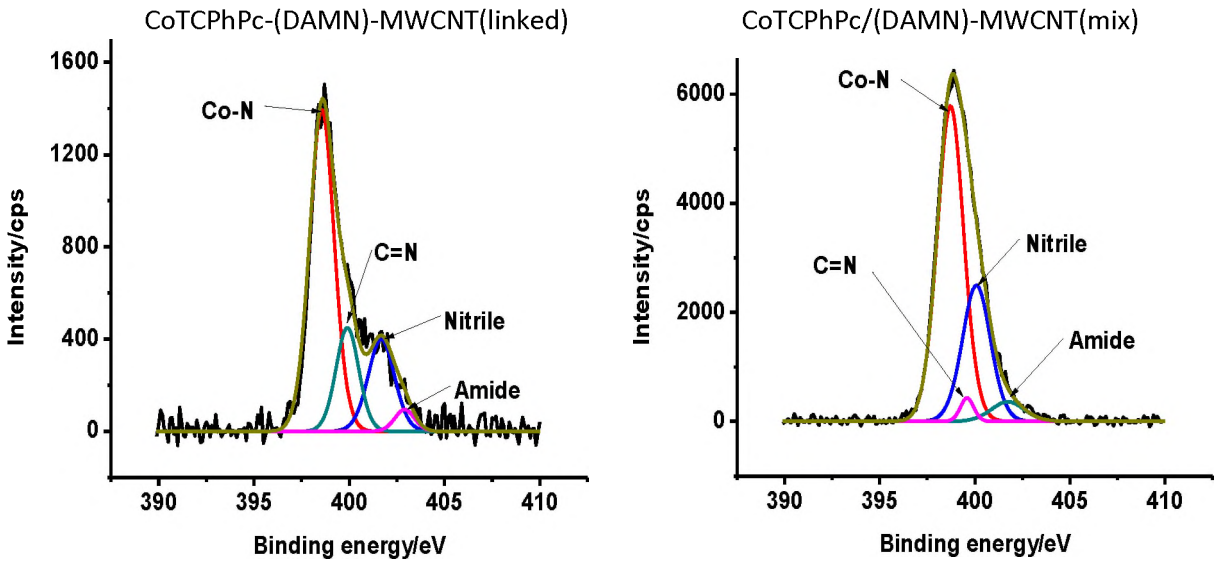

Fig. 3.15 XPS N1s spectra for CoTCPhPc (**2**) and (DAMN)-MWCNT conjugates

3.5.5 TEM

Figure 3.16 shows the TEM images of the different electrode modifiers. The images show that covalently linking the (DAMN)-MWCNT to CoTCPhPc(**2**) results in clustering of the nanomaterials. (DAMN)-MWCNT shows mainly the MWCNTs, whereas, CoTCPhPc(**2**)/(DAMN)-MWCNT(mix) shows clusters around the MWCNTs. However, the nanoconjugates show dominance of the multiwalled carbon nanotubes.

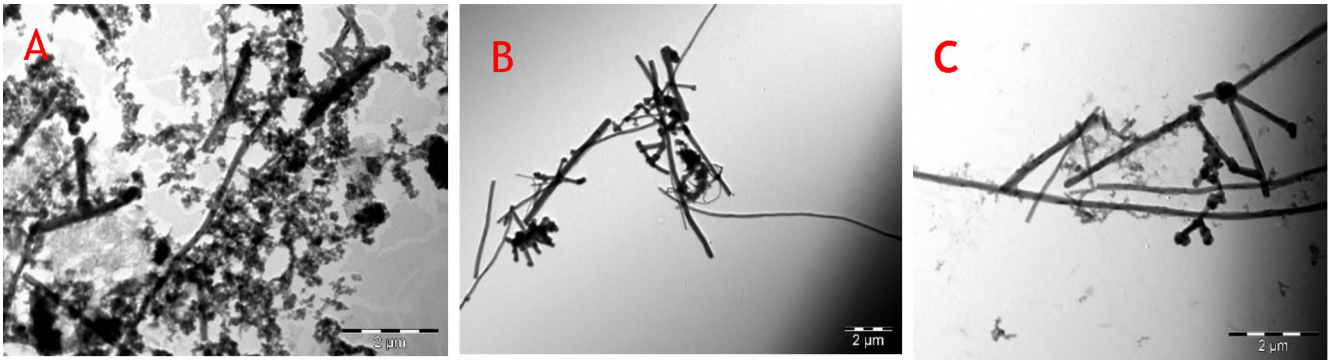

Fig. 3.16 TEM images A) CoTCPhPc(**2**)-(DAMN)-MWCNT(linked) B) (DAMN)-MWCNT and C) CoTCPhPc(**2**)/(DAMN)-MWCNT (mix).

3.6. Zinc octacarboxy phthalocyanine(6) conjugates formed by ππ stacking of GONS and Pc

3.6.1. UV/Vis spectra

A Q band at 696 nm (**Table 3.3**) characterizes ZnOCPc(**6**) (structure shown as an insert in **Fig. 3.17**). There is a slight red shifting of the Q band for ZnOCPc(**6**)-GONS compared to ZnOCPc(**6**) alone [128]. Red shifting of porphyrin spectra was also reported when porphyrins were assembled on reduced graphene oxide [149] and was attributed to flattening of the former also due to ππ interaction discussed above for CoTCPhPc(**2**)/(DAMN)-MWCNT(mix) [147]. The broadening of the spectra below 600 nm is due to the absorption by rGONS or GONS, which was also observed above for complex **4**-GONS, and complex **2**-MWCNT conjugates. For ZnOCPc(**6**) alone, the emission spectrum was a mirror image of the excitation spectrum and the latter was similar to the absorption spectrum (**Fig. 3.18A**). For ZnOCPc(**6**)-GONS (**Fig. 3.18B**) or ZnOCPc(**6**)-rGONS (**Fig. 3.18C**), excitation is different from absorption due to absorption by GONS or rGONS, respectively.

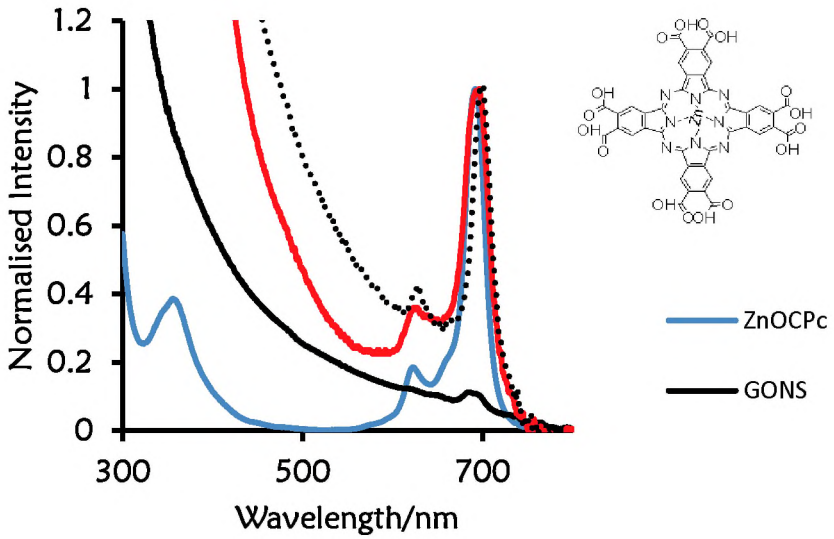

Figure 3.17 Ground state absorption spectra of ZnOCPc(**6**) and conjugates in DMSO {insert shows structure of ZnOCPc(**6**)}.

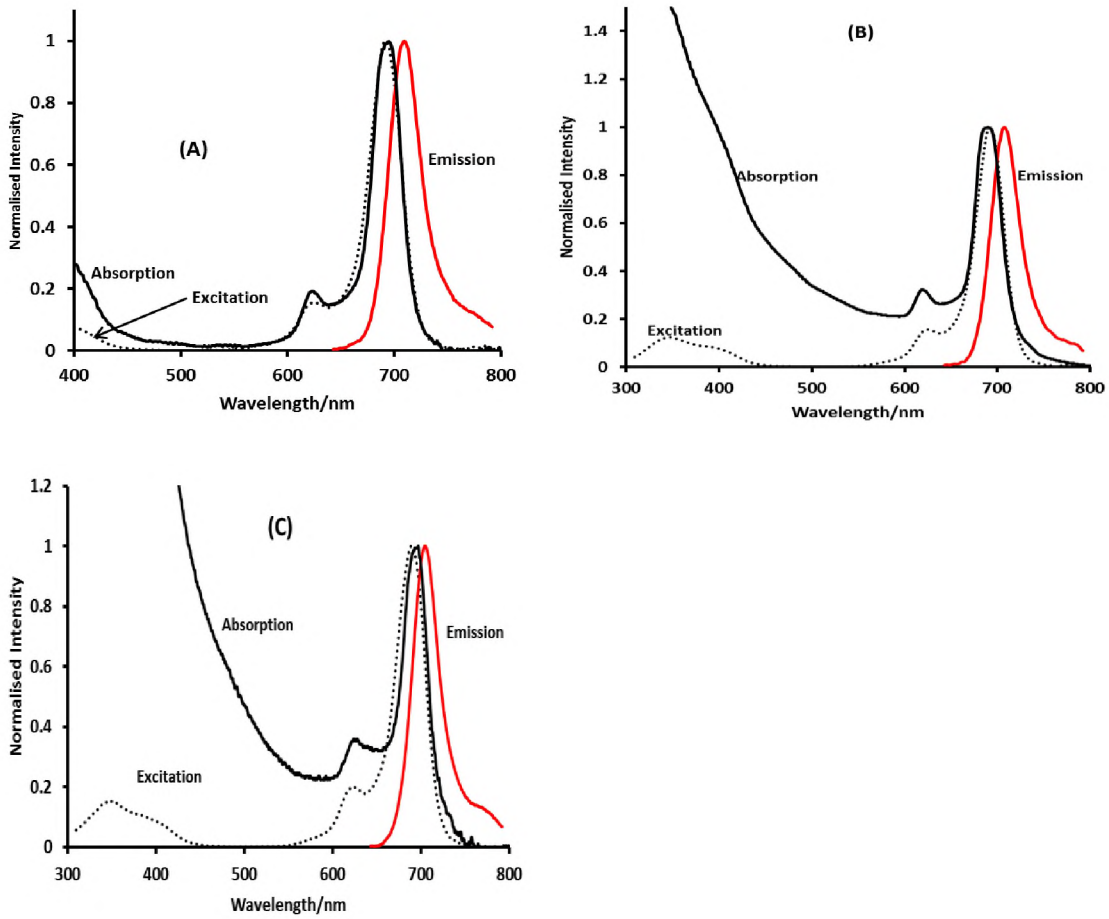

Fig. 3.18 Ground state absorption, emission and excitation spectra of (A)ZnOCPc(**6**), (B) ZnOCPc(**6**)-GONS and (C) ZnOCPc(**6**)-rGONS in DMSO.

3.6.2. FTIR Spectra

The broad peak centered around 3300 cm^{-1} in ZnOCPc(**6**) and GONS, **Fig. 3.19**, shows the presence of the O-H stretching vibrations of the carboxylic functionalities further broadened as they overlap with the C-H stretch at 2969 cm^{-1}. There is a more defined sp^2 carbon peak around 2800 cm^{-1} for ZnOCPc(**6**)-rGONS and rGONS. This can be a result of the ring carbons in the Pc in the case of the former and the restoration of the aromaticity in the case of the latter. The COO^- stretching band was observed at 1373 cm^{-1} while the

peak at 1673 cm^{-1} is the CO double bond [150], for ZnOCPc(**6**)-rGONS and rGONS.

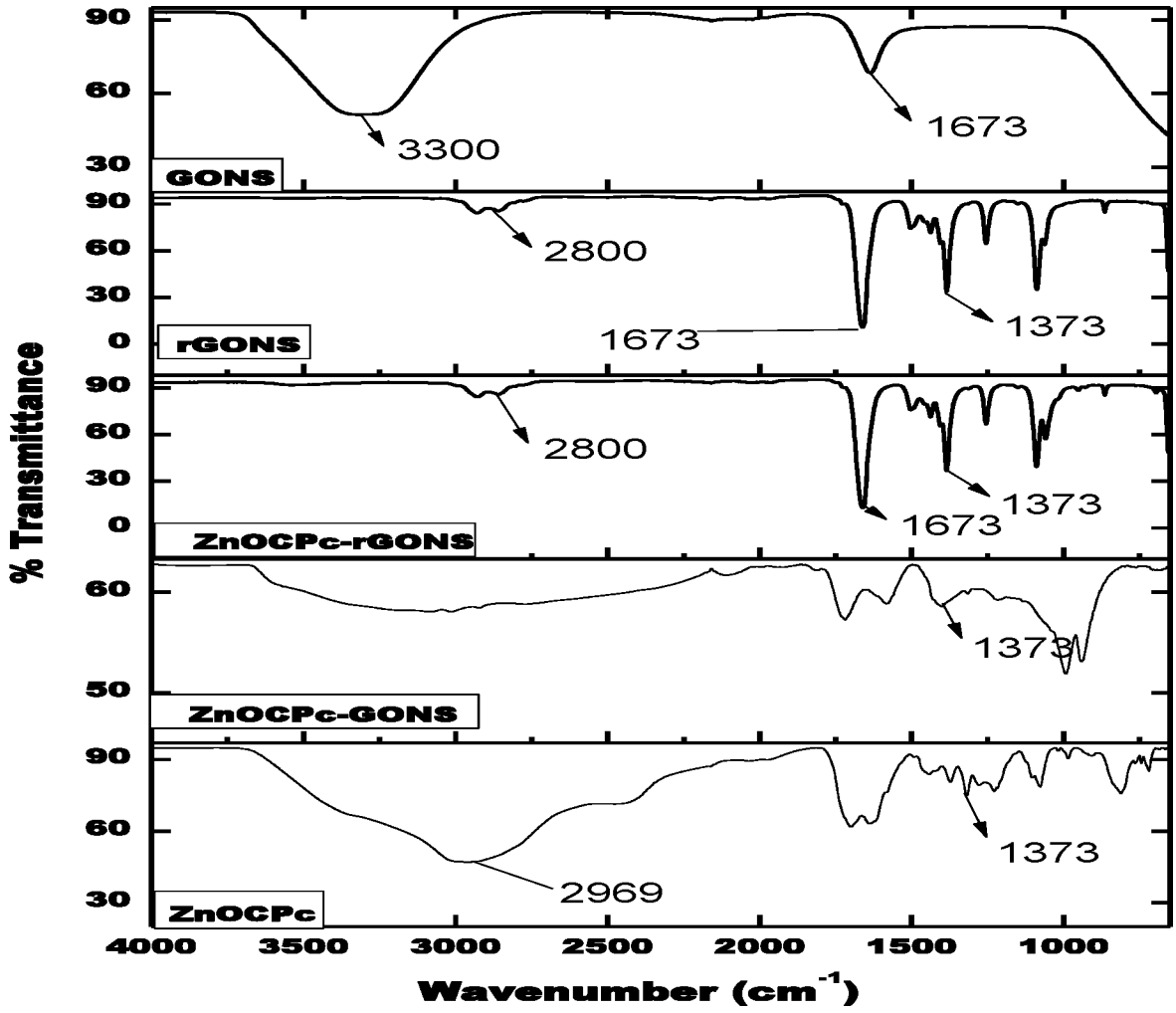

Figure 3.19. FT-IR spectra for GONS, rGONS, ZnOCPc(**6**)-rGONS, ZnOCPc(**6**)-GONS and ZnOCPc (**6**).

3.6.3. Thermogravimetric Analysis.

From the themograms in **Fig. 3.20**, it can be observed that the nanomaterials suffered gradual loss of mass at temperature below 150 °C. As discussed above, **Fig. 3.5**, steep loss for GONS compared to rGONS can be attributed to the loss of labile oxygen as CO and or CO_2 [151]. ZnOCPc(**6**) alone is more

stable than the rGONS, GONS and their resulting conjugates as evidenced by a lower percentage loss. The ZnOCPc(**6**)-GONS suffered similar mass loss as GONS, but maintained a higher mass than GONS throughout the temperature range This is an indication that adsorption of ZnOCPc(**6**) stabilized the GONS. The observed mass loss in the ZnOCPc(**6**)-GONS conjugate serves to explain that not all the oxygen atoms are stabilized by conjugation. Again it was observed that the inclusion of ZnOCPc(**6**) resulted in a lower percentage loss (below 600 °C) in ZnOCPc(**6**)-rGONS, compared to rGONS alone, confirming the strong bond between the Pc and the nanosheets just as was case for ZnOCPc(**6**)-GONS. However, at around 700 °C, there is loss of weight in ZnOCPc(**6**)-rGONS, which is attributed to the loss of the Pc from the nanosheets. Less mass loss was observed with rGONS and its conjugates (ZnOCPc(**6**)-rGONS) compared to GONS or ZnOCPc(**6**)-GONS.

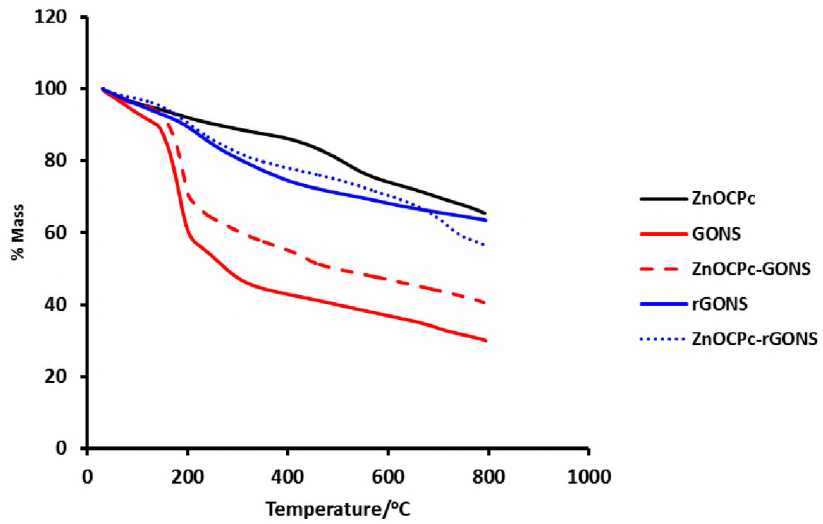

Fig.3.20 Thermogravimetric Analysis of GONS, rGONS and conjugates with ZnOCPc(**6**).

3.6.4. XPS

The survey scans (**Fig. 3.21A**) for rGONS, GONS, ZnOCPc(**6**)-rGONS and ZnOCPc(**6**)-GONS show the characteristic peaks at around 284 eV, 399 eV, 531 eV and 1022 eV respectively corresponding to C 1s, N 1s, O 1s, and Zn 2p {N 1s and Zn 2p for ZnOCPc(**6**) conjugates} binding energies.

The high-resolution C 1s spectra are shown in **Fig.3.21B-D**. The carbon-carbon peaks are centred at lower binding energies than carbon-oxygen peaks in the C 1s spectra [152]. The latter peaks correspond to different forms of oxygens. The reduction of GONS to rGONS resulted in the binding energies of carbon-carbon bonds decreasing as shown in **Fig. 3.21B** and **C**. There is significant change in proportions of C-C and C=C configuration upon reduction. The C-C peak is more pronounced in GONS while C=C peaks dominate in rGONS, which suggest the significant change of configuration from sp^3 to sp^2. There was no significant change in the carbon to oxygen ratio upon reduction of GONS to rGONS, which may be a result of oxygen retention after reduction in the form of water molecules [151].

There is a decrease in binding energy for C-C bond upon conjugation of ZnOCPc(**6**); from 283.24 eV for GONS (**Fig. 3.21B**) to 282.95 eV for ZnOCPc(**6**)-GONS (**Fig. 3.21D**) representing a downshift of 0.29 eV indicating an increase in the electron density upon conjugation. This is also observed with the C=C bond shifting from 284.92 eV for GONS (**Fig. 3.21B**) to 284.20 eV (**Fig 3.21D**) representing a downshift of 0.72 eV. The downshift in binding energy is expected due to the negatively charged Pc increasing the electron

density on GONS. There is however an increase in binding energy of C=C bond upon conjugation; from 284.64 eV for rGONS (**Fig. 3.21C**) to 284.82 eV for ZnOCPc(**6**)-rGONS (**Fig. 3.21E**) representing an upshift of 0.18 eV. A similar shift is also observed for the C-C bond from 282.66 eV for rGONS to 282.92 eV for ZnOCPc(**6**)-rGONS representing an upshift of 0.26 eV. The upshift in the case of rGONS can be attributed to electron donation to the Pc upon conjugation thereby reducing the electron density [128]. Multiple peaks under the O 1s peak are indicative of the different chemical environments, which depicts the multiple functional oxygens in the GONS such as epoxy groups, hydroxyl and carbonyl groups, **Fig 3.21F-H**.

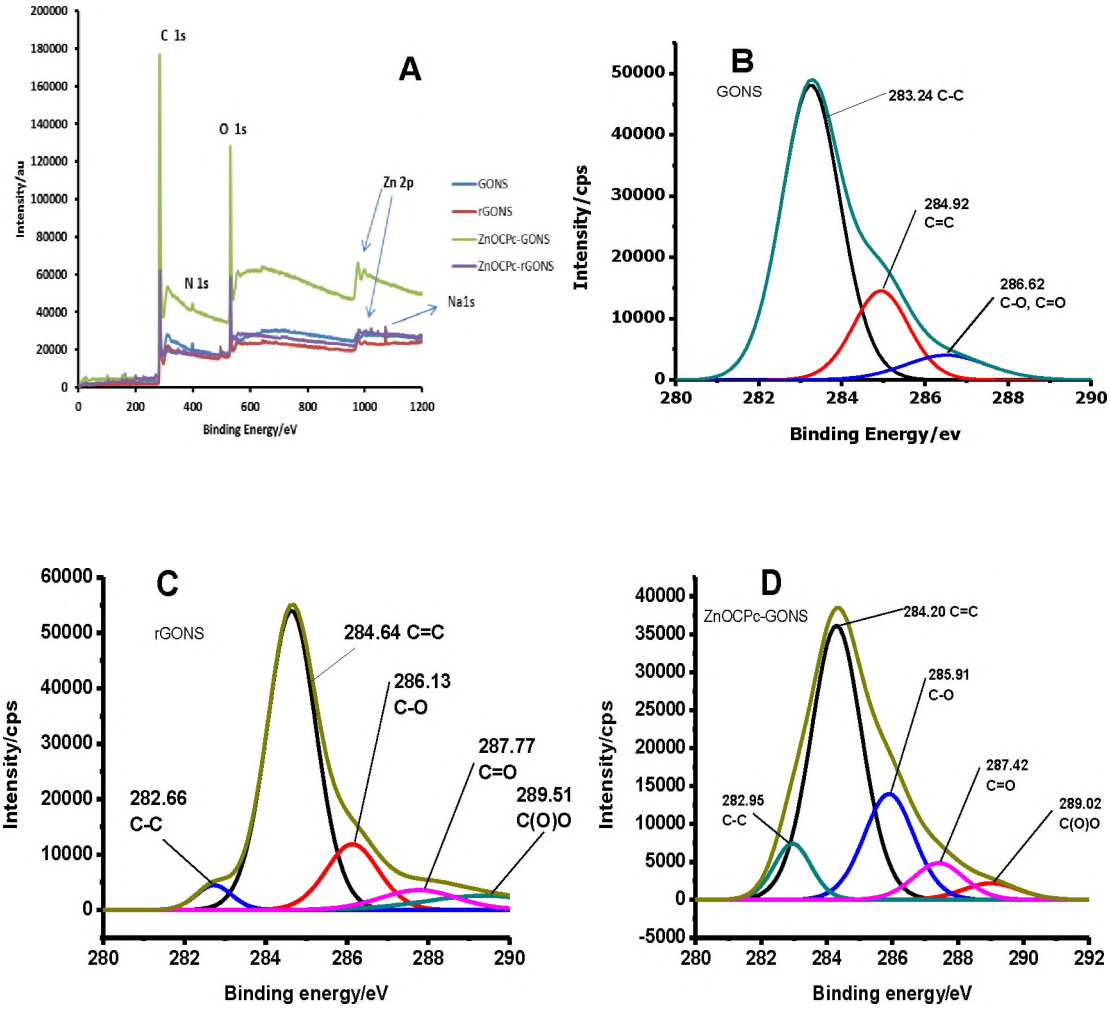

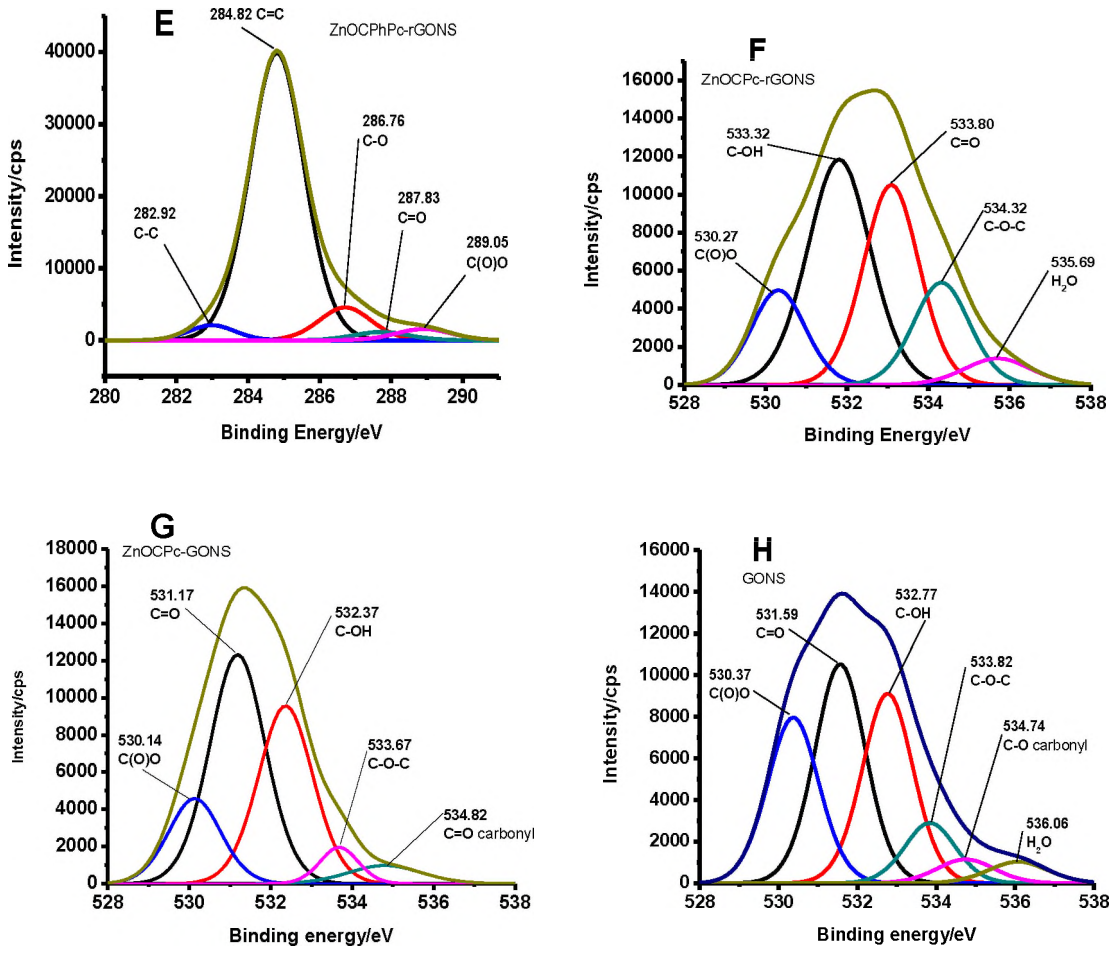

Figure 3.21. (A) XPS spectra survey scan for GONS, rGONS, ZnOCPc(**6**)-GONS and ZnOCPc(**6**)-rGONS. C 1s high resolution scans for (B) GONS, (C) rGONS, (D) ZnOCPc(**6**)-GONS and (E) ZnOCPc(**6**)-rGONS. O1s high resolution scans for (F) ZnOCPc(**6**)-rGONS, (G) ZnOCPc(**6**)-GONS and (H) GONS.

3.7. Conclusion.

XPS results show successful incorporation of heteroatoms into GONS and confirms the successful conjugation of phthalocyanines to different nanomaterials. The fabrication of MPc nanoparticles is confirmed by TEM and the size of the resultant nanoparticles are shown to vary with the size of the

bulk MPc molecule. Thermal analysis shows that GONS doping results in improved stability of GONS.

Chapter Four

4. Electrode modification and Characterisation.

This Chapter deals with electrode modification and the different techniques used to interrogate the modified electrode surfaces. Drop dry substrate (glassy carbon electrode or plate) modification approach was utilised in this work. The electrode modifiers were utilised as single entities, as conjugates sequentially added to the electrode surface, either mixed or linked prior to electrode modification. Covalent or π-π linkages were utilised. Gold nanoparticles containing conjugates were linked either to MPcs or carbon based nanomaterialsby either Au-N or Au-S bonds or both.

Scanning electron microscopy (SEM), scanning electrochemical microscopy (SECM), time of flight secondary ion mass spectrometry (TOF-SIMS and cyclic voltammetry were used to characterise the modified electrodes.

4.1 Scanning electron microscopy (SEM).

4.1.1 Phthalocyanines nanoparticles.

The nanoparticles of all phthalocyanine complexes were adsorbed onto the electrode, **Fig. 4.1**, (using CoPc (**3**) and CoTAPc(**5**) as examples). SEM images were taken to show the changes in the morphology as phthalocyanines are converted into their nanosized form on glassy carbon plate (GCP). Pcs have a tendency to aggregate and hence form bulky clusters of different morphology depending on the nature of aggregation. Hence, they appear as either needles or big bolus materials as shown in (**Fig. 4.1A and C**). Upon forming NPs, aggregation is minimised and either the bolus or the needle like structures are broken down into smaller particles (**Fig. 4.1B and 4.1D**).

C D

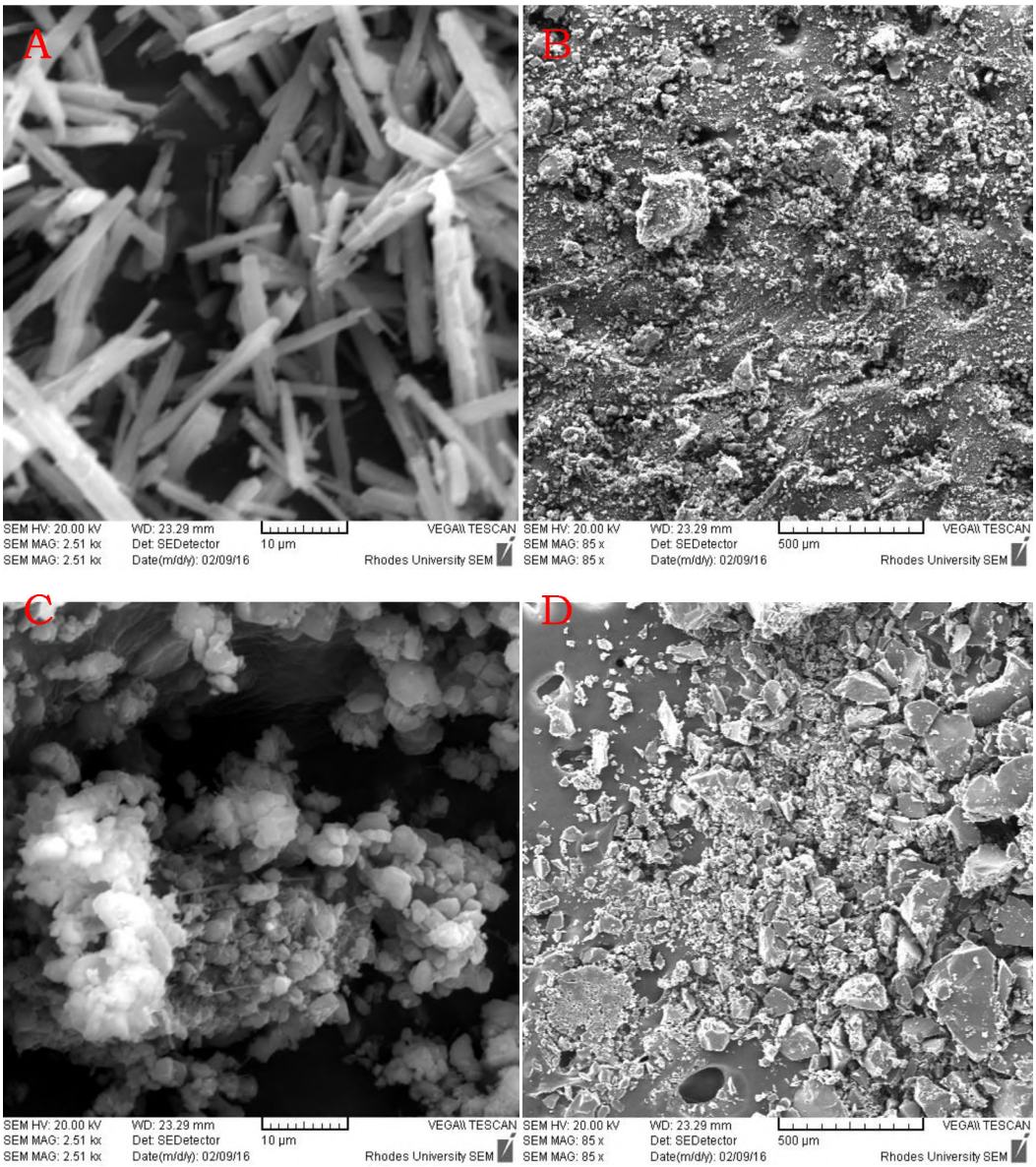

Fig.4.1 SEM images for electrode modifiers (A) CoPc(**3**), (B) CoPc**NP**(**3**), (C) CoTAPc(**5**), (D) CoTAPc**NP**(**5**).

4.1.2 CoTCPhPc(2) and MWCNT conjugates

Complex **2** was linked to or mixed with MWCNT before electrode modification and is used as an example of all MWCNT containing electrodes since similar behaviour was observed for all these electrodes. The SEM images **(Fig. 4.2)** obtained show different morphologies of the modifiers on the modified surface.

This is testimony to the different catalytic surfaces, which then result in differing electrode surface roughness. The CoTCPhPc(**2**)-(DAMN)-MWCNT(linked) or CoTCPhPc(**2**)/(DAMN)-MWCNT(mix) modified electrodes clearly show the presence of multiwalled carbon nanotubes with CoTCPhPc(**2**)-DAMN-MWCNT(linked) revealing sheet like structures which might be evidence of the presence of clustered phthalocyanines. Clustering was also observed under TEM in **Fig. 3.16.** The CoTCPhPc(**2**)/(DAMN)-MWCNT(mix)-GCP shows a higher density of (DAMN)-MWCNT compared to CoTCPhPc(**2**)-(DAMN)-MWCNT(linked)-GCP, **Fig. 4.2**. The absence of (DAMN)-MWCNT is unquestionable on bare and CoTCPhPc (**2**) electrode surfaces, **Fig. 4.2**. Thus, the comparison of the bare glassy carbon plate and the differently modified plates show significant morphological changes upon modification.

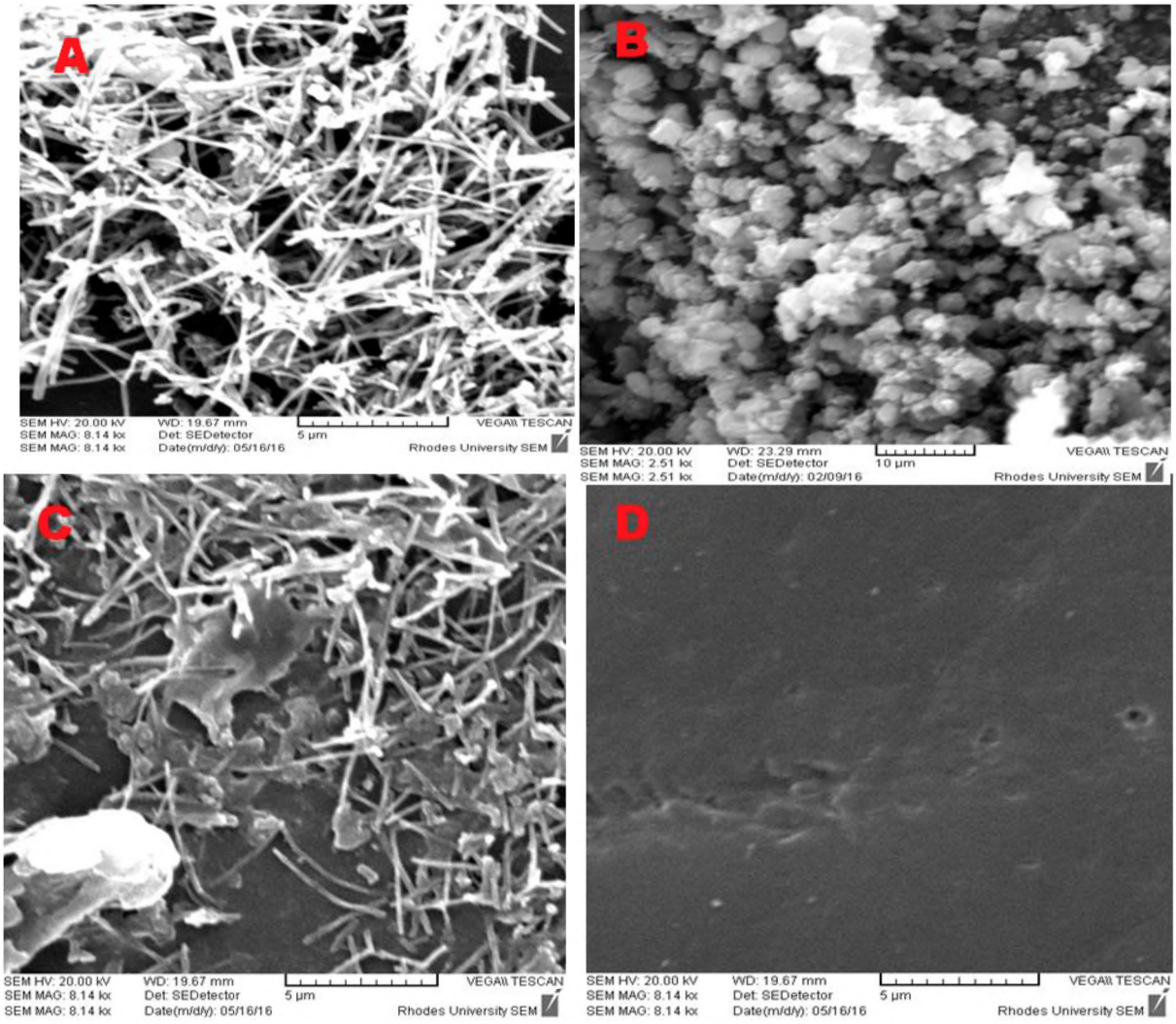

Figure 4.2. SEM images of (A) CoTCPhPc(**2**)-(DAMN)-MWCNT(linked)-GCE, (B) CoTCPhPc(**2**), (C) CoTCPhPc(**2**)/(DAMN)-MWCNT(mix)-GCE and (D) Bare GCE

4.1.3. Complex 4 and GONS conjugates.

Complex **4** is used as an example for GONS containing electrodes. GONS resemble a more open sheet structure suggestive of the thin, less stacked individual sheets using (DAMN)-SNDGONS as an example (**Fig. 4.3A**). Upon conjugating GONS to phthalocyanines the electrode morphology significantly changes, {sing CoMCPhPc(**4**)-(DAMN)-SNDGONS(linked)-GCP as an example}.

The modified electrode shows a rough and less open morphology that might be because of multiple attachments between different layers (**Fig. 4.3B**). Such morphology is thought to be advantageous as it offers significantly increased surface area and open edge sites, which are much needed for the electrochemical reaction sites [122,153].

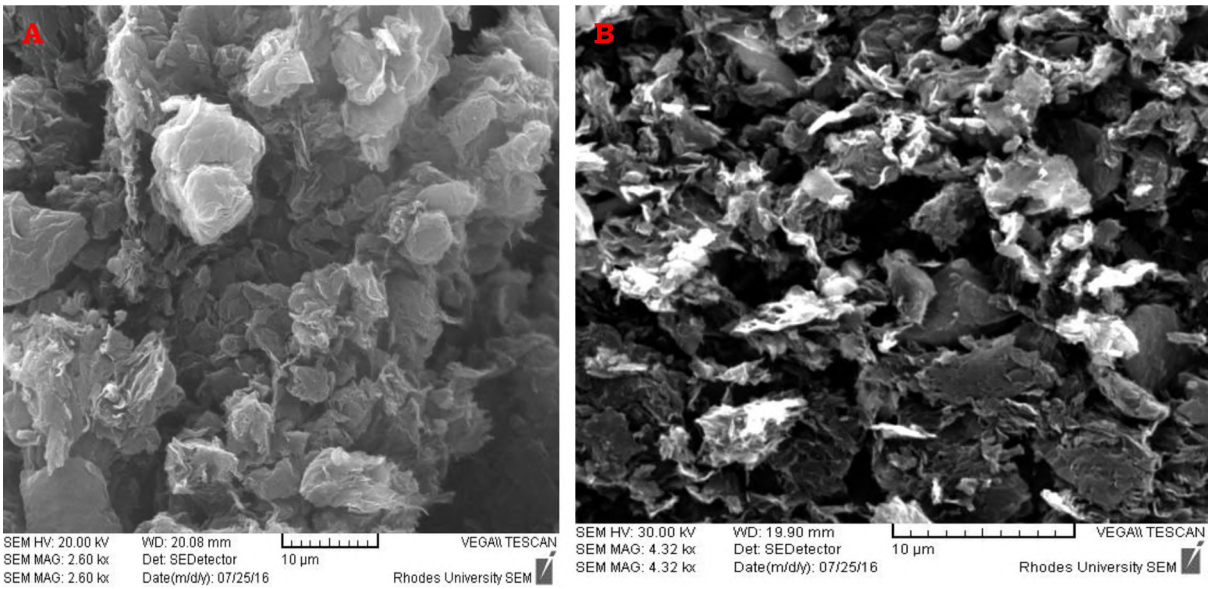

Fig.4.3. SEM images for (A) (DAMN)-SNDGONS-GCP and (B) CoMCPhPc(**4**)-(DAMN)-SNDGONS(linked)-GCP.

4.2 Time of flight secondary ionization mass spectrometry (TOF-SIMS).

Fig. 4.4 shows the TOF-SIMS images for the CoTAPhPc(**1**)@MWCNT-GCE (using complex **1** as an example). The cobalt image shows small dots of concentrated ion signal. The other main relevant carbocations present are $C_3H_7^+$, $C_4H_7^+$, $C_7H_7^+$and $C_3H_9N_2^+$, with $C_3H_9N_2^+$ showing the most ion concentration overall and cobalt the least, which makes sense since cobalt would be in the smallest abundance in a Pc. Similar molecular ions were also

reported for highly ordered pyrolytic graphite [154] and pyridinic N doped graphene [155].

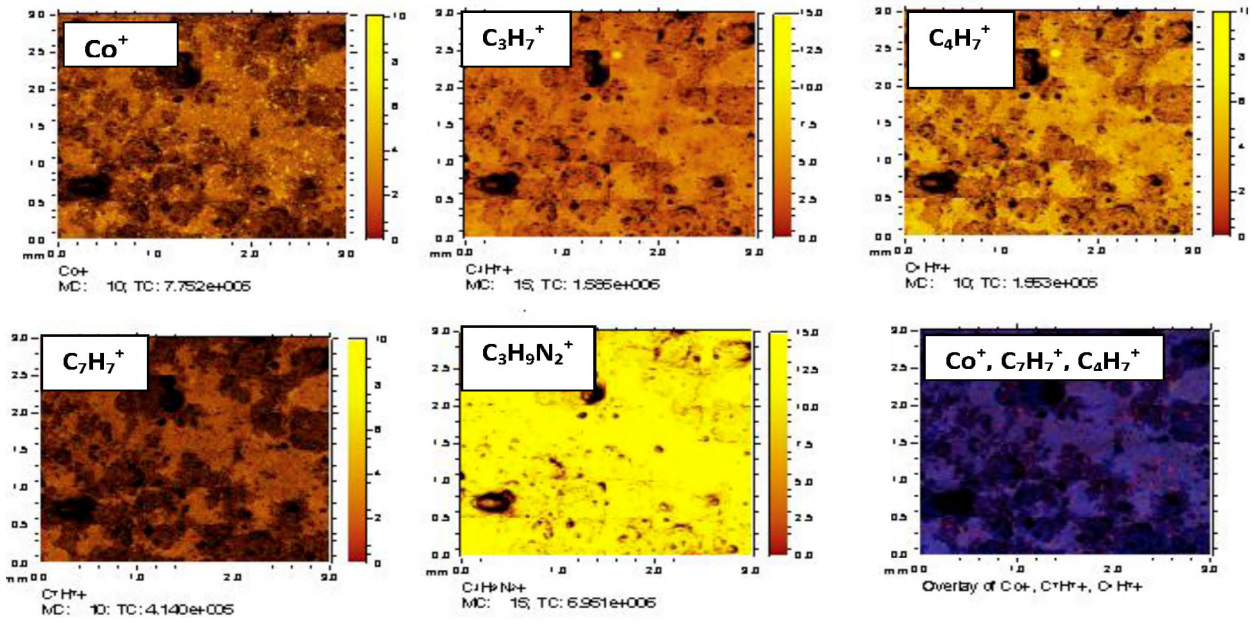

Fig.4.42D TOF-SIMS images for CoTAPhPc(**1**)@MWCNT-GCE in positive mode.

4.3. Scanning Electrochemical Microscopy.

Scanning electrochemical microscopy was used to characterize the probes (complex **1** in the presence of rGONS and MWCNT used as examples). Area scans were done to show the conductivity of the modified electrodes. **Fig.4.5** (**A-C**) shows that bare GCE electrode has an almost uniformly conducting surface and the least recorded currents. Modified electrodes (using CoTAPhPc(**1**)@MWCNT-rGONS(seq)-GCE and CoTAPhPc(**1**)@MWCNT-GCE as examples) show improved currents compared to the bare GCE, which is indicative of possible catalytic nature. CoTAPhPc(**1**)@MWCNT-GCE (**Fig. 5B**)

has larger currents compared to other MWCNT based electrodes as discussed below.

The approach curves in **Fig. 4.5D**, show changes in tip current as the ultra-micro electrode (UME) tip approaches the substrate in a feedback mode experiment in the presence of Fe^{2+} / Fe^{3+} redox mediator. When a sufficiently positive potential is applied to the tip, the oxidation of Fe^{2+} to Fe^{3+} occurs. When the tip is closer to a conductive substrate surface, the Fe^{3+} diffuses to the substrate where it is reduced back to Fe^{2+}. This results in additional flux of Fe^{2+} to UME tip resulting in increased currents. For insulating surface, the current decreases. **Fig. 4.5D** shows approach curves for conducting surfaces of bare GCE, CoTAPhPc(**1**) based electrodes and non-conducting Teflon surface.

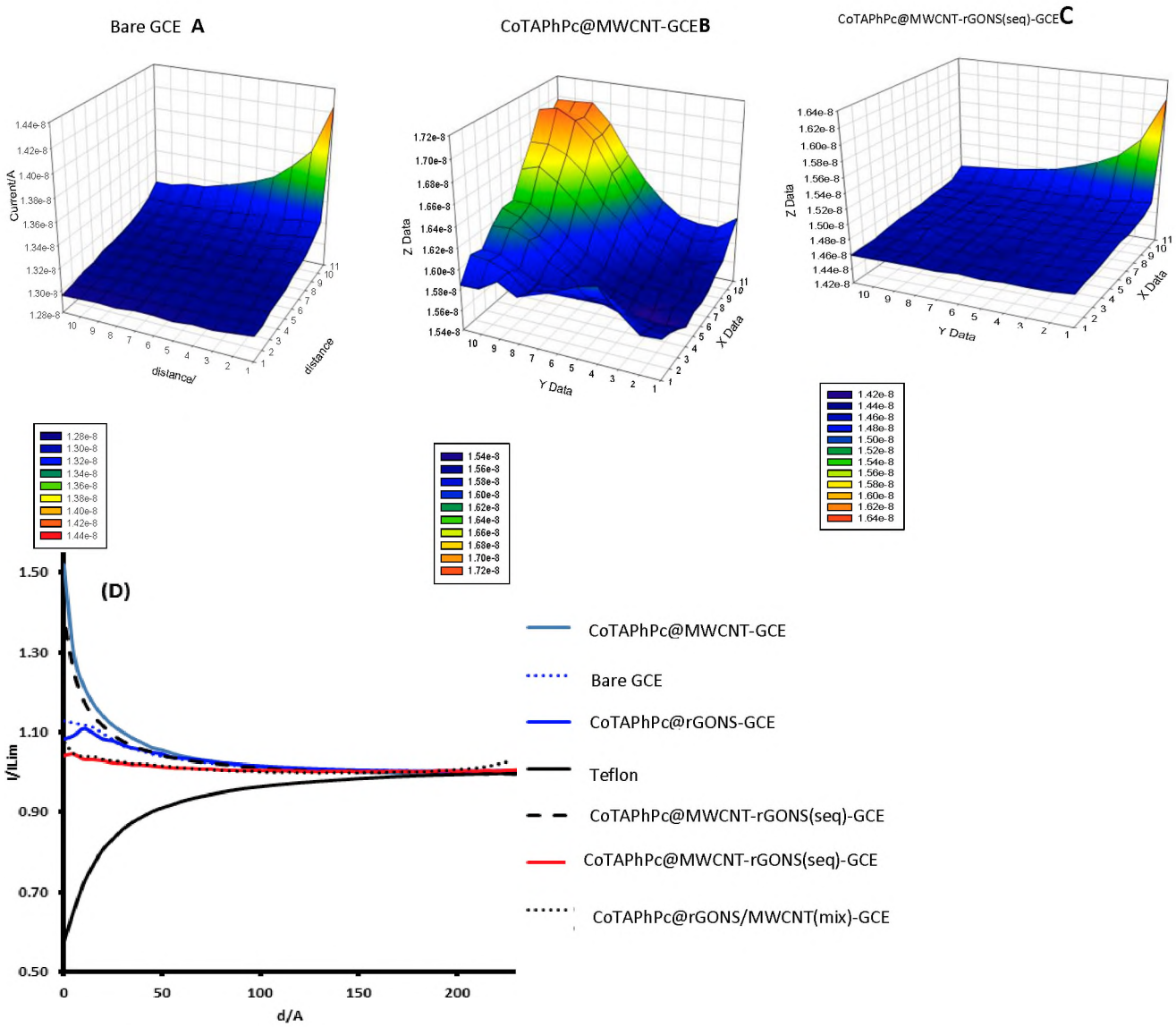

Figure 4.5. Scanning electrochemical microscopy images: Bare GCE (A), CoTAPhPc(**1**)@MWCNT-GCE (B), CoTAPhPc(**1**)@MWCNT-rGONS(seq)-GCE (C) and approach curves (D), using 2.5 µm UME in 5 mM $[FeCN_6]^{3-/4-}$ in 0.1 M KCl.

4.4 Cyclicvoltammetry

Complexes **1** and **4** are new hence will be discussed first in this section.

4.4.1 CoTAPhPc (1) and its conjugates

4.4.1.1 Individual nanomaterials and effect of bulk CoTAPhPc(1) versus CoTAPhPcNP (1)

Fig. 4.6A shows cyclic voltammograms for the modified electrodes in 1 mM $[Fe(CN)_6]^{3-/4-}$ in 0.1 M KCl. The peak potential separation (ΔE) for a reversible system such as $[Fe(CN)_6]^{3-/4-}$ is a good measure of the electron transfer ability of the electrode, with lower values depicting a good electron transfer ability, **Table 4.1**. It can be noted that rBDGONS and its Pc conjugate have the worst electron transfer ability. Modification of the bare electrode with CoTAPhPc**NP** (0.071 V), CoTAPhPc**NP**@rGONS-GCE (0.071 V), and rGONS-GCE (0.076 V) results in electrode conductivity which is slightly higher or similar to bare glassy carbon electrode at 0.073 V (**Table 4.1**). Incorporation of nanosized Pc results in improved electron transfer ability (compare CoTAPhPc**NP**(**1**)@rGONS-GCE, ΔE = 0.071 V with CoTAPhPc(**1**)@rGONS-GCE, ΔE = 0.088 V). Since CoTAPhPc(**1**)@rGONS-GCE (with ΔE = 0.088 V) behaved poorly compared to CoTAPhPc**NP**(**1**)@rGONS-GCE (with ΔE = 0.071 V), hence only nanosized complex **1** was used together with doped GONS in further experiments. The capacitance of rGONS, rBDGONS and rNDGONS were also determined in ferricyanide solution using Electrochemical Impedance Spectroscopy (EIS)to establish the capacitative nature of the probes and followed theorder rGONS (1.0 mF) > rBDGONS 0.88 mF > rNDGONS (0.36 mF). When the capacitance is 1, this means that the surface behaves more like a capacitor. Therefore, rGONS behaves more like a capacitor compared to rNDGONS or rBDGONS hence lower ΔE for rGONS.

The surface roughness factors for the modified electrodes were determined using $[Fe(CN)_6]^{3-/4-}$ redox system and applying Randles–Sevcik Eq. (4.1) for reversible systems [156]:

$$I_p = 2.69x10^5 n^{3/2} ACD^{1/2} v^{1/2} \quad 4.1$$

where I_p, n, A, C, D and $v$are the peak current, the number of electrons involved, the surface area, the concentration of $[Fe(CN)_6]^{3-/4-}$, the diffusion coefficient of $[Fe(CN)_6]^{3-/4-}$ and the scan rate, respectively. From the D value for $K_3[Fe(CN)_6]$ = 7.6 x10^{-6} cm^2 s^{-1} [157] and n = 1, the surface roughness factors (ratio of I_{pa} experimental/I_{pa} theoretical; were determined for all the probes and the corresponding real electrode areas {(roughness factor x theoretical surface area (= 0.071 cm^2)} were determined and used below for the calculation of surface coverage. **Fig. 4.6B** shows the CVs for CoTAPhPc(**1**) based electrodes in pH 7 buffer solution with a weak Co^{III}/Co^{II} process near ~ 0 V, shifted to less positive potentials compared to literature [158], due to the presence of electron donating NH_2 groups which make oxidation easier. Co^{III}/Co^{II} process is known to be very difficult to observe for adsorbed CoPc complexes [159], hence this couple is not well defined in **Fig. 4.6B**. The peak near 0.7 V is then assigned to ring based oxidation. Using the effective (real) area of the electrode and the data from Co^{III}/Co^{II}peak, **Fig. 4.6B**, the surface coverage was calculated using **Eq. (4.2)** [160].

$$\Gamma = \frac{Q}{nFA} \quad 4.2$$

where Γ is the film surface coverage, n is the number of transferred electrons, F is the Faraday constant and A is the effective area of the electrode area.

Γ values in Table 4.1 for single nanomaterial modified electrodes are either lower or higher than 1 x 10^{-10} mol cm^{-2} approximated for a monolayer of a Pc molecule lying flat on the electrode surface [161]. Lower surface coverage suggest different orientation compared to the rest of the electrode modifiers.

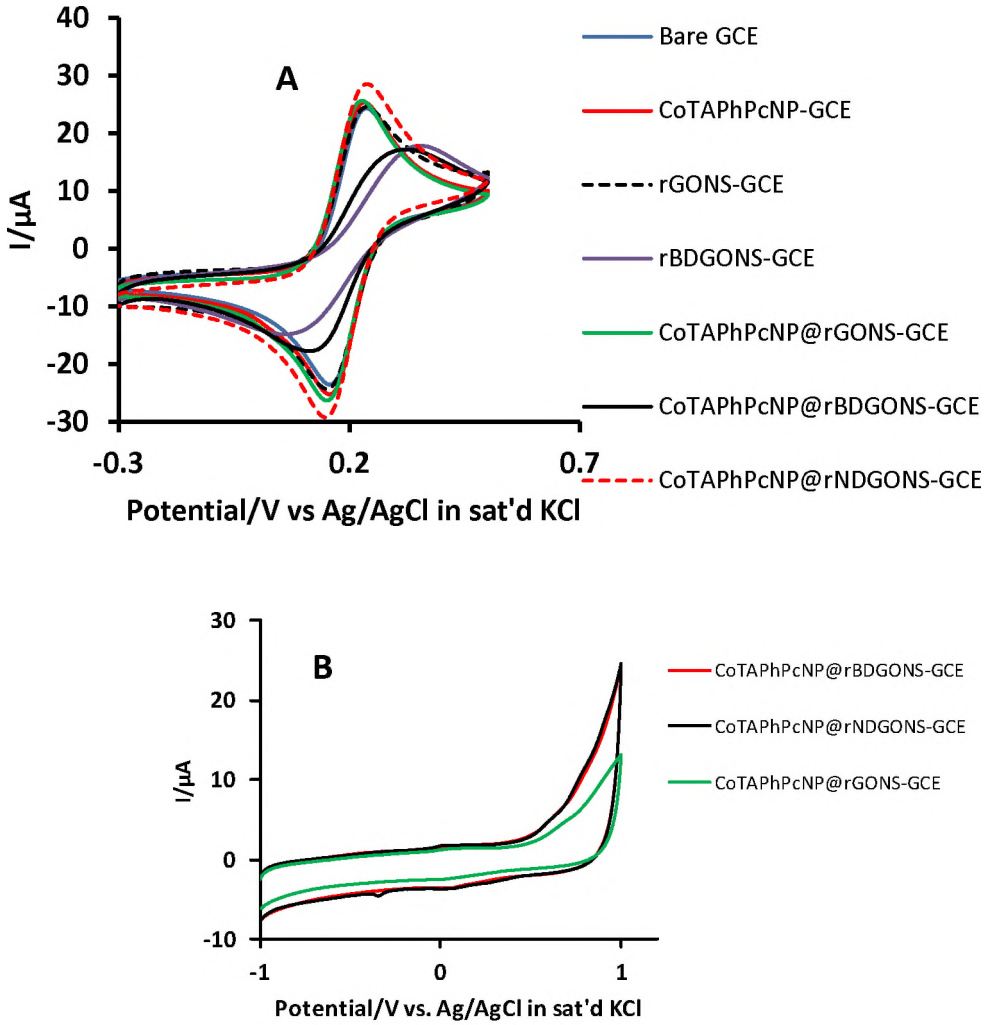

Figure 4.6 Cyclic voltammograms of the CoTAPhPc**NP**(**1**) and B/N doped GONS modified electrodes in (A) 1 mM $[Fe(CN)_6]^{3-/4-}$ in 0.1 M KCl, (B) in pH 7 buffer. Scan rate 100 mV/s.

Table 4.1. A summary of peak separation, surface roughness and film surface coverages of CoTAPhPc(**1**) based electrodes.

a-undetermined because of absence any cobalt redox couple in supporting

GCE modifier	**ΔE_p for $Fe(CN)_6^{3-/4-}$**	**Γ (mol.cm^{-2})**
Bare GCE	0.073	a
Individual nanomaterials		
rGONS-GCE	0.076	a
rNDGONS-GCE	0.081	a
rBDGONS-GCE	0.24	a
rPDGONS-GCE	0.12	a
rPNDGONS-GCE	0.14	a
rSDGONS-GCE	0.073	a
MWCNT-GCE	0.14	a
AuNRs-GCE	0.076	a
Linked or mixed nanomaterials		
MWCNT/rGONS(mix)-GCE	0.30	a
rGONS/MWCNT(mix)-GCE	0.11	a
rGONS/AuNRs(mix)-GCE	0.073	a

electrolyte;"@" = Pc adsorbed onto the nanomaterials; "/" =a mixture of different nanomaterials; "-" accompanied by linked=covalent bond between Pc and

GCE modifier	**ΔE_p for $Fe(CN)_6^{3-/4-}$**	**Γ (mol.cm^{-2})**
rSDGONS-AuNRs(linked)-GCE	0.071	a
rNDGONS-AuNRs(linked)-GCE	0.071	a
rSNDGONS-AuNRs(linked)-GCE	0.071	a
Pc alone		
CoTAPhPc(**1**)-GCE	0.19	1.32 x 10^{-11}
CoTAPhPc**NP**(**1**)-GCE	0.071	3.85 x 10^{-9}
Single Nanomaterial-Pc modified electrodes, Section 4.4.1.1		
CoTAPhPc(**1**)@rGONS-GCE	0.088	1.58 x 10^{-11}
CoTAPhPc**NP**(**1**)@rGONS-GCE	0.071	3.94 x 10^{-9}
CoTAPhPc**NP**(**1**)@rBDGONS-GCE	0.169	2.90 x 10^{-9}
CoTAPhPc**NP**(**1**)@rNDGONS-GCE	0.080	3.50 x 10^{-9}
CoTAPhPc**NP**(**1**)@rPDGONS-GCE	0.10	1.99 x 10^{-11}
CoTAPhPc**NP**(**1**)@rPNDGONS-GCE	0.086	2.03 x 10^{-10}
CoTAPhPc(**1**)@MWCNT-GCE	0.11	3.15 x 10^{-11}
CoTAPhPc**NP**(**1**)@MWCNT-GCE	0.078	3.41 x 10^{-9}

GCE modifier	**ΔE_p for $Fe(CN)_6^{3-/4-}$**	**Γ (mol.cm^{-2})**
AuNRs and GONS; Section 4.4.1.2		
CoTAPhPc**NP**(**1**)-AuNRs(linked)-GCE	0.12	a
CoTAPhPc**NP**(**1**)-@rGONS/AuNRs(mix)-GCE	0.096	a
CoTAPhPc**NP**(**1**)@rNDGONS-AuNRs(linked)-GCE	0.076	a
CoTAPhPc**NP**(**1**)@rSDGONS-AuNRs(linked)-GCE	0.073	a
CoTAPhPc**NP**(**1**)@rSNDGONS-AuNRs(linked)-GCE	0.085	a
CoTAPhPc**NP**(**1**)@rSNDGONS-AuNRs(seq)-GCE	0.15	a
CoTAPhPc**NP**(**1**)@AuNRs-rSNDGONS(seq)-GCE	0.078	a
MWCNT an GONS based electrodes; Section 4.4.1.3		
CoTAPhPc(**1**)@MWCNT-GCE	0.11	3.15 x 10^{-11}
CoTAPhPc**NP**(**1**)@MWCNT-GCE	0.078	3.41 x 10^{-9}
CoTAPhPc(**1**)@rGONS-GCE	0.088	1.58 x 10^{-11}
CoTAPhPc(**1**)@MWCNT/rGONS(mix)-GCE	0.12	2.08 x 10^{-11}
CoTAPhPc(**1**)@MWCNT-rGONS(seq)-GCE	0.078	7.46 x 10^{-11}
CoTAPhPc(**1**)@rGONS-MWCNT-(seq)-GCE	0.098	3.63 x 10^{-11}
CoTAPhPc(**1**)@MWCNT-GCE	0.11	3.15 x 10^{-11}

GCE modifier	**ΔE_p for $Fe(CN)_6^{3-/4-}$**	**Γ (mol.cm^{-2})**
AuNRs and MWCNT; Section 4.4.1.4		
CoTAPhPc**NP**(**1**)@MWCNT-GCE	0.078	3.41×10^{-9}
CoTAPhPc(**1**)@MWCNT-GCE	0.11	3.15×10^{-11}
CoTAPhPc**NP**(**1**)@AuNRs-GCE	0.12	3.43×10^{-9}
CoTAPhPc(**1**)@AuNRs-GCE	0.073	2.52×10^{-9}
CoTAPhPc**NP**(**1**)@MWCNT/AuNRs(mix)-GCE	0.097	3.84×10^{-9}
CoTAPhPc(**1**)@MWCNT/AuNRs(mix)-GCE	0.084	3.23×10^{-9}

nanomaterials or two different nanomaterials; "-" accompanied by seq= sequential adsorption of nanomaterial on another; DAMN = diaminomaleonitrile; mix = mixed before electrode modification; seq = sequentially added to the electrode; "r" in front of GONS = reduced; if no "r", the GONS were not reduced.

4.4.1.2 Complex 1 with AuNRs and doped GONS

N, S, SN, dopedGONS, were linked to AuNRs via Au-N and Au-S or both bonds and represented as linked in **Table 4.1**. Cyclic voltammetry of the modified electrodes were recorded in 1 mM $Fe(CN)_6^{3-/4-}$ and 0.1 M KCl electrolyte (**Fig. 4.7**). The voltammograms are characterised by an extra peak at potentials close to 0 V which can be attributed to the redox behaviour of AuNRs as reported in literature [64]. Different modifications resulted in varying peak potential separations indicative of different electron transfer abilities. As stated before lower peak potential separation (ΔE) implies good electron transfer ability.

The electrodes containing AuNRs were compared to CoTAPhPc**NP**(**1**) alone or with rGONS, rSDGONS, rNDGONS or rSNDGONS in **Table 4.1**. When comparing rSDGONS-AuNRs(linked)-GCE (0.071 V) = rNDGONS-AuNRs(linked)-GCE (0.071 V) = rSNDGONS-AuNRs(linked)-GCE (0.071 V) = CoTAPhPc**NP**(**1**)-GCE (0.071 V) >rGONS/AuNRs(mix)-GCE (0.073 V) there is not much difference in (ΔE) values between these electrodes and when compared to the bare GCE (at 0.073). AuNRs (ΔE = 0.076 V) on their own are worse than in the presence of pristine and doped rGONS. On addition of CoTAPhPc**NP**(**1**) to AuNRs based the electrodes, there is a significant increase in ΔE for CoTAPhPc**NP**(**1**)-AuNRs(linked)-GCE (0.12 V), CoTAPhPc**NP**(**1**)@rSNDGONS-AuNRs(linked)-GCE (0.085 V) and CoTAPhPc**NP**(**1**)@rGONS/AuNRs(mix)-GCE (0.096 V) compared to the electrodes in the absence of CoTAPhPc**NP**(**1**), showing slow electron transfer ability. Sequential addition of nanomaterials is favoured when rSNDGONS is placed on the electrode first for CoTAPhPc**NP**(**1**)@AuNRs-rSNDGONS(seq)-GCE (0.078 V) than when AuNRs are placed first in CoTAPhPc**NP**(**1**)@rSNDGONS-AuNRs(seq)-GCE (0.15 V) or when rSNDGONS are first linked with AuNRs in CoTAPhPc**NP**(**1**)@rSNDGONS-AuNRs(linked)-GCE (0.085 V). Γ could not be calculated due to lack of clear Pc peaks in the supporting electrolyte.

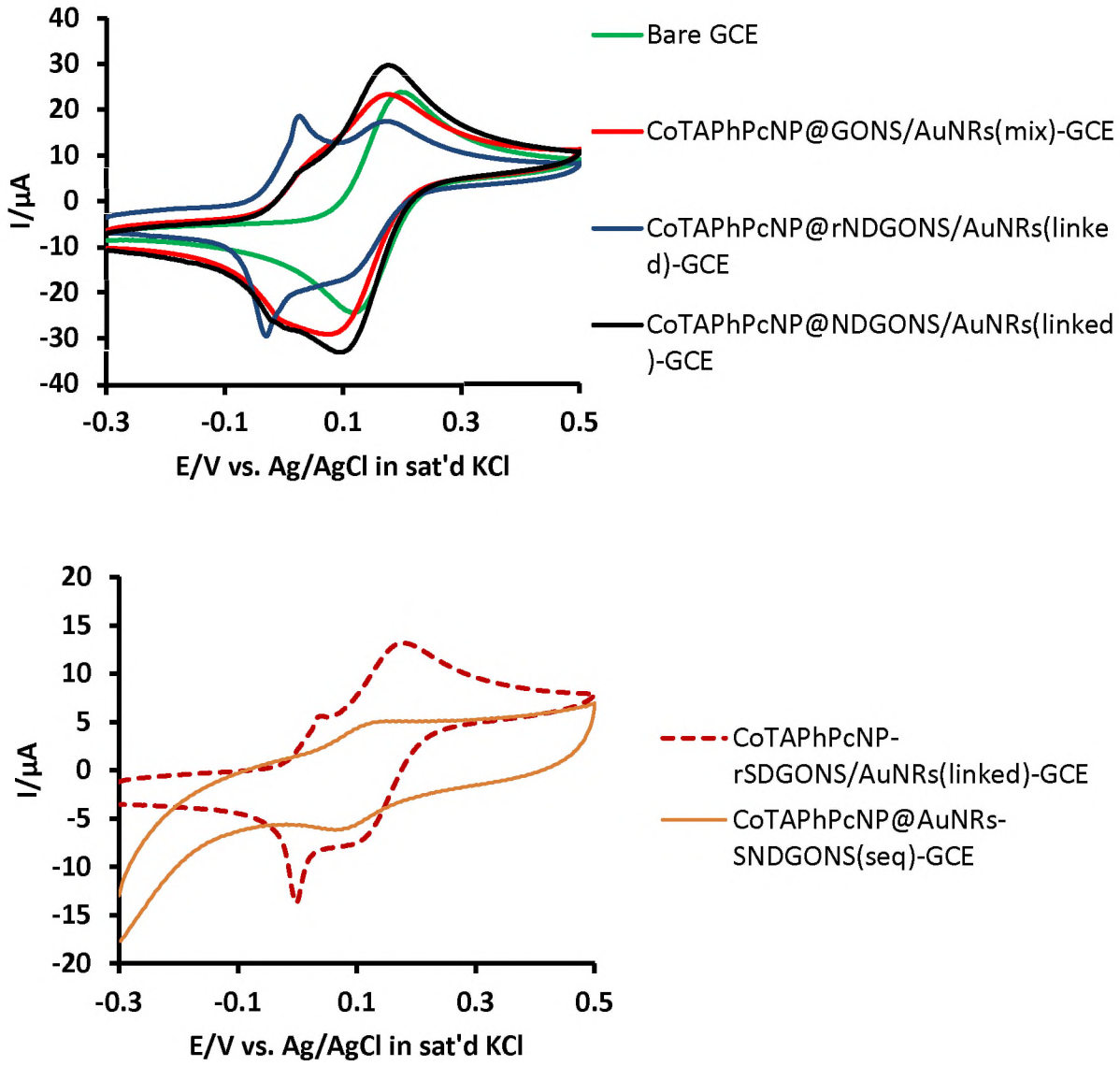

Fig. 4.7. Cyclic voltammograms of selected CoTAPhPc**NP**(**1**), doped GONS-AuNRs modified electrodes in (A) 1mM $[Fe(CN)_6]^{3-/4-}$ in 0.1 M KCl, Scan rate 100 mV.

4.4.1.3. Complex 1 and MWCNT/rGONS conjugates

When MWCNT are mixed over 24 h, ππ interaction are possible. To study the effect of multiple carbon based nanomaterials on Pcs, pristine rGONS and MWCNTs were either sequentially added to the electrode surface or mixed prior to electrode modification after which the MPc was then added on top. **Fig. 4.8** shows the cyclic voltammograms for a selection of modified electrodes

in 1 mM $[Fe(CN)_6]^{3-/4-}$ and 0.1 M KCl. ΔE values are listed in **Table 4.1**. It is clear from the ΔE values that mixing MWCNT and r-GONS before adsorbing them onto the electrode {in CoTAPhPc(**1**)@MWCNT/rGONS(mix)-GCE, (ΔE = 0.12 V)} is less favored compared to sequentially adding the carbon materials to the electrode {in CoTAPhPc(**1**)@rGONS-MWCNT(seq)-GCE, ΔE = 0.098, (MWCNT first on GCE) and {CoTAPhPc(**1**)@MWCNT-rGONS(seq)-GCE, ΔE = 0.078 V,(rGONS first on GCE)}. When rGONS are placed on the electrode alone for CoTAPhPc(**1**)@rGONS-GCE, ΔE = 0.088, or before MWCNT and CoTAPhPc(**1**)@MWCNT-rGONS(seq)-GCE, ΔE = 0.078, there is better electron transfer properties than when MWCNTs are placed before rGONS (for CoTAPhPc(**1**)@rGONS-MWCNT(seq)-GCE, ΔE =0.098). Placing rGONS on the electrode first might assist in reducing the stacking of rGONS. MWCNTs improve the properties for rGONS electrode if the latter is placed first on the electrode in CoTAPhPc(**1**)@MWCNT-rGONS(seq)-GCE, ΔE = 0.078. Direct mixing of rGONS and MWCNT does not harness the electron transfer properties of either material. Thus, it is suggested that in order to use these materials effectively they must be used to modify electrodes in a sequential manner.

The cyclic voltammograms for modified electrodes (containing CoTAPhPc(**1**), where there is a peak due to Co^{III}/Co^{II}) in pH 4 buffer are shown in **Fig. 4.8**. Γ values in **Table 4.1** for all the catalysts containing MWCNT and GONS are less than 1×10^{-10} mol.cm^{-2} which is expected for a monolayer of a Pc molecule lying flat on the electrode surface [161]. The values may suggest that the molecules are not lying flat on the electrode. For bulk complex **1**, the largest

surface coverage is observed for CoTAPhPc(**1**)@MWCNT-rGONS-GCE. Thus when rGONS are deposited first on the electrode, followed by MWCNTs, the surface coverage is larger.

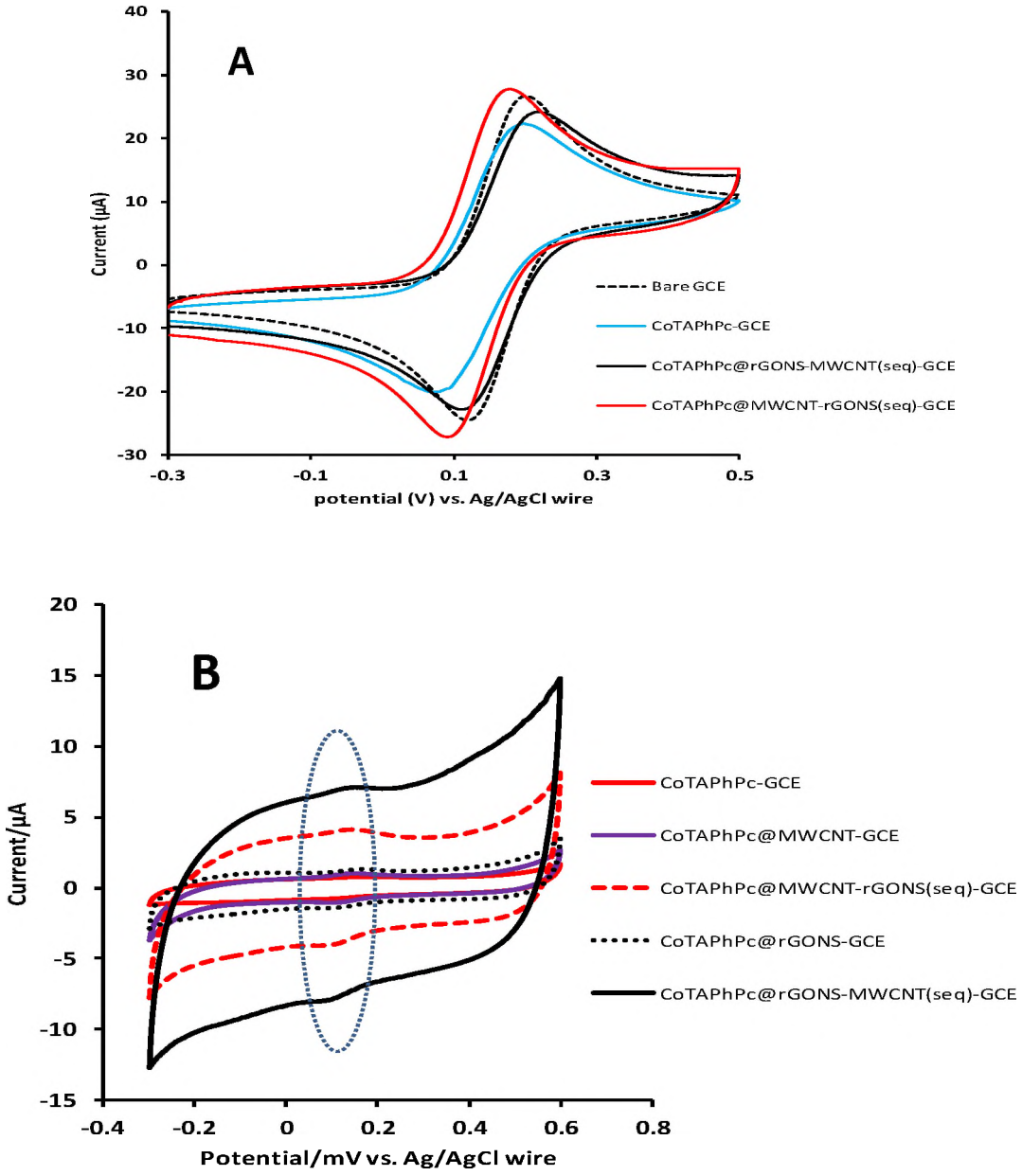

Figure 4.8. Cyclic voltammograms of CoTAPhPc(**1**)/MWCNT/rGONS modified electrodes in 1 mM $[Fe(CN)_6]^{3-/4-}$ in 0.1 M KCl and in pH 4 buffer solution in the absence of L- Cysteine. Scan rate 100 mV/s.

4.4.1.4 Complex 1 with MWCNTs and AuNRs.

For these studies, AuNRs were mixed with MWCNT and the effect on MPc**NP** or Pc alone compared to when the two nanomaterials are employed separately. **Fig. 4.9A** shows the cyclic voltammograms for a selection of modified electrodes in 1 mM $Fe(CN)_6^{3-/4-}$ in 0.1 M KCl. The peaks near 0 V are only observed in the presence of AuNRs, hence are attributed to their redox process as discussed above. AuNP oxidation peaks are known to be the range 0–400 mV is being compared to bulk Au oxidation peak which occurs at 850 mV [162]. Hence the observed peak near 0 V is attributed to Au(0) oxidation. The Au peaks are not clear for CoTAPhPc(**1**)-AuNRs(linked)-GCE.

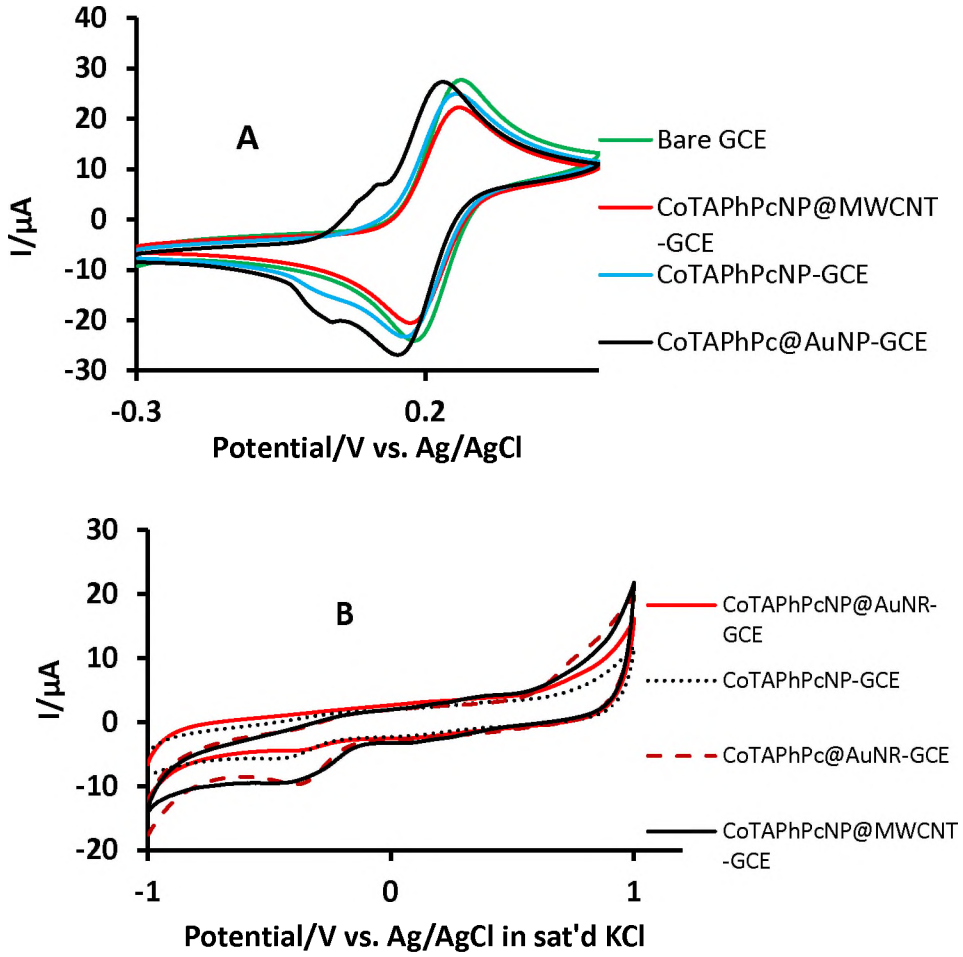

Fig.4.9 A selection of cyclic voltammograms of the CoTAPhPc(**1**)/MWCNT/AuNRs modified electrodes in (A) 1 mM $[Fe(CN)_6]^{3-/4-}$ in 0.1M KCl and (B) pH 7 buffer. Scan rate 100 mV/s.

4.4.2 Conjugates of CoMCPhPc (4) and doped GONS.

Covalently linked and separately adsorbed GONS with Pc on top are compared. The effect of doping the graphene oxide nanosheets with sulphur and nitrogen singly and combined is also investigated in these scenarios. To investigate the electron transfer ability of the modified electrode surface, cyclic voltammetry was done in 1 mM $Fe(CN)_6^{3-/4-}$ (in 0.1 M KCl) (**Fig. 4.10A**) as discussed before. The voltammetric information was summarised in **Table 4.2** and shows that dopingGONS improves electron transfer ability of the

modifiers and also that CoMCPhPc (**4**) performs poorly in the absence of any GONS. There is synergic effect from the dopants since S/N doped graphene oxide nanosheets results in the improvement of electron transfer ability; compare CoMCPhPc(**4**)-(DAMN)-SDGONS(linked)-GCE (0.119) or CoMCPhPc(**4**)-(DAMN)-NDGONS(linked)-GCE (0.119 V) with CoMCPhPc(**4**)-(DAMN)-SNDGONS(linked)-GCE (0.095 V) for linked composites and CoMCPhPc(**4**)@(DAMN)-SDGONS-GCE (0.097 V), or CoMCPhPc(**4**)@(DAMN)-NDGONS-GCE (0.098 V) with CoMCPhPc(**4**)@(DAMN)-SNDGONS-GCE (0.064 V) for separately adsorbed modification. Remember lowerpeak potential separation implies good electron transfer ability.

The CoMCPhPc(**4**) based electrodes were cycled in pH 7 buffer, **Fig. 4.10B**. A weak Co^{III}/Co^{II} process is observed near ~ 0 V, shifted to less positive potentials compared to literature [158] due to differences in solution media and MPc substituent. The Co^{II}/Co^{I} peak is observed near -0.5 V, **Fig. 4.10B.** The effective electrode areas and the charge Q, obtained from the Co^{III}/Co^{II} process in **Fig. 4.10B**, were then used to determine the surface as discussed above.

The surface coverages reported here ($4.71 \times 10^{-10} - 4.27 \times 10^{-9}$) were higher than 1×10^{-10} reported for phthalocyanine lying flat on the surface of the electrode [161] suggesting that both the covalent linking and the underlying graphene moieties in separate modification hinders the metallophthalocyanines from lying parallel to the electrode surface. Surface coverages in this range have been reported before for covalently linked phthalocyanines and multiwalled carbon nanotubes [163]. The highest

surface coverages were observed for CoMCPhPc(**4**)@(DAMN)-NDGONS-GCE (4.27×10^{-9}) ≈ CoMCPhPc(**4**)@(DAMN)-SNDGONS-GCE (4.25×10^{-9}). The higher surface coverages indicate the increase in the electrode surface area which offers more electrocatalytic surface. Surface coverages were lower for CoTAPhPc(**1**) alone or with GONS, 1.32×10^{-11} or 1.58×10^{-11} respectively but higher for the corresponding CoMCPhPc(**4**), 1.37×10^{-9}. It could also reflect that CoMCPhPc(**4**) with one substituent is vertically oriented with CoTAPhPc(**1**) having four substituents favouring a different orientation.

Table 4.2. Electrochemical parameters, of CoMCPhPc based electrodes

Modified GCE	**ΔE_p $Fe(CN)_6^{3-/4-}$ (0.1 M KCl)**	**Γ (mol. cm^{-2})**
Bare GCE	0.073	-
CoMCPhPc(**4**)-GCE	0.349	1.37×10^{-9}
CoMCPhPc(**4**)-(DAMN)-GONS(linked)-GCE	0.125	1.03×10^{-9}
CoMCPhPc(**4**)-(DAMN)-SDGONS(linked)-GCE	0.119	7.49×10^{-10}
CoMCPhPc(**4**)-(DAMN)-NDGONS(linked)-GCE	0.119	1.16×10^{-9}
CoMCPhPc(**4**)-(DAMN)-SNDGONS(linked)-GCE	0.095	2.28×10^{-9}
CoMCPhPc(**4**)@(DAMN)-GONS-GCE	0.138	3.21×10^{-9}
CoMCPhPc(**4**)@(DAMN)-SDGONS-GCE	0.097	4.71×10^{-10}
CoMCPhPc(**4**)@(DAMN)-NDGONS-GCE	0.098	4.27×10^{-9}
CoMCPhPc(**4**)@(DAMN)-SNDGONS-GCE	0.064	4.25×10^{-9}

[a] "@" = Pc adsorbed onto the nanomaterials; "-" accompanied by linked=covalent bond between Pc and nanomaterials or two different nanomaterials; "-" accompanied by seq= sequential adsorption of nanomaterial on another. DAMN = diaminomaleonitrile; "r" in front of GONS = reduced; if no "r", the GONS were not reduced.

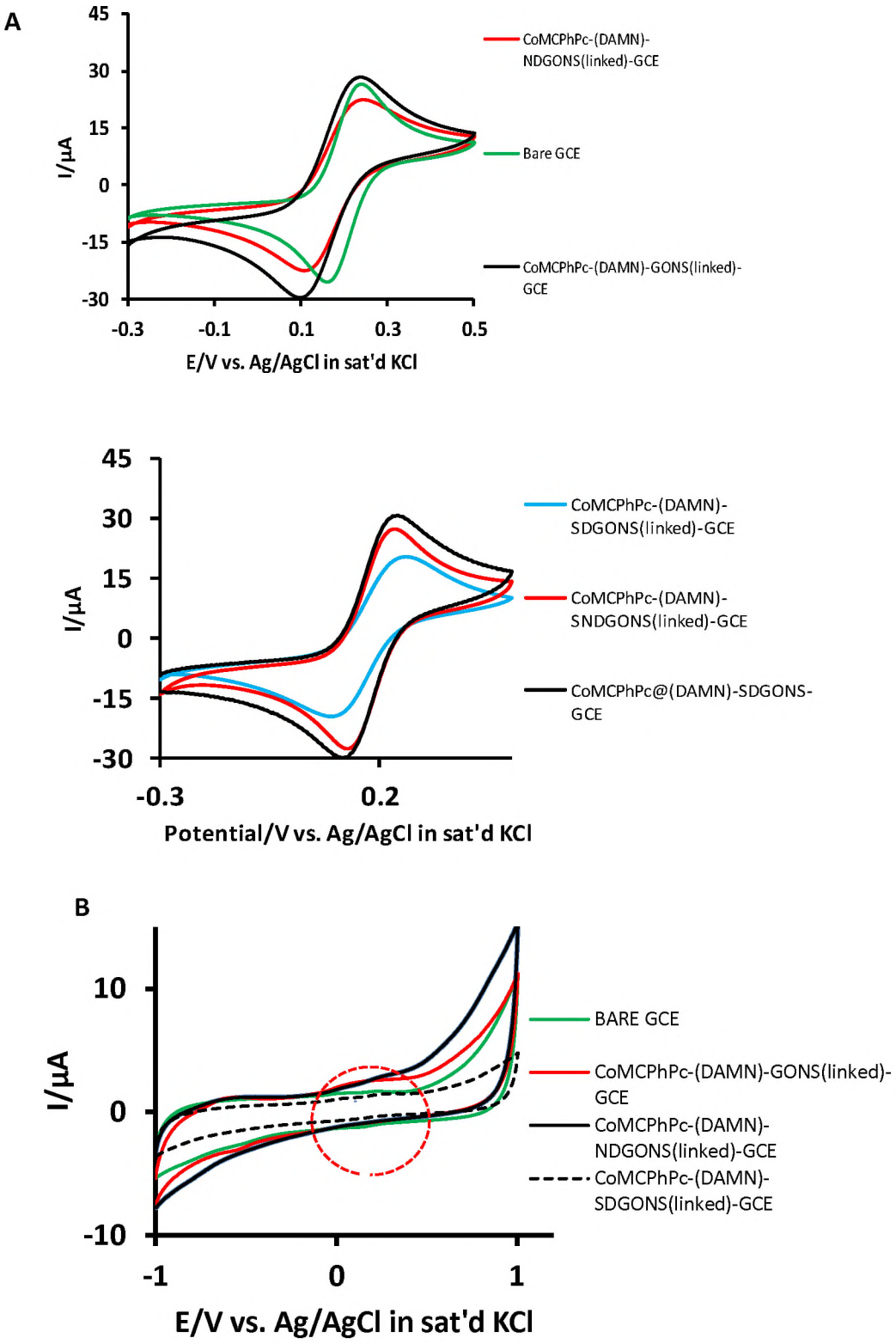

Figure 4.10. Cyclic voltammograms of a selection of CoMCPhPc(**4**) based electrodes in (A) 1mM $[Fe(CN)_6]^{3-/4-}$ in 0.1 M KCl, (B) in pH 7 buffer. Scan rate 100 mV.

4.4.3 CoPc (3) and CoTAPc (5) based electrodes.

CoPc**NP**(**3**) and CoTAPc**NP**(**5**) were added on top of either rGONS or rSDGONS to check the effect of the substituent groups. Their bulk forms were not studied in the presents of the nanomaterials.

The following observations can be deduced from the peak potential separation values in **Table 4.3** and **Fig. 4.11.**

1. Electrodes containing rSDGONS show better electron transfer ability compared to those containing pristine rGONS (compare CoTAPc**NP**(**5**)-rSDGONS-GCE (0.076 V) with CoTAPc**NP**(**5**)-rGONS-GCE (0.256 V); and CoPc**NP**(**3**)-rSDGONS-GCE (0.071) with CoPc**NP**(**3**)-rGONS-GCE (0.379 V).
2. CoTAPc (**5**) performed better than CoPc (**3**) in the presence of rGONS and alone which might imply that the presence of NH_2 enhances electron transfer.

The surface coverages were determined as described before using **Fig. 11B**. Γ values in **Table 4.3** for all electrodes are in some cases higher than 1 x 10^{-10} mol cm^{-2} approximated for a monolayer of a Pc molecule lying flat on the electrode surface [161]. Surface coverages increased in the order CoPc**NP**-rGONS < CoTAPc**NP**(**5**)-rSDGONS-GCE < CoPc(**3**)-GCE < CoPc**NP**(**3**)-GCE < CoPc**NP**(**3**)-rSDGONS-GCE < CoTAPc**NP**(**5**)-rGONS-GCE < CoTAPc**NP**(**5**)-GCE < CoTAPc(**5**)-GCE. CoTAPc(**5**) in the absence of rSDGONS has the best surface coverage which might affect the catalytic activity in **Chapter 5**.

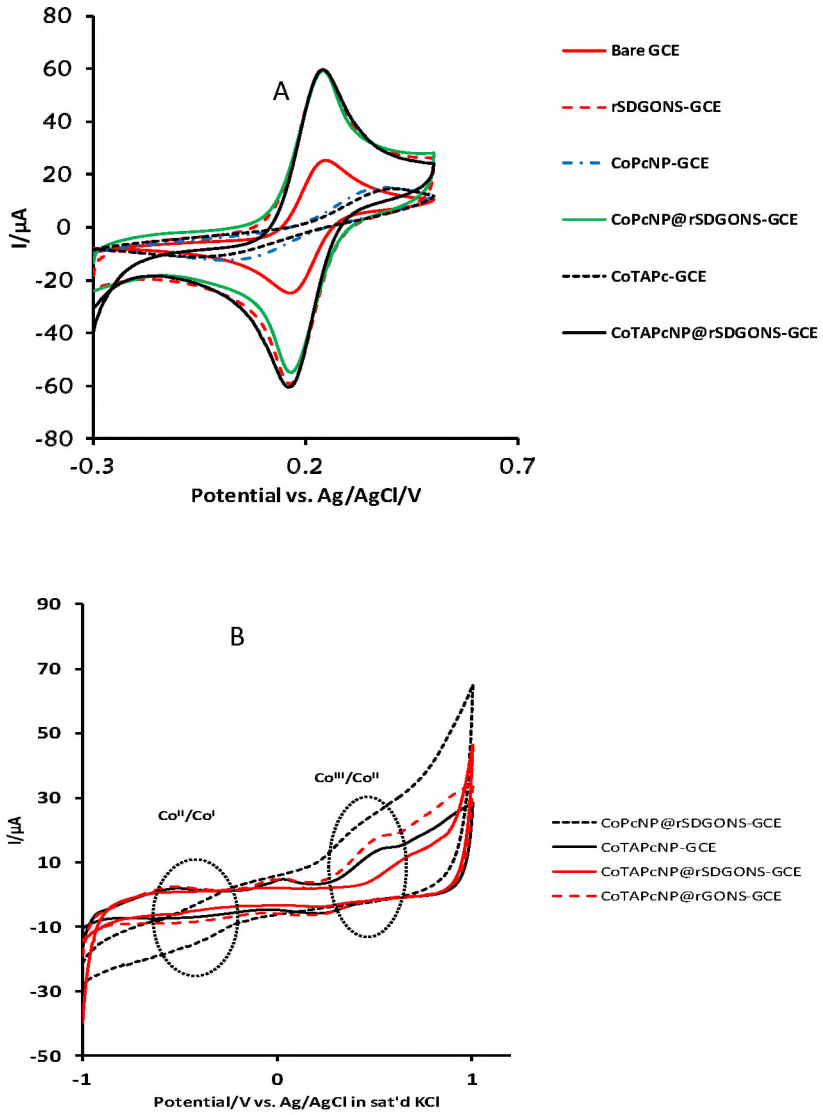

Fig. 4.11 Cyclic voltammograms of a selection of CoTAPc(**5**) and CoPc (**3**) conjugates modified electrodes in (A) 1mM $[Fe(CN)^{3-/4-}$ in 0.1 M KCl, (B) in pH 7 buffer. Scan rate 100 mV/s.

Table 4.3. Electrochemical parameters, H_2O_2 detection potential and currents for the **Complex 3** and **5** modified electrodes.

GCE modifier	ΔE_p $Fe(CN)_6^{3-/4-}$ (0.1 M KCl)	Γ (mol.cm^{-2})
Bare GCE	0.073	-
rGONS-GCE	0.076	a
rSDGONS-GCE	0.073	a
CoPc-GCE	0.394	2.53 x 10^{-10}
CoPc**NP**(**3**)-GCE	0.339	3.21 x 10^{-10}
CoPc**NP**(**3**)@rGONS-GCE	0.379	7.20 x 10^{-10}
CoPc**NP**(**3**)@rSDGONS-GCE	0.071	4.45 x 10^{-10}
CoPc**NP**(**3**)@rNDGONS-GCE	0.090	1.31 x 10^{-10}
CoPc**NP**(**3**)@rPDGONS-GCE	0.13	1.34 x 10^{-9}
CoPc**NP**(**3**)@rPNDGONS-GCE	0.17	2.01 x 10^{-10}
CoTAPc(**5**)-GCE	0.364	2.94 x 10^{-9}
CoTAPc**NP**(**5**)- GCE	0.311	6.71 x 10^{-10}
CoTAPc**NP**(**5**)@rGONS-GCE	0.256	6.54 x 10^{-10}
CoTAPc**NP**(**5**)@rSDGONS-GCE	0.076	1.17 x 10^{-10}

[a] no peak; "@" = Pc adsorbed onto the nanomaterials; "/" =a mixture of different nanomaterials; "r" in front of GONS = reduced; if no "r", the GONS were not reduced.

4.4.4. CoTCPhPc(**2**) covalently linked to MWCNTs based electrodes.

Covalently linked and mixed CoTCPhPc(**2**) and MWCNT were used to modify glassy carbon electrodes in order to study the effects of linking as opposed to mixing the two. **Table 4.4** and **Fig. 4.12A** show the anodic and cathodic peak separations (ΔE) of the modified electrodes. The order of electron transfer ability is as follows CoTCPhPc(**2**)/(DAMN)-MWCNT(mix)-GCE (0.411 V) < CoTCPhPc(**2**)-GCE (0.193 V) < CoTCPhPc(**2**)-(DAMN)-MWCNT(linked)-GCE (0.110 V) < (DAMN)-MWCNT-GCE (0.103 V) < Bare GCE (0.073 V). The trend reveals that CoTCPhPc(**2**)-(DAMN)-MWCNT(linked)-GCE shows better electron transfer ability than CoTCPhPc(**2**)/(DAMN)-MWCNT(mix)-GCE and CoTCPhPc alone.

Γ values in **Table 4.4** for all electrodes are higher than 1 x 10^{-10} mol cm^{-2} approximated for a monolayer of a MPc molecule lying flat on the electrode surface [161]. This is plausible since the Pc in question is bulky and linked or mixed with multiwalled carbon nanotubes hence disturbing the planar orientation on the electrode surface**.** However, Γ values were also large compared to for CoPc(**3**) and CoTAPhPc(**1**) as explained before.

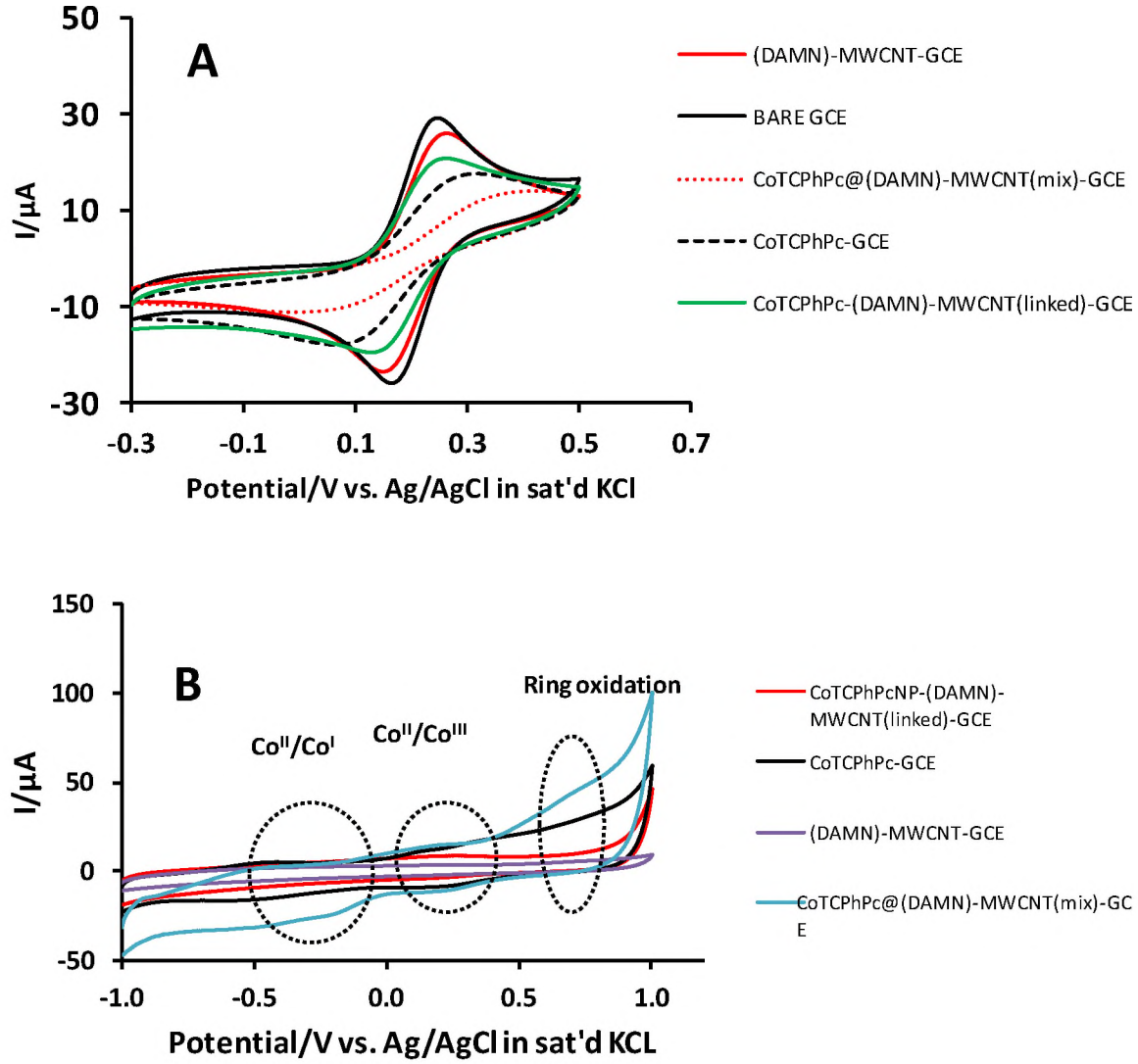

Fig. 4.12. Cyclic voltammograms of a selection of CoTCPhPc(**2**)/DAMN-MWCNT modified electrodes in (A) 1 mM $[Fe(CN)_6]^{3-/4-}$ in 0.1 M KCl, (B) in pH 7 buffer. Scan rate 100 mV/s.

Table. 4.4. Electrochemical parameters of the modified electrodes.

GCE modifier	ΔE_p $Fe(CN)_6^{3-/4-}$ (0.1 M KCl)	Surface Roughness Factor	Γ (mol.cm^{-2})
Bare GCE	0.073	-	-
(DAMN)- MWCNT-GCE	0.103	-	-
CoTCPhPc(**2**)-GCE	0.193	10.62	9.7 x 10^{-10}
CoTCPhPc(**2**)-(DAMN)-MWCNT(linked)-GCE	0.110	8.14	1.0 x 10^{-9}
CoTCPhPc(**2**)/DAMN-MWCNT(mix)-GCE	0.411	12.04	5.5 x 10^{-10}

[a] "/" =a mixture of different nanomaterials; "-" covalent bond. DAMN = diaminomaleonitrile; mix = mixed before electrode modification;

4.5. Conclusions.

Electrochemical analysis of the nanoprobes show that the modified electrodes resulted in higher effective electrode area, an observation that is supported by the morphological changes as seen on SEM images. This implies an increase in the surface area on which the catalysed reactions are to occur. SECM results confirms the enhanced currents on the modified electrodes. Generally, nanosized MPcs showed improved electron transfer abilities both when alone and in their nanoconjugates with other nanomaterials as compared to their bulk counterparts.

Chapter Five.

5. Electrocatalysis.

In this Chapter, the developed nanoprobes are examined for electrocatalysis of either hydrogen peroxide or L-cysteine. The nanoprobes are tested for both electro oxidation (L-cysteine and hydrogen peroxide) and electro reduction of hydrogen peroxide.

5.1. L-cysteine on CoTAPhPc (1) electrodes

Only the bulk CoTAPhPc (**1**) based electrodes were employed for L-cysteine detection. Reduced GONS and MWCNTs individually, mixed or separately were added to the electrode followed by addition of CoTAPhPc (**1**). The effects of the nanomaterials on the electrocatalytic activity of CoTAPhPc (**1**) were evaluated.

5.1.1 Cyclic voltammetry

The acidic media (pH 4) was selected so that the oxidation product of L-cysteine does not precipitate out of solution. **Fig.5.1** shows the L-cysteine oxidation peak on the different electrodes. L-cysteine peaks were only observed in the presence of CoTAPhPc(**1**), showing that the complex is responsible for the catalysis. The dip in the current on the return scan for the oxidation of L-cysteine on modified surfaces (**Fig. 5.1**) is typical of electrocatalysis for some analytes such as hydrazine and L-cysteine on CoPc modified electrodes [164,165].

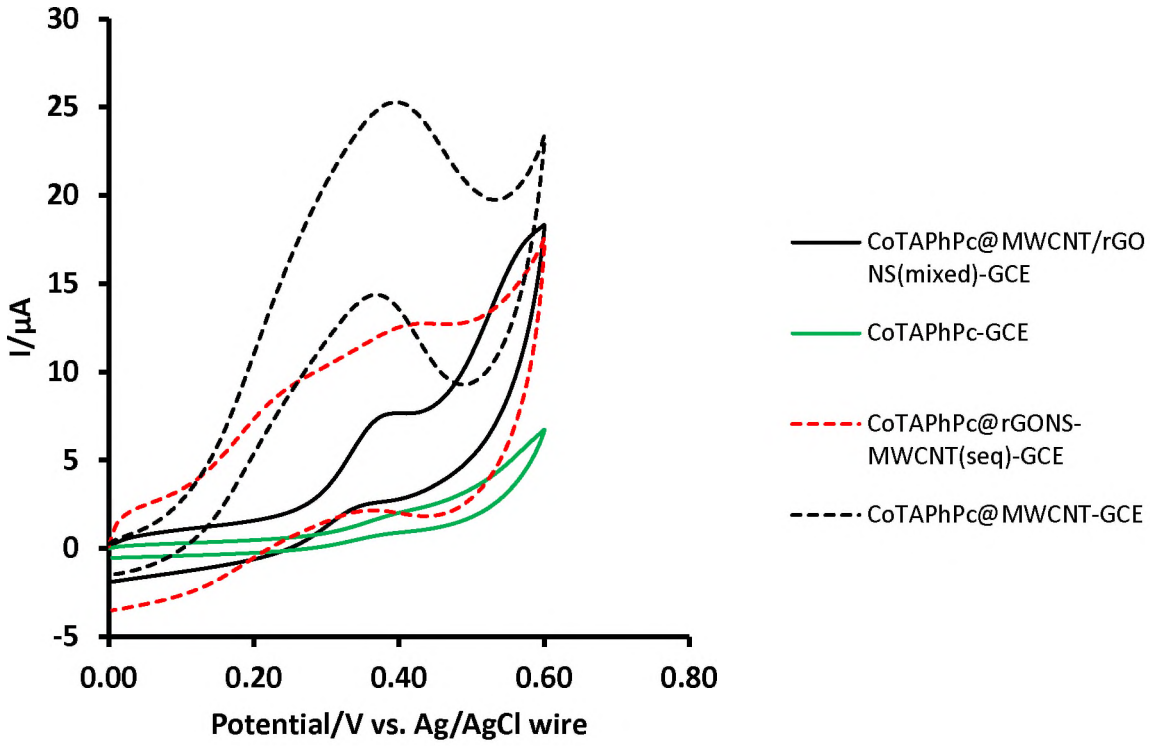

Fig. 5.1 Cyclic voltammograms of modified electrodes in 2 mM L-cysteine. pH 4 buffer. Scan rate 100 mV/s.

The potentials for L-cysteine oxidation on CoTAPhPc@MWCNT-GCE, CoTAPhPc(**1**)@rGONS-MWCNT(seq)-GCE and CoTAPhPc(**1**)-GCE electrodes were similar at ~0.40 V. CoTAPhPc(**1**)@MWCNT-rGONS(seq)-GCE (where rGONS are deposited first on the electrode) gave a slightly more positive potential at ~ 0.46 V, **Table 4.1**. This electrode also had a larger surface coverage. These potentials are lower than reported for L-cysteine oxidation on cobalt tetraaminophthalocyanine CoTAPc(**5**)@MWCNT-GCE at 0.63 V [103], showing the importance of the Pc with the spacer between the amino group and the Pc ring. CoTAPhPc(**1**)@MWCNT-GCE was the best probe in terms of currents for cysteine electro-oxidation, **Fig. 5.1**.

Table 5.1. Detection potentials for L-cysteine on electrodes based on Complex **1** modification

GCE modifier	**E/V for L-cysteine oxidation in pH 4 buffer**	**Γ (x 10^{-11})**
Bare GCE	a	-
CoTAPhPc(**1**)@MWCNT/rGONS(mix)-GCE	0.38	2.08
CoTAPhPc(**1**)@MWCNT-rGONS(seq)-GCE	0.46	7.46
CoTAPhPc(**1**)@rGONS-MWCNT(seq)-GCE	0.41	3.63
CoTAPhPc(**1**)@MWCNT-GCE	0.42	3.15
CoTAPhPc(**1**)@rGONS-GCE	0.43	1.58
CoTAPhPc(**1**)-GCE	0.41	1.32

[a] no L-cysteine peak; [a] "@" = Pc adsorbed onto the nanomaterials; "/" =a mixture of different nanomaterials; "-" accompanied by seq = sequential modification; mix = mixed before electrode modification; seq = sequentially added to the electrode; "r" in front of GONS = reduced; if no "r", the GONS were not reduced.

To test for the reusability, the electrode was continuously cyclized in the presence of 2 mM L-cysteine (figures not shown). The presence of both rGONS and MWCNT in CoTAPhPc(**1**)@MWCNT/rGONS(mix)-GCE resulted in less passivation of the electrode. Generally, the inclusion of rGONS in the probes resulted in resistance to passivation for all electrodes.

CoTAPhPc(**1**)@MWCNT-GCE (as an example) was employed for the determination of Tafel slopes due to its high electrocatalytic activity (in terms of current) for L-cysteine detection compared to the other electrodes. **Fig. 5.2A** and **B** show linear plots of current versus square root of scan rate and the plot of peak potential versus log scan rate for L-cysteine oxidation, respectively. The plot in **Fig. 5.2A** confirms that the catalytic oxidation of L-cysteine is diffusion controlled. The relationship between peak potential and scan rate for an irreversible diffusion-controlled process is given by **Eq. 5.1,** [160]

$$E_p = \frac{b}{2}\log v + K \qquad 5.1$$

Where E_p is the peak potential, b is the Tafel slope, v is the scan rate and K is a constant. The plot of E_p versus log v (**Fig. 5.2B**) gave a linear relationship and the Tafel slope was 106 mV decade^{-1}. The Tafel slope as observed in this work, suggests that the transfer of a first one-electron is rate controlling [166].

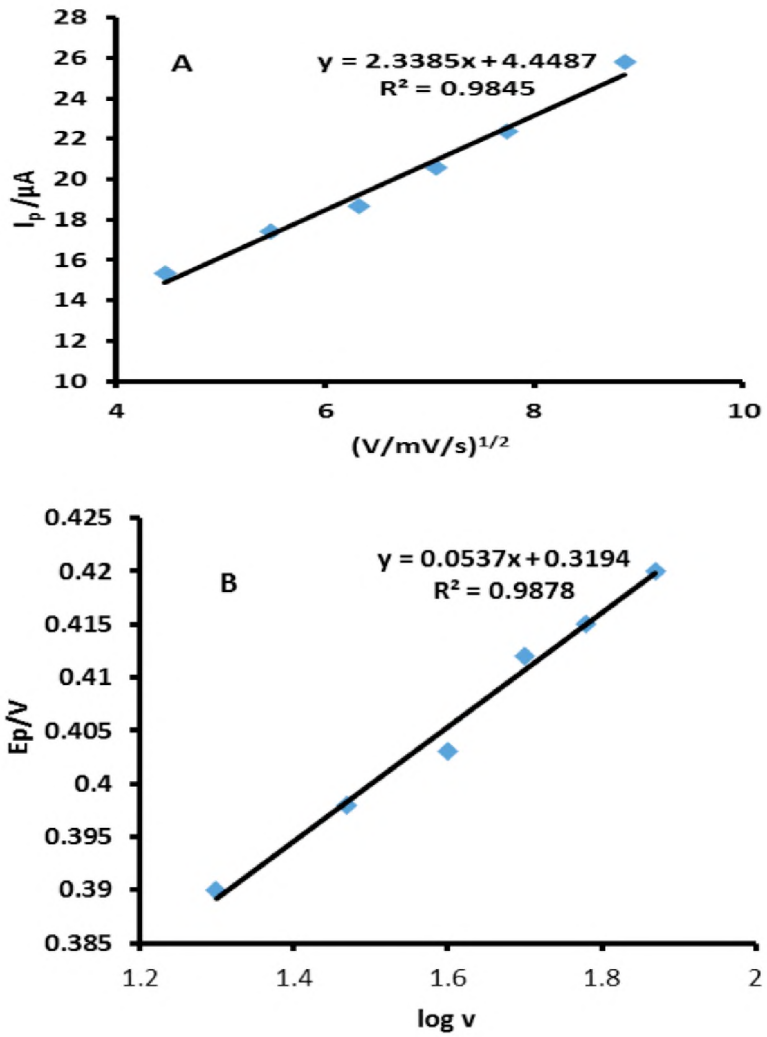

Fig. 5.2 A: Plot of I_{pc} vs. $\upsilon^{1/2}$ and B: Plot of peak potential vs. log scan rate in L-cysteine oxidation on CoTAPhPc(**1**)@MWCNT-GCE.

5.1.2. Chronoamperometric analysis.

Chronoamperometry data was used to determine catalytic rate constants for the oxidation of L-cysteine. CoTAPhPc(**1**)@MWCNT-GCE, CoTAPhPc(**1**)@MWCNT-rGONS(seq)-GCE, CoTAPhPc(**1**)@rGONS-MWCNT(seq)-GCE and CoTAPhPc(**1**)@MWCNT/rGONS(mix)-GCE were employed as examples. **Fig. 5.3A** shows the chronoamperometric evolutions

on CoTAPhPc(**1**)@MWCNT-GCE as an example. The inset shows a linear relationship between current and concentration.

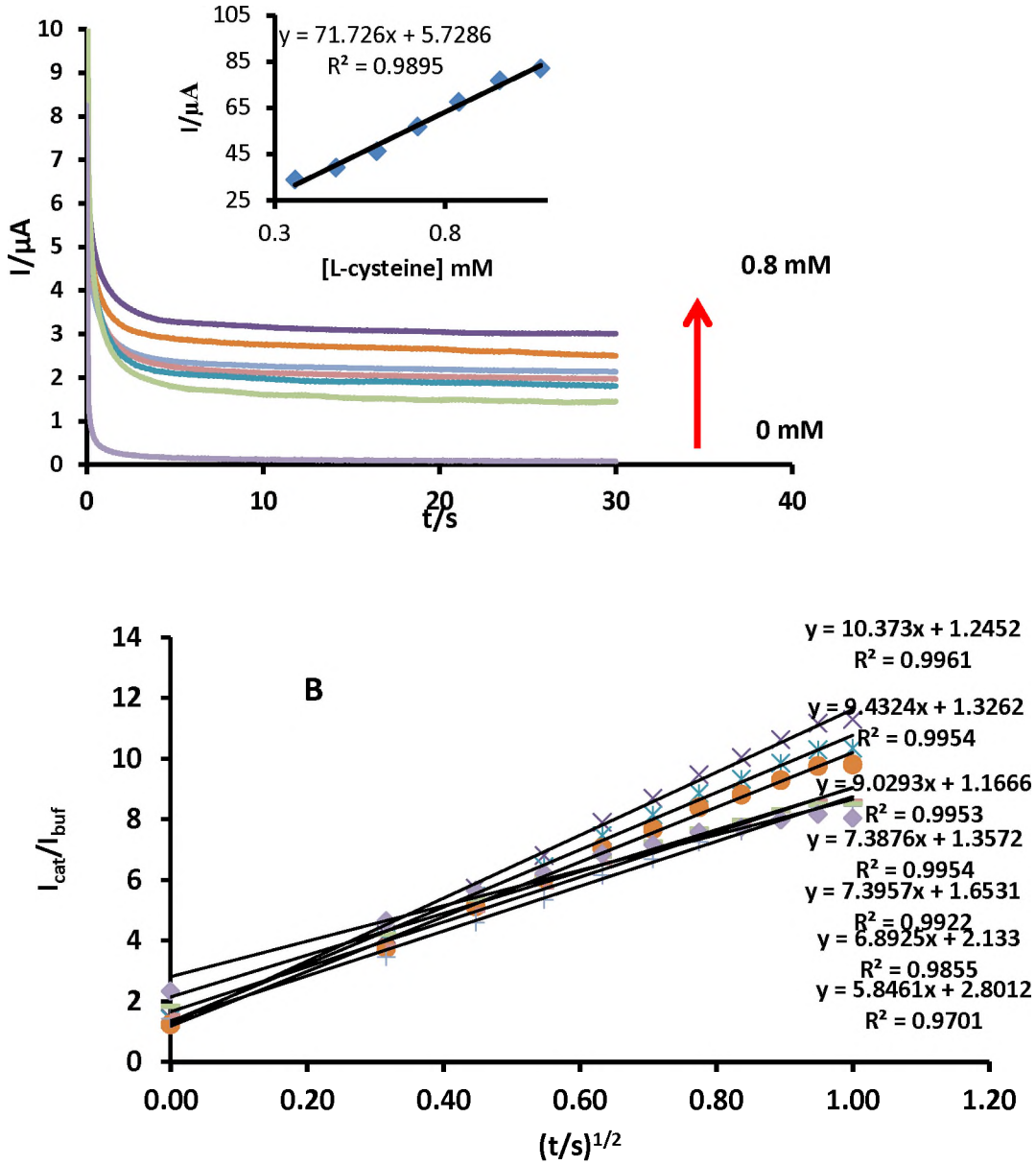

Fig. 5.3 Chronoamperograms for CoTAPhPc(**1**)@MWCNT-GCE in different concentrations of L-cysteine (A) plot of current versus time and (B) Plots of (I_{cat}/I_{buf}) versus $t^{1/2}$ (0.27 mM, 0.40 mM, 0.44 mM, 0.50 mM, 0.57 mM, 0.67 mM, 0.80 mM).

The slopes in **Fig 5.3A** insert (plot of current vs. concentration)showed the following trend CoTAPhPc(**1**)@MWCNT-GCE (71.72 mAM^{-1}) > CoTAPhPc(**1**)@MWCNT-rGONS(seq)-GCE (41.6 mAM^{-1}) > CoTAPhPc(**1**)@rGONS-MWCNT(seq)-GCE(8.03 mAM^{-1}) > CoTAPhPc(**1**)-MWCNT/rGONS(mix)-GCE (1.86 mAM^{-1}), **Table 5.2**. Thus, CoTAPhPc(**1**)@MWCNT-GCE showed higher slope (71.72 mA M^{-1}) and thelowest limit of detection (LOD) of 0.03 μM using the 3δ/slope ratio notation (where δ is the standard deviation of the blank), **Table 5.2**. The LOD value for CoTAPhPc(**1**)@MWCNT-GCE is an improvement compared to reported values in **Table 5.2**[103,167,168]. CoTAPhPc(**1**)@MWCNT-GCE was followed by CoTAPhPc(**1**)@MWCNT-rGONS(seq)GCE in terms of slope of plot in **Fig. 5.3A** insert but the latter was worse than CoTAPhPc(**1**)@rGONS-MWCNT(seq)-GCE in terms of LOD. Thus even though the presence of MWCNT with CoTAPhPc gives a good detection limit, layer by layer modification of electrodes containing rGONS and MWCNT also gives reasonable LOD values when MWCNT are placed on the electrode first. As stated in Chapter 4, the presence of MWCNTs assist in enhancing the electron transfer properties when layered. In **Fig. 5.3A**the catalytic current (I_{cat}) is dominated by the rate at which L-cysteine is oxidized on CoTAPhPc(**1**)@MWCNT-GCE. The slopes of the plots of (I_{cat}/I_{buf}) versus $t^{1/2}$ were used to calculate the rate constant according to **Eq. 5.2**[169].

$$\frac{I_{cat}}{I_{buf}} = \gamma^{1/2}\pi^{1/2} = \pi^{1/2}(k_{cat}Ct)^{1/2} \qquad (\mathbf{5.2})$$

where I_{cat} and I_{buf} are currents in the presence and absence of L-cysteine respectively, k_{cat} is the catalytic rate constant, C is the concentration of L-cysteine and t is the time elapsed in seconds. The plots (figures not shown) of the square of slopes obtained from **Fig. 5.3B** (using CoTAPhPc(**1**)@MWCNT-GCE as an example) versus concentration of L-cysteine were done for CoTAPhPc(**1**)@MWCNT-GCE, CoTAPhPc(**1**)@MWCNT/rGONS(mix)-GCE, CoTAPhPc(**1**)@MWCNT-rGONS(seq)-GCE and CoTAPhPc(**1**)@rGONS-MWCNT(seq)-GCE. Linear relationships were observed and represented by **Eq. 5.3 - 5.6**

CoTAPhPc(**1**)@MWCNT-GCE

$$y = 145.21[L-cysteine](\frac{s^{-1}}{mM}) - 8.7107s^{-1}, R^2 = 0.961 \quad (5.3)$$

CoTAPhPc(**1**)@rGONS-MWCNT(seq)-GCE

$$y = 2.7602[L-cysteine](\frac{s^{-1}}{mM}) - 1.2428s^{-1}, R^2 = 0.9706 \quad (5.4)$$

CoTAPhPc(**1**)@MWCNT-rGONS(seq)-GCE

$$y = 10.178[L-cysteine](\frac{s^{-1}}{mM}) + 24.524s^{-1}, R^2 = 0.9564 \quad (5.5)$$

CoTAPhPc(**1**)@MWCNT/rGONS(mix)-GCE.

$$y = 0.9271[L-cysteine](\frac{s^{-1}}{mM}) - 1.6337s^{-1}, R^2 = 0.9827 \quad (5.6)$$

where the slope of this plot is equal to πk and the values of $k$are listed in **Table 5.2**.Thevalue for CoTAPhPc(**1**)@MWCNT-GCE and CoTAPhPc(**1**)@MWCNT-rGONS(seq)-GCE are an improvement to that given in literature (1.93×10^3 $M^{-1}s^{-1}$) for L-cysteine detection on Nile blue A modified electrode[170]. This makes the probes developed here suitable for the detection of L-cysteine.

Table. 5.2. Comparative LODs for the electrocatalysed oxidation of L-cysteine using different catalytic systems

Modified Electrode	Slope of calibration curve	k/ $M^{-1}s^{-1}$	pH	LOD/μM	Ref.
CoPc(**3**)-carbon paste		-	7	0.5	[168]
CoOHETPc-SAM-AuE		-	4	0.52	[167]
FeOHETPc-SAM-AuE		-	4	0.52	[167]
CoTAPhPc(**1**)@MWCNT-GCE	71.72	4.62×10^4	4	0.03	T W
CoTAPhPc(**1**)@MWCNT-rGONS(seq)-GCE	41.6	3.24×10^3	4	2.24	TW
CoTAPhPc(**1**)@rGONS-MWCNT(seq)-GCE	8.03	8.78×10^2	4	0.11	TW
CoTAPhPc(**1**)@MWCNT/rGONS(mix)-GCE	1.86	2.94×10^2	4	6.39	TW

[a]**OHETPc =** octa(hydroxyethylthio) phthalocyanine, SAM = self-assembled monolayer, AuE gold electrode; [a] "@" = Pc adsorbed onto the nanomaterials; "/" =a mixture of different nanomaterials; "-" accompanied by seq = sequential modification; mix = mixed before electrode modification; seq = sequentially added to the electrode; "r" in front of GONS = reduced; if no "r", the GONS were not reduced; TW = this work

5.2Hydrogen peroxide detection on CoTAPhPc (1) electrodes in comparison with unsubstituted CoPc (3).

5.2.1Complex 1 with GONS

5.2.1.1 Cyclic voltammetry.

Most probes under investigation exhibited both oxidation and reduction peaks in 1 mM hydrogen peroxide in pH 7 buffer solution with the reduction being more pronounced in most cases (**Fig. 5.4**). Oxidation during hydrogen

peroxide detection is more attractive since it does not suffer interference from oxygen reduction. Except for CoPc**NP**@rPDGONS-GCE, allCoTAPhPc**NP**(**1**)and CoPc**NP** (**3**)containing electrodes showed both electrocatalytic oxidation and reduction of hydrogen peroxide as shown in **Fig. 5.4** and **Table 5.3**, while the ones containing GONS only without CoTAPhPc**NP** (**1**) or CoPc**NP** (**3**) showed thereduction peaks. For all the electrodes the oxidation peak was observed in the potential window 0.71 V to 0.83 V while the reduction peak appeared in the window -0.33 V to - 0.59 V which is comparable to values reported elsewhere with reduction peaks at -0.6 V [171] and -0.4 V [172] and oxidation peak of 0.86 V [173].

Table. 5.3. Electrochemical parameters of the Complex **1** or **3**, P/N/B GONS modified electrodes

GCE modifier	**E/V (H_2O_2) reduction pH 7**	**E/V (H_2O_2) oxidation pH 7 buffer**	**Background corrected currents/μA for H_2O_2 reduction**	**Background corrected currents/μA for H_2O_2 oxidation**
Bare GCE	-0.58	-	3.85	-
rGONS-GCE	-0.49	-	16.95	-
rBDGONS-GCE	-0.69	-	13.78	-
rNDGONS-GCE	-0.56	-	23.08	-
rPDGONS-GCE	-0.55	-	13.76	-
rPNDGONS-GCE	-	-	-	-
CoPc(**3**)-GCE	-0.43	0.75	13.01	23.19
CoPc**NP**(**3**)-GCE	-0.39	0.76	43.54	66.20
CoPc**NP**(**3**)@rGONS-GCE	-0.41	0.74	12.90	35.04
CoPc**NP**(**3**)@rNDGONS-GCE	-0.40	0.80	27.25	37.80
CoPc**NP**(**3**)@rPDGONS-GCE	-0.41	-	16.61	-
CoPc**NP**(**3**)@rPNDGONS-GCE	-0.40	0.75	18.07	27.95
CoTAPhPc(**1**)-GCE	-0.37	0.83	9.04	-
CoTAPhPc(**1**)@rGONS-GCE	-0.51	0.71	9.19	-
CoTAPhPc**NP**(**1**)-GCE	-0.33	0.78	19.31	48.04
CoTAPhPc**NP**(**1**)@rGONS-GCE	-0.39	0.76	20.01	6.85
CoTAPhPc**NP**(**1**)@rNDGONS-GCE	-0.48	0.74	59.33	22.14
CoTAPhPc**NP**(**1**)@rPDGONS-GCE	-0.52	0.80	22.41	25.51
CoTAPhPc**NP**(**1**)@rPNDGONS-GCE	-0.59	0.79	78.11	56.00

[a] "@" = Pc adsorbed onto the nanomaterials; "r" in front of GONS = reduced; if no "r", the GONS were not reduced.

GCE modifier	**E/V (H_2O_2) reduction pH 7**	**E/V (H_2O_2) oxidation pH 7 buffer**	**Background corrected currents/μA for H_2O_2 reduction**	**Background corrected currents/μA for H_2O_2 oxidation**
CoTAPhPc**NP**(**1**)@rBDGONS-GCE	-0.38	0.77	16.95	2.32

The inclusion of graphene moieties (except for rBDGONS) in the electrodes, enhanced the reduction currents of the CoTAPhPc**NP**(**1**)**:** CoTAPhPc**NP**(**1**)@rBDGONS-GCE (16.95 V) < CoTAPhPc**NP**(**1**)-GCE (19.31 μA) < CoTAPhPc**NP**(**1**)@rGONS-GCE (20.01 μA) < CoTAPhPc**NP**(**1**)@rPDGONS-GCE (22.41 μA) < CoTAPhPc**NP**(**1**)@rNDGONS-GCE (59.33 μA) < CoTAPhPc**NP**(**1**)@rPNDGONS-GCE (78.11 μA). Considering only reduction currents, for CoTAPhPc**NP**(**1**), the presence of co-doped N/P in CoTAPhPc**NP**(**1**)@rPNDGONS-GCE resulted in enhanced currents compared to individually doped GONS/Pc composites, showing the advantage of co-doping. N doped (CoTAPhPc**NP**(**1**)@rNDGONS-GCE, 59.33 μA) showed improved currents compared to P doped (CoTAPhPc**NP**(**1**)@rPDGONS-GCE, 22.41 μA) and pristine (CoTAPhPc**NP**(**1**)@rGONS-GCE, 20.01 μA), showing enhanced electron transfer ability of N doped GONS. B doped GONS show the least current. For CoPc**NP**(**3**), N doped (CoPc**NP**(**3**)@rNDGONS-GCE (27.25 μA) gave larger currents than P doped (CoPc**NP**(**3**)@rPDGONS-GCE (16.61μA) as observed for CoTAPhPc**NP**(**1**). However P/N co-doped GONS in CoPc**NP**(**3**)@rPNDGONS-GCE (18.07 μA) resulted in lower currents than N doping in CoPc**NP**(**3**)@rNDGONS-GCE (27.25 μA), but higher than P doping in CoPc**NP**(**3**)@rPDGONS-GCE (16.61μA). These observations confirm the importance of N doping. The lack of improvement for co-doped in CoPc**NP**(**3**)@rPNDGONS-GCE compared to CoPc**NP**(**3**)@rPDGONS-GCE or

CoPc**NP**(**3**)@rNDGONS-GCE, **Table 5.3,** may be attributed to high oxygen content in P/N co-doped (rPNDGONS, 3.23%; rPDGONS, 2.66%; rNDGONS, 1.29%). Interestingly, CoPc**NP**(**3**)-GCE gave the larger reduction currents than CoTAPhPc**NP**(**1**)-GCE, this could be related to the small particle size for the latter, **Fig. 3.9**{CoPc**NP**(**3**) = 6.50 nm, CoTAPhPc**NP** (**1**) = 14.00 nm}. This is very plausible, as the small size would mean more metal centres are accessible for catalysis. For unsubstituted CoPc**NP** (**3**), there is no advantage of pristine or doped GONS, since the largest catalytic current for hydrogen peroxide detection (both oxidation and reduction) was observed for CoPc**NP**(**3**)-GCE and not on any of the electrodes containing GONS. However, there is a huge advantage of having GONS for CoTAPhPc**NP**(**1**) with the highest oxidation and reduction currents being observed in the presence of co-doped GONS in CoTAPhPc**NP**(**1**)@rPNDGONS-GCE. It is possible that the presence of amino groups in CoTAPhPc**NP**(**1**) could enhance electron transfer, which is enhanced by co-doped rPNDGONS. There is no clear correlation between current and surface coverage in **Table 4.1**.

The electrodes were also tested for their resistance to fouling by running 20 successive cycles in 1 mM hydrogen peroxide. **Fig. 5.5** shows CoPc**NP**(**3**)@rPNDGONS-GCE and CoTAPhPc**NP**(**1**)@rPNDGONS-GCE as examples. All CoTAPhPc(**1**) based electrodes showed similar stability behaviour as shown in **Fig. 5.5**. The same applies to CoPc(**3**) based electrodes. It can be generally concluded that CoTAPhPc**NP**(**1**) based electrodes were prone to extensive fouling following electro oxidation (**Fig. 5.5**). CoPc**NP**(**3**)

based electrodes show significant resistance to fouling during electro-oxidation of hydrogen peroxide.

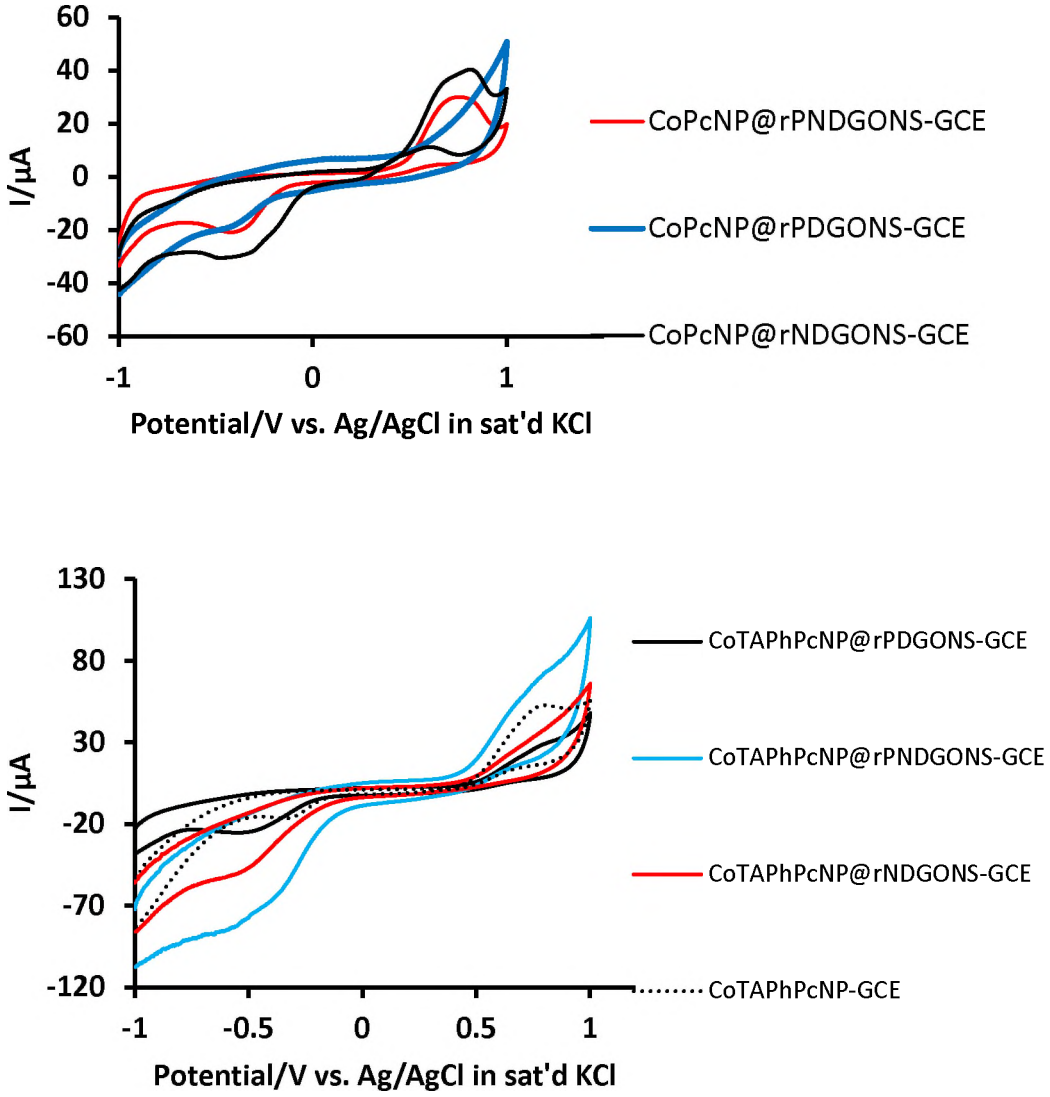

Fig. 5.4. Cyclic voltammograms of selected modified electrodes in 1 mM hydrogen peroxide in pH 7 buffer.

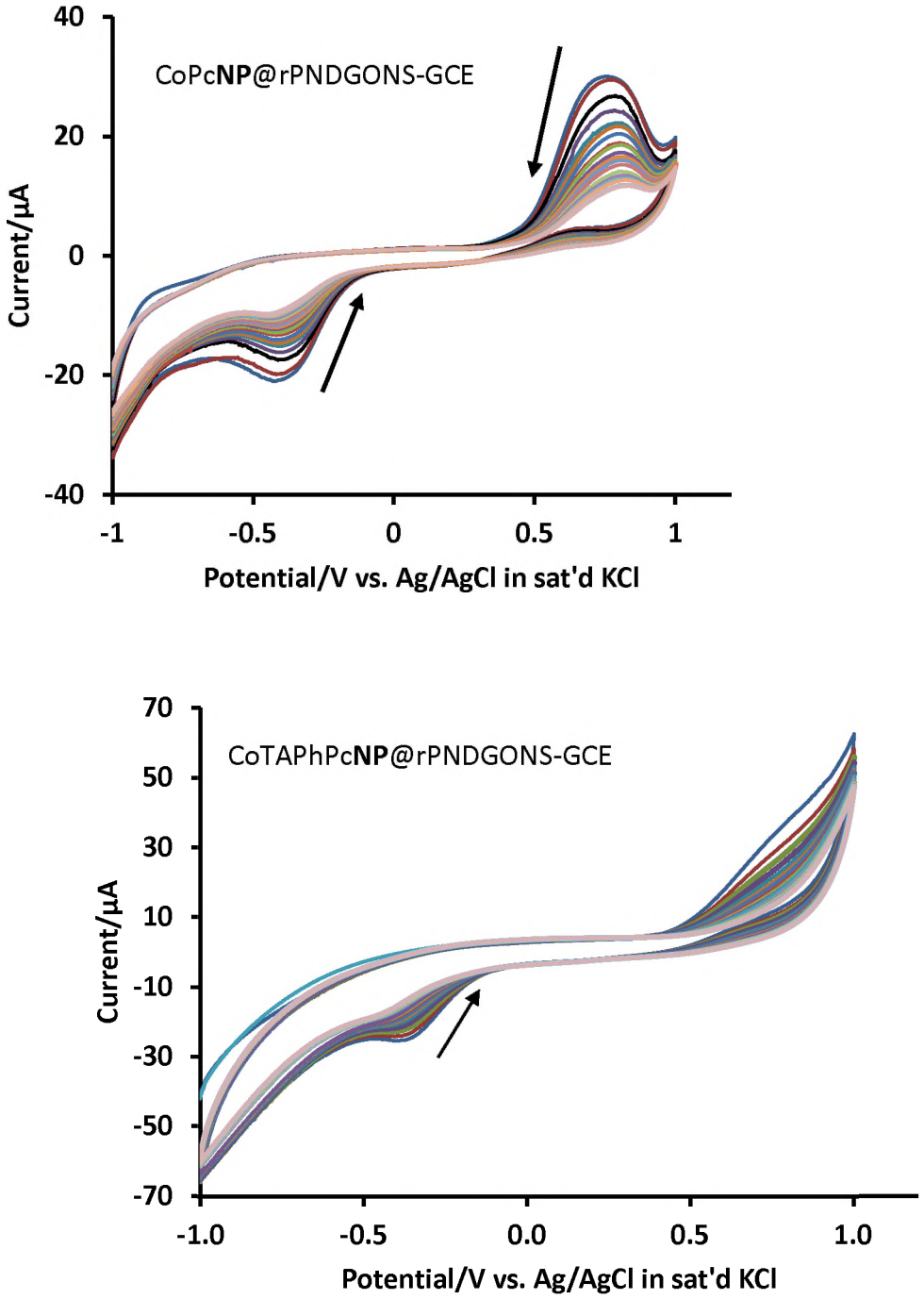

Fig. 5.5. Cyclic voltammogrammes (20 successive scans) in 1 mM hydrogen peroxide. Scan rate of 100 mV/s. pH = 7 buffer.

5.2.1.2. Kinetic studies

Only two probes were evaluated for oxidation detection as the others either showed an unstable oxidation peak or did not show a peak at all. To appreciate the extent of reversibility of the reactions taking place on the modified electrode surface, electrodes were scanned at different rates in 1 mM hydrogen peroxide in pH 7 buffer (**Fig. 5.6** forCoPc**NP**(**3**)@rPNDGONS-GCE as an example, similar behaviour was observed for all the electrodes and the plots are not shown). It was noted that the peak potential was dependent on the scan rate indicative of an irreversible reaction, **Fig. 5.6(a)**. The linear plot of square root of scan rate versus current, **Fig. 5.6(b)** indicates diffusion control. This is further confirmed by the slope of log $I_p$versus log v with a slope of 0.46 in **Fig 5.6(c)**. The slope of such plot can inform on whether a reaction is diffusion controlled or is dominated by adsorption. For adsorption-dominated reactions, the slope is 1 and 0.5 for diffusion controlled reactions. The value of 0.46 is close to 0.5, hence confirming diffusion control [81]. Diffusion controlled reactions are facile in nature which shows the efficiency of the electrocatalysts developed in this work. The steeper the gradient of the plot of peak current versus the square root of scan rate (**Fig. 5.6(b)**), the faster the reaction on the modified electrode. The gradient of the plots increases in the order (units = $\mu A/(mV.s^{-1})^{½}$: CoPc**NP**(**3**)@rPNDGONS-GCE reduction (1.50) < CoPc**NP**(**3**)@rPNDGONS-GCE oxidation (1.82) < CoPc**NP**(**3**)@rNDGONS-GCE reduction (1.84) < CoPc**NP**(**3**)@rPDGONS-GCE reduction (1.88) = CoPc**NP**(**3**)@rNDGONS-GCE oxidation (1.88) < CoTAPhPc**NP**(**1**)@rPDGONS-GCE reduction (2.20) <

CoTAPhPc**NP**(**1**)@rNDGONS-GCE oxidation (2.50) < CoTAPhPc**NP**(**1**)@rPNDGONS-GCE reduction (3.74).

It is noteworthy that the CoTAPhPc**NP**(**1**) based electrodes show faster reaction than corresponding CoPc**NP**(**3**) based electrodes. Compare (units = $\mu A/(mV.s^{-1})^{½}$:

(i) CoTAPhPc**NP**(**1**)@rPNDGONS-GCE (reduction, 3.74) with CoPc**NP**(**3**)@rPNDGONS-GCE (oxidation,1.82) and CoPc**NP**(**3**)@rPNDGONS-GCE (reduction,1.50).

(ii) CoTAPhPc**NP**(**1**)@rNDGONS-GCE (oxidation, 2.50) with CoPc**NP**(**3**)@rNDGONS-GCE (reduction,1.84) and CoPc**NP**(**3**)@rNDGONS-GCE (oxidation,1.88).

(iii) CoTAPhPc**NP**(**1**)@rPDGONS-GCE (reduction, 2.20) with CoPc**NP**(**3**)@rPDGONS-GCE (reduction,1.88).

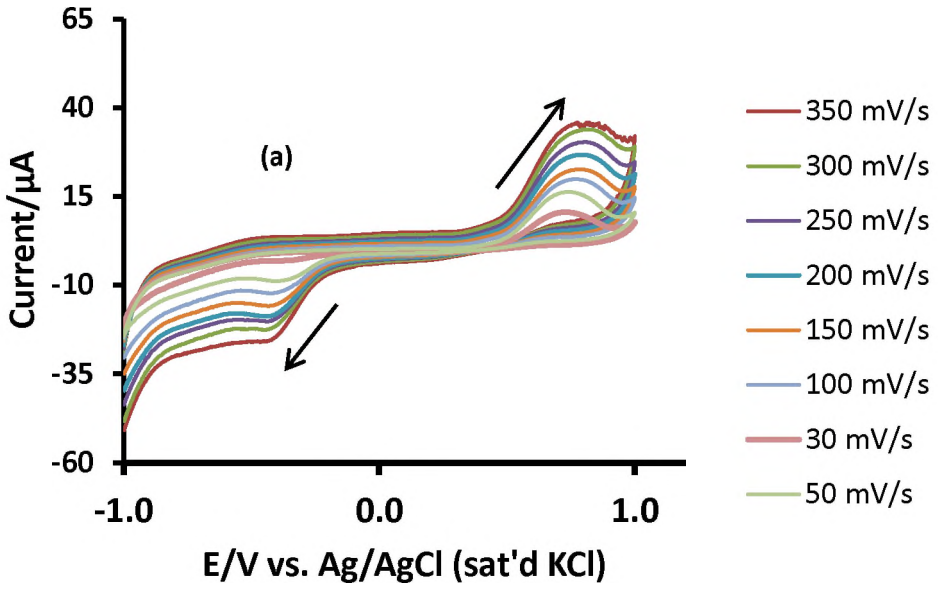
65
40
15
-10
-35
-60
Current/µA
(a)
-1.0
0.0
1.0
E/V vs. Ag/AgCl (sat'd KCl)
350 mV/s
300 mV/s
250 mV/s
200 mV/s
150 mV/s
100 mV/s
30 mV/s
50 mV/s

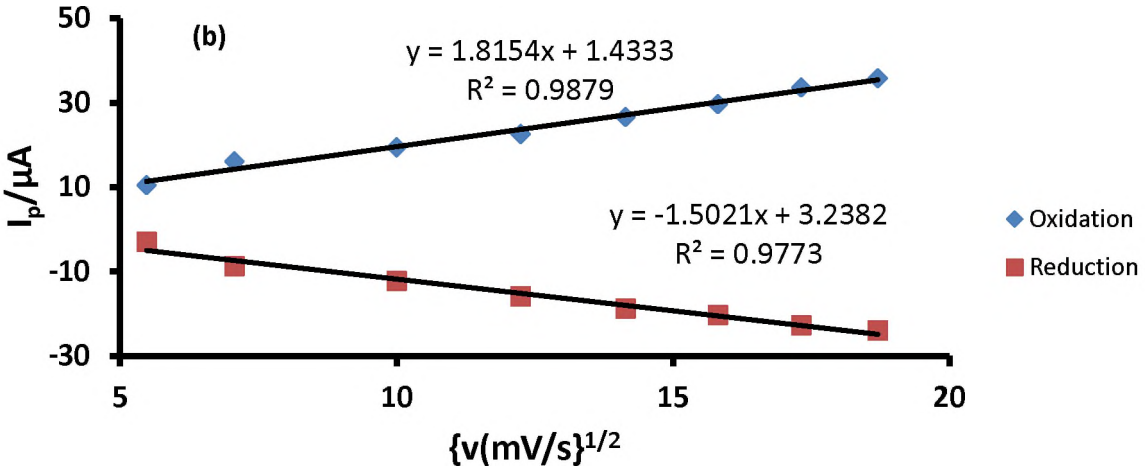
50
30
10
-10
-30
I_p/µA
(b)
y = 1.8154x + 1.4333
R² = 0.9879
y = -1.5021x + 3.2382
R² = 0.9773
5
10
15
20
{v(mV/s}$^{1/2}$
Oxidation
Reduction

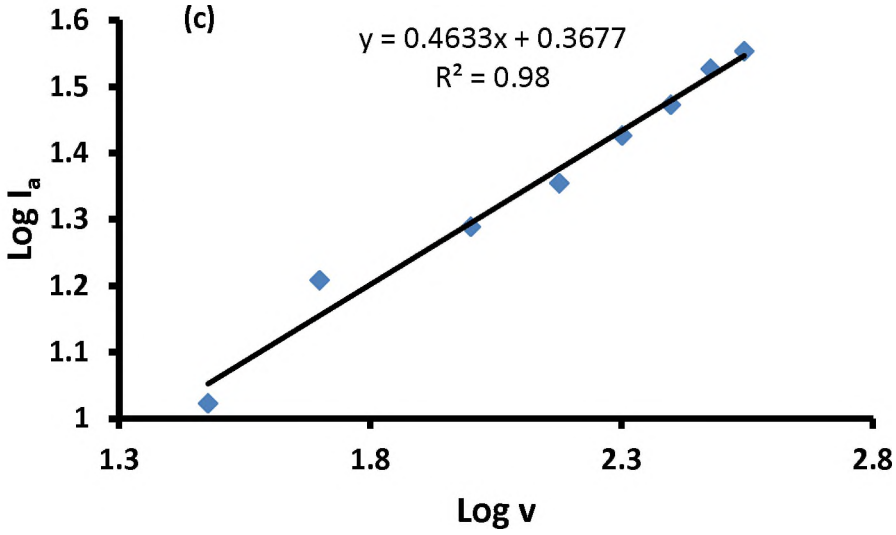
1.6
1.5
1.4
1.3
1.2
1.1
1
Log I_a
(c)
y = 0.4633x + 0.3677
R² = 0.98
1.3
1.8
2.3
2.8
Log v

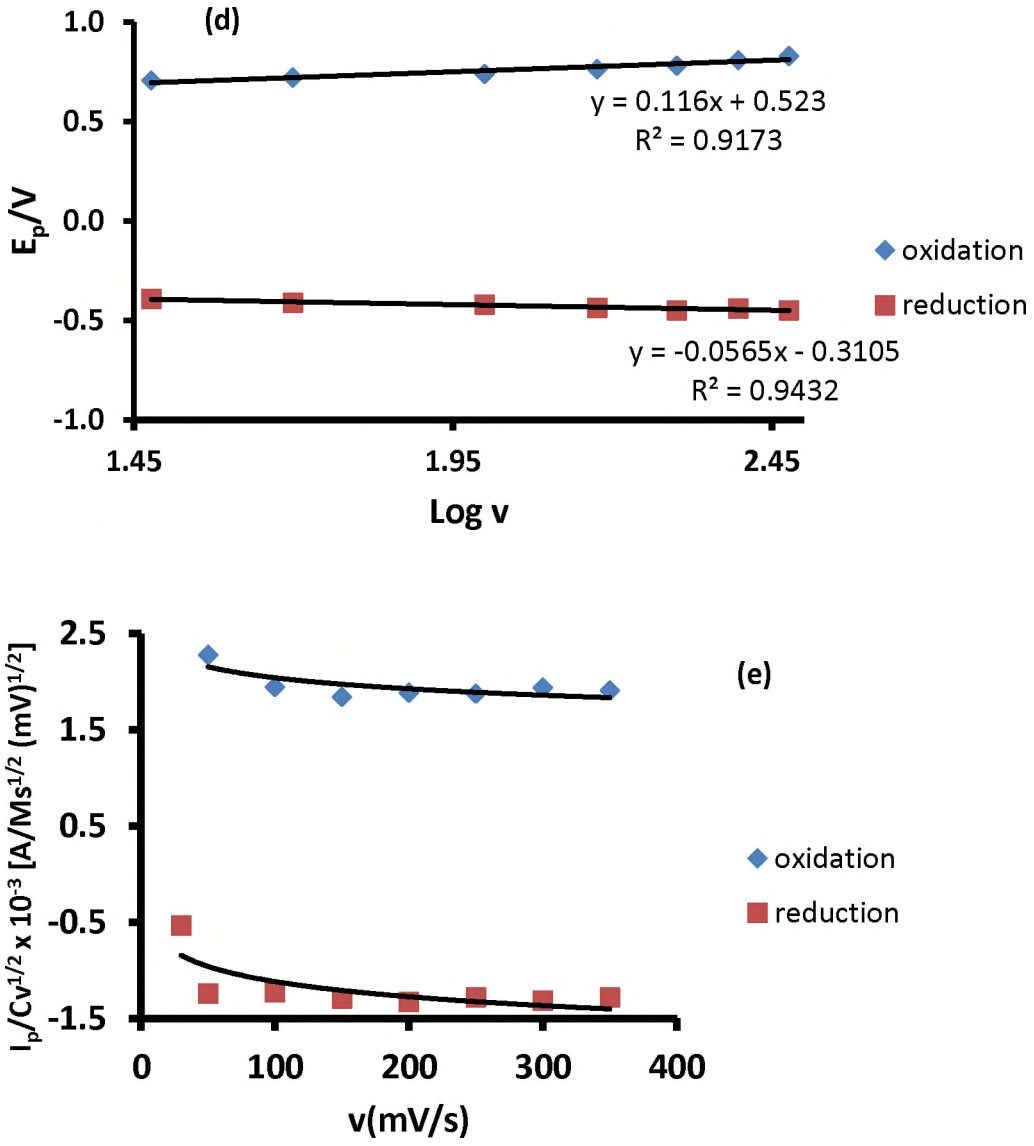

Fig. 5.6. Cyclic voltammograms at different scan rates (a) and corresponding plots of (b) peak currents vs. $v^{1/2}$, (c) log current vs log v, (d) E_p vs log v and (e) $i_p/v^{½}C$ for CoPc**NP**(**3**)@rPNDGONS-GCE. 1 mM hygrogen peroxide in pH 7 buffer.

Irreversible diffusion controlled electrochemical reactions are governed by **Eqn 5.1**[160].The plot of E_p versus log v (**Fig. 5.6(d)**) gave linear relationships with Tafel slopes ranging from 50 mV/decade to 366 mV/decade, **Table 5.4**. Tafel slopes higher than 120 mV/decade have no kinetic meaning. It is noteworthy that Tafel slopes for CoTAPhPc**NP**(**1**) based electrodes are lower

compared to those of the corresponding CoPc**NP**(**3**) based electrodes except for rNDGONS. The oxidation reactions showed the highest Tafel slopes suggesting follow up chemical reactions after the electrocatalytic reaction. The shape of the plots of $I_p/v^{½}C$ vs. v confirms chemical complication during electrocatalytic oxidation of hydrogen peroxide on the surface of CoPc**NP**(**3**)-rPNDGONS-GCE electrode, **Fig. 5.6**(**e**)[174].

Table 5.4. Catalytic rate constants and Tafel slopes of **complex 1** and **3** based electrodes

Electrode	**Tafel Slope (mV/decade)**	**k ($M^{-1}s^{-1}$)**
Oxidation		
CoPc**NP**(**3**)-GCE	366	6.38×10^5
CoPc**NP**(**3**)@rNDGONS-GCE	268	2.987×10^4
CoPc**NP**(**3**)@rPDGONS-GCE	79	6.44×10^2
CoPc**NP**(**3**)@rPNDGONS-GCE	232	2.663×10^5
Reduction		
CoPc**NP**(**3**)-GCE	319	7.11×10^2
CoPc**NP**(**3**)@rNDGONS-GCE	118	9.16×10^4
CoPc**NP**(**3**)@rPDGONS-GCE	79	6.435×10^2
CoPc**NP**(**3**)@rPNDGONS-GCE	113	9.898×10^2
CoTAPhPc**NP**(**1**)-GCE	219	8.69×10^2
CoTAPhPc**NP**(**1**)@rGONS-GCE	92	6.1×10^1
CoTAPhPc**NP**(**1**)@rBDGONS-GCE	59	8.9×10^1
CoTAPhPc**NP**(**1**)@rNDGONS-GCE	187	1.0×10^3
CoTAPhPc**NP**(**1**)@rPDGONS-GCE	50	6.003×10^2
CoTAPhPc**NP**(**1**)@rPNDGONS-GCE	82	2.904×10^3

[a] "@" = Pc adsorbed onto the nanomaterials; "r" in front of GONS = reduced; if no "r", the GONS were not reduced.

To confirm the adsorptive nature of hydrogen peroxide, reaction intermediates or its oxidation products on the electrode surface, linear sweep voltammetry was done for the anodic reaction of CoPc**NP**(**3**)@rPNDGONS-GCE and cathodic reactions of CoTAPhPc**NP**(**1**)@rNDGONS-GCE(as examples since all electrodes showed similar behaviour) in 1 mM hydrogen peroxide (**Fig. 5.7A,** CoPc**NP**(**3**)@rPNDGONS-GCE as example). The Langmuir adsorption theory was applied and a plot of the ratio of hydrogen peroxide concentration to catalytic current against concentration of hydrogen peroxide was linear (**Fig. 5.7B, Eqn 5.7** [175]) which is indicative of adsorption further consolidating the observed high Tafel slopes.

$$\frac{[H_2O_2]}{I_{cat}} = \frac{1}{\beta I_{max}} + \frac{[H_2O_2]}{I_{max}} \qquad 5.7$$

Where β is the adsorption equilibrium constant, I_{max} is the maximum current and I_{cat} is the catalytic current. From the slope and the intercept of **Fig. 5.7B**, the adsorption equilibrium constants β were established to be 3.7 x 10^2 M^{-1} and 1.26 x 10^3 M^{-1} for the anodic reaction of CoPc**NP**(**3**)@rPNDGONS-GCE and cathodic reactions of CoTAPhPc**NP**(**1**)@rNDGONS-GCE respectively. Using **equation 5.8**, which relates Gibbs energy (ΔG) changes to the adsorption equilibrium constant β, were found to be -14.84 kJ mol^{-1} and -17.69 kJ mol^{-1} for CoPc**NP**(**3**)@rPNDGONS-GCE and CoTAPhPc**NP**(**1**)@rNDGONS-GCE respectively, These values are comparable to those reported elsewhere for high Tafel slopes [175].

$$\Delta G^{\circ} = -RT\ln\beta \qquad 5.8$$

where R is the molar gas constant and T is room temperature.

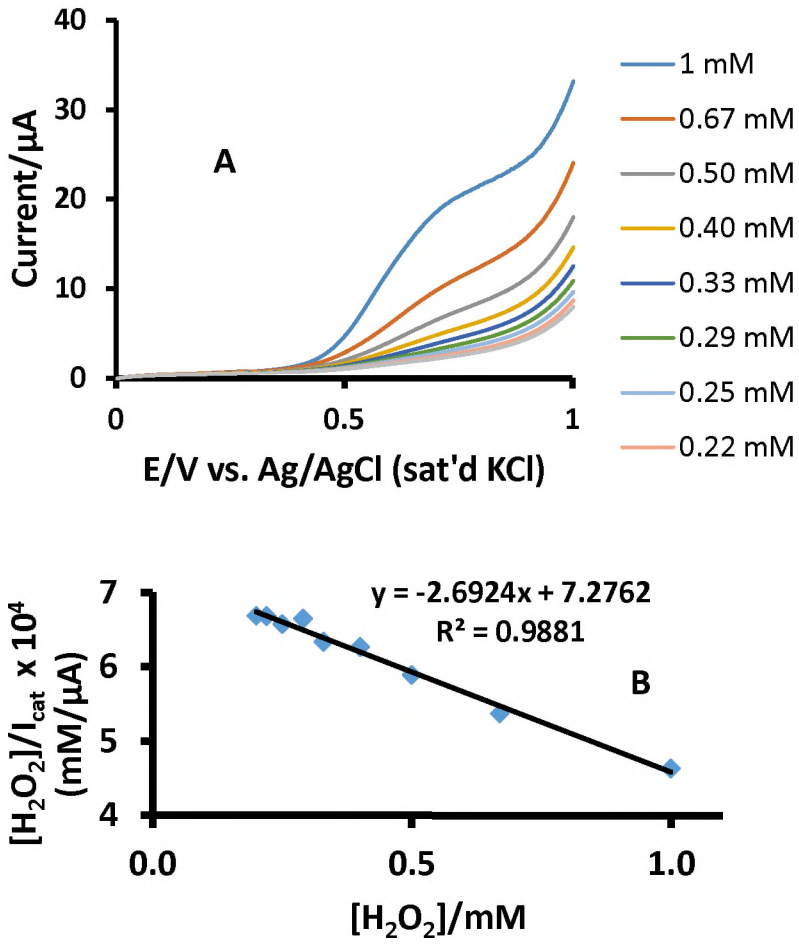

Fig. 5.7. (A) Linear sweep voltammograms and (B) Langmuir adsorption isotherm plot for CoPc**NP**(**3**)@rPNDGONS-GCE. pH 7 buffer.

5.2.1.3. Chronoamperometry studies.

To evaluate the sensitivity and catalytic rate constants for the modified electrode, chronoamperometry studies were performed, **Fig. 5.8**. CoTAPhPc**NP**(**1**)@rNDGONS-GCE is used as an example, **Fig. 5.8** (similar plots were obtained for the rest of the electrodes hence are not shown). The values of limit of detection (LOD) were calculated as described above using

the inserts in **Fig. 5.8A**. Most electrodes showed LODs in the nano molar range which is a significant improvement to literature values [143,175–179] as shown in **Table 5.5.** For CoTAPhPc**NP** (**1**), N doping (as compared to B doping) improves the effect of graphene on the electrocatalytic activity of phthalocyanines. When pristine rGONS are employed together with CoTAPhPc**NP**(**1**), there is lower sensitivity for the detection of hydrogen peroxide.It is also noteworthy that co-doped GONS result in improved LOD as compared to single element doping. The limits of detection reported here are very remarkable since hydrogen peroxide only become toxic in the body at concentrations above 50 μM [104,180]. In addition, the significance of the probes in this section is that oxidation of hydrogen peroxide was employed. Oxidation does not suffer from oxygen reduction, which is the major interferent in hydrogen peroxide detection, resulting in improved detection limits.

Plotting the ratio of catalytic currents and buffer currents (I_{cat}/I_{buf}) against the square root of time ($t^{½}$), **equation 5.2** [169], produced linear relationships of varying gradients for different concentrations, **Fig. 5.8b**. The catalytic currents during the rapid decay period are dominated by the rate of either the electrooxidation reaction or electro reduction reaction of hydrogen peroxide.

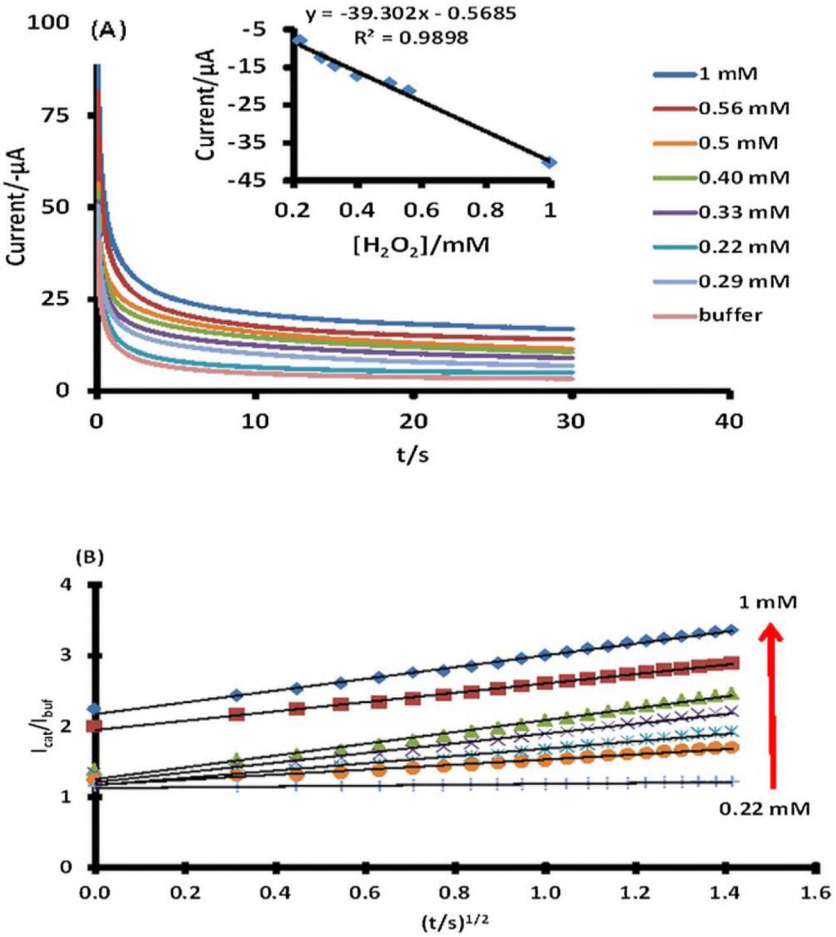

Fig. 5.8. (A) Chronoamperograms (insert = dependence of concentration on current), (B) Plots of I_{cat}/I_{buf} versus $t^{1/2}$ (1 mM, 0.56 mM, 0.5 mM, 0.4 mM, 0.33 mM, 0.29 mM, 0.22 mM, at -0.48 V.) for CoTAPhPc**NP**(**1**)@rNDGONS-GCE.

Plotting the square of the slopes (from **Fig. 5.8b**) against the respective concentrations gave linear plots whose slope is equal to πk where k is the rate constant (figures not shown, but represented by equations **5.9 – 5.18**).

Oxidation

CoPc**NP**(**3**)-rNDGONS-GCE

$$y = 93.848[H_2O_2]\left(\frac{s^{-1}}{mM}\right) - 17.356s^{-1}, R^2 = 0.9788 \quad 5.9$$

CoPc**NP**(**3**)-rPNDGONS-GCE

$$y = 836.57[H_2O_2]\left(\frac{s^{-1}}{mM}\right) - 178.25s^{-1}, R^2 = 0.9696 \quad 5.10$$

Reduction

CoPc**NP**(**3**)-rNDGONS-GCE

$$y = 4.5406[H_2O_2]\left(\frac{s^{-1}}{mM}\right) - 0.9343s^{-1}, R^2 = 09199 \quad 5.11$$

CoPc**NP**(**3**)-rPDGONS-GCE

$$y = 2.0216[H_2O_2]\left(\frac{s^{-1}}{mM}\right) - 0.3848s^{-1}, R^2 = 09401 \quad 5.12$$

CoPc**NP**(**3**)-rPNDGONS-GCE

$$y = 7.4329[H_2O_2]\left(\frac{s^{-1}}{mM}\right) - 2.3729s^{-1}, R^2 = 0977 \quad 5.13$$

CoTAPhPc**NP**(**1**)-rPNDGONS-GCE

$$y = 9.122[H_2O_2]\left(\frac{s^{-1}}{mM}\right) - 1.2829s^{-1}, R^2 = 09723 \quad 5.14$$

CoTAPhPc**NP**(**1**)-rPDGONS-GCE

$$y = 1.8858[H_2O_2]\left(\frac{s^{-1}}{mM}\right) - 0.2576s^{-1}, R^2 = 09797 \quad 5.15$$

CoTAPhPc**NP**(**1**)-rNDGONS-GCE

$$y = 3.095[H_2O_2](\frac{s^{-1}}{mM}) - 0.7633s^{-1}, R^2 = 0.9975 \quad 5.16$$

CoTAPhPc**NP**(**1**)-rBDGONS-GCE

$$y = 0.2808[H_2O_2](\frac{s^{-1}}{mM}) - 0.13696s^{-1}, R^2 = 0.9685 \quad 5.17$$

CoTAPhPc**NP**(**1**)-rGONS-GCE

$$y = 0.1918[H_2O_2](\frac{s^{-1}}{mM}) - 0.0092, R^2 = 0.9981 \quad 5.18$$

The k values are larger for oxidation compared to reduction. For the reduction, CoPc**NP**(**3**)-rNDGONS-GCE gave the largest k value, **Table 5.4**. This compares very well with those reported by Ganesan and Ramaraj [181] who obtained catalytic rate constants ranging from 8 x 10^1 $M^{-1}s^{-1}$ to 1.29 x 10^3 $M^{-1}s^{-1}$ on poly (NiIIteta) modified electrodes.Thus N and P doping (as compared to B doping) improves the effect of graphene on the electrocatalytic activity of phthalocyanines. When pristine rGONS is employed together with CoTAPhPc**NP**(**1**), there is lower sensitivity for the detection of hydrogen peroxide.

Table 5.5. Comparative LODs for the electrocatalyzed reactions of hydrogen peroxide using different Complex **1** and **3** catalytic systems.

[a] Au-polyCoTAPc = polymerised Co tetraamino phthalocyanine; "@" = Pc adsorbed onto the nanomaterials; "/" =a mixture of different nanomaterials; "r" in front of GONS = reduced; if no "r", the GONS were not reduced; CSPE = carbon screen printed electrode; HRP = horse radish peroxidase; FTO = fluorine doped tin oxide

Electrode	Reaction	pH	LOD/nM	Ref
CoPc**NP**(**3**)@rNDGONS-GCE	oxidation	7	2.95	This work
	reduction	7	9.73	This work
CoPc**NP**(**3**)@rPDGONS-GCE	reduction	7	25.8	This work
CoPc**NP**(**3**)@rPNDGONS-GCE	oxidation	7	4.48	This work
	reduction	7	7.84	This work
CoTAPhPc**NP**(**1**)@rGONS-GCE	reduction	7	400	This work
CoTAPhPc**NP**(**1**)-rNDGONS-GCE	reduction	7	8.2	This work
CoTAPhPc**NP**(**1**)@rPDGONS-GCE	reduction	7	7.36	This work
CoTAPhPc**NP**(**1**)@rPNDGONS-GCE	reduction	7	1.21	This work
CoTAPhPc**NP**(**1**)@rBDGONS-GCE	reduction	7	95	This work
Pt-Au/rGONS/GCE	oxidation	7.4	310	[176]
CoPc(**3**)-CSPE	oxidation	7.5	71	[177]
PussianBlue-CSPE	oxidation	7.5	1300	[177]
Os-wired HRP-CSPE	oxidation	7.5	13.7	[177]
Nanoporous platinum–cobalt alloy		7	100	[175]
Prussian blue-based artificial peroxidase		7.4	1000	[178]
Prussian blue- modified FTO		7.4	50 000	[179]
GCE-polyCoTAPc		7.4	145	[143]
Au-polyCoTAPc		7.4	364	[143]

5.2.2. Complex 1 with AuNRs-GONS

5.2.2.1. Cyclic voltammetry

As in the previous section, nanoprobes developed in this section are characterised by both electrooxidation and electro reduction of hydrogen peroxide (**Fig. 5.9**). However, with successive cyclisation, the oxidation peak disappears due toelectrode fouling (**Fig 5.10,** using CoTAPhPc**NP**(**1**)@rSDGONS-AuNRs(linked)-GCE and CoTAPhPc**NP**(**1**)@AuNRs-rSNDGONS(seq)-GCE as examples), while the reduction peak is still present after 20 scans. For this reason, only the reduction peaks were further evaluated in this section. The intense reverse oxidation peak (which appears as a dip on return scan) observed during the cathodic scan, is due to the reformation of the active CoTAPhPc(**1**)catalyst on the electrode surface, which oxidizes the hydrogen peroxide molecules [182]. This was also observed for L-cysteine **Fig. 5.1.**

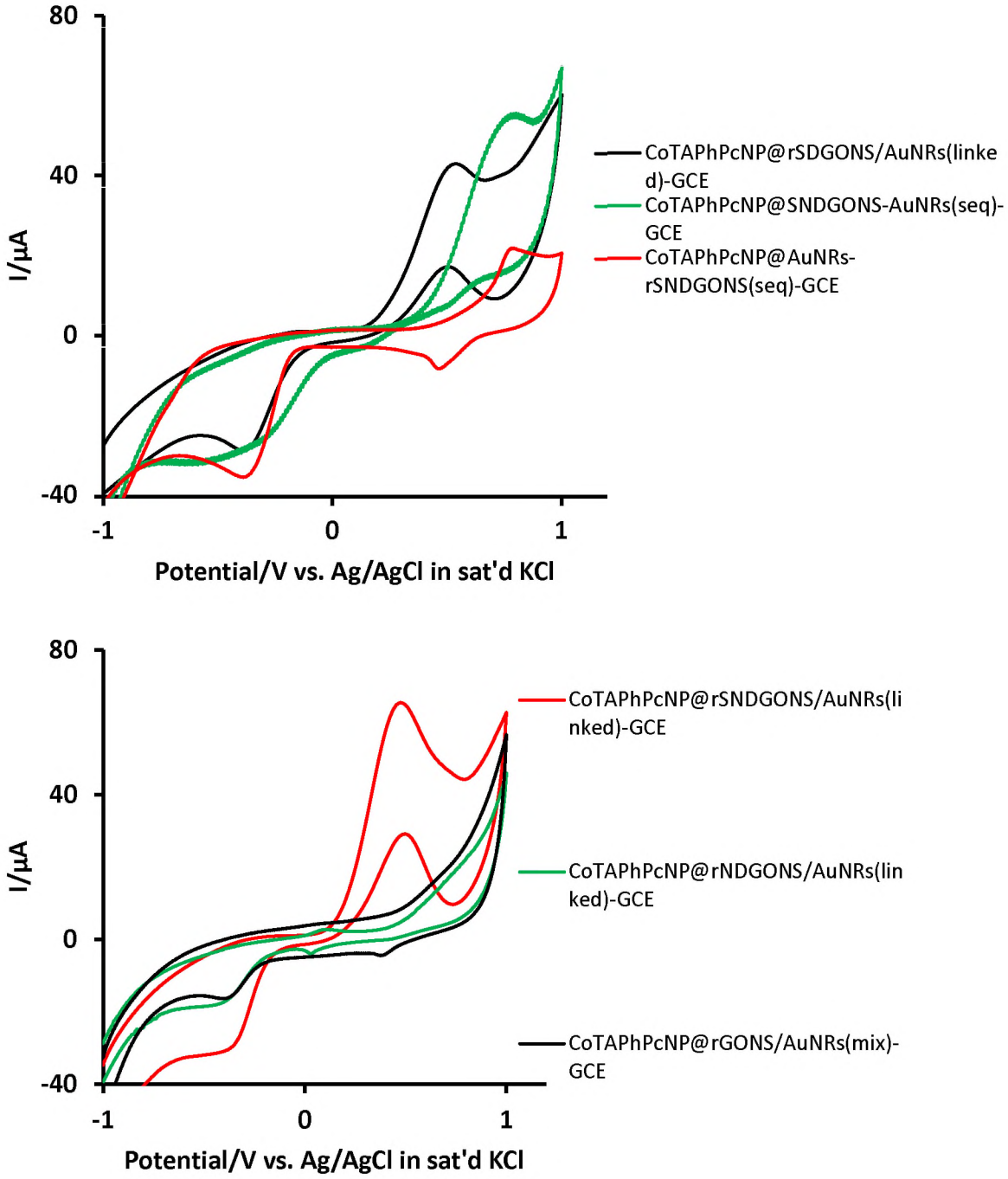

Fig 5.9 Cyclic voltammograms of selected modified electodes in 1 mM hydrogen peroxide, in pH 7 buffer. Scan rate 100 mV/s.

The reduction potentials ranged from -0.29 V to -0.64 V (**Table 5.6, Fig. 5.9**) which are in the range of literature reported values [171–173,183]. Using the hydrogen peroxide reduction potentials, we can make the following observation:

(1) The least negative reduction potentials were observed on CoTAPhPc**NP**(**1**)-AuNRs(linked)-GCE and AuNRs-GCE, both at -0.29 V, hence showing the importance of AuNRs in lowering overpotetials for H_2O_2 reduction.

(2) The presence of pristine or doped GONS on their own (in the absence of AuNRs) does not result in less negative potential values for H_2O_2 on complex **1**. Compare CoTAPhPc**NP**(**1**)@rSNDGONS-GCE (-0.41 V); CoTAPhPc**NP**(**1**)@rNDGONS-GCE (-0.48); CoTAPhPc**NP**(**1**)@rSDGONS-GCE (-0.50); and CoTAPhPc**NP**(**1**)@rGONS-GCE (-0.39) with CoTAPhPc**NP**(**1**)-GCE (-0.35 V).

(3) The H_2O_2 reduction potentials on complex **1** in the presence of pristine and doped GONS are less negative in the presence of AuNRs. Compare CoTAPhPc**NP**(**1**)@rSNDGONS-AuNRs(linked)-GCE (-0.37 V) with CoTAPhPc**NP**(**1**)@rSNDGONS-GCE (-0.41 V); CoTAPhPc**NP**(**1**)@rNDGONS-AuNRs(linked)-GCE (-0.45 V) with CoTAPhPc**NP**(**1**)@rNDGONS-GCE (-0.48V); and CoTAPhPc**NP**(**1**)@rSDGONS-AuNRs(linked)-GCE (-0.39 V) with CoTAPhPc**NP**(**1**)@rSDGONS-GCE (-0.50V). This shows that AuNRs results in lowering of potential to less negative values.

(4) Co-doping results in less negative reduction potentials for H_2O_2 compared to individual doping. Compare CoTAPhPc**NP**(**1**)@rSNDGONS-AuNRs(linked)-GCE (-0.37 V) with CoTAPhPc**NP**(**1**)@rSDGONS-

AuNRs(linked)-GCE (-0.39 V) and CoTAPhPc**NP**(**1**)@rNDGONS-AuNRs(linked)-GCE (-0.45 V). Also compare CoTAPhPc**NP**(**1**)@rSNDGONS-GCE (-0.41 V) with CoTAPhPc**NP**(**1**)@rSDGONS-GCE (-0.50 V) and CoTAPhPc**NP**(**1**)@rNDGONS-GCE (-0.48 V).

(5) Sequential doping when rSNDGONS are placed first on the electrode in CoTAPhPc**NP**(**1**)@AuNRs-rSNDGONS(seq)-GCE (-0.39 V) has a slightly more negative potential than when the two are linked in CoTAPhPc**NP**(**1**)@rSNDGONS-AuNRs(linked)-GCE (-0.37 V)

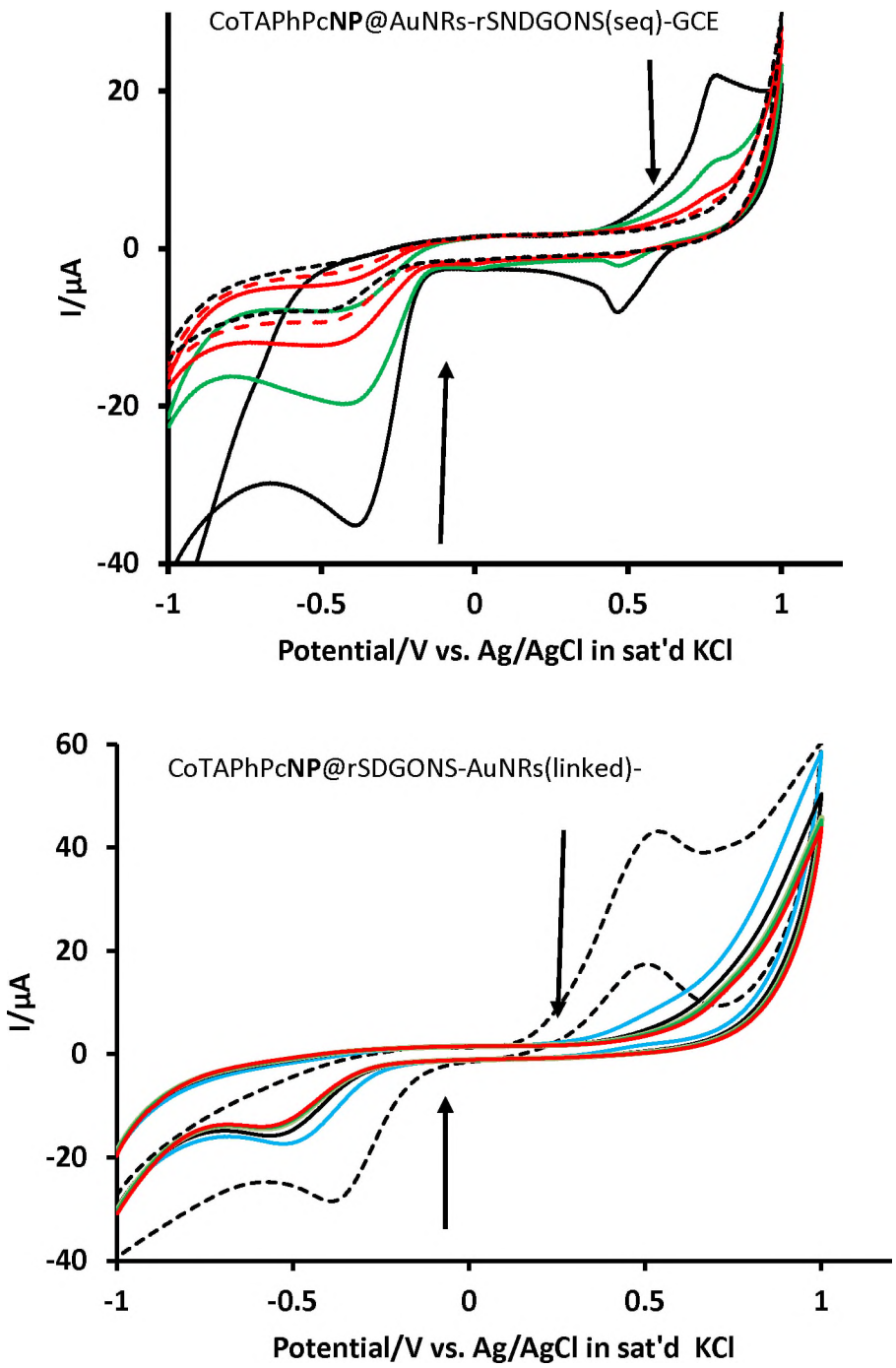

Fig 5.10 Cyclic voltamogrammes (20 successive cycles, only 1, 5, 10, 15 and 20th scan shown) in 1 mM hydrogen peroxide. Scan rate of 100 mV/s. pH = 7 buffer.

Table 5.6. Detection potential and currents for the Complex 1, S-N doped GONS modified electrodes.

[a] "@" = Pc adsorbed onto the nanomaterials; "/" =a mixture of different nanomaterials; "-" when

Modified GCE	**Tafel slopes**	**Slope of Ip vs $v^{1/2}$/ μA(mV s)$^{-1/2}$**	**E/V (H_2O_2) reduction pH 7 buffer**	**Background corrected currents/μA H_2O_2 reduction**
Bare GCE	-	-	-0.58	3.85
rSNDGONS-GCE	-	-	-0.64	14.15
AuNRs-GCE	-	-	-0.29	20.07
rGONS-AuNRs(linked)-GCE	-	-	-0.39	9.70
rSDGONS-AuNRs(linked)-GCE	-	-	-0.42	4.44
rNDGONS-AuNRs(linked)-GCE	-	-	-0.54	3.10
rSNDGONS-AuNRs(linked)-GCE	-	-	0.40	5.27
CoTAPhPc**NP**-GCE	219	-	-0.35	19.31
CoTAPhPc**NP**(**1**)@rGONS-GCE	92	1.77	-0.39	20.01
CoTAPhPc**NP**(**1**)@rGONS/AuNRs(mix)-GCE	310	0.77	-0.38	10.44
CoTAPhPc**NP**(**1**)@rSDGONS-GCE	870	12.55	-0.50	89.41
CoTAPhPc**NP**(**1**)@rNDGONS-GCE	187	-	-0.48	59.33
CoTAPhPc**NP**(**1**)@rSNDGONS-GCE	278	1.38	-0.41	29.04
CoTAPhPc**NP**(**1**)-AuNRs(linked)-GCE	-	-	-0.29	17.29
CoTAPhPc**NP**(**1**)@rSDGONS-AuNRs(linked)-GCE	530	1.51	-0.39	26.86
CoTAPhPc**NP**(**1**)@rNDGONS-AuNRs(linked)-GCE	291	1.32	-0.45	20.56

accompanied by linked = covalent bond; "-" when accompanied by seq = sequential modification; mix

Modified GCE	**Tafel slopes**		**E/V (H_2O_2) reduction pH 7 buffer**	**Background corrected currents/μA H_2O_2 reduction**
CoTAPhPc**NP**(**1**)@rSNDGONS-AuNRs(linked-GCE	90	4.07	-0.37	29.03
CoTAPhPc**NP**(**1**)@rSNDGONS-AuNRs(seq)-GCE	98	3.11	-0.32	26.12
CoTAPhPc**NP**(**1**)@AuNRs-rSNDGONS(seq)-GCE	89	4.47	-0.39	32.62

= mixed before electrode modification; seq = sequentially added to the electrode; "r" in front of GONS = reduced; if no "r", the GONS were not reduced.

The general observations regarding background corrected currents in **Table 5.6** are as follows:

1. In general, the presence of complex **1** resulted in better currents than when the nanomaterials are used alone, suggesting that complex**1** is responsible for catalysis. AuNRs are the exception since currents decrease for CoTAPhPc**NP**(**1**)-AuNRs(linked)-GCE (17.29 μA) compared to AuNRs-GCE (20.07 μA) alone.
2. The presence of doped GONS on their own (in the absence of AuNRs) improves currents. Compare CoTAPhPc**NP**(**1**)@rSNDGONS-GCE (29.04 μA); CoTAPhPc**NP**(**1**)@rNDGONS-GCE (59.33 μA); and CoTAPhPc**NP**(**1**)@rSDGONS-GCE (89.41 μA) with CoTAPhPc**NP**(**1**)-GCE (19.31 μA). For doped GONS, individual S or N doping results in more improved currents compared to S/N co-doping. Compare CoTAPhPc**NP**(**1**)@rSNDGONS-GCE (29.04 μA) with

CoTAPhPc**NP**(**1**)@rNDGONS-GCE (59.33 μA) or CoTAPhPc**NP**(**1**)@rSDGONS-GCE (89.41 μA). As explained above for P/N doping, this may be attributed to higher oxygen content of rSNDGONS (8.62 %) compared to rNDGONS (1.29 %) and rSDGONS (1.79 %) according to XPS data (**Table. 3.2**).

3. The reduction currents for CoTAPhPc**NP**(**1**) in the presence of pristine GONS are not improved by the presence of AuNRs. Compare CoTAPhPc**NP**(**1**)@rGONS/AuNRs(mix)-GCE (10.44 μA) with CoTAPhPcNP(**1**)@rGONS-GCE (20.01μA). This is also observed for N or S doped GONS in CoTAPhPc**NP**@rNDGONS-AuNRs(linked)-GCE (20.56 μA) and CoTAPhPc**NP**(**1**)@rSDGONS-AuNRs(linked)-GCE (26.86μA), where the presence of AuNRs, negatively affects the current compared to CoTAPhPc**NP**(**1**)@rNDGONS-GCE (59.33 μA) and CoTAPhPc**NP**(**1**)@rSDGONS-GCE (89.41 μA), respectively (without AuNRs). There is no advantage of AuNRs on the reduction currents in the presence of S/N co-doped GONS. Compare CoTAPhPc**NP**(**1**)@rSNDGONS-GCE (29.04 μA) with CoTAPhPc**NP**(**1**)@rSNDGONS-AuNRs(linked)-GCE (29.03 μA).
4. Sequential addition in CoTAPhPc**NP**(**1**)@AuNRs-rSNDGONS(seq)-GCE (32.62 μA) where rSNDGONS is placed first on the electrode showed much better detection currents than when AuNRs are placed first in CoTAPhPc**NP**(**1**)@rSNDGONS-AuNRs(seq)-GCE (26.12 μA) or when rSNDGONS are first linked with AuNRs in

CoTAPhPc**NP**(**1**)@rSNDGONS-AuNRs(linked)-GCE (29.03 μA) or in the absence of AuNRs CoTAPhPc**NP**(**1**)@rSNDGONS-GCE (29.04 μA).

5.2.2.2. Kinetic studies

To investigate the reversibility of the electrocatalytic behaviour of the modified electrode surfaces, cyclic voltammetry was done at different scan rates, **Fig 5.11A** {using CoTAPhPc**NP**(**1**)@rSNDGONS-AuNRs(linked)-GCE as an example}. It was noted that the peak potential shifted with change in scan rates, evidence for an irreversible reaction. Since the oxidation peak showed significant fouling in the presence of hydrogen peroxide, only the reduction peaks were investigated for all the electrode surfaces as discussed above.

Plots of E_p vs log υ are shown in **Fig. 5.11B** (for CoTAPhPc**NP**(**1**)@rSNDGONS-AuNRs(linked)-GCE as an example). The electrodes reported here are characterised by high Tafel slopes expressing a significant extent of irreversibility, **Table 5.6**. The values of the Tafel slopes ranged from 89 V to 870 mV/decade.

The abnormally high Tafel slopes (above the normal 60-120 mV decade^{-1}) are suggestive of chemical complication whereby the electrocatalytic reaction is followed by adsorption of intermediates or products on the electrode surface [184,185]. Such complication is usually evidenced by electrode fouling as demonstrated in **Fig 5.10**. Tafel slopes for sequentially modified electrodes (CoTAPhPc**NP**(**1**)@AuNRs–SNDGONS(seq)-GCE and CoTAPhPc**NP**(**1**)@SNDGONS-AuNRs(seq)-GCE) as well as for

CoTAPhPc**NP**(**1**)@SDGONS-AuNRs(linked)-GCE are within the 60-120 mV decade^{-1} range, suggesting less chemically complicated electrode reactions.

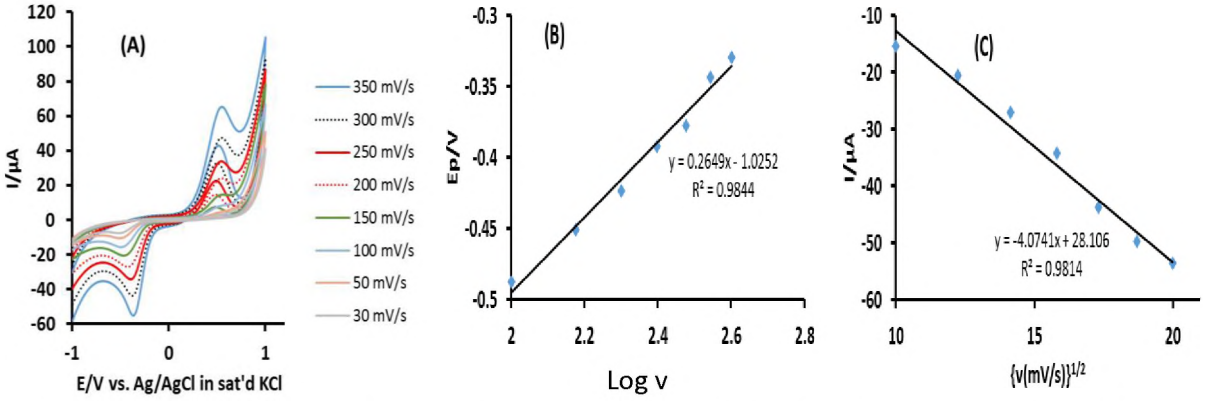

Fig. 5.11. (A) cyclic voltammograms for the detection hydrogen peroxide at different scan rates, (B) plot of peak potential vs. log v and (C) plot of Ip vs. $v^{1/2}$, in 1 mM hydrogen peroxide. pH 7 buffer. Electrode: CoTAPhPc**NP**(**1**)@SNDGONS-AuNRs(linked)-GCE. Scan rate 100 mV/s

The plots of the square root of scan rates against currents displayed a linear relationship showing that the reaction is diffusion controlled, **Fig. 5.11C**. As discussed above, diffusion controlled reactions are facile in their nature and this is expected of an efficiently catalysed reaction. Also as stated abovethe gradient of such plots can therefore be used as a measure of efficiency of the catalyst. For a selection of the modified electrodes, the gradient of the plots are shown in **Table 5.6**. These observations show that heteroatom doped graphene oxide nanosheets perform better than pristine graphene oxide nanosheets.

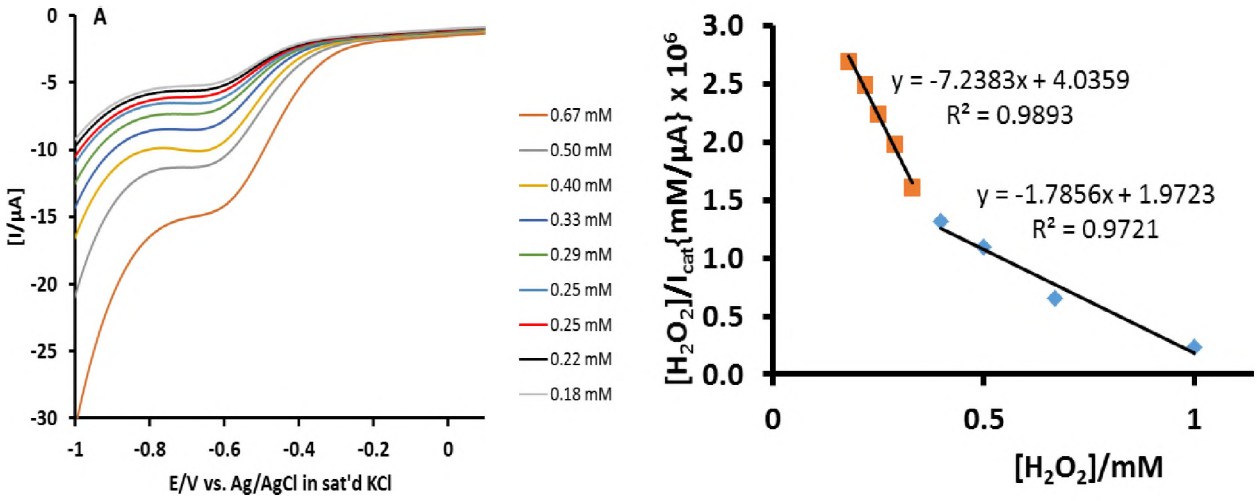

Fig. 5.12. (A) Linear sweep voltammograms and (B) Langmuir adsorption isotherm plot for CoTAPhPc**NP**(**1**)@rSDGONS-AuNRs(linked)-GCE in 1 mM hydrogen peroxide. pH 7 buffer. Scan rate 100 mV/s

Since the probes under study showed abnormally high Tafel slopes coupled with significant electrocatalytic surface passivation, linear sweep voltammetry (**Fig. 5.12A)** was done for the cathodic reaction of CoTAPhPc**NP**(**1**)@rSDGONS-AuNRs(linked)-GCE (as an example since it had an abnormally high Tafel slope at 530 mV decade^{-1}) in hydrogen peroxide in order to understand the adsorptive behaviour of the electrodes. Linear plots of the ratio of hydrogen peroxide concentration to catalytic current against concentration of hydrogen peroxide was obtained (**Fig. 5.12B,Equation 5.7**) showing adsorption behaviour further consolidating the abnormally high Tafel slope.

The electrocatalytic reduction of hydrogen peroxide showed different mechanisms at low and high concentrations of hydrogen peroxide as shown by two linear plots in these respective regions (**Fig. 5.12B**). The slopes and the intercepts of these respective slopes (**Fig. 5.12B)** were then used to deduce the Langmuir adsorption equilibrium constants (β = 1.79 x 10^3 M^{-1} and 1 x

10^3 M^{-1}) for low and high concentrations, respectively.The two adsorption equilibrium constants may be attributed to different adsorptive behavior of either the intermediate or the products of catalysis on the modified electrode surface with change in analyte concentration. These equilibrium constants culminate to Gibbs energy changes (ΔG^o) (using **equation 5.8**) due to adsorption of values -18.55 $kJmol^{-1}$ and -17.35 $kJmol^{-1}$, for low and high concentrations, respectively similar to the values reported in the previous section. These values are comparable to those reported elsewhere for high Tafel slopes [175].

Despite confirming chemical complication at the electrode surface, the negative ΔG^o values confirm spontaneous electro reduction of hydrogen peroxide at the surface of the modified electrode confirming the electrocatalytic efficiency of the probe under study.

5.2.2.3. Chronoamperometry studies.

The variation of detection currents with concentrations were investigated by chronoamperometry, **Fig 5.13A.** The limits of detection were calculated as described above and using the insert in **Fig. 5.13A** (using CoTAPhPc**NP**(**1**)@rSNDGONS-AuNRs(linked)-GCE as an example).The following conclusions can be drawn from the LOD value in **Table 5.7** for the composites containing CoTAPhPc**NP**(**1**):

(1) CoTAPhPc**NP**(**1**)-AuNRs(linked)-GCE (linked)-GCE (LOD = 21.1 μM) is the worst performing with the highest LOD among the electrode modifiers reported in this section. AuNRs on their own do not improve

LOD of CoTAPhPc**NP**(**1**)-GCE (LOD = 2.10 μM). Pristine GONS in CoTAPhPc**NP**(**1**)@rGONS-GCE (LOD = 0.40 μM) performs better than AuNRs on their own in CoTAPhPc**NP**(**1**)-AuNRs(linked)-GCE (LOD = 21.1 μM). The combination of AuNRs and pristine GONS in CoTAPhPc**NP**(**1**)@rGONS/AuNRs(mix)-GCE (LOD = 2.76 μM) shows better performance than when AuNRs are alone in CoTAPhPc**NP**(**1**)-AuNRs(linked)-GCE (LOD = 21.1 μM), again confirming the need of combining AuNRs with other nanomaterials.

(2) Nitrogen doping in CoTAPhPc**NP**(**1**)@rNDGONS-GCE (LOD = 0.0082μM) results in more improved LOD than co-doping or rSDGONS in CoTAPhPc**NP**(**1**)@rSNDGONS-GCE (LOD = 0.011 μM) or CoTAPhPc**NP**(**1**)@rSDGONS-GCE (LOD = 0.0091 μM). However it was observed in the previous section that N doping performed worst as compared to P doping in CoTAPhPc**NP**(**1**)@rPNDGONS-GCE (LOD = 0.0012 μM) and CoTAPhPc**NP**(**1**)@rPDGONS-GCE (0.0074 μM) though the order of magnitude was the same**Table 5.5**.

(3) Sequential addition in CoTAPhPc**NP**(**1**)@AuNRs-rSNDGONS(seq)-GCE (0.016μM) where rSNDGONS is placed first on the electrode) showed much better detection limit than when AuNRs are placed first in CoTAPhPc**NP**(**1**)@rSNDGONS-AuNRs(seq)-GCE (0.025 μM), showing the importance of the order in which electrodes are modified.

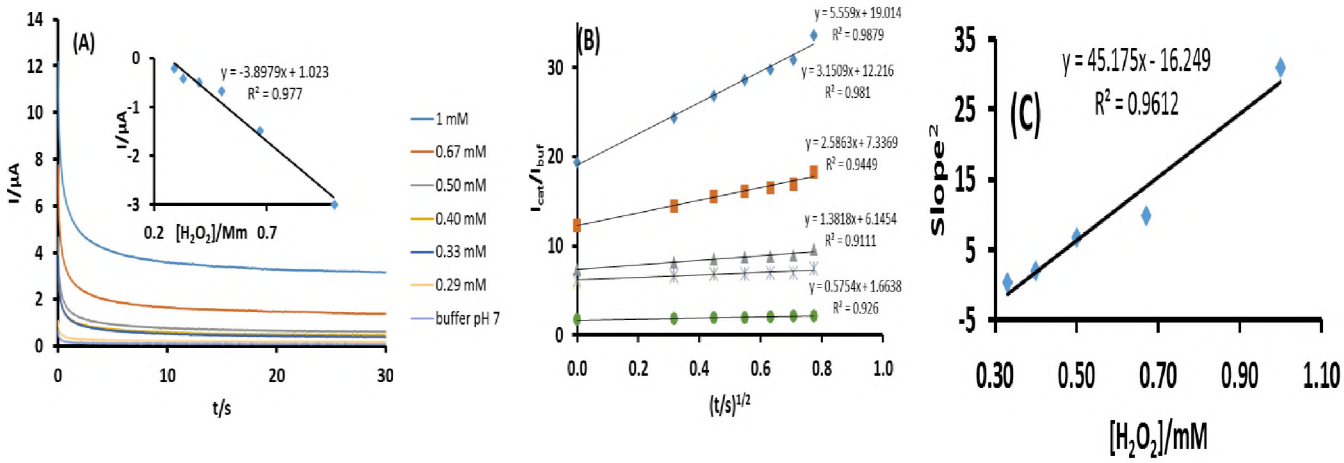

Fig. 5.13. (A) Chronoamperogramms on CoTAPhPc**NP**(**1**)@rSNDGONS-AuNRs(linked)-GCE at different concentrations of hydrogen peroxide, insert = corresponding calibration curve, (B) plots of current ratio versus square root of time, and (C) plots of square of gradients of plots in B versus concentration of hydrogen. pH 7 buffer. Reduction potential – 0.37 V.

Table 5.7. Limits of detection and catalytic rate constants for the cathodic detection of hydrogen peroxide

Modified GCE	**pH**	**LOD/μM**	**k($M^{-1}s^{-1}$)**	**Ref**
CoTAPhPc**NP**(**1**)@**GCE**	7	2.10	8.69 x 10^2	TW
CoTAPhPc**NP**(**1**)@AuNRs-GCE	7	21.2	1.76× 10^2	TW
CoTAPhPc**NP**(**1**)@rGONS-GCE	7	0.40	6.10 × 10^1	TW
CoTAPhPc**NP**(**1**)@rNDGONS-GCE	7	0.0082	1.00 × 10^3	TW
CoTAPhPc**NP**(**1**)@rSDGONS-GCE	7	0.0091	2.74 x 10^3	TW
CoTAPhPc**NP**(**1**)@rGONS-AuNRs(linked)-GCE	7	2.76	5.08 × 10^2	TW
CoTAPhPc**NP**(**1**)@rSDGONS-AuNRs(linked)-GCE	7	0.016	2.81 × 10^3	TW
CoTAPhPc**NP**@rNDGONS-AuNRs(linked)-GCE	7	0.019	6.30 × 10^2	TW
CoTAPhPc**NP**(**1**)@rSNDGONS-AuNRs(linked)-GCE	7	0.012	1.44 × 10^4	TW
CoTAPhPc**NP**(**1**)@AuNRs-rSNDGONS(seq)-GCE	7	0.016	1.52 × 10^4	TW
CoTAPhPc**NP**(**1**)@rSNDGONS-AuNRs(seq)-GCE	7	0.025	2.52 × 10^3	TW
CoTAPhPc**NP**(**1**)@rSNDGONS-GCE	7	0.011	9.14 X 10^2	TW

Modified GCE	**pH**	**LOD/μM**	**k($M^{-1}s^{-1}$)**	**Ref**
CNT-CSPE	7.4	3 100	-	[177]
CoPc-CSPE	7.4	1 300	-	[177]
PB-CSPE	8	0.071		[177]
Oswired HRP-CSPE	13.3	0.014		[177]
GONS/CoPc–COOH	7.4	60	-	[186]
SPAuE–PA–MnTAPc	7.4	0.117	-	[163]

[a]PB-prussian blue; CSPE-carbon screen printed electrode; HRP-horse radish peroxidise; TAPc-tetra amino phthalocyanine; SPAuE-screen printed gold electrode, CNT-carbon nanotubes; "@" = Pc adsorbed onto the nanomaterials; "/" =a mixture of different nanomaterials; "-" accompanied by linked = covalent bond; "-" accompanied by seq = sequential modification; mix = mixed before electrode modification; seq = sequentially added to the electrode; "r" in front of GONS = reduced; if no "r", the GONS were not reduced; TW = this work

The LODs (**Table 5.7**) were found to be appreciably low considering that hydrogen peroxide only becomes toxic in the physiological environments at concentrations above 50 mM [104] as stated above.The values reported here for the LODs are comparable and even better that those reported elsewhere making the probes in this work a promising platform for hydrogen peroxide detection(**Table 5.7**) [163,177,186]. LOD values reported in this section are generally less favourable than those reported above for rPDGONS, rPNDGONS and rNDGONS showing the importance of GONS on their own and chemical reduction prior to application.

The rate constant k wasobtained by plotting the square of the slopes (from **Fig. 5.13B**) against the respective concentrations gave linear plots (**Fig. 5.13C**) whose slope is equal to πk. The plots are represented by **equations 5.19 – 5.27.**

CoTAPhPc**NP**(**1**)@rGONS/AuNRs(mix)-GCE:

$$y = 1.5962[H_2O_2]\left(\frac{s^{-1}}{mM}\right) - 1.0289s^{-1}, R^2 = 0.9186 \quad 5.19$$

CoTAPhPc**NP**(**1**)@NDGONS-AuNRs(linked)-GCE:

$$y = 1.9805[H_2O_2]\left(\frac{s^{-1}}{mM}\right) - 0.3048s^{-1}, R^2 = 0.9568 \quad 5.20$$

CoTAPhPc**NP**(**1**)@rSDGONS-AuNRs(linked)-GCE:

$$y = 8.8377[H_2O_2]\left(\frac{s^{-1}}{mM}\right) - 2.8544s^{-1}, R^2 = 0.9975 \quad 5.21$$

CoTAPhPc**NP**(**1**)@rSNDGONS-AuNRs(linked)-GCE:

$$y = 45{,}175[H_2O_2]\left(\frac{s^{-1}}{mM}\right) - 16.249s^{-1}, R^2 = 0.9612 \quad 5.22$$

CoTAPhPc**NP**(**1**)@AuNRs-rSNDGONS(seq)-GCE

$$y = 47.839[H_2O_2]\left(\frac{s^{-1}}{mM}\right) - 12.28s^{-1}, R^2 = 0.9937 \quad 5.23$$

CoTAPhPc**NP**(**1**)@rSNDGONS-AuNRs(seq)-GCE

$$y = 7.9386[H_2O_2]\left(\frac{s^{-1}}{mM}\right) - 2.3079, R^2 = 0.9869 \quad 5.24$$

CoTAPhPc**NP**(**1**)-GCE:

$$y = 2.731[H_2O_2]\left(\frac{s^{-1}}{mM}\right) - 0.3262s^{-1}, R^2 = 0.9348 \quad 5.25$$

CoTAPhPc**NP**(**1**)@rSNDGONS-GCE

$$y = 2.8708[H_2O_2]\left(\frac{s^{-1}}{mM}\right) - 0.6105, R^2 = 0.9781 \quad 5.26$$

CoTAPhPc**NP**(**1**)@rSDGONS-GCE

$$y = 8.613[H_2O_2]\left(\frac{s^{-1}}{mM}\right) - 0.0939, R^2 = 0.9791 \quad 5.27$$

The catalytic rate constants range from 6.10 x 10^1 to 1.52 x 10^4 (**Table 5.7**). In the presence of AuNRs, these values display the synergistic effect of co-doping the graphene oxide nanosheets.The high rate constant values of CoTAPhPc**NP**(**1**)@AuNRs-SNGONS(seq)-GCE shows again that when GONS are placed on the electrode before AuNRs, there is improved catalysis and confirming that the order of placing materials on the electrode surface is important. It is however difficult to compare linked probes to sequentially adsorbed ones since the quantities of the modifiers vary with the method.

5.2.3. MWCNTs based electrodes.

5.2.3.1. Cyclic voltammetry.

The reduction peaks for hydrogen peroxide were observed in the potential window between -0.28 V to -0.59V as shown in **Table 5.8**and **Fig. 5.14**which is comparable to a number of other studies with reduction potentials of -0.6 V [171], and -0.4 V vs Ag/AgCl [172] as stated above.The oxidation peaks are observed from 0.77 to 0.86 V. The peaks near 0 V in the presence of AuNRs are due their redox processes as observed above.The currents for H_2O_2

detection on CoTAPhPc**NP**(**1**)@MWCNT-GCE were much higher (at 68.80 μA) compared to the rest of the electrodes, **(Fig. 5.14B and Table 5.8)** making this electrode the best even though it has slightly more negative reduction potential at -0.40 V. Large currents do not correlate with the low surface coverage value in **Table 4.1**. It is also worth noting that AuNRs alone result in significant lowering of the reduction potential of the analyte (**Table. 5.7**) though there is no apparent effect on the oxidation potential. The nanosized Pc (CoTAPhPc**NP**(**1**)–GCE, 19.31μA) gave better current signals than bulk CoTAPhPc(**1**)-GCE at 9.04 μA, this is also the case in the presence of MWCNTs (compare CoTAPhPc**NP**(**1**)@MWCNT-GCE, 68.80 μA with CoTAPhPc(**1**)@MWCNT-GCE, 16.24μA),**Fig. 5.14B**, **Table 5.8.** For the conjugates containing all three components, the presence of nanosized Pc resulted in higher currents (compare CoTAPhPc**NP**(**1**)@MWCNT/AuNRs(mix)-GCE, 16.97 μA, with CoTAPhPc(**1**)@MWCNT/AuNRs(mix)-GCE, 10.13 μA) (**Table 5.8**), where the former gave higher currents than the latter.All the observations above show the importance of using nanosized Pc. However, for AuNRs, there is no change in current for CoTAPhPc**NP**(**1**)-AuNRs(linked)-GCE compared to CoTAPhPc(**1**)@AuNRs-GCE alone. Thus, AuNRs reduces the advantage of nanosized Pc, in terms of current even though the potential is favourable.The weak current response for CoTAPhPc(**1**)@AuNRs-GCE would adversely affect the limits of detection to be discussed later.

Table 5.8. Electrochemical parameters for the modified electrodes based on Complex **1** and **2** withMWCNTs.

a – no signal; "@" = Pc adsorbed onto the nanomaterials; "/" =a mixture of different nanomaterials; "-" accompanied by linked = covalent bond. DAMN = diaminomaleonitrile; mix = mixed before electrode modification; seq = sequentially added to the electrode

GCE modifier	**E/V (H_2O_2) reduction pH 7 buffer**	**E/V (H_2O_2 oxidation) pH 7**	**Background corrected Reduction currents/μA in pH 7 buffer**
Bare GCE	-0.58	a	3.85
MWCNT-GCE	-0.59	a	8.70
AuNRs-GCE	-0.29	0.80	20.07
CoTAPhPc(**1**)-GCE	-0.37	0.83	9.04
CoTAPhPc**NP**(**1**)-GCE	-0.33	0.86	19.31
CoTAPhPc(**1**)@MWCNT-GCE	-0.53	a	16.24
CoTAPhPc**NP**(**1**)@MWCNT-GCE	-0.40	0.80	68.80
CoTAPhPc(**1**)@AuNRs-GCE	-0.28	0.80	17.29
CoTAPhPc**NP**(**1**)@AuNRs-GCE	-0.29	0.77	17.29
CoTAPhPc(**1**)@MWCNT/Au NR(mix)-GCE	-0.29	0.78	10.13
CoTAPhPc**NP**(**1**)@MWCNT/ AuNR(mix)-GCE	-0.29	0.78	16.97
CoTCPhPc(**2**)-GCE	-0.40	-	11.41
CoTCPhPc(**2**)/(DAMN)-MWCNT(mix)-GCE	-0.29	-	24.53
CoTCPhPc(**2**)-(DAMN)-MWCNT(linked)-GCE	0.33	-	37.41

The probes were also tested against fouling during the detection of hydrogen peroxide, **Fig. 5.15** using CoTAPhPc**NP**(**1**)@MWCNT-GCE as an example. All the probes investigated show loss of signal. However, the inclusion of gold nanoparticles improved the stability of the probes. The cause of passivation may be due to adsorption of hydrogen peroxide, its reaction intermediates or products on the electrode surface. The oxidation peak suffers most from fouling in all tested electrodes as compared to the reduction peak (**Fig. 5.15**) as discussed above for other electrodes.

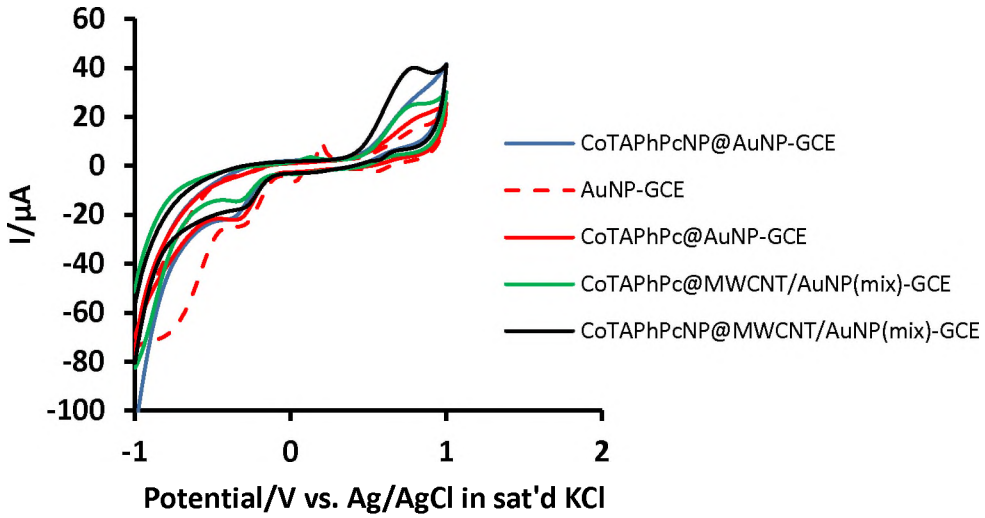

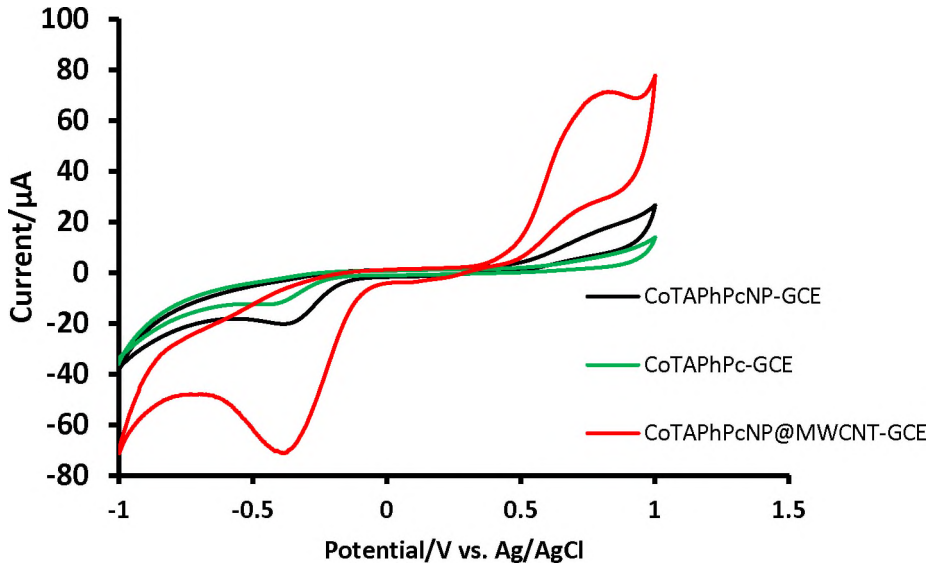

Fig 5.14. CVs of selected probes in 1 mM hydrogen peroxide at scan rate 100 mV/s (A) gold nanoparticles modified electrodes and (B) multiwalled carbon nanotubes based electrodes. pH = 7 buffer.

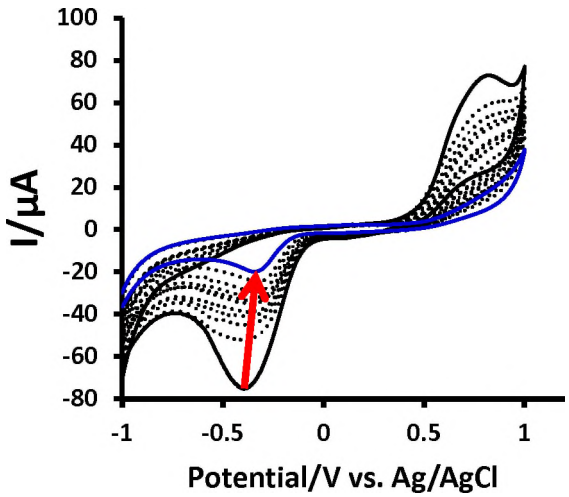

Fig 5.15 Cyclic votamogrammes (20 successive scans, but not all shown) of CoTAPhPc**NP**(**1**)@MWCNT-GCEin 1 mM hydrogen peroxide. Scan rate of 100 mV/s. pH = 7 buffer.

5.2.3.2. Kinetic studies

Fig. 5.16A shows the CVs for H_2O_2 detection at different scan rates (using CoTAPhPc**NP**(**1**)@MWCNT-GCE as an example). The accompanying shift in the peak potential as the scan rate increases is evidence for an irreversible electro-reduction (or oxidation) of hydrogen peroxide on the surfaces of the modified electrodes. There is a linear increase in the current signal when plotted against the square root of scan rate which shows that the electro reduction of hydrogen peroxide is diffusion controlled, **Fig. 5.16B** [187].

The plot of E_p versus log υ (**Fig. 5.16C**) gave linear relationships with Tafel slopes observed to be 135 mV/decade, 219 mV/decade, 82 mV/decade for CoTAPhPc**NP**(**1**)@MWCNT-GCE, CoTAPhPc**NP**(**1**)-GCE and CoTAPhPc**NP**(**1**)@MWCNT/AuNRs(mix)-GCE, respectively. As stated already the high Tafel slopes above 120 mV/decade have no kinetic meaning and are

usually indicative of an electrode surface passivation (which is confirmed by **Fig. 5.15**) due to follow up chemical reactions soon after the electron transfer [188]. Tafel slope for CoTAPhPc**NP**(**1**)@MWCNT/AuNRs(mix)-GCE is lower than 120 mV/decade, suggesting less passivation of the electrode and that one electron is transferred during the rate-determining step.

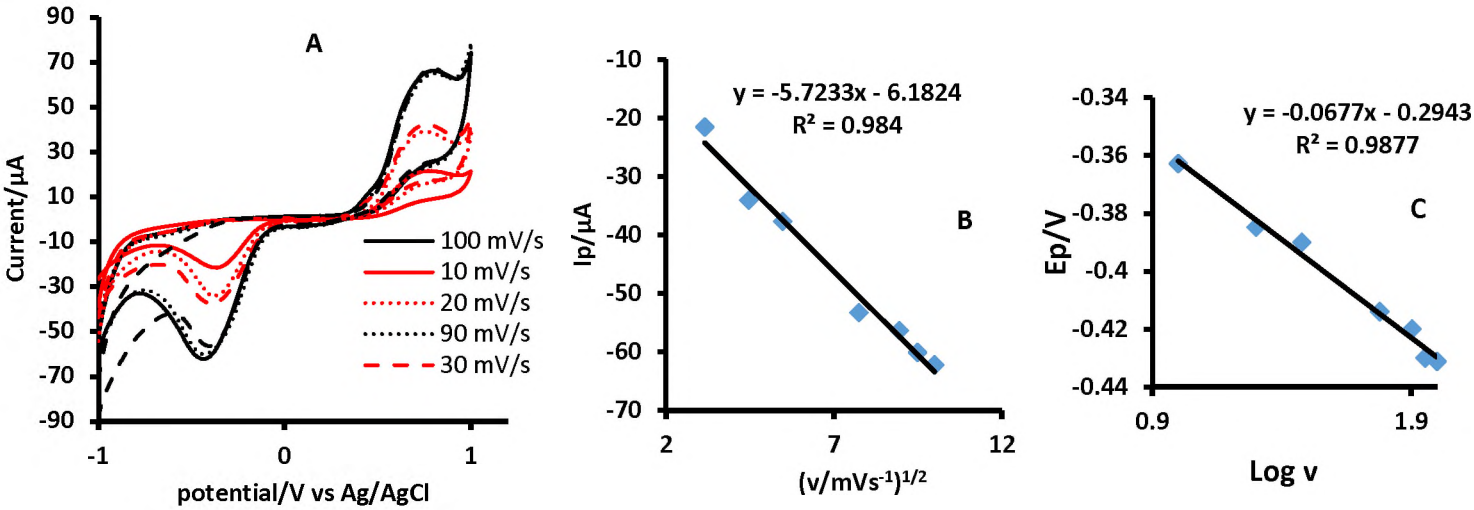

Fig 5.16 (A) cyclicvoltammograms for the detection of hydrogen peroxide at different scan rates, (B) Plot of Ip vs. $v^{1/2}$ and (C) plot of peak potential vs. log scan rate in 1 mM hydrogen peroxide using CoTAPhPc**NP**(**1**)@MWCNT-GCE. pH 7 buffer.

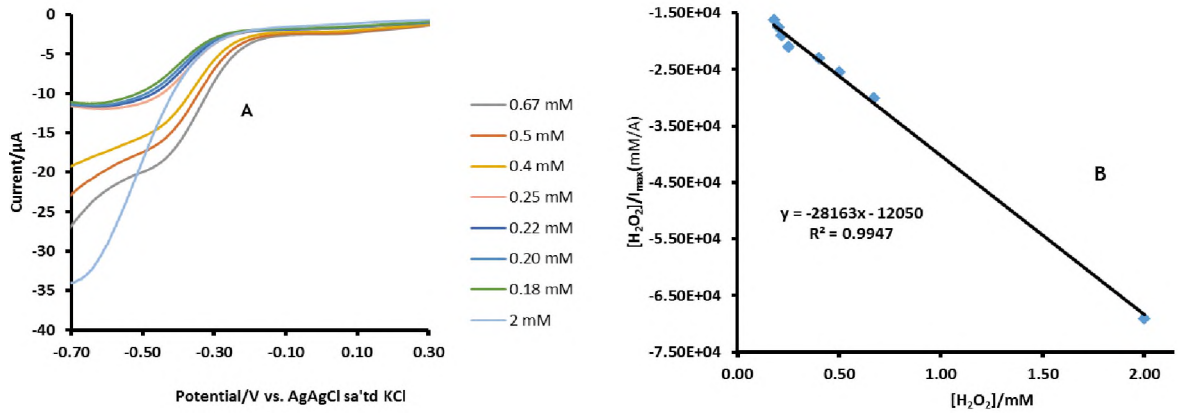

Fig. 5.17 (A) Linear sweep voltammograms and (B)Langmuir adsorption isotherm Plot. pH 7 buffer.

Linear sweep voltammetry was done to show adsorption behaviour of the electrodes and explain the Tafel slopes. **Fig 5.17 (A)** shows LSV plots obtained after keeping the electrode in a stirred solution for 20 minutes. Applying the Langmuir adsorption theory (**Equation 5.7**)[175]) a plot of the ratio of hydrogen peroxide concentration to catalytic current against concentration of hydrogen peroxide gave a linear plot which is indicative of adsorption further consolidating the observed high Tafel slopes.

From the slope and the intercept of **Fig 5.17 (B)**, the adsorption equilibrium constant β was established to be 2.34 x 10^3 M^{-1}. Using **equation 5.8**, ΔG^o was found to be -19.22 kJ/mol, slightly more negative than reported above for other electrodes. This value is in the same range as reported for high Tafel slopes [175].

5.2.3.3 Chronoamperometry studies.

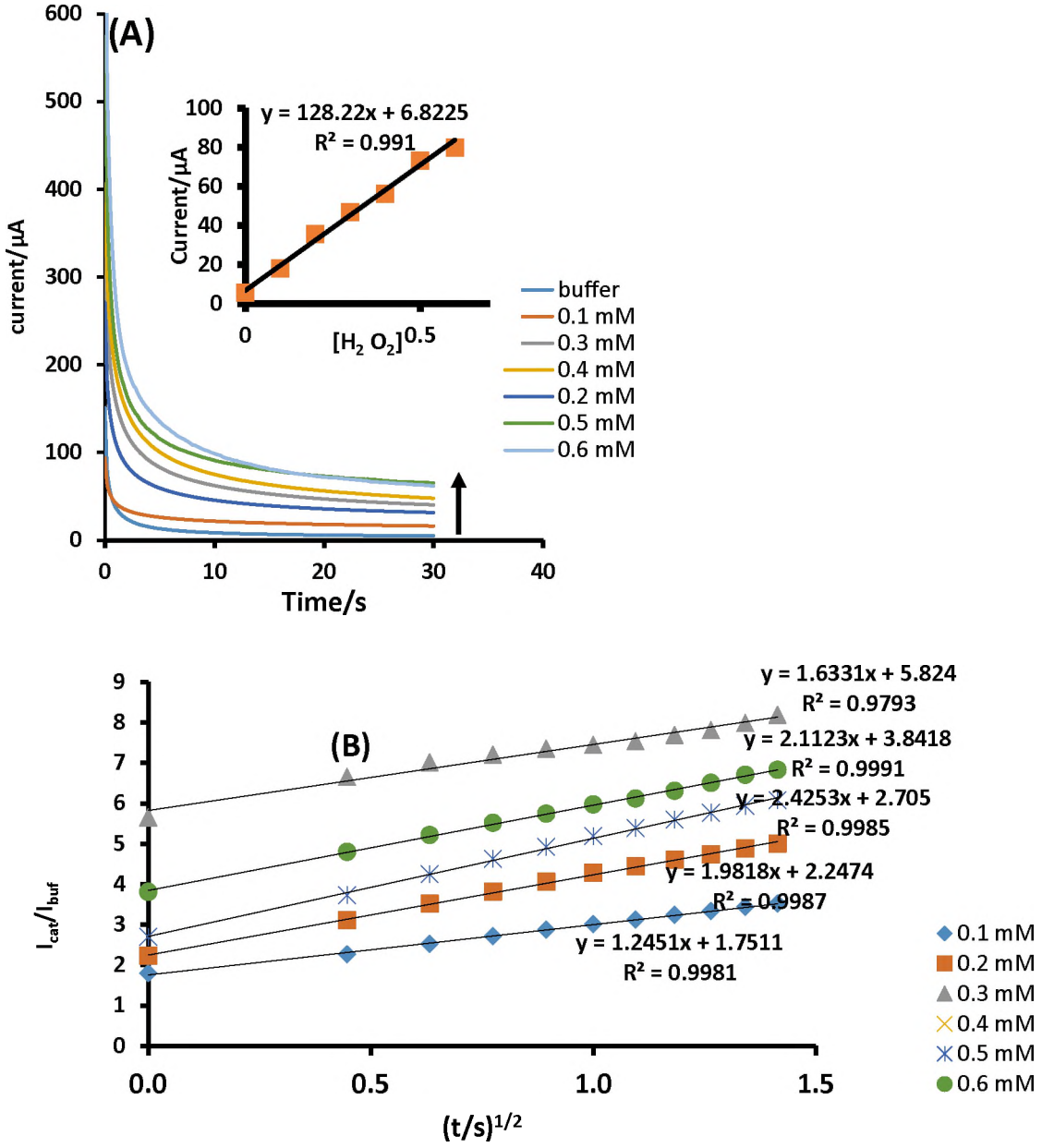

Fig. 5.18. (A) Chronoamperogramms for CoTAPhPc**NP**(**1**)@MWCNT-GCE in different concentrations of hydrogen peroxide. (insert) calibration curve for CoTAPhPc**NP**(**1**)@MWCNT-GCE and (B) current ratios vs square root of time. pH 7 buffer. Potential -0.40 V.

Table. 5.9 Comparative LODs for the electrocatalysed reduction of hydrogen peroxide using Complex **1**and **2**

Electrode[a]	**pH**	**k M^{-1} s^{-1}**	**LOD,10^{-7} M**	**Ref**
Nanoporous platinum–cobalt alloy	7	-	1	[178]
Prussian blue-based artificial peroxidase	7.4	-	10	[179]
Prussian blue- modified FTO	7.4	-	500	[189]
GCE-polyCoTAPc	7.4	-	1.45	[143]
Au-polyCoTAPc	7.4	-	3.64	[143]
Cobalt oxide nanoparticles	7	-	0.4	[190]
Silver nanoparticle assemblies	7	-	2000	[191]
CoPc**NP**(**3**)-GCE (oxidation)	7	6.38 x 10^5	0.81	TW
CoPc**NP**(**3**)-GCE (reduction)	7	7.11 x 10^2	0.90	TW
CoPc**NP**(**3**)@rSDGONS-GCE(reduction)	7	1.38 x 10^4	0.52	TW
CoPc**NP**(**3**)@rSDGONS-GCE(oxidation)	7	4.36 x 10^4	0.15	TW
CoTAPcNP(**5**)-GCE (reduction)	7	3.70 x 104	1.72	TW
CoTAPc**NP**(**5**)@rSDGONS-GCE	7	1.45 x 10^4	0.57	TW
CoTAPhPc**NP**(**1**)@MWCNT-GCE	7	3.45 x 10^3	1.61	TW
CoTAPhPc**NP**(**1**)@AuNRs-GCE	7	1.76 x 10^2	212	TW
CoTAPhPc**NP**(**1**)@MWCNT/AuNR(mix)-GCE	7	1.56 x 10^3	16.92	TW
CoTCPhPc(**2**)/(DAMN)-MWCNT(mix)-GCE	7	1.10 x 10^3 8.7 x 10^2	0.097	TW
CoTCPhPc(**2**)-(DAMN)-MWCNT (linked)-GCE	7		0.0033	TW

[a]poly = polymerized, TAPc = tetraaminophthalocyanines, FTO = fluoride doped tin oxide.**"@"** = Pc adsorbed onto the nanomaterials; "/" =a mixture of different nanomaterials; DAMN = diaminomaleonitrile; mix = mixed before electrode modification; seq = sequentially added to the electrode; "r" in front of GONS = reduced; if no "r", the GONS were not reduced; TW = this work.

The calibration, catalytic rate constants and limits of detection were determined using chronoamperometry, **Fig. 5.18** (using CoTAPhPc**NP**(**1**)@MWCNT-GCE as an example). Hydrogen peroxide concentration changes showed a linear response to peak currents, **Fig. 5.18** insert. Plots of the ratio of catalytic currents and buffer currents (I_{cat}/I_{buf}) against square root of time within the rapid decay region gave linear plots of varying slopes characterized by an increase in the slopes as concentrations increased (**Fig. 5.18B**). The slopes of the plots were used to calculate the catalytic rate constants according to **equation 5.2**.

Plotting the square of the slopes against the respective concentrations (figures not shown) gave linear plots whose slope is equal to πk where k is the rate constant represented by **equations 5.28 – 5.30.**

CoTAPhPc**NP**(**1**)@MWCNT-GCE =

$$y = 10.837[H_2O_2](\frac{s^{-1}}{mM}) - 0.9659s^{-1}, R^2 = 0.9978 \qquad 5.28$$

CoTAPhPc**NP**(**1**)@MWCNT/AuNRs(mix)-GCE =

$$y = 4.9542[H_2O_2](\frac{s^{-1}}{mM}) - 0.4928s^{-1}, R^2 = 0.9978 \qquad 5.29$$

CoTAPhPc**NP**(**1**)@AuNRs-GCE =

$$y = 0.5525[H_2O_2](\frac{s^{-1}}{mM}) - 0.1334, R^2 = 0.9854 \qquad 5.30$$

The rate constants were found to be 3.45 x 10^3 $M^{-1}s^{-1}$ for CoTAPhPc**NP**(**1**)@MWCNT-GCE, 1.58 x $10^3M^{-1}s^{-1}$ for CoTAPhPc**NP**(**1**)@MWCNT/AuNRs(mix)-GCE and 1.76 x 10^2M^{-1} $s^{-1}$for CoTAPhPc**NP**(**1**)@AuNRs-GCE as examples. The largest rate constant is observed for CoTAPhPc**NP**(**1**)@MWCNT-GCE. The rate constant values compare very well with those reported by Ganesan and Ramaraj [181]as stated above. Limits of detection (LOD) values were calculated as before.The probes showed LOD in the micro molar range, which are higher than reported above for GONS and Pc showing the importance of GONS. The best LOD was observed for CoTAPhPc**NP**(**1**)@MWCNT-GCE, showing the importance of combining nanosized Pc with MWCNT but not with AuNRs.

5.3. Hydrogen peroxide detection on CoTCPhPc(2) with (DAMN)-MWCNTs conjugates based electrodes.

5.3.1. Cyclic voltammetry

While bare GCE and (DAMN)-MWCNT-GCE showed no oxidation peak (but showed a reduction peak) (**Fig. 5.19A**), the incorporation of the CoTCPhPc(**2**) resulted in the emergence of the oxidation peak for hydrogen peroxide, **Fig. 5.19B**. However, the reduction peak was employed in order to compare all the electrodes. Covalently linking the Pc to the carbon nanotubes significantly improves both the oxidation and reduction currents as can be seen in **Fig. 5.19.** The peak currents are the largest for the CoTCPhPc(**2**)-(DAMN)-MWCNT(linked)-GCE.

The probes reported here show very attractive reduction overpotentials ranging from -0.29 V and -0.40 V, **Table 5.8** for the detection of hydrogen peroxide. The potential values are in the range of the CoTAPhPc(**1**)@MWCNT-GCE electrodes in **Table 5.8**. It can also be noted that the incorporation of (DAMN)-MWCNT significantly lowers the overpotentials; Compare CoTCPhPc(**2**)-GCE (-0.40 V), with CoTCPhPc(**2**)/(DAMN)-MWCNT(mix)-GCE (-0.29 V) or CoTCPhPc(**2**)-(DAMN)-MWCNT(linked)-GCE (-0.33 V) while also improving the background corrected detection currents; Compare CoTCPhPc(**2**)-GCE (11.41 μA), with CoTCPhPc(**2**)/(DAMN)-MWCNT(mix)-GCE (24.53 μA) or CoTCPhPc(**2**)-(DAMN)-MWCNT(linked)-GCE (37.41 μA) (**Table 5.8** and **Fig. 5.19**). Thus, CoTCPhPc(**2**)-(DAMN)-MWCNT(linked) gave the largest catalytic currents of the CoTCPhPc (**2**) electrodes, even though it was not the best in terms of potential. Such observations can be attributed to the covalent bond formation as confirmed by both XPS and FTIR, which improves the sharing of the π electron system of the MPcs and MWCNT, enhancing the electrocatalytic behaviour of the modified electrode.

The stability of the electrodes was tested by running twenty consecutive scans in 1 mM hydrogen peroxide. The electrodes were characterized by more loss of oxidation currents with scan number compared to reduction currents as observed above for other electrodes (**Fig. 5.5**).

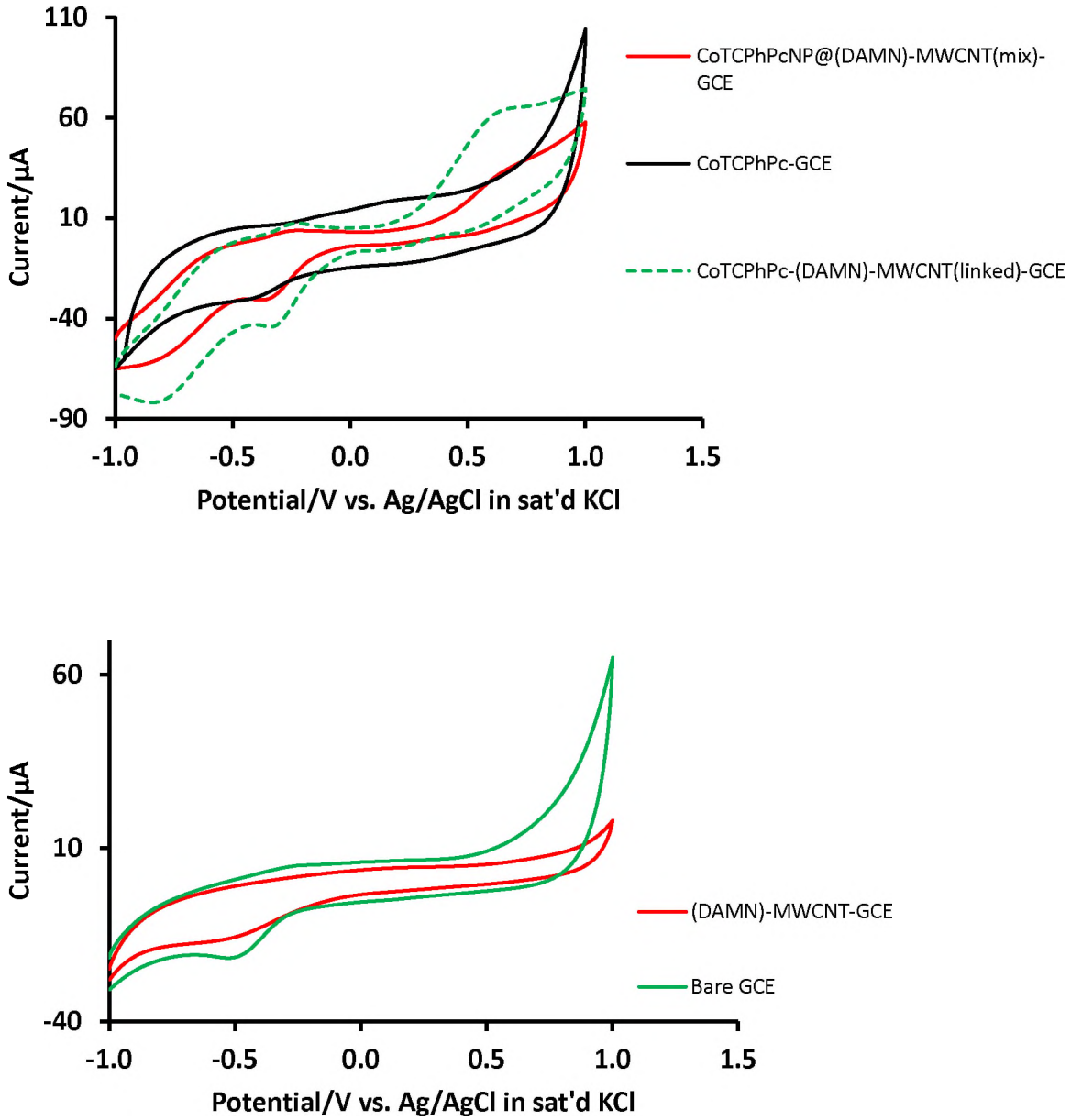

Fig. 5.19. Cyclic voltammograms of modified electrodes in 1 mM hydrogen peroxide in pH 7 buffer.

5.3.2. Kinetic studies of hydrogen peroxide detection

Detection of hydrogen peroxide at the surface of the modified electrodes was also done at different scan rates to establish the reversibity of the catalyzed reaction. There was a shift in the peak potential as well as the peak current as the scan rate was varied evident of an irreversible reaction in a manner similar to **Figure 5.16A**.

Tafel slopes were determined as explained above. Both the CoTCPhPc(**2**)/(DAMN)-MWCNT(mix)-GCE (210 mV/decade) and CoTCPhPc(**2**)-(DAMN)-MWCNT(linked)-GCE (123 mV/decade) are characterized by high Tafel slopes above the normal 60 – 120 decade which may suggest adsorption of either the products or the intermediates on the modified electrode surface as discussed above. This has also been attributed to mechanisms in which a chemical step is the rate determining step [192].

Using **eqn 5.7** and plots similar to **Fig. 5.17,** the adsorption equilibrium constant β was established to be 9.71 x 10^4 $M^{-1}$and using equation **5.8**, ΔG° was found to be -17.18 $kJmol^{-1}$ for CoTCPhPc(**2**)-(DAMN)-MWCNT(linked)-GCEwhich is almost similar to -17.69 kJ mol^{-1} obtained for CoTAPhPc(**1**)@rGONS-GCE. This value shows spontaneity and hence the high catalytic rate constants observed below.

Rotating disk electrode was also used to investigate the electrocatalytic activity of the modified electrode surface towards the reduction of hydrogen peroxide, **Fig. 5.20,** using (CoTCPhPc(**2**)/(DAMN)-MWCNT(mix)-GCE as an example). If the reduction of hydrogen peroxide on the electrode surface is

controlled by the mass transfer in solution, then the relationship between current and rotation speed obeys the Koutecky-Levich (**eq. 5.31**)[160,193].

$$\frac{1}{I_1} = \frac{1}{nFAc_o k\Gamma} + \frac{1}{0.62nFAD^{2/3}v^{-1/6}c_o\omega^{1/2}} \qquad 5.31$$

where A, k, Γ, I_l, D, v, ω, F, n and c_o are the effective electrode area, the catalytic rate constant, the surface coverage, limiting current, diffusion coefficient, the kinematic viscosity, the rotation speed, Faraday constant, number of electrons involved and the bulk concentration of the reactant in solution respectively.

A plot of I^{-1} versus $\omega^{-1/2}$ was characterised by two regions as shown in **Fig.5.20(B)** with higher speeds being characterised by higher catalytic rate constants (at 1.1 x 10^3 M^{-1} s^{-1} at high speeds and 8.7 x 10^2 M^{-1} s^{-1} at low speeds), **Table 5.9**. This might serve to indicate a very facile reaction at the surface of the modified electrode governed by mass transfer processes in solution hence the more turbulent the solution the faster the reaction. The catalytic rate constants are comparable to other values reported in this thesis for hydrogen peroxide determined by chronoamperometry in **Table 5.4** and **5.9**.

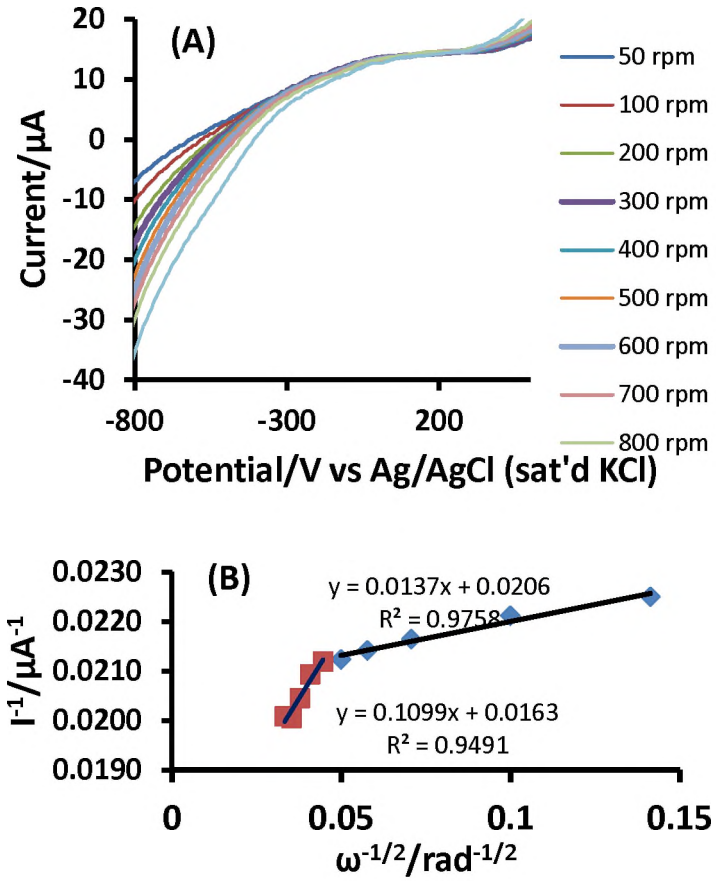

Figure 5.20. (A) Rotating disk voltammograms for 1 mM Hydrogen peroxide at CoTCPhPc(**2**)/(DAMN)-MWCNT(mix)-GCE surface with different rotation speeds and (B) Koutecky-Levich plots

5.3.3 Square wave voltammetry

One of the most important characteristics of a catalytic platform being utilised as a good sensor candidate, is the ability to detect the analyte at very low concentrations. Voltammetric techniques such as square wave are known to be useful for electrocatalytic detection of a wide range of analytes. This work employs square wave voltammetry to determine limits of detection calculated using $3\sigma/s$ as discussed above. **Fig.5.21** {CoTCPhPc(**2**)/(DAMN)-MWCNT(mix)-GCE as an example} shows the variation of current with change

in concentration. Appreciably low limits of detection were obtained. CoTCPhPc(**2**)/(DAMN)-MWCNT(mix)-GCE (9.74 nM) and CoTCPhPc(**2**)-(DAMN)-MWCNT(linked)-GCE (0.33 nM). These results are much an improvement to literature values [189–191] and the rest of the MWCNT based electrodes in **Table 5.9**, demonstrating the importance of covalent linkage and the presence of an amine group as reported before [194]**.** In fact the LOD for CoTCPhPc(**2**)-(DAMN)-MWCNT(linked)-GCE is the best reported in this thesis.

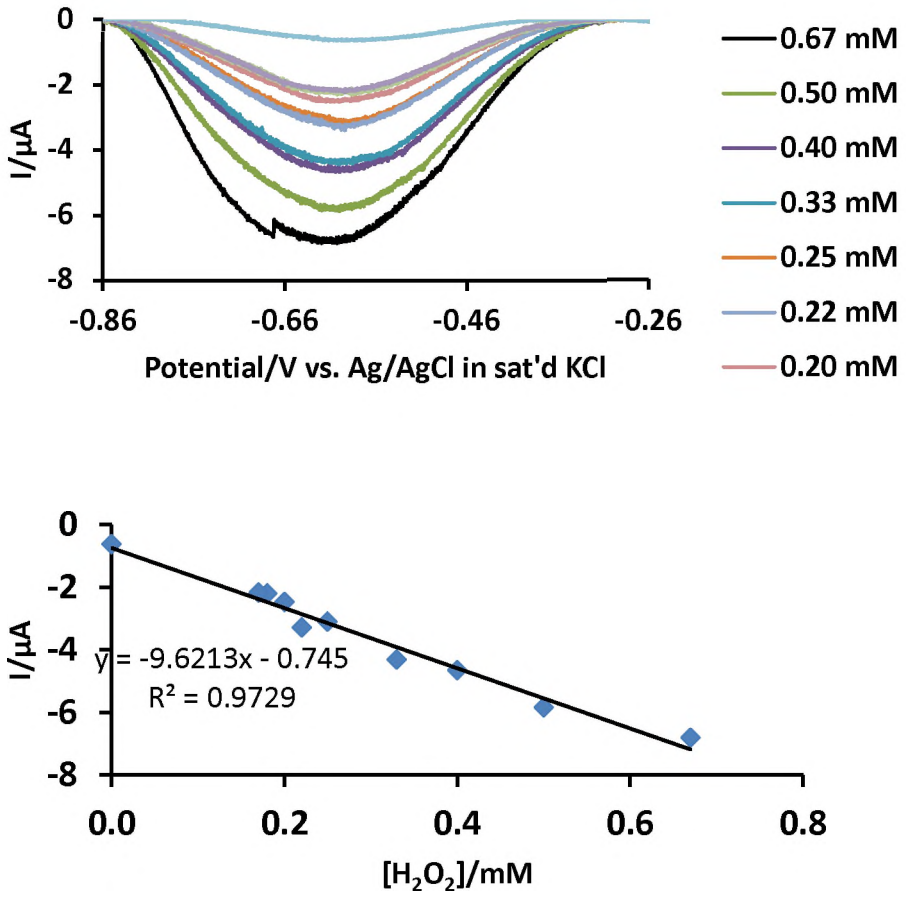

Fig 5.21. Square wave voltammograms for electro reduction of 1 mM hydrogen peroxide and plots of current versus H_2O_2 concentration on CoTCPhPc(**2**)/(DAMN)-MWCNT(mix)-GCE, pH 7 buffer.

5.4 Hydrogen peroxide detection on CoPc (3) and CoTAPc (5) based electrodes

5.4.1 Cyclic Voltammetry

As before, the probes described in this section are characterised by both oxidation and reduction peaks for hydrogen peroxide **(Fig. 5.22**, **Table 5.10**). The oxidation peaks were observedin the ranges 0.40 V to 0. 75 V while the reduction peaks were observed in the range -0.25V to -0.62 V. Electrodes containing rSDGONS showed relatively largepotentials for the oxidation and reduction of hydrogen peroxide. The high overpotentials for rSDGONS were also observed in **Table 5.6** for CoTAPhPc(**1**)@rSDGONS-GCE. However superior background corrected reduction peak currents were observed for rSDGONS based electrodes: compare CoPc**NP**(**3**)@rSDGONS-GCE (121.79 mA) with CoPc**NP**(**3**)@rGONS-GCE (20.32 mA) or CoPc**NP**(**3**)-GCE (43.54 mA); and CoTAPc**NP**(**5**)@rSDGONS-GCE (105.11 mA) with CoTAPc**NP**(**5**)@rGONS-GCE (23.92 mA) or CoTAPc**NP**(**5**)-GCE (22.17 mA). The same trend was observed for electro-oxidation processes **(Table 5.10)**. Thus rSDGONS improves catalysis. The increase in currents was also observed in **Table 5.6** for CoTAPhPc**NP**(**1**)@rSDGONS-GCE. It should also be noted that sulphur and nitrogen [195] are more electron withdrawing compared to carbon hence this difference in electronegativities will offer an enhanced electron driving force thereby improving the electrocatalytic behaviour of the metallophthalocyanine.In terms of both oxidation and reduction currents, CoPc**NP**(**3**)@rSDGONS-GCE performed better than CoTAPc**NP**(**5**)@rSDGONS-GCE. The superior behaviour of CoPc**NP**(**3**)(6.50 nm) compared to

CoTAPc**NP**(**5**)(9.98 nm), could be related to nanoparticle size given in brackets. The nanoparticles for CoPc**NP**(**3**) are smaller in size than those of CoTAPc**NP**(**5**) hence improving catalytic activity due the larger surface area of CoPc**NP**(**3**).

Stability tests were done for the modified electrodes by running 20 or 50 successive voltammograms (as indicated on the **Fig. 5.23**) in 1 mM hydrogen peroxide. CoPc**NP**(**3**) showed distinct H_2O_2 reduction and oxidation peaks, which were still evident after 20 cycles. While rSDGONS-GCE is characterised by relatively high reduction and oxidation peak currents (**Table 5.10**), the electrode is highly prone to fouling during hydrogen peroxide detection with no oxidation nor reduction peaks after 20 cycles. While all the electrodes suffered some signal loss, it is noteworthy that all CoPc**NP**(**3**) containing probes significantly resisted fouling when compared to CoTAPc**NP** electrodes.

Table 5.10. Hydrogen peroxide detection potential and currents for **Complex 3** and **5** modified electrodes.

GCE modifier	**Reduction Tafel slopes of selected electrodes**	**E/V (H_2O_2) reduction pH 7 buffer**	**E/V (H_2O_2) oxidation pH 7 buffer**	**Background corrected currents/μA H_2O_2 reduction**	**Background corrected currents/μA H_2O_2 oxidation**
Bare GCE	-	-0.58	-	3.85	a
rGONS-GCE	-	0.61	-	7.17	a
rSDGONS-GCE	-	-0.62	0.65	64.2	25.9
CoPc(**3**)-GCE	-	-0.43	0.75	13.01	23.19
CoPc**NP**(**3**)-GCE	366	-0.39	0.70	43.54	66.20
CoPc**NP**(**3**)@rGONS-GCE	-	-0.41	0.70	20.32	35.04
CoPc**NP**(**3**)@rSDGONS-GCE	165	-0.57	0.60	121.79	111.06
CoTAPc(**5**)-GCE	-	-0.25	-	17.32	-
CoTAPc**NP**(**5**)-GCE	148	-0.27	0.44	22.17	14.88
CoTAPc**NP**(**5**)@rGONS-GCE	-	-0.26	0.40	23.92	20.22
CoTAPc**NP**(**5**)@rSDGONS-GCE	72	-0.53	0.67	105.11	72.45

[a] "@" = Pc adsorbed onto the nanomaterials; "r" in front of GONS = reduced; if no "r", the GONS were not reduced.

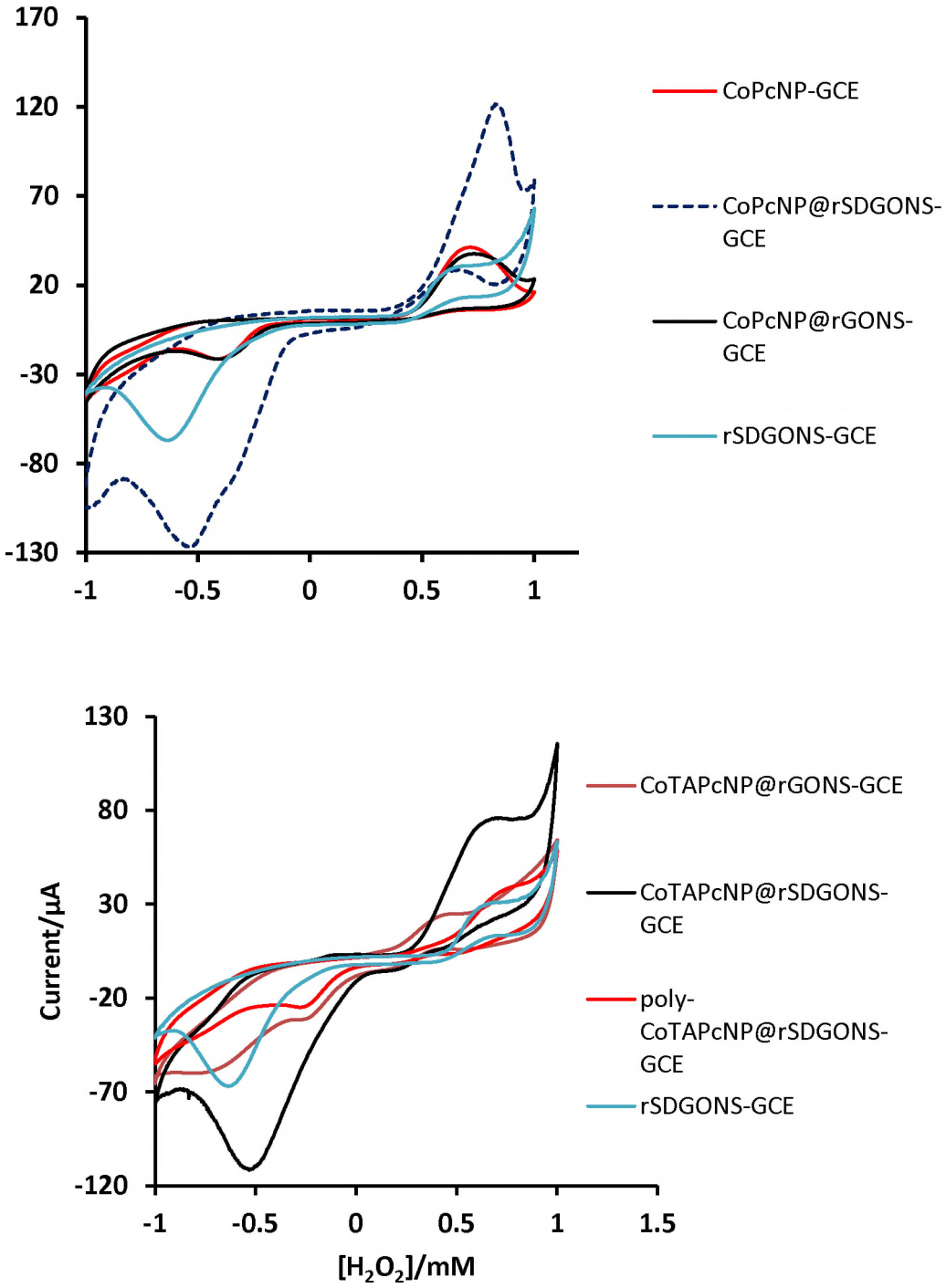

Fig 5.22. Cyclic voltammograms of modified electodes in 1 mM hydrogen peroxide at pH 7. Scan rate 100 mV/s.

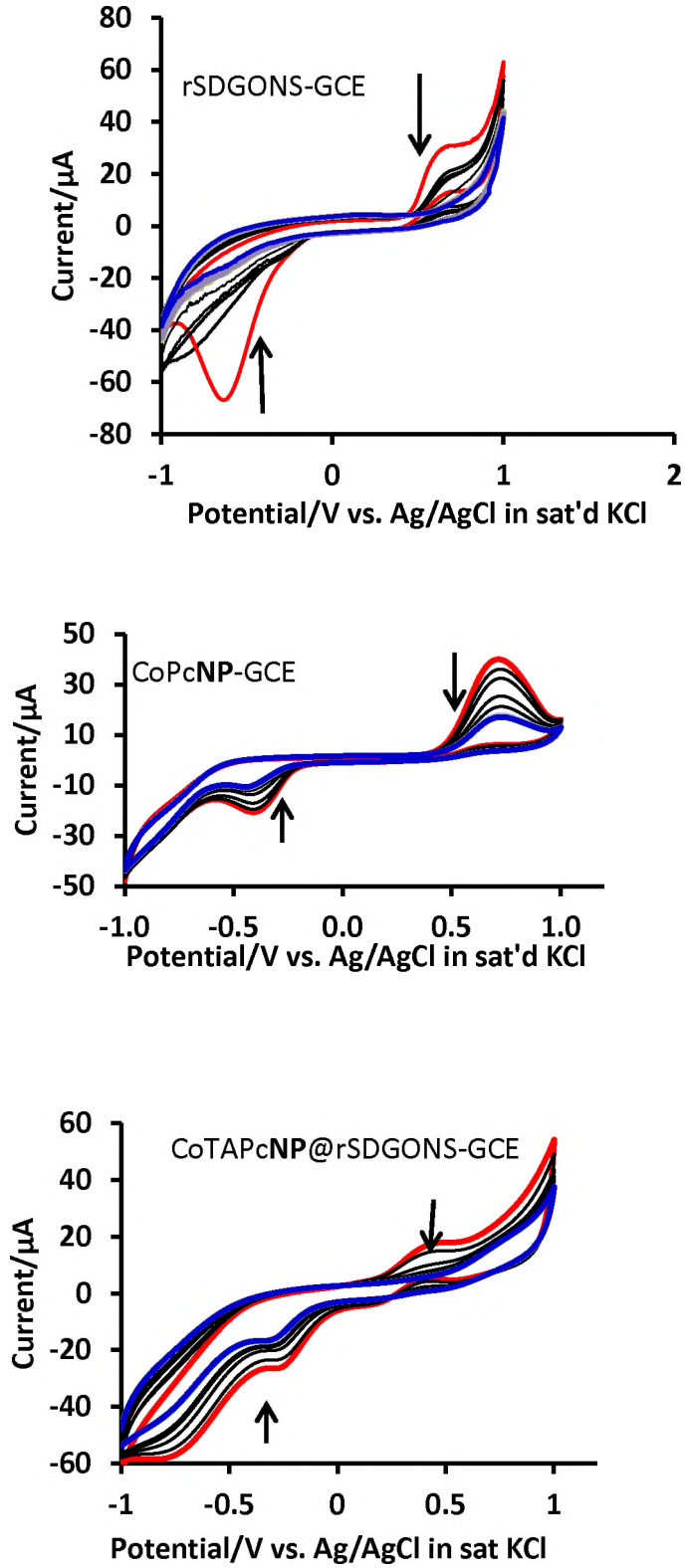

Fig. 5.23. Cyclic voltammograms (20 successive scans, not all intermediate cycles are shown) in 1 mM hydrogen peroxide. Scan rate of 100 mV/s. pH = 7 buffer.

5.4.2. Kinetic studies

While both CoTAPc**NP**(**5**)and CoPc**NP**(**3**) based electrodes showed both oxidation and reduction peaks (**Table 5.10**), only CoPc**NP**(**3**) based electrodes were further evaluated for both oxidation and reduction peaks after both peaks had shown significant resistance to fouling, whereas only reduction peaks were employed for CoTAPc**NP**(**5**), due to its extensive oxidation peak fouling. Tafel slopes were high in some instances in **Table 5.10**. As stated above high Tafel slope values above the normal 60–120 mV/decade are related to electrochemical steps or to substrate-catalyst interactions in a reaction intermediate [166,184]. A figure similar to **Fig. 5.6** was obtained showing a linear relationship between the peak currents and square roots of scan rates which is testimony to diffusion controlled electrocatalytic detection of hydrogen peroxide [166,184].

Linear sweep voltammetry (LSV) was used to explain the high Tafel slope observed. **Figure 5.24(A**) (using CoPc**NP**(**3**)-GCE as an example) showsLSV plots obtained after keeping the electrode in a stirred solution for 20 min (to allow for adsorption). Applying the Langmuir adsorption theory (**Equation 5.7**[175]), a plot of the ratio of hydrogen peroxide concentration to catalytic current against concentration of hydrogen peroxide was linear, which is indicative of adsorption further consolidating the observed high Tafel slopes.

From the slope and the intercept of **Figure 5.24(B**), the adsorption equilibrium constant β was established to be 1.27 X 10^3 M^{-1}. Using **equation 5.8**, ΔG was found to be -17.71 $kJmol^{-1}$ for CoPc**NP**(**3**)-GCE, similar to

CoTCPhPc(**2**)-(DAMN)-MWCNT(linked)-GCE discussed above. This value is comparable to those reported elsewhere for high Tafel slopes [175].

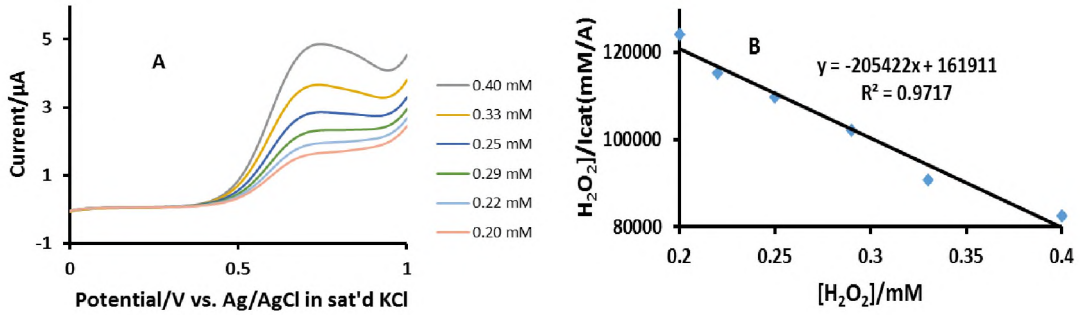

Fig. 5.24. (A) Linear sweep voltammograms and (B) Langmuir adsorption isotherm Plot for CoPc**NP**(**3**)-GCE in 1 mM hydrogen peroxide. pH 7 buffer. Electroxidation currents employed.

5.4.3. Chronoamperometry studies

Chronoamperometry was employed to determine the electrode catalytic rate constants and limits of detection using plots similar to those shown in **Fig. 5.18**.

From the linear plots of the square of the slopes against the respective concentrations, k, the rate constants were obtained and represented by **Eqs. 5.32– 5.37**.

Reduction:

CoTAPc**NP**(**5**)-GCE:

$$y = 117.13[H_2O_2]\left(\frac{s^{-1}}{mM}\right) - 7.1161, R^2 = 0.9758 \qquad 5.32$$

CoTAPc**NP**(**5**)@rSDGONS-GCE:

$$y = 287.79[H_2O_2]\left(\frac{s^{-1}}{mM}\right) - 77.365s^{-1}, R^2 = 0.9431 \quad 5.33$$

CoPc**NP**(**3**)-GCE:

$$y = 2.2348[H_2O_2]\left(\frac{s^{-1}}{mM}\right) - 0.6794, R^2 = 0.9912 \quad 5.34$$

CoPc**NP**(**3**)@rSDGONS-GCE:

$$y = 43.394[H_2O_2]\left(\frac{s^{-1}}{mM}\right) - 10.772, R^2 = 0.9526 \quad 5.35$$

Oxidation:

CoPc**NP**(**3**)-GCE:

$$y = 2005.1[H_2O_2]\left(\frac{s^{-1}}{mM}\right) - 288.31, R^2 = 0.9906 \quad 5.36$$

CoPc**NP**(**3**)@rSDGONS-GCE

$$y = 137.11[H_2O_2]\left(\frac{s^{-1}}{mM}\right) - 20.471, R^2 = 0.9717 \quad 5.37$$

The rate constants, (**Table 5.9**) on CoPc**NP**(**3**)-GCE for oxidation are the largest. For reduction, the largest rate constant is observed for CoTAPc**NP**(**5**)-GCE. The catalytic rate constants are significantly high as compared to values reported elsewhere [181] but comparable to the other electrodes in **Table 5.4**, indicating a facile reaction on the modified electrode surfaces. Limits of

detection (LOD) values were calculated using the 3σ notation, as explained already. In general, from **Table 5.9**, oxidation gives better LOD than reduction, considering the same electrode modifier. The presence of rSDGONS does improve LOD with CoPc**NP**(**3**)@rSDGONS-GCE being better than CoPc**NP**(**3**)-GCE for both H_2O_2 reduction and oxidation; and CoTAPc**NP**(**5**)@rSDGONS-GCE better than CoTAPc**NP**(**5**)-GCE (**Table 5.9**). This confirms further the importance of nanomaterials in enhancing the electrocatalytic behaviour of phthalocyanines. The lowest (hence best) detection limit was obtained for CoPc**NP**(**3**)@rSDGONS-GCE at 0.015μM among electrodes discussed in this section but **Table 5.9** shows CoTCPhPc(**2**)-(DAMN)-MWCNT(linked)-GCE at 0.33 nm to be the best. Complex **2** is however the only one determined by square wave voltammetry while the rest were determined by chronoamperometry.

5.5. CoMCPhPc (4) based electrodes

5.5.1. Cyclic voltammetry

Fig. 5.25 shows the cyclic voltammograms for H_2O_2 detection in pH 7 buffer. Both the oxidation and reduction peaks were obtained, but only reduction peaks are listed in **Table 5.11** since as will be shown belowand discussed abovefor other electrodes, the oxidation peaks showed less stability. The probes developed here could detect hydrogen peroxide at reduction potentials in the range -0.44 V to -0.71 V (**Fig. 5.25, Table 5.11**) which are within literature values [171–173,183,196] and are similar to other values discussed for other Pcs above. The general observation is that covalent linking of MPc to GONS result in significantly less negative detection overpotentials as

compared to sequential modification. Compare CoMCPhPc(**4**)-(DAMN)-GONS(linked)-GCE (-0.44 V) and CoMCPhPc(**4**)@(DAMN)-GONS-GCE (-0.55 V); CoMCPhPc(**4**)-(DAMN)-SDGONS(linked)-GCE(-0.55 V) andCoMCPhPc(**4**)@(DAMN)-SDGONS-GCE (-0.57 V); CoMCPhPc(**4**)-(DAMN)-SNDGONS(linked)-GCE(-0.53 V) and CoMCPhPc(**4**)@(DAMN)-SNDGONS-GCE (-0.71 V), **Table 5.11**. For both the linked or sequential electrodes, S/N followed by Ndoping of GONS in the nanoconjugate resulted in larger currents. The improvement in detection currents upon doping could be because of less oxygen moieties, which disturbs the sp^2 configuration and hence compromising the conduction ability of graphene oxide. The oxygen moieties are less following doping hence results in even more improved detection currents [197]. Sulphur doping seem to have very little influence in changing the detection currents of pristine graphene oxide; compare CoMCPhPc(**4**)-(DAMN)-GONS(linked)-GCE (10.73 μA) with CoMCPhPc(**4**)-(DAMN)-SDGONS(linked)-GCE (13.31 μA) for covalently linked species and CoMCPhPc(**4**)@(DAMN)-GONS-GCE (54.52 μA) with CoMCPhPc(**4**)@(DAMN)-SDGONS-GCE (56.82 μA) for sequential modification (**Table. 5.11**).

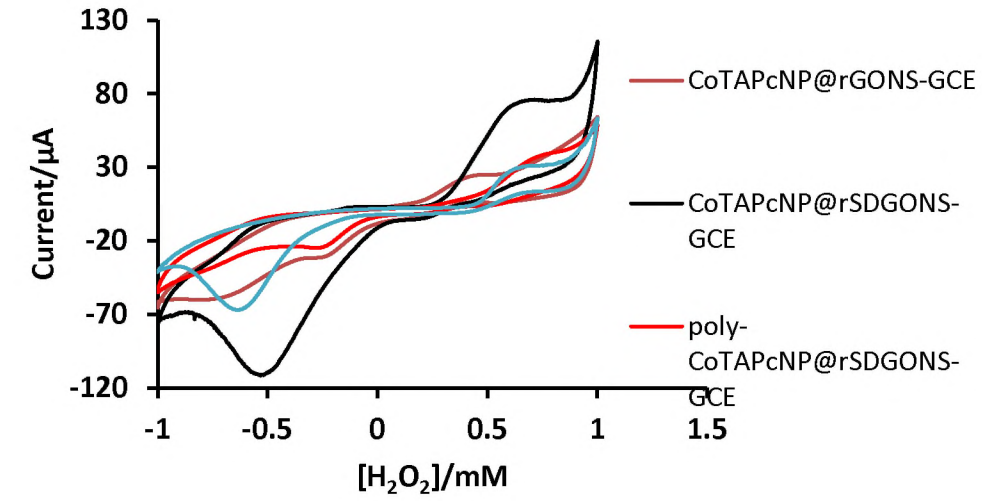

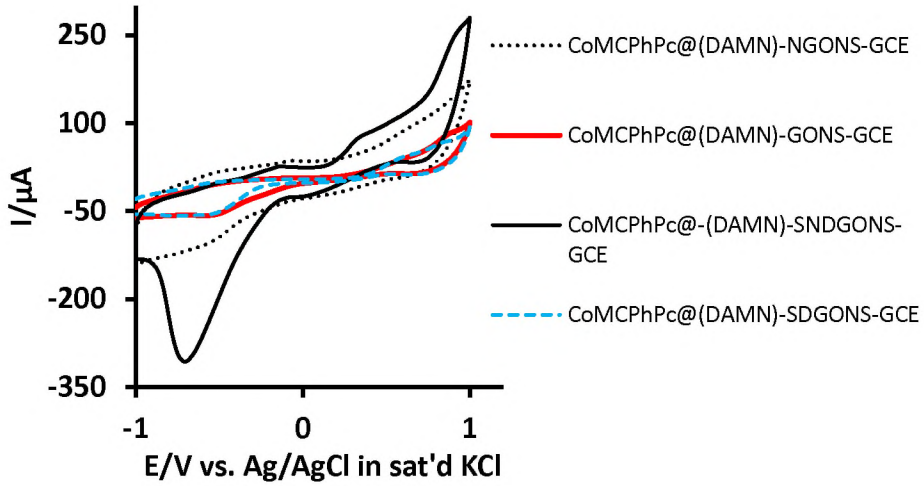

Fig 5.25. Cyclic voltammograms of modified electrodes in 1 mM hydrogen peroxide, in pH 7 buffer. Scan rate 100 mV/s

Table 5.11. H_2O_2 detection potential and currents for the modified electrodes based on complex **4**.

Modified GCE	**E/V (H_2O_2) reduction pH 7 buffer**	**Background corrected currents/μA H_2O_2 reduction**
Bare GCE	-0.58	3.85
CoMCPhPc(**4**)-GCE	-0.44	17.61
CoMCPhPc(**4**)-(DAMN)-GONS(linked)-GCE	-0.44	10.73
CoMCPhPc(**4**)-(DAMN)-SDGONS(linked)-GCE	-0.55	13.31
CoMCPhPc(**4**)-(DAMN)-NDGONS(linked)-GCE	-0.53	21.41
CoMCPhPc(**4**)-(DAMN)-SNDGONS(linked)-GCE	-0.53	30.00
CoMCPhPc(**4**)@(DAMN)-GONS-GCE	-0.55	54.52
CoMCPhPc(**4**)@(DAMN)-SDGONS-GCE	-0.57	56.82
CoMCPhPc(**4**)@(DAMN)-NDGONS-GCE	-0.57	77.07
CoMCPhPc(**4**)@(DAMN)-SNDGONS-GCE	-0.71	280.31

[a] "@" = Pc adsorbed onto the nanomaterials; "-" accompanied by linked = covalent bond. DAMN = diaminomaleonitrile; "r" in front of GONS = reduced; if no "r", the GONS were not reduced.

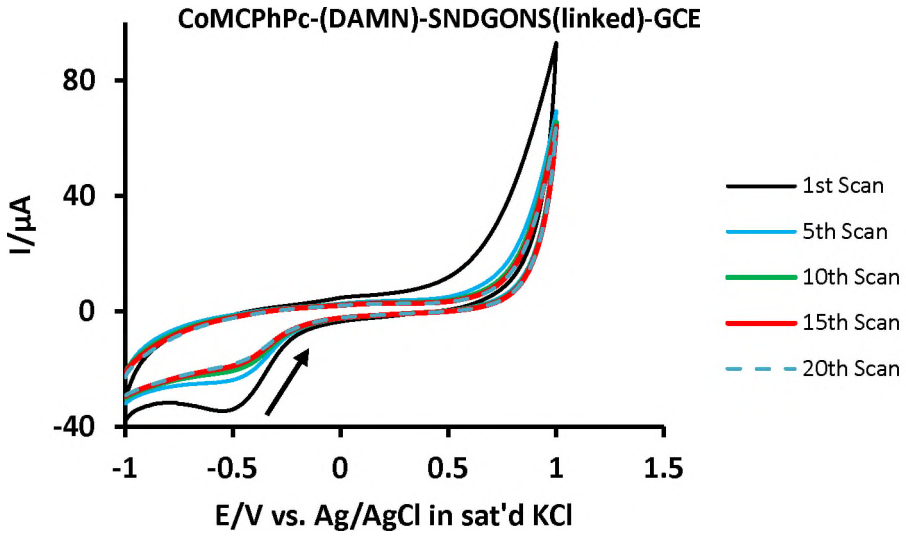
CoMCPhPc-(DAMN)-SNDGONS(linked)-GCE
80
40
0
-40
I/µA
-1
-0.5
0
0.5
1
1.5
E/V vs. Ag/AgCl in sat'd KCl
1st Scan
5th Scan
10th Scan
15th Scan
20th Scan

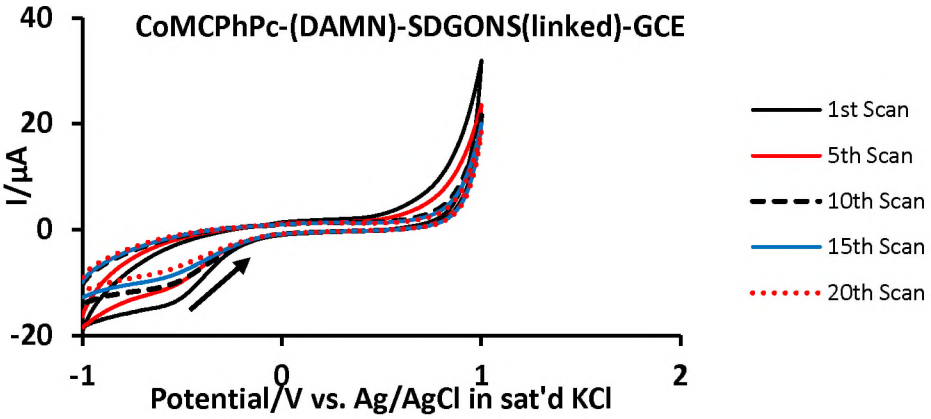
CoMCPhPc-(DAMN)-SDGONS(linked)-GCE
40
20
0
-20
I/µA
-1
0
1
2
Potential/V vs. Ag/AgCl in sat'd KCl
1st Scan
5th Scan
10th Scan
15th Scan
20th Scan

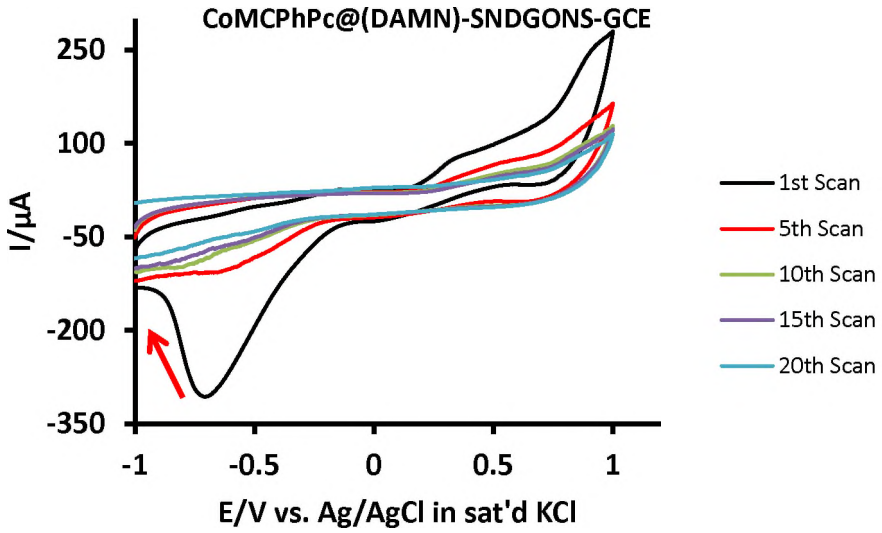
CoMCPhPc@(DAMN)-SNDGONS-GCE
250
100
-50
-200
-350
I/µA
-1
-0.5
0
0.5
1
E/V vs. Ag/AgCl in sat'd KCl
1st Scan
5th Scan
10th Scan
15th Scan
20th Scan

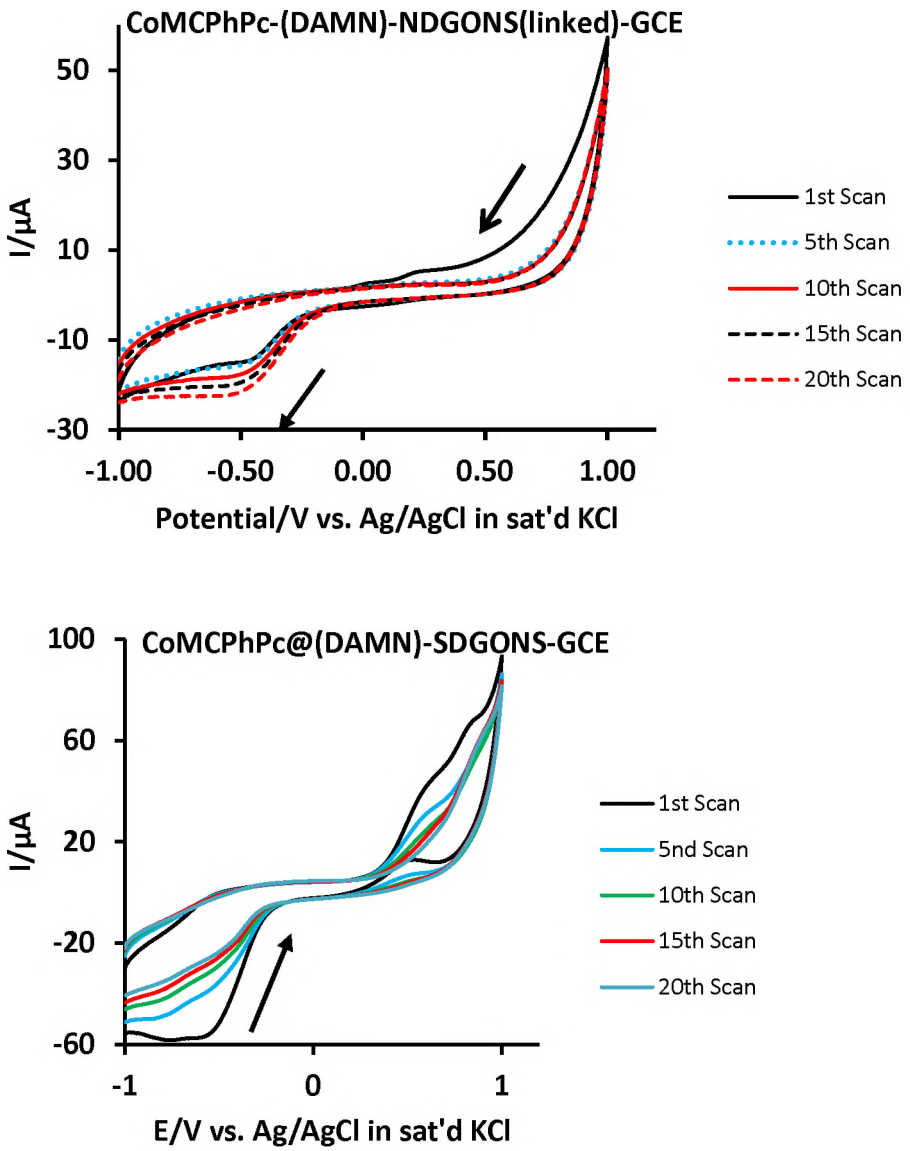

Fig 5.26. Cyclic voltammograms (20 successive cycles, only 1, 5, 10, 15 and 20th scan shown) in 1 mM hydrogen peroxide. Scan rate of 100 mV/s. pH = 7 buffer.

The stability of the developed probes was investigated by running 20 successive scans in 1 mM hydrogen peroxide and it was observed that nitrogen doping resulted in significant stability, **Fig. 5.26** (see for example CoMCPhPc(**4**)-(DAMN)-NDGONS(linked)-GCE). CoMCPhPc(**4**)-(DAMN)-NDGONS(linked)-GCE saw the detection currents improving with successive

scans. Sulphur doped graphene showed a greater extent of fouling as shown in **Fig 5.26,** with no clear peaks after 20 scans for CoMCPhPc(**4**)@(DAMN)-SDGONS-GCE. Generally, while the covalently linked probes showed lower detection currents than the sequentially modified probes, the former showed higher resistance to fouling. High currents observed from sequentially modified probes may suggest that more of complex **4** is in the probe than what results from probes modified with pre-covalently linked modifiers.

5.5.2 Kinetic studies of hydrogen peroxide detection

The electrodes were scanned at varying rates in 1 mM hydrogen peroxide in the potential window -1 V to +1 V {**Fig. 5.27** CoMCPhPc(**4**)-GCE as an example}. For all the probes under investigation, it was noted that the peak potential varied linearly with the logarithm of the scan rate, which is indicative of irreversible reaction at the surface of the electrode, **Fig. 5.27C**. Almost all Tafel slopes obtained in this work fell in the normal range 30 mV/decade to 120 mV/decade [184] as shown in **Table 5.12 and Fig 5.27**for the linked probes yet very abnormally high for the sequential modification. The abnormally high Tafel slopes for the sequentially modified probes are characteristic of chemical complication where products and/or intermediates may adsorb on the electrode surface [184] as discussed above. This may be plausible as such behaviour could be the same contributing to substantial electrode surface fouling observed for these electrodes as discussed above.

To confirm the possible interaction between hydrogen peroxide and the electrode (hence to explain the high Tafel slopes), XPS O1s signal was

recordedbefore analysis in the presence of pH 7 buffer and after analysis to eliminate the signal contribution of the buffer. It was observed that the main peaks before hydrogen peroxide analysis at 529.1 eV, 531.1 eV and 533.5 eV corresponding to C(O)O, C=O and COH respectively shifted after analysis to 528.9 eV, 531.3 eV and 533.2 eV. C(O)O dominates C-OH before analysis and vice versa after analysis, (**Fig. 5.28**). These observations could indicate adsorption of H_2O_2 or its oxidation products during electrocatalysis.

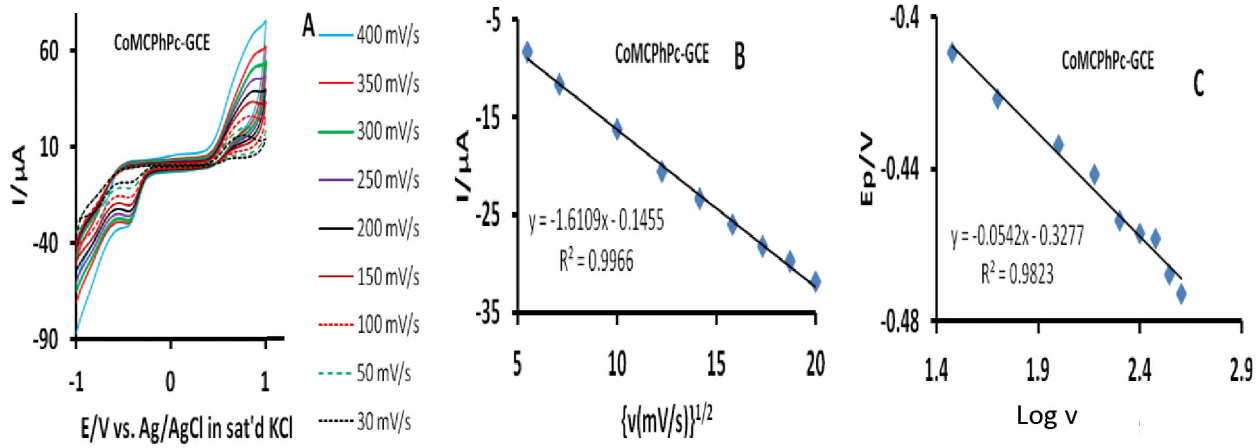

Fig. 5.27. (A) cyclic voltammograms of the detection hydrogen peroxide at different scan rates, (B) plot of Ip vs. $v^{1/2}$ and (C) plot of peak potential vs. log v, in 1 mM hydrogen peroxide. pH 7 buffer. Electrode: CoMCPhPc(**4**)-GCE.

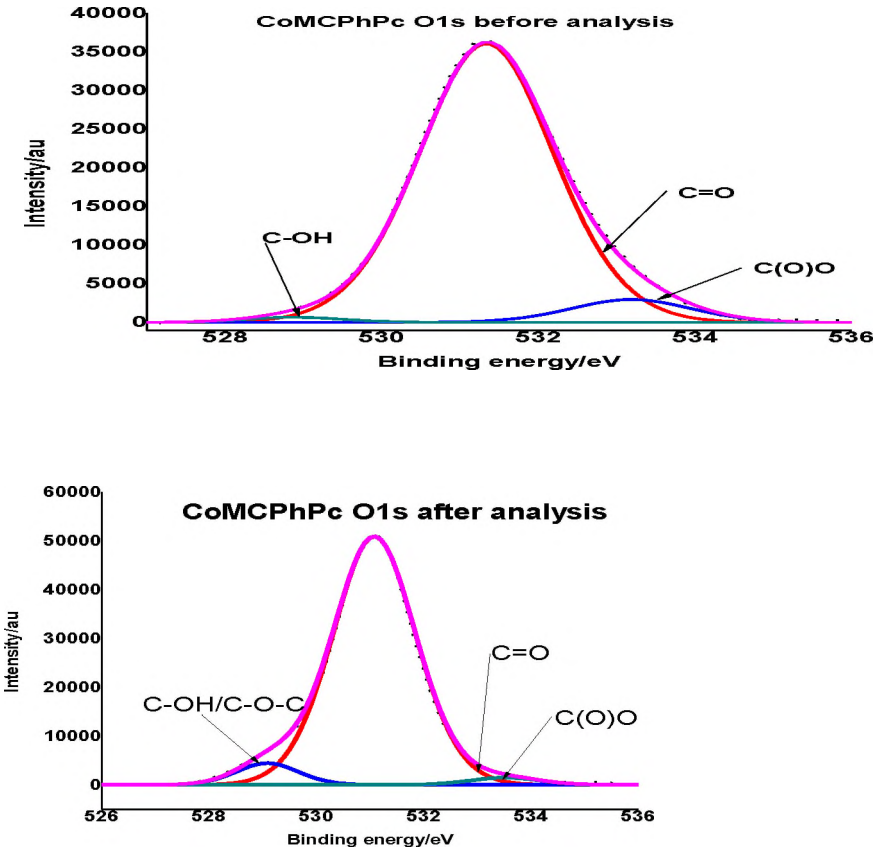

Fig 5.28 The effect of hydrogen peroxide catalysis on the electrode modifier Electrode: CoMCPhPc(**4**)-GCE.

The linearity obtained in the plot of peak current against the square root of scan rate is evidence for a diffusion-controlled reaction **Fig. 5.27B**. As already stated, the steeper the gradient of such a plot the faster the electrocatalytic reduction reaction. The gradient of the plots increase in the order (units = $\mu A/(mV.s^{-1})^{½}$: CoMCPhPc(**4**)-(DAMN)-SDGONS(linked)-GCE (0.84) < CoMCPhPc(**4**)-(DAMN)-GONS(linked)-GCE (1.32) < CoMCPhPc(**4**)-GCE (1.61) < CoMCPhPc(**4**)-(DAMN)-NDGONS(linked)-GCE (1.63) < CoMCPhPc(**4**)-(DAMN)-SNDGONS(linked)-GCE (1.91) < CoMCPhPc(**4**)@(DAMN)-SDGONS-GCE (4.68) < CoMCPhPc(**4**)@(DAMN)-GONS-GCE (5.45)

<CoMCPhPc(**4**)@(DAMN)-SNDGONS-GCE (8.85)< CoMCPhPc(**4**)@(DAMN)-NDGONS-GCE (14.37). It is of noteworthy that co-doping has a significant advantage over single element doping in speeding up the electro reduction reaction for the linked probes where MPc is linked to GONS; Compare (units = $\mu A/(mV.s^{-1})^{½}$: CoMCPhPc(**4**)-(DAMN)-SNDGONS(linked)-GCE (1.91) with CoMCPhPc(**4**)-(DAMN)-SDGONS(linked)-GCE (0.84)andCoMCPhPc(**4**)-(DAMN)-NDGONS(linked)-GCE (1.63). The facile reactions observed on the sequentially modified electrode surfaces may be because the metal centre, which happens to be reaction centre,is more exposed to the reactants unlike in their covalently linked counterparts. It can also be postulated that there could be more reaction centres in the latter hence the high currents observed.

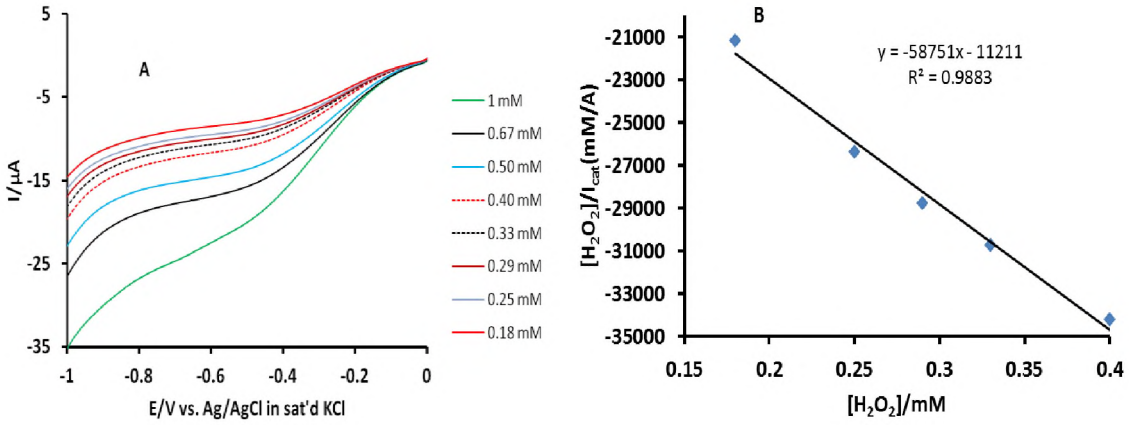

Fig. 5.29. (A) Linear sweep voltammograms and (B) Langmuir adsorption isotherm plot for CoMCPhPc(**4**)-(DAMN)-SNDGONS(linked)-GCE in 1 mM hydrogen peroxide. pH 7 buffer.

Linear sweep voltammetry was done for the cathodic reaction of CoMCPhPc(**4**)-(DAMN)-SNDGONS(linked)-GCE (as an example since all

electrodes showed similar behaviour) in 1 mM hydrogen peroxide (**Fig. 5.29**) to understand the adsorptive behaviour of the electrodes. By applying Langmuir adsorption theory, a linear plot of the ratio of hydrogen peroxide concentration to catalytic current against concentration of hydrogen peroxide was obtained (**Fig. 5.29, Eqn 5.7**) which is indicative of adsorption behaviour further consolidating the relatively high Tafel slope.

The slope and the intercept of **Fig. 5.29B** were then used to deduce the adsorption equilibrium constant (β = 5.24 x 10^3 M^{-1}). **Using equation 5.8**, ΔG^o was found to be -21.22 $kJmol^{-1}$. This value is comparable to those reported elsewhere for high Tafel slopes [175] but larger than reported above for other CoPc based electrodes in this work.

5.5.3. Chronoamperometry studies.

Chronoamperometry showed that the catalytic currents were dominated by electro-catalysed reduction of hydrogen peroxide **(Fig. 5.30,** CoMCPhPc(**4**)-GCE as an example). The plots of the ratio of catalytic currents to buffer currents against the square root of time, **equations 5.2** [169] produced linear relationships of varying gradients for different concentrations, **Fig. 5.30**.

Plotting the square of the slopes (from **Fig. 5.30B**) against the respective concentrations gave linear plots (**Fig. 5.30C**) whose slope is equal to πk where k is the rate constant. The plots are represented by equations **5.38 – 5.46.**

CoMCPhPc(**4**)-GCE:

$$y = 1.0309[H_2O_2]\left(\frac{s^{-1}}{mM}\right) - 0.3657s^{-1}, R^2 = 0.9858 \qquad 5.38$$

CoMCPhPc(**4**)-GONS(linked)-GCE:

$$y = 8.2206[H_2O_2]\left(\frac{s^{-1}}{mM}\right) - 1.5066s^{-1}, R^2 = 0.9905 \quad 5.39$$

CoMCPhPc(**4**)-SDGONS(linked)-GCE:

$$y = 9.484[H_2O_2]\left(\frac{s^{-1}}{mM}\right) - 2.08382s^{-1}, R^2 = 0.9959 \quad 5.40$$

CoMCPhPc(**4**)-NDGONS(linked)-GCE:

$$y = 0.5279[H_2O_2]\left(\frac{s^{-1}}{mM}\right) - 0.0631s^{-1}, R^2 = 0.9351 \quad 5.41$$

CoMCPhPc(**4**)-SNDGONS(linked)-GCE:

$$y = 8.8461[H_2O_2]\left(\frac{s^{-1}}{mM}\right) - 1.6519s^{-1}, R^2 = 0.9922 \quad 5.42$$

CoMCPhPc(**4**)@GONS(seq)-GCE:

$$y = 0.1225[H_2O_2]\left(\frac{s^{-1}}{mM}\right) - 1.0336s^{-1}, R^2 = 0.9963 \quad 5.43$$

CoMCPhPc(**4**)@SDGONS(seq)-GCE:

$$y = 0.5006[H_2O_2]\left(\frac{s^{-1}}{mM}\right) - 0.1175s^{-1}, R^2 = 0.9617 \quad 5.44$$

CoMCPhPc(**4**)@NDGONS(seq)-GCE:

$$y = 3.0333[H_2O_2]\left(\frac{s^{-1}}{mM}\right) - 0.6213s^{-1}, R^2 = 0.9873 \quad 5.45$$

CoMCPhPc(**4**)@SNDGONS(seq)-GCE:

$$y = 965.1[H_2O_2]\left(\frac{s^{-1}}{mM}\right) - 221.77s^{-1}, R^2 = 0.9073 \qquad 5.46$$

From **equations 5.37 – 5.45**, the catalytic rate constants were evaluated to be in the range 3.90 x 10^1 to 3.07 x 10^5 $M^{-1}s^{-1}$ (**Table. 5.12**). Sulphur containing GONS show appreciably high catalytic rate constants for both linked and sequential electrodes. These values are in agreement or an improvement to the previously reported literature values [181,198], also in the same range as in **Table 5.4**. The probes showed very low LODs in the nanomolar ranges (**Table 5.12**) as observed for **1**-GONS in **Table 5.5** but lower than for complex **5** in **Table 5.9**. The best detection limit in this section was obtained for CoMCPhPc(**4**)@(DAMN)-SNDGONS-GCE at 1.58 nm. It is however important to note that direct comparison between the linked and sequentially formed electrodes is difficult since the amounts of the components on the electrodes may not be the same as noted above.

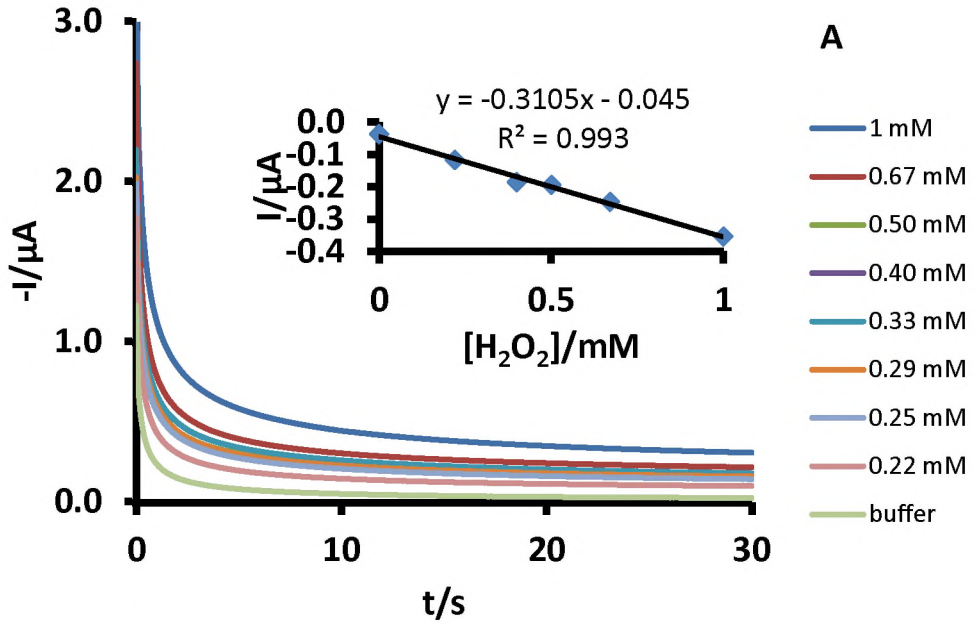
A
3.0
2.0
1.0
0.0
-I/µA
0
10
20
30
t/s
y = -0.3105x - 0.045
R² = 0.993
0.0
-0.1
-0.2
-0.3
-0.4
I/µA
0
0.5
1
[H2O2]/mM
1 mM
0.67 mM
0.50 mM
0.40 mM
0.33 mM
0.29 mM
0.25 mM
0.22 mM
buffer

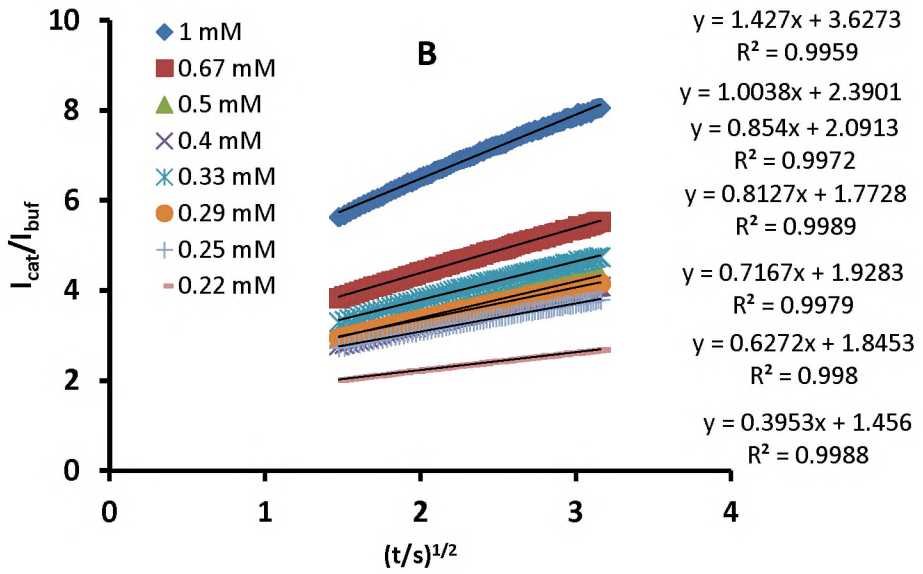
B
10
8
6
4
2
0
Icat/Ibuf
0
1
2
3
4
(t/s)1/2
1 mM
0.67 mM
0.5 mM
0.4 mM
0.33 mM
0.29 mM
0.25 mM
0.22 mM
y = 1.427x + 3.6273
R² = 0.9959
y = 1.0038x + 2.3901
y = 0.854x + 2.0913
R² = 0.9972
y = 0.8127x + 1.7728
R² = 0.9989
y = 0.7167x + 1.9283
R² = 0.9979
y = 0.6272x + 1.8453
R² = 0.998
y = 0.3953x + 1.456
R² = 0.9988

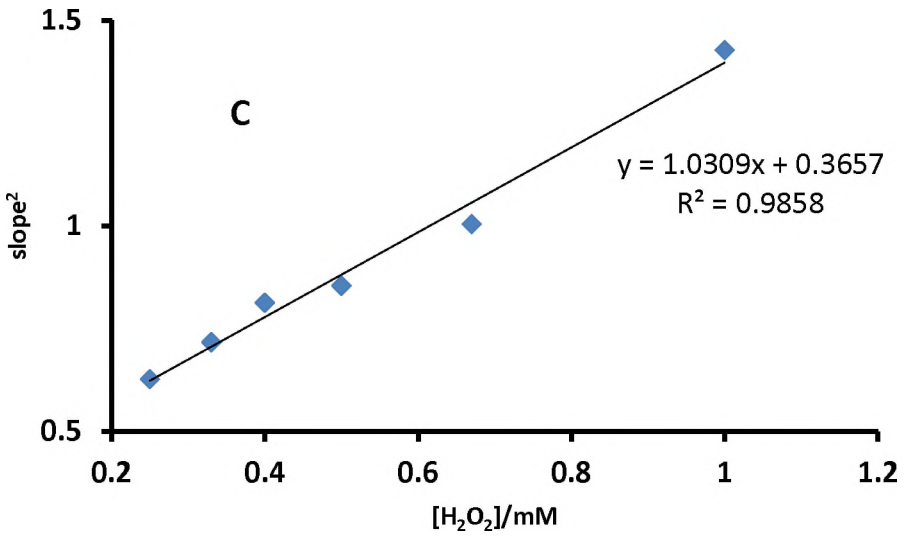

Fig. 5.30. (A) Chronoamperogramms on CoMCPhPc(**4**)-GCE at different concentrations of hydrogen peroxide, insert = corresponding calibration curve, (B) plots of current ratio versus square root of time, and (C) plots of square of gradients of plots in B versus concentration of hydrogen. pH 7 buffer. Reduction potential – 0.44 V.

Table 5.12 Complex 4 electrode performance characteristics

Modified GCE	pH	Tafel Slope (mV/decade)	LOD/nM	k ($M^{-1}s^{-1}$)	Ref
CoMCPhPc(**4**)-GCE	7	108	19.52	3.28×10^2	TW
CoMCPhPc(**4**)-(DAMN)-GONS(linked)-GCE	7	123	32.24	2.62×10^3	TW
CoMCPhPc(**4**)-(DAMN)-SDGONS(linked)-GCE	7	82	5.44	3.01×10^3	TW
CoMCPhPc(**4**)-(DAMN)-NDGONS(linked)-GCE	7	96	3.55	1.68×10^2	TW
CoMCPhPc(**4**)-(DAMN)-SNDGONS(linked)-GCE	7	117	4.53	2.82×10^3	TW
CoMCPhPc(**4**)@(DAMN)-GONS-GCE	7	416	7.86	3.90×10^1	TW
CoMCPhPc(**4**)@(DAMN)-SDGONS-GCE	7	236	6.98	1.59×10^2	TW
CoMCPhPc(**4**)@(DAMN)-NDGONS-GCE	7	100	15.71	9.66×10^2	TW
CoMCPhPc(**4**)@(DAMN)-SNDGONS-GCE	7	618	1.58	3.07×10^5	TW
rGONS/CoPc–COOH	7.4	-	60 000	-	[186]
SPAuE–PA–MnTAPc	7.4	-	117	-	[163]
CPE	8	-	5610	6.46×10^2	[198]
poly (Ni^{II}teta)	13.3	-	-	1.77×10^3 1.29×10^3	[181]

[a] "@" = Pc adsorbed onto the nanomaterials; "/" =a mixture of different nanomaterials; "-" covalent bond. DAMN = diaminomaleonitrile; mix = mixed before electrode modification; seq = sequentially added to the electrode; "r" in front of GONS = reduced; if no "r", the GONS were not reduced;SPAuE = screen printed gold electrode; CPE =carbon paste electrode; Ni^{II}teta= nickeltetraazacyclotetradecane

5.6 Conclusions

The developed nanoprobes were capable of effective electrooxidationof hydrogen peroxide and L-cysteine and electro reduction of hydrogen peroxide. Carbon based nanomaterials resulted in improvements in detection currents of MPcs. Covalent linkage of doped GONS resulted in the lowering of overpotentials while covalent linkage of MWCNTs resulted in both higher detection currents and low overpotentials. The inclusion of these nanomaterials also improved the stability of the nanoprobes. AuNRs based nanoprobes exhibited lowered detection overpotentials though they were prone to fouling in catalytic platforms containing GONS during detection cycles. It was also noted that the smaller the size of the MPc**NP** the better the detection currents with CoPc**NP**(**3**) based electrodes giving excellent electro-oxidation rate constants and significant resistance to fouling when compared to both CoTAPc**NP**(**5**) and CoTAPhPc**NP**(**1**) based electrodes. Sulphur doping results in high catalytic currents.

Chapter Six

6. Optical Sensing

This chapter focuses on fluorescence sensing of hydrogen peroxide using composites of ZnOCPc (**6**) and graphene oxide nanosheets. The sensing mechanism is based on the restoration of fluorescence of the conjugates as the concentration of the analyte increases.Hydrogen peroxide fluorescence sensing was done to compare with electrocatalysis presented in Chapter 5.

6.1. Fluorescence quenching

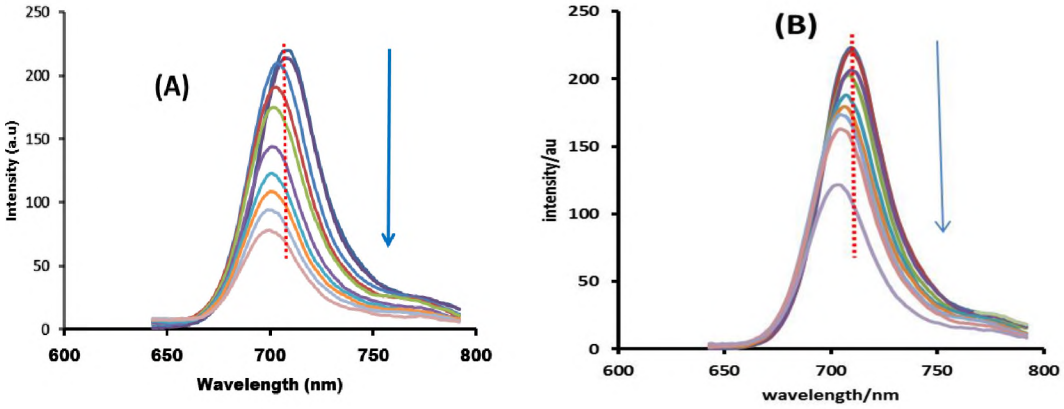

Fig.6.1 Quenching of ZnOCPc(**6**) in the presence of increasing concentrations of (A) GONS and (B) rGONS in DMSO. Excitation wavelength, 624 nm. [ZnOCPc(**6**)]=2 x 10^{-6}, [GONS] or [rGONS]=0 μgml^{-1} to 150 μgml^{-1}

There is increased quenching of fluorescence of ZnOCPc (**6**) in **Fig. 6.1** with increasing amounts of GONS or rGONS. There is also a shift in the emission peaks of ZnOCPc(**6**) to the blue as the concentration of either GONS or rGONS increases. Fluorescence quantum yields were calculated using established methods [199] and unsubstituted ZnPc as a standard in DMSO used: Φ_F = 0.20 [200]. The fluorescence quantum yield for ZnOCPc (**6**) (Φ_F = 0.14) was slightly reduced in both ZnOCPc(**6**)-rGONS and ZnOCPc(**6**)-GONS to 0.11 and

0.10, respectively due to quenching by GONS or rGONS, **Table 6.1.** Fluorescence lifetime for ZnOCPc(**6**) (**Table 6.1**) was however not quenched in the presence of rGONS or GONS, **Table 6.1**. There were no significant changes in the emission spectral intensity of ZnOCPc(**6**) (in the absence of GONS or rGONS) on addition of hydrogen peroxide.

Table 6.1 Photophysical properties of ZnOCPc(**6**) and conjugates in DMSO

Material	λ_{abs} (nm)	λ_{em} (nm)	Φ_f	τ_F
ZnOCPc	696	707	0.14	2.29
ZnOCPc-rGONS	696	705	0.10	2.29
ZnOCPc-GONS	698	707	0.11	2.29

6.2. Hydrogen peroxide sensing with ZnOCPc(6)-GONS conjugates

Hydrogen peroxide enhances the fluorescence of ZnOCPc (**6**) initially quenched by GONS and rGONS, **Fig. 6.1** but was enhanced by hydrogen peroxide, **Fig. 6.2.**A red-shift was observed accompanied by fluorescence "turn on" during the addition of increased amounts of hydrogen peroxide to ZnOCPc(**6**)-rGONS in **Fig. 6.2B**, corresponding to the blue shifting on quenching in **Fig. 6.1.** There was however no significant shift on "turn on" in the case of the ZnOCPc(**6**)-GONS in **Fig. 6.2A**. This lack of significant shift was also observed between porphyrin-GONS on "turn on" upon addition of iron III ions by Liu et. al. [149]. The observed shifts in the emission spectra is largely dependent on the degree of flattening of the Pcs on graphene moieties.

The rGONS have significant π-π interactions with the Pcs resulting in pronounced flattening of the Pc as compared to the case of GONS. Upon the addition of hydrogen peroxide there is disruption of the π-π stacking followed by less Pc flattening hence the observed blue shift [201]. It is also important to note that the restoration of the fluorescence is depend end on the concentration ranges investigated. Higher hydrogen peroxide concentrations would result in larger fluorescence enhancement changes. However, the aim physiological hydrogen peroxide concentrations [201].

It can be suggested that the enhancement observed is due to the action of hydrogen peroxide as a spacer between the fluorescent metallophthalocyanine and the quencher. Being a good oxidizing agent, hydrogen peroxide may result in further oxidation of the grapheme moieties thereby interrupting the prior interaction between the graphene sheets and the MPc and hence the restoration of the fluorescence. In order to evaluate the fluorescence enhancement sensitivity of the probe, the fluorescence intensities of the ZnOCPc(**6**)-GONS or ZnOCPc(**6**)-rGONS in the absence (F_0) and presence (F) of H_2O_2 were investigated using **Eq. (6.1).**

$$\frac{F}{F_o} = 1 + K[H_2O_2] \qquad 6.1.$$

where K is the Stern–Volmer quenching rate constant. It should be noted that **Eq. (6.1)** relates to F/F_0 (due to enhancement of fluorescence) instead of F_0/F usually employed for quenching of fluorescence.

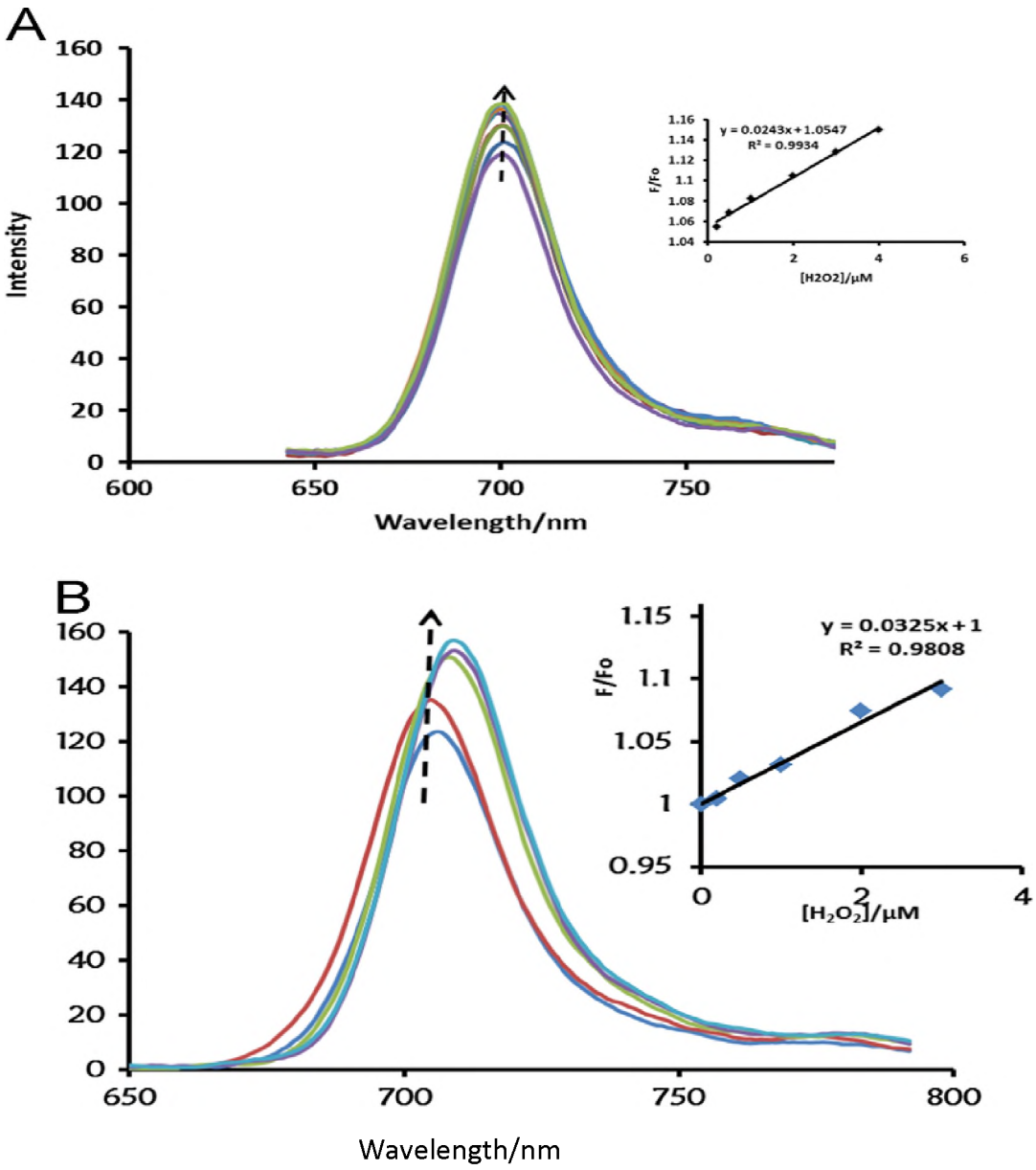

Fig. 6.2 Fluorescence enhancement of ZnOCPc(**6**)-GONS [H_2O_2] = 0.2; 0.5; 1; 2; 3; 4 μM (A) and ZnOCPc(**6**)-rGONS [H_2O_2] = 0; 0.2; 0.5; 2; 3 μM (B) in the presence of H_2O_2. Inserts = the Stern Volmer plots

As displayed in the insets in **Fig. 6.2**, plots of F/F_0 against H_2O_2 concentrations were linear. The value of K for ZnOCPc(**6**)-GONS was 0.024 M^{-1} and for ZnOCPc(**6**)-rGONS, the value was 0.032 M^{-1}, showing better

sensitivity for ZnOCPc(**6**)-rGONS. The limit of detection (LOD) was evaluated as already described for electrocatalysis. ZnOCPc(**6**)-GONS and ZnOCPc(**6**)-rGONS have LODs of 3.86 μM and 2.82 μM respectively for (n = 10) and measured at 15 min intervals to allow stabilisation of the instrument. These values are higher than those for QDs-Pc reported elsewhere [202] but however comparable to values found elsewhere [203] but higher than electrocatalysis, Chapter 5, showing that the latter is more sensitive.

6.3. Sensor selectivity

The ZnOCPc(**6**)-rGONS and ZnOCPc(**6**)-GONS's selectivity was tested against a number of physiological interferences, **Fig. 6.3**. To as tock solution of each conjugate, H_2O_2 was added to make a concentration of 5 x 10^{-6} M and the fluorescence measured. The obtained signal is the control. To this stock solution, the interferents were individually added and the percentage fluorescence intensity change determined. An increase in the fluorescence intensity is denoted positive and decrease denoted negative in **Table6.2**. The decrease mean fluorescence quenching while increase mean enhancement upon interferent addition. An increase in the ZnOCPc(**6**) fluorescence signal was observed only for TBHP (tert-butyl hydroperoxide),nitrate and urea in the presence of rGONS, **Fig. 6.3** and **Table 6.2**. The rest of the analytes show decrease in signals. The changes in intensity are however very low and hence there is negligible interference. Nitrite showed the highest fluorescence intensity change.

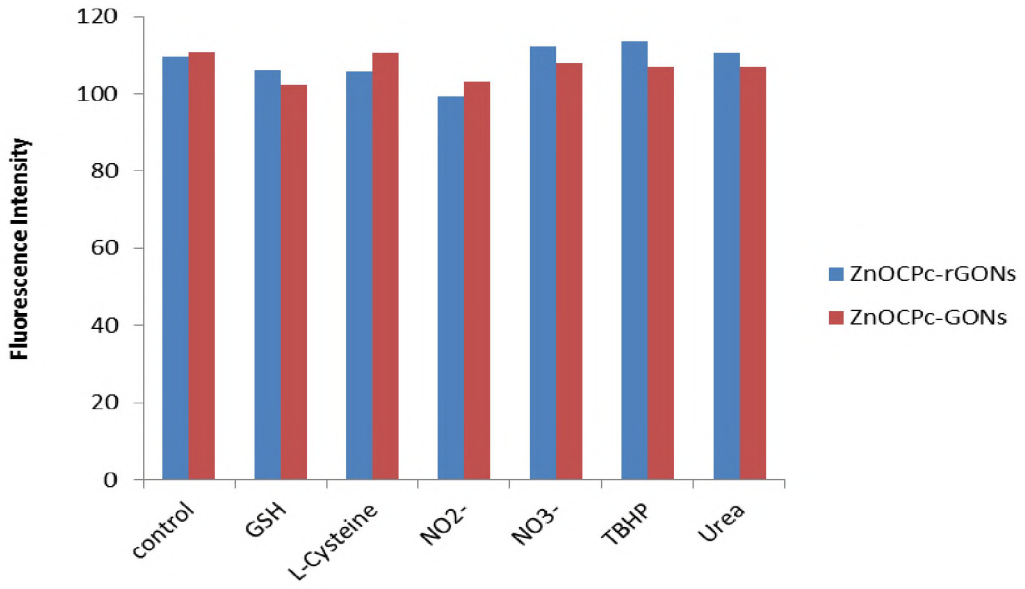

Fig. 6.3. Effects of biologically active species on the fluorescence of ZnOCPc(**6**)-GONS conjugates. Control comprises of ZnOCPc(**6**)-GONS-H_2O_2 [H_2O_2] = 5 x 10^{-6} M. The others have the interferents added at concentration 5 x 10^{-5} M.

Table 6.2. Percentage Fluorescence Intensity (%FI) change of co-existing biological active species on the detection of H_2O_2 by ZnOCPc(**6**)-rGONS and ZnOCPc(**6**)-GONS.

Species	**ZnOCPc(6)-GONS (%FI) change**	**ZnOCPc(6)-rGONS (%FI) change**
GSH	-0.04	-0.04
L-Cysteine	-0.004	-0.04
NO_2^-	-0.08	-0.10
NO_3^-	-0.03	+0.03
TBHP[a]	-0.04	+0.01
Urea	-0.04	+0.01

[a]tert-Butylhydroperoxide

6.4. Conclusion

ZnOCPc(**6**)-rGONS showed better detection sensitivity and lower limits of detection as compared to ZnOCPc(**6**)-GONS. The optical probes are promising platforms for the detection of hydrogen peroxide. The LODs reported here are in the upper range of some determined electrochemically.

Chapter Seven

7.1 Conclusions

Glassy carbon electrode was successfully modified by cobalt tetra aminophenoxy phthalocyanine {CoTAPhPc (**1**)} in the presence of reduced graphene oxide nanosheets (rGONS) and multi-walled carbon nanotubes (MWCNTs) and used for the detection of L-cysteine as a test analyte. CoTAPhPc(**1**)@MWCNT-GCE was found to be a better sensor for L-cysteine than the other probes incorporating rGONS in terms of detection currents and limits of detection. Sequential layers of MWCNT and rGONS improves conductivity compared to CoTAPhPc (**1**) alone or when MWCNT/rGONS are mixed. It was observed that inclusion of rGONS results in resistance to passivation. Generally, the inclusion of the carbon-based nanomaterials resulted in the improvement of the properties of the phalocyanine towards electrical conductivity hence L-cysteine detection. The low detection limit 30 nM indicate CoTAPhPc(**1**)@MWCNT-GCE can be used as potential platform for the detection and quantification of L-cysteine.

This work also demonstrates the essence of combining MPc with nanomaterials (metallic and carbon based) for electrode modification for hydrogen peroxide electro-oxidation and electro-reduction. Carbon based nanomaterials (multiwalled carbon nanotubes and graphene oxide nanosheets) enhanced detection currents of MPcs and significantly resulted in low limits of detection. These properties were even improved more upon heteroatom doping of GONS. While the incorporation of AuNRs did not result in improvement of detection currents of most conjugates, they significantly lowered the detection overpotentials. The same effect was observed for

covalently linked carbon based nanomaterial MPc conjugates. The nanosizing of Pcs resulted in improved detection currents and low detection overpotentials. It was also observed that MPc**NP** based electrodes had exhibited stable electrocatalytic platforms compared to their bulk counterparts. This work also demonstrates the importance of GONS reduction, doping and co-doping. It has been observed that reduction of GONS improves detection currents while doping makes the conjugates even better, improving even more upon co-doping.

Most of the MPc based modified electrodes were capable of both electrooxidation and electro reduction detection of hydrogen peroxidethough electrooxidation resulted in pronounced electrode fouling. Cobalt phthalocyanine nanosized (**3**) based electrodes however, showed a very stable electro-oxidation peak, which was resistant to fouling. Electro-oxidation is favourable due to its oxygen free interference. CoPc**NP**(**3**)-GCE and CoPc**NP**(**3**)@rSDGONS-GCE electrooxidation had very high catalytic rate constants of 6.38 x 10^5 $M^{-1}s^{-1}$ and 4.36 x 10^4 $M^{-1}s^{-1}$respectively and detection limits of 8.12 μM and 1.49 μM respectively. Though these are not the best LODs reported in this work, they are very good for the reason that they are not prone to much interference.

Linear scan voltammetry was used to demonstrate that the electrocatalytic behavior of the developed platforms was energetically feasible as demonstrated by favourably high Gibbs energies. Generally, the kinetic data suggest strong substrate catalyst interaction as evidenced by relatively high Tafel slopes.

Optical sensors for hydrogen peroxide were also developed from ZnOCPc(**6**) conjugated to grapheme oxide moieties through π-π interactions. The MPc based fluorescence was switched off on conjugation because of photo induced electron transfer. ZnOCPc(**6**)-rGONS showed a higher quenching constant value of 0.032 M^{-1} compared to that of ZnOCPc(**6**)-GONS0.024M^{-1}. Both conjugates had their fluorescence restored linearly with increasing concentrations of hydrogen peroxide. ZnOCPc(**6**)-rGONS had a lower LOD of 2.82 μM as compared to that of ZnOCPc(**6**)-GONS of 3.86 μM. The selectivity of the novel nanoprobe was tested by sensing hydrogen peroxide in the presence of interfering ion sat concentrations ten fold that of the hydrogen peroxide and results obtained showed that the signal was kept at less than 1% deviation hence insignificant interference. Probesfor hydrogen peroxide sensing have potential in areas such as clinical diagnosis and environmental monitoring. Hydrogen peroxide only becomes toxic to the body at elevated concentrations (> 50 μM) therefore the present work offers not only an attractive analytical significance but also physiological relevance.

In summary the presence of nanomaterials resulted in enhanced electrocatalytic properties of the MPcs. Electrochemical detection of hydrogen peroxide was better than fluorescence enhancement due to low fluorescence of ZnOCPc (**6**) in general.

7.2 Future Perspectives.

After observing that non-metallic doped carbon based nanomaterials result in improved electrocatalytic properties of phthalocyanines, it would be

interesting to try to see how doping with non-precious metallic elements would affect the electrocatalysis. While it is good that this work demonstrates the ability of gold nanoparticles in lowering the over potential of conjugates of MPcs and carbon based nanomaterials, it will be noble to investigate the effect of non-precious metallic nanoparticles since they are more economically accessible than gold. It will also be interesting to find ways of covalently linking the modifiers not only among themselves, but also to the electrode surface in an effort to come up with more stable and reproducible nanoprobes.

Since ZnOCPc(**6**) conjugates are water soluble and less aggregated, it will be interesting to do the same studies in aqueous media to confirm that the nanoprobes can be applied in environmental and biological environments. The use of more fluorescent molecules such as boron-dipyrromethenes (BODIPYs) and porphyrins or their MPc derivatives could see the development of better optical nanoprobes. Such molecules could be conjugated to differently modified carbon nanomaterials and yield a less expensive fluorescence sensor platform.

References

[1] V.N. Nemykina, E.A. Lukyanets, Rev. Accounts Ark. (i) (2010) 136–208.

[2] L.A. Muehlmann, M.C. Rodrigues, J.P.F. Longo, M.P. Garcia, K.R. Py-Daniel, A.B. Veloso, P.E.N. de Souza, S.W. da Silva, R.B. Azevedo, J. Nanobiotechnology 13 (2015) 1–11.

[3] N.V. Velloso, L.A. Muehlmann, J. Paulo, F. Longo, J. Rodrigues, D. Cervelle, Chemotherapy 1 (2012) 3–6.

[4] I. Mfouo-Tynga, H. Abrahamse, Int. J. Mol. Sci. 16 (2015) 10228–10241.

[5] M.A. Dahlen, Ind. Eng. Chem. 31 (1939) 839–847.

[6] C.W. Foster, J. Pillay, J.P. Metters, C.E. Banks, Sensors (Switzerland) 14 (2014) 21905–21922.

[7] S. Griveau, M. Gulppi, J. Pavez, J.H. Zagal, F. Bedioui, Electroanalysis 15 (2003) 779–785.

[8] J. Pillay, S. Vilakazi, J. Porphyr. Phthalocyanines 16 (2012) 785–792.

[9] T. Basova, V. Plyashkevich, A. Hassan, A.G. Gürek, G. Gümüş, V. Ahsen, Sensors Actuators, B Chem. 139 (2009) 557–562.

[10] D.G. Zhu, M.C. Petty, Sensors Actuators B 2 (1990) 265–269.

[11] H. Dumrul, F. Yuksel, Polyhedron 63 (2013) 83–90.

[12] V.N. Nemykin, S. V Dudkin, F. Dumoulin, C. Hirel, Rev. Accounts Ark.

(i) (2014) 142–204.

[13] S.S. Erdem, I. V Nesterova, S.A. Soper, R.P. Hammer, J. Org. Chem 73 (2008) 5003–5007.

[14] M. Haas, S. Liu, A. Neels, S. Decurtins, Eur. J. Org. Chem. 1 (2006) 5467–5478.

[15] K. Müller, M. Richter, D. Friedrich, I. Paloumpa, U.I. Kramm, D. Schmeißer, Solid State Ionics 216 (2012) 78–82.

[16] N. Pereira-Rodrigues, R. Cofré, J.H. Zagal, F. Bedioui, Bioelectrochemistry 70 (2007) 147–154.

[17] S. Nyoni, T. Nyokong, Polyhedron 98 (2015) 47–54.

[18] Y. Yan, S. Lu, B. Li, R. Zhu, J. Zhou, S. Wei, J. Phys. Chem. A 110 (2006) 10757–10762.

[19] B.N. Achar, G.M. Fohlen, J.A. Parkers, J. Keshavayya, Polyhedron 6 (1987) 1463–1467.

[20] M.A. Zolfigol, A.R. Pourali, S. Sajjadifar, S. Farahmand, Der Pharma Chem. 4 (2012) 1397–1403.

[21] T. Saito, T. Kawanishi, A. Kakuta, Jpn. J. Appl. Phys. 30 (1991) L1182.

[22] H.. Chen, K.. Jiang, M. Wang, S.. Yang, J. Photochem. Photobiol. A Chem. 117 (1998) 149–152.

[23] W.Y. Tong, A.B. Djuris, H.W. Lin, S. Gwo, J. Phys. Chem. B 2006, 110

(2006) 17406–17413.

[24] Y. Zhang, S.F. Ali, E. Dervishi, Y. Xu, Z. Li, D. Casciano, A.S. Biris, Am. Chemcial Soc. 4 (2010) 3181–3186.

[25] S. Liu, T.H. Zeng, M. Hofmann, E. Burcombe, J. Wei, R. Jiang, J. Kong, Y. Chen, ACS Nano 5 (2011) 6971–6980.

[26] Z. Zhu, L. Garcia-Gancedo, A.J. Flewitt, H. Xie, F. Moussy, W.I. Milne, Sensors (Basel). 12 (2012) 5996–6022.

[27] M.R. Maschmann, P.B. Amama, A. Goyal, Z. Iqbal, T.S. Fisher, Carbon N. Y. 44 (2006) 2758–2763.

[28] A. Mansour, M. Razafinimanana, M. Monthioux, M. Pacheco, A. Gleizes, Carbon N. Y. 45 (2007) 1651–1661.

[29] M.R. Maschmann, P.B. Amama, A. Goyal, Z. Iqbal, R. Gat, T.S. Fisher, Carbon N. Y. 44 (2006) 10–18.

[30] V. Saini, A.S. Biris, E. Dervishi, Z. Li, A.R. Biris, D. Lupu, R.B. Little, S. Trigwell, Z. Rahman, D. Saini, Part. Sci. Technol. 26 (2008) 521–528.

[31] H.K. Youn, J. Kim, W.S. Ahn, Mater. Lett. 65 (2011) 3055–3057.

[32] G. Wang, B. Wang, J. Park, J. Yang, X. Shen, J. Yao, Carbon N. Y. 47 (2009) 68–72.

[33] S. Stankovich, D.A. Dikin, R.D. Piner, K.A. Kohlhaas, A. Kleinhammes, Y. Jia, Y. Wu, S.T. Nguyen, R.S. Ruoff, Carbon N. Y. 45 (2007) 1558–

1565.

[34] G. Wang, J. Yang, J. Park, X. Gou, B. Wang, H. Liu, J. Yao, J. Phys. Chem. B 112 (2008) 8192–8195.

[35] H. Takehara, M. Fujiwara, M. Arikawa, M.D. Diener, J.M. Alford, Carbon N. Y. 43 (2005) 311–319.

[36] J.M. Hunter, J.L. Fye, E.J. Roskamp, M.F. Jarrold, J. Phys. Chem. 98 (1994) 1810–1818.

[37] J. Shen, Y. Zhu, C. Chen, X. Yang, C. Li, Chem. Commun. 47 (2011) 2580–2582.

[38] X. Yan, X. Cui, L. Li, J. Am. Chem. Soc. 132 (2010) 5944–5945.

[39] M. Zhang, L. Bai, W. Shang, W. Xie, H. Ma, Y. Fu, D. Fang, H. Sun, L. Fan, M. Han, C. Liu, S. Yang, J. Mater. Chem. 22 (2012) 7461–7467.

[40] M. Shao, S. Zhuo, ACS Nano 6 (2012) 6532–6532.

[41] M. Sakho, O.S. Oluwafemi, S. Perumbilavil, J. Mater. Sci. Mater. Electron. 27 (2016) 10926–10933.

[42] Y. Zhang, H. Gao, J. Niu, B. Liu, New J. Chem. 38 (2014) 4970–4974.

[43] H. Cui, K. Zhang, Y. Zhang, Y. Sun, J. Wang, W. Zhang, J.H.T. Luong, Biosens. Bioelectron. 46 (2013) 113–118.

[44] L. Cui, T. Pu, Y. Liu, X. He, Electrochim. Acta 88 (2013) 559–564.

[45] H. Hosseini, M. Mahyari, A. Bagheri, A. Shaabani, Biosens.

Bioelectron. 52 (2014) 136–142.

[46] I. Kruusenberg, L. Matisen, K. Tammeveski, Int. J. Electrochem. Sci. 8 (2013) 1057–1066.

[47] B. Qiu, Z. Lin, J. Wang, Z. Chen, J. Chen, G. Chen, Talanta 78 (2009) 76–80.

[48] X. Sun, F. Li, G. Shen, J. Huang, X. Wang, Analyst 139 (2014) 299–308.

[49] B. Wang, Y. Wu, X. Wang, Z. Chen, C. He, Sensors Actuators, B Chem. 190 (2014) 157–164.

[50] X. Wang, B. Wang, J. Zhong, F. Zhao, N. Han, W. Huang, M. Zeng, J. Fan, Y. Li, Nano Res. 9 (2016) 1–10.

[51] H. Xu, J. Xiao, B. Liu, S. Griveau, F. Bedioui, Biosens. Bioelectron. 66 (2015) 438–444.

[52] T. Mugadza, T. Nyokong, Electrochim. Acta 54 (2009) 6347–6353.

[53] W. Lu, N. Li, W. Chen, Y. Yao, Carbon N. Y. 47 (2009) 3337–3345.

[54] T. Taniguchi, H. Tateishi, S. Miyamoto, K. Hatakeyama, Part. Part. Syst. Characterisation 30 (2013) 1063–1070.

[55] N.A. Kumar, H. Nolan, N. Mcevoy, E. Rezvani, R.L. Doyle, E.G. Lyons, G.S. Duesberg, J. Mater. Chem. A 1 (2013) 4431–4435.

[56] X. Li, H. Wang, J.T. Robinson, H. Sanchez, G. Diankov, J. Am. Chem.

Soc. 131 (2009) 15939–15944.

[57] Z. Wen, X. Wang, S. Mao, Z. Bo, H. Kim, S. Cui, G. Lu, X. Feng, J. Chen, Adv. Mater. 24 (2012) 5610–5616.

[58] D. Long, W. Li, L. Ling, J. Miyawaki, I. Mochida, S. Yoon, Langmuir 26 (2010) 16096–16102.

[59] Y. Hu, J. Jin, P. Wu, H. Zhang, C. Cai, Electrochim. Acta 56 (2010) 491–500.

[60] J. Song, L. Xu, R. Xing, Q. Li, C. Zhou, D. Liu, H. Song, Sci. Rep. 4 (2014) 1–7.

[61] M. Shanmugam, K. Kim, J. Electroanal. Chem. 776 (2016) 82–92.

[62] F. Shi, J. Xi, F. Hou, L. Han, G. Li, S. Gong, C. Chen, W. Sun, Mater. Sci. Eng. C 58 (2016) 450–457.

[63] S. Iijima, Nature 354 (1991) 56–58.

[64] A. Maringa, E. Antunes, T. Nyokong, Electrochim. Acta 121 (2014) 93–101.

[65] K.A. Kozek, K.M. Kozek, W. Wu, S.R. Mishra, J.B. Tracy, Chem. Mater. 25 (2013) 4537–4544.

[66] T. Tangkuaram, C. Ponchio, T. Kangkasomboon, P. Katikawong, W. Veerasai, Biosens. Bioelectron. 22 (2007) 2071–2078.

[67] X. Xia, Y. Xia, Front. Phys. 9 (2014) 378–384.

[68] S.E. Skrabalak, J. Chen, Y. Sun, X. Lu, L. Au, C.M. Cobley, Y. Xia, Acc. Chem. Res. 41 (2008) 1587–1595.

[69] L. Ruiyi, L. Ling, B. Hongxia, L. Zaijun, Biosens. Bioelectron. 79 (2016) 457–466.

[70] G. Bharath, A. Naldoni, K.H. Ramsait, A. Abdel-Wahab, R. Madhu, E. Alsharaeh, N. Ponpandian, J. Mater. Chem. A 4 (2016) 6385–6394.

[71] J. Li, X. Lin, Sensors Actuators, B Chem. 126 (2007) 527–535.

[72] P. Kannan, S. Sampath, S.A. John, J. Phys. Chem. C 114 (2010) 21114–21122.

[73] N. Alexeyeva, L. Matisen, A. Saar, P. Laaksonen, K. Kontturi, K. Tammeveski, J. Electroanal. Chem. 642 (2010) 6–12.

[74] A.J. Jeevagan, S.A. John, RSC Adv. 3 (2013) 2256–2264.

[75] A. Maringa, T. Nyokong, J. Porphyrins Phthalocyanines 18 (2014) 642–651.

[76] M. Pal, V. Ganesan, Langmuir 25 (2009) 13264–13272.

[77] M. Pal, V. Ganesan, J. Electroanal. Chem. 672 (2012) 7–11.

[78] A.A. Saeed, B. Singh, N. Abbas, M. Issa, Electroanal. 2 27 (2015) 1086–1096.

[79] S. Khene, S. Moeno, T. Nyokong, Polyhedron 30 (2011) 2162–2170.

[80] N. Li, M. Zhu, M. Qu, X. Gao, X. Li, W. Zhang, J. Zhang, J. Ye, J.

Electroanal. Chem. 651 (2011) 12–18.

[81] S. Nyoni, T. Nyokong, Electrochim. Acta 136 (2014) 240–249.

[82] K. Wang, J. Xu, K. Tang, H. Chen, 67 (2005) 798–805.

[83] B.O. Agboola, A. Mocheko, J. Pillay, K.I. Ozoemena, J. Porphyrins Phthalocyanines 12 (2008) 1289–1299.

[84] J. Pillay, S. Vilakazi, J. Porphyrins Phthalocyanines 16 (2012) 785–792.

[85] T. Mugadza, A Thesis Submitted in Fulfillment of the Requirements for the Degree of Doctor of Philosophy, Rhodes University, 2010.

[86] B.B.J. Piersma, W. Greatbatch, Plarinum Met. Rev 30 (1986) 120–129.

[87] K. Ogura, S. Yamasaki, J. Appl. Electrochem. 15 (1985) 279–284.

[88] Q. Sheng, D. Zhang, Q. Wu, J. Zheng, H. Tang, Anal. Methods 7 (2015) 6896–6903.

[89] J.H. Zagal, S. Griveau, J.F. Silva, T. Nyokong, F. Bedioui, Coord. Chem. Rev. 254 (2010) 2755–2791.

[90] D.A. Geraldo, J. Limson, T. Nyokong, Electrochim. Acta 53 (2008) 8051–8057.

[91] A. Ashraf, Y. Wu, M.C. Wang, N.R. Aluru, S.A. Dastgheib, S. Nam, Biosens. Bioelectron. 30 (2014) 12827–36.

[92] W. Szymczak, N. Menzel, W.G. Kreyling, K. Wittmaack, Int. J. Mass

Spectrom. 254 (2006) 70–84.

[93] K. Norrman, N.B. Larsen, F.C. Krebs, Sol. Energy Mater. Sol. Cells 90 (2006) 2793–2814.

[94] S.E. Ventosa, W. Schuhmann, P. Chem, C. Phys, Phys. Chem. Chem. Phys. 17 (2015) 28441–28450.

[95] C.G. Zoski, J. Electrochem. Soc. 163 (2016) 3088–3100.

[96] C. Lee, J. Kwak, A.J. Bardt, Proc. Nati. Acad. Sci. USA 87 (1990) 1740–1743.

[97] P. Sun, O. Laforge, M. V Mirkin, Phys. Chem. Chem. Phys. 9 (2007) 802–823.

[98] D. Hynek, M. Zurek, P. Babula, V. Adam, R. Kizek, in:, Mod. Electrochem. Methods Nano, Surf. Corros. Sci., InTechOpen, 2014, pp. 139–170.

[99] J. Yin, W. Ren, G. Yang, J. Duan, X. Huang, R. Fang, C. Li, T. Li, Y. Yin, Y. Hou, S.W. Kim, G. Wu, Mol. Nutr. Food Res. 60 (2016) 134–146.

[100] L.A. Herzenberg, A. Leonore, United States Patent Number 5 607 974, 1997.

[101] A.P. Gutierrez, M.R. Argote, S. Griveau, J.H. Zagal, S.G. Granados, A.A. Ordas, F. Bedioui, J. Chil. Chem. Soc. 57 (2012) 1244–1247.

[102] R. Devasenathipathy, V. Mani, S.M. Chen, K. Kohilarani, S. Ramaraj,

Int. J. Electrochem. Sci. 10 (2015) 682–690.

[103] S. Nyoni, T. Mugadza, T. Nyokong, Electrochim. Acta 128 (2014) 32–40.

[104] B. Halliwell, M.V. Clement, L.H. Long, FEBS Lett. 486 (2000) 10–13.

[105] M.B. Hampton, S. Orrenius, FEBS Lett. 414 (1997) 552–556.

[106] L.H. Long, P.J. Evans, B. Halliwell, Biochem. Biophys. Res. Commun. 262 (1999) 605–609.

[107] X. Qiao, S. Liao, C. You, R. Chen, Catalysts 5 (2015) 981–991.

[108] M. Razdan, D.S. Hall, P.G. Keech, D.W. Shoesmith, Electrochim. Acta 83 (2012) 410–419.

[109] P. Wu, Z. Cai, Y. Gao, H. Zhang, C. Cai, Chem. Commun. 47 (2011) 11327–11329.

[110] K.L. Stewart, A.A. Gewirth, Langmuir 23 (2007) 9911–9918.

[111] X. Liu, C. Qi, T. Bing, X. Cheng, D. Shangguan, Anal. Chem. 81 (2009) 3699–3704.

[112] A.P. De Silva, S. Moody, G.D. Wright, Analyst 134 (2009) 2385–2393.

[113] O. Adegoke, S. Khene, T. Nyokong, J Fluoresc. 23 (2013) 963–974.

[114] O.J. Achadu, T. Nyokong, New J. Chem. 40 (2016) 8727–8736.

[115] K. Ozoemena, N. Kuznetsova, T. Nyokong, J. Photochem. Photobiol. A Chem. 139 (2001) 217–224.

[116] T. Mthethwa, T. Nyokong, Photochem. Photobiol. Sci. 14 (2015) 1346–1356.

[117] S. D'Souza, E. Antunes, T. Nyokong, Inorganica Chim. Acta 367 (2011) 173–181.

[118] E.O. Keiichi Sakamoto, Prog. Org. Coatings 31 (1997) 139–145.

[119] W. Gao, L.B. Alemany, L. Ci, P.M. Ajayan, Nat Chem 1 (2009) 403–408.

[120] L. Niu, Z. Li, W. Hong, J. Sun, Z. Wang, L. Ma, J. Wang, S. Yang, Electrochim. Acta 108 (2013) 666–673.

[121] Z. Sheng, L. Shao, J. Chen, W. Bao, F. Wang, X. Xia, ACS Nano 5 (2011) 4350–4358.

[122] F. Razmjooei, K.P. Singh, M.Y. Song, J.S. Yu, Carbon N. Y. 78 (2014) 257–267.

[123] K. Sanusi, E.K. Amuhaya, T. Nyokong, J. Phys. Chem. C 118 (2014) 7057–7069.

[124] P. Moyo, T. Mugadza, G. Mehlana, U. Guyo, Res. Chem. Intermed. 42 (2016) 6511–6529.

[125] K.E. Sekhosana, T. Nyokong, J. Mol. Struct. 1117 (2016) 140–146.

[126] A.B. Shivanandareddy, M. Kumar, V. Lakshminarayanan, RSC Adv. 5 (2015) 47692–47700.

[127] T. Mugadza, T. Nyokong, Electrochim. Acta 55 (2010) 2606–2613.

[128] X. Zhou, X. Wang, B. Wang, Z. Chen, C. He, Y. Wu, Sensors Actuators, B Chem. 193 (2014) 340–348.

[129] Z. Lin, G.H. Waller, Y. Liu, M. Liu, C. Wong, Nano Energy 2 (2013) 241–248.

[130] Y. Sheng, X. Tang, E. Peng, J. Xue, J. Mater. Chem. B 1 (2012) 512–521.

[131] G. Fazio, L. Ferrighi, C. Di Valentin, J. Catal. 318 (2014) 203–210.

[132] I. Uddin, P. Poddar, N. Phogat, Mater. Focus 2 (2013) 80–85.

[133] G. Zhou, E. Paek, G.S. Hwang, A. Manthiram, Nat. Commun. 6 (2015) 7760–7770.

[134] S. Yang, L. Zhi, K. Tang, X. Feng, J. Maier, K. Müllen, Adv. Funct. Mater. 22 (2012) 3634–3640.

[135] Y. Wang, Y. Shao, D.W. Matson, J. Li, Y. Lin, ACS Nano 4 (2010) 1790–1798.

[136] C. Wang, L. Sun, Y. Zhou, P. Wan, X. Zhang, J. Qiu, Carbon N. Y. 59 (2013) 537–546.

[137] I. Herrmann-Geppert, U.I. Kramm, J. Radnik, S. Fiechter, P. Bogdanoff, J. Electrochem. Soc. 156 (2009) B1283–B1292.

[138] J.Y. Kim, P.J. Reucroft, M. Taghiei, V.R. Pradhan, I. Wender, Energy & Fuels 8 (1994) 886–889.

[139] Y. Su, Y. Zhang, X. Zhuang, S. Li, D. Wu, F. Zhang, X. Feng, Carbon N. Y. 62 (2013) 296–301.

[140] Z.W. Liu, F. Peng, H.J. Wang, H. Yu, W.X. Zheng, J. Yang, Angew. Chemie - Int. Ed. 50 (2011) 3257–3261.

[141] F. Vitale, I. Fratoddi, C. Battocchio, E. Piscopiello, L. Tapfer, M.V. Russo, G. Polzonetti, C. Giannini, Nanoscale Res. Lett. 6 (2011) 1–9.

[142] R.O. Ogbodu, E.K. Amuhaya, P. Mashazi, T. Nyokong, Spectrochim. Acta - Part A Mol. Biomol. Spectrosc. 149 (2015) 231–239.

[143] P. Mashazi, C. Togo, J. Limson, T. Nyokong, J. Porphyr. Phthalocyanines 14 (2010) 252–263.

[144] S. Barazzouk, C. Daneault, Nanomaterials 2 (2012) 187–205.

[145] G.I. Cárdenas-Jirón, M.A. Gulppi, C.A. Caro, R. del Río, M. Páez, J.H. Zagal, Electrochim. Acta 46 (2001) 3227–3235.

[146] Z. Li, C. He, Z. Wang, Y. Gao, Y. Dong, C. Zhao, Z. Chen, Y. Wu, W. Song, Photochem. Photobiol. Sci. 15 (2016) 910–919.

[147] M.-E. Ragoussi, G. Katsukis, A. Roth, J. Malig, G. de la Torre, D.M. Guldi, T. Torres, J. Am. Chem. Soc. 136 (2014) 4593–4598.

[148] X. Cai, Y. Zhang, X. Zhang, J. Jiang, J. Mol. Struct. THEOCHEM 801 (2006) 71–80.

[149] H.X.H. Z. D. Liu, PLoS One 7 (2012) 50367–50374.

[150] J.I. Paredes, A. Marti, J.M.D. Tasco, A. Martı, Langmuir 24 (2008) 10560–10564.

[151] B.Y.S. Chang, N.M. Huang, M.N. An'amt, A.R. Marlinda, Y. Norazriena, M.R. Muhamad, I. Harrison, H.N. Lim, C.H. Chia, Int. J. Nanomedicine 7 (2012) 3379–3387.

[152] G. Sobon, J. Sotor, J. Jagiello, R. Kozinski, M. Zdrojek, M. Holdynski, P. Paletko, J. Boguslawski, L. Lipinska, K.M. Abramski, Opt. Express 20 (2012) 1946319473.

[153] R. Li, Z. Wei, X. Gou, W. Xu, RSC Adv. 3 (2013) 9978.

[154] A. Ashraf, Y. Wu, M.C. Wang, N.R. Aluru, S.A. Dastgheib, S.W. Nam, Langmuir 30 (2014) 12827–12836.

[155] Z. Luo, S. Lim, Z. Tian, J. Shang, L. Lai, B. MacDonald, C. Fu, Z. Shen, T. Yu, J. Lin, J. Mater. Chem. 21 (2011) 8038–8044.

[156] A.J. Bard, L.R. Faulkner, Fundamentals and Applications, 2nd ed., JOHN WILEY & SONS, INC., New York, 2001.

[157] J.J. Gooding, V.G. Praig, E. a Hall, Anal. Chem. 70 (1998) 2396–2402.

[158] A. Sivanesan, S.A. John, Electrochim. Acta 54 (2009) 7458–7463.

[159] S. Griveau, J. Pavez, J.H. Zagal, F. Bedioui, J. Electroanal. Chem. 497 (2001) 75–83.

[160] A. Salimi, C.E. Banks, R.G. Compton, Phys. Chem. Chem. Phys. 5 (2003) 3988–3993.

[161] Z. Li, M. Lieberman, W. Hill, Langmuir 17 (2001) 4887–4894.

[162] R.A. Masitas, F.P. Zamborini, J. Am. Chem. Soc. 134 (2012) 5014–5017.

[163] P. Mashazi, T. Mugadza, N. Sosibo, P. Mdluli, S. Vilakazi, T. Nyokong, Talanta 85 (2011) 2202–2211.

[164] S. Maree, T. Nyokong, J. Electroanal. Chem. 492 (2000) 120–127.

[165] L. Aldous, R.G. Compton, Phys. Chem. Chem. Phys. 13 (2011) 5279–5287.

[166] C.A. Caro, F. Bedioui, J.H. Zagal, Electrochim. Acta 47 (2002) 1489–1494.

[167] K.I. Ozoemena, T. Nyokong, P. Westbroek, Electroanalysis 15 (2003) 1762–1770.

[168] S.S. Khaloo, M.K. Amini, S. Tangestaninejad, S. Shahrokhian, R. Kia, J. Iran. Chem. Soc. 1 (2004) 128–135.

[169] M.H. Pournaghi-Azar, R. Sabzi, J. Electroanal. Chem. 543 (2003) 115–125.

[170] A.A. Ensafi, S. Behyan, Sensors Actuators, B Chem. 122 (2007) 282–288.

[171] X. Yang, J. Bai, Y. Wang, X. Jiang, X. He, Analyst 137 (2012) 4362–4367.

[172] X. Qin, H. Wang, X. Wang, Z. Miao, Y. Fang, Q. Chen, X. Shao, Electrochim. Acta 56 (2011) 3170–3174.

[173] L. Zhang, Z. Fang, Y. Ni, G. Zhao, Int. J. Electrochem. Sci. 4 (2009) 407–413.

[174] E.K. A.D. Özel, Z. DurmusS, I. Yılmaz, A. Cukurovalı, Acta Chim. Slov. 56 (2009) 797–806.

[175] A.S. Adekunle, B.B. Mamba, B.O. Agboola, K.I. Ozoemena, Int. J. Electrochem. Sci. 6 (2011) 4388–4403.

[176] G. Yu, W. Wu, X. Pan, Q. Zhao, X. Wei, Q. Lu, Sensors 15 (2015) 2709–2722.

[177] H.G. Zhan-Hong Li, B. Viguier, S.-G. Sun, And, Jean-Louis Marty, Sensors 13 (2013) 5028–5039.

[178] C. Xu, F. Sun, H. Gao, J. Wang, Anal. Chim. Acta 780 (2013) 20–27.

[179] A.A. Karyakin, E.E. Karyakin, Sensors Actuators B Chem. 57 (1999) 268–273.

[180] B. Halliwell, M. Veronique, L. Hua, FEBBS Lett. 486 (2000) 14–17.

[181] V. Ganesan, R. Ramaraj, J. Appl. Electrochem. 31 (2001) 585–590.

[182] I.G. Casella, M. Contursi, Electroanalysis 24 (2012) 752–758.

[183] R. Thangamuthu, Y. Pan, S. Chen, Sensors Actuators B. Chem. 151 (2011) 377–383.

[184] J.M. Zen, A. Senthil Kumar, M.R. Chang, Electrochim. Acta 45 (2000) 1691–1699.

[185] M.E.G. Lyons, C.A. Fitzgerald, M.R. Smyth, Analyst 119 (1994) 855–861.

[186] I.S. Hosu, Q. Wang, A. Vasilescu, S.F. Peteu, V. Raditoiu, S. Railian, V. Zaitsev, K. Turcheniuk, Q. Wang, M. Li, R. Boukherroub, S. Szunerits, RSC Adv. 5 (2015) 1474–1484.

[187] Y. Shi, Z. Liu, B. Zhao, Y. Sun, F. Xu, Y. Zhang, Z. Wen, H. Yang, Z. Li, J. Electroanal. Chem. 656 (2011) 29–33.

[188] S. Patra, N. Munichandraiah, J. Chem. Sci. (Bangalore, India) 121 (2009) 675–683.

[189] K.S. Tseng, L.C. Chen, K.C. Ho, Sensors Actuators, B Chem. 108 (2005) 738–745.

[190] A. Salimi, R. Hallaj, S. Soltanian, H. Mamkhezri, Anal. Chim. Acta 594 (2007) 24–31.

[191] C.M. Welch, C.E. Banks, A.O. Simm, R.G. Compton, Anal. Bioanal. Chem. 382 (2005) 12–21.

[192] N.A. Tapan, J. Prakash, Turkish J. Eng. Environ. Sci. 29 (2005) 95–103.

[193] E. Higuchi, H. Uchida, M. Watanabe, J. Electroanal. Chem. 583 (2005) 69–76.

[194] T. Mugadza, T. Nyokong, Synth. Met. 160 (2010) 2089–2098.

[195] H.L. Poh, P. Šimek, Z. Sofer, M. Pumera, ACS Nano 7 (2013) 5262–5272.

[196] G. Scandurra, A. Arena, C. Ciofi, G. Saitta, Sensors (Basel). 13 (2013) 3878–3888.

[197] L.S. Panchakarla, A. Govindaraj, C.N.R. Rao, Inorganica Chim. Acta 363 (2010) 4163–4174.

[198] R. Ojani, J. Raoof, R. Babazadeh, J. Chinese Chem. Soc. 57 (2010) 1042–1049.

[199] S. Fery-Forgues, D. Lavabre, J. Chem. Educ. 76 (1999) 1260–1264.

[200] A. Ogunsipe, J. Chen, T. Nyokong, New J. Chem. 28 (2004) 822–827.

[201] S.Y. J. R. Stone, Antioxid. Redox Signal. 8 (2006) 243–270.

[202] O. Adegoke, S. Khene, T. Nyokong, J. Fluoresc. 23 (2013) 963–974.

[203] Q. Xu, J. Wang, Z. Wang, Biosensors 2719 (2009) 2496–2508.